The Pennsylvania State University

The Graduate School

Department of Materials Science and Engineering

DAMAGE-FREE PATTERNING OF FERROELECTRIC LEAD ZIRCONATE TITANATE THIN FILMS FOR MICROELECTROMECHANICAL SYSTEMS VIA CONTACT PRINTING

A Dissertation in

Materials Science and Engineering

by

Aaron Welsh

Submitted in Partial Fulfillment

of the Requirements

for the Degree of

Doctor of Philosophy

May 2016

The dissertation of Aaron Welsh was reviewed and approved* by the following:

Susan Trolier-McKinstry
Professor of Ceramic Science and Engineering
Dissertation Advisor
Chair of Committee

Clive A. Randall
Professor of Materials Science and Engineering

Michael T. Lanagan
Professor of Engineering Science and Mechanics

Michael A. Hickner
Associate Professor of Materials Science and Engineering

Suzanne Mohney
Professor of Materials Science and Engineering and Electrical Engineering
Chair, Intercollege Graduate Degree Program in Materials Science and Engineering

*Signatures are on file in the Graduate School

ABSTRACT

This thesis describes the utilization and optimization of the soft lithographic technique, microcontact printing, to additively pattern ferroelectric lead zirconate titanate (PZT) thin films for application in microelectromechanical systems (MEMS). For this purpose, the solution wetting, pattern transfer, printing dynamics, stamp/substrate configurations, and processing damages were optimized for incorporation of PZT thin films into a bio-mass sensor application. This patterning technique transfers liquid ceramic precursors onto a device stack in a desired configuration either through pattern definition in the stamp, substrate or both surfaces.

It was determined that for ideal transfer of the pattern from the stamp to the substrate surface, wetting between the solution and the printing surface is paramount. To this end, polyurethane-based stamp surfaces were shown to be wet uniformly by polar solutions. Patterned stamp surfaces revealed that printing from raised features onto flat substrates could be accomplished with a minimum feature size of 5 μm. Films patterned by printing as a function of thickness (0.1 to 1 μm) showed analogous functional properties to continuous films that were not patterned. Specifically, 1 μm thick PZT printed features had a relative permittivity of 1050 ± 10 and a loss tangent of 2.0 ± 0.4 % at 10 kHz; remanent polarization was 30 ± 0.4 $\mu C/cm^2$ and the coercive field was 45 ± 1 kV/cm; and a piezoelectric coefficient $e_{31,f}$ of -7 ± 0.4 C/m^2. No pinching in the minor hysteresis loops or splitting of the first order reversal curve (FORC) distributions was observed.

Non-uniform distribution of the solution over the printed area becomes more problematic as feature size is decreased. This resulted in solutions printed from 5 μm wide raised features exhibiting a parabolic shape with sidewall angles of ~ 1 degree. As an alternative, printing solutions from recesses in the stamp surface resulted in more uniform solution thickness transfer

across the entire feature widths, with increased sidewall angles of ~ 35 degrees. This was at the cost of degrading line edge definition from ~ 200 nm to ~ 500 nm. The loss of line edge definition was mitigated through the combined use of printing from stamp recesses onto raised substrate features. This allowed for printing of PZT features down to 1 μm wide. Solutions could also be transferred onto both fixed and free standing cantilever structures patterned into a substrate surface.

Optimization of the stamp removal from the substrate was crucial in increasing sidewall angles of printed PZT films. It was determined that solutions gel once deposited onto the stamp before printing. As a result, printed films could not redistribute easily after transfer had occurred. Through a combination of varying peeling directions and peeling rates, it was possible to deposit thin film PZT on a pre patterned feature ~ 1 μm wide with sidewall angles > 80 degrees.

These printing techniques were utilized in printing a 250 nm thick 30/70 PZT onto pre-patterned cantilever structures for use in a bio-functionalized, mass sensing resonating structure in collaboration with a bio-nanoelectromechincal sensing research group from the University of Toulouse, France. The features ranged in lateral size from 30 down to 1 μm. The printed devices exhibited a relative permittivity of 500 ± 10 and a loss tangent of 0.9 ± 0.1 %. The hysteresis loops were well formed, without pinching of the loops, and exhibited remanent polarizations of 24 ± 0.5 μC/cm^2, and coercive fields of 110 ± 1 kV/cm. Dry etched features of the same size and thickness displayed a relative permittivity of 445 ± 8 and a loss tangent of 0.9 ± 0.1 %. The hysteresis loops exhibited pinched loops with remanent polarizations of 24 ± 0.7 μC/cm^2, and coercive fields of 112 ± 2 kV/cm. Upon cycling, the dry etched films developed a 20 kV/cm imprint with reduced remanent polarizations to 20.5 ± 0.5 μC/cm^2.

An understanding of the influence of patterning on the material properties is essential to predicting and controlling the behavior of polycrystalline films for MEMS applications. The influence of pinning centers on domain wall motion, particularly near feature sidewalls, in patterned features was explored in reactive ion etched (RIE) and microcontact printed films with the same thickness (i.e. 1 μm) and lateral feature size (i.e. 5 and 10 μm). This was accomplished by measuring global dielectric nonlinearity through Rayleigh and minor hysteresis measurements. For comparative purposes, local quantitative mapping of the piezoelectric nonlinearity was undertaken through the use of band excitation piezo-response force microscopy (BE-PFM). The printed and etched films exhibited differing microstructures which precluded quantitative direct comparisons. However, qualitative trends were identified. The dielectric aging rate of all Rayleigh parameters for the etched films increased with increases in perimeter length. In particular, the aging of the dielectric irreversible/reversible Rayleigh ratio ($\alpha/\varepsilon_{init}$) increased from -7 ± 0.6 %/decade to -11.6 ± 0.7 %/decade (600 to 5 μm in width, respectively). In contrast, the printed films showed very slight aging rates. BE-PFM measurements revealed that defects from the etching process introduced large concentrations of pinning centers near the patterned sidewalls, resulting in reductions in the piezoelectric irreversible/reversible Rayleigh ratio ($\alpha/d_{33,init}$) as far as 750 nm from the sidewall. Transmission electron microscopy (TEM) and energy dispersive spectroscopy (EDS) showed that variations in stoichiometry of crystal quality were not the predominant factor controlling the decreased domain wall mobility near sidewalls. In contrast to the etched films, printed films showed an increase in $\alpha/d_{33,init}$ as the sidewall was approached due to mechanical declamping from the substrate.

TABLE OF CONTENTS

LIST OF FIGURES ix

LIST OF TABLES xxi

ACKNOWLEDGEMENTS xxii

Chapter 1 Introduction 1

- 1.1 Patterning of Ferroelectric Thin Films for MEMS 1
- 1.2 Thesis Organization 6

Chapter 2 Low-Cost, Damage-Free Patterning of Lead Zirconate Titanate Films 7

- 2.1 Introduction 8
- 2.2 Experimental Procedure 11
  - 2.2.1 Stamp Fabrication 11
  - 2.2.2 PZT Processing 12
  - 2.2.3 Measurements 14
- 2.3 Results and Discussion 16
  - 2.3.1 Printing with Polyurethane-Based Stamps 16
  - 2.3.2 PZT Prints 18
  - 2.3.3 Microstructural Characterization 19
  - 2.3.4 Electrical Characterization 20
- 2.4 Conclusions 25

Chapter 3 Increasing Sidewall Angles of Contact Printed Piezoelectric Thin Films 27

- 3.1 Introduction 28
- 3.2 Experimental Procedure 30
  - 3.2.1 Recess Printed PZT Film Fabrication 30
  - 3.2.2 Patterned Substrate Fabrication 31
  - 3.2.3 Released Cantilever Fabrication 31
- 3.3 Results and Discussion 32
  - 3.3.1 Recess Printing from Patterned Stamps 32
  - 3.3.2 Printing on Patterned Substrates 41
  - 3.3.3 Printing on Released Cantilevers 50
  - 3.3.4 Mechanical Testing of Released Cantilevers 54
- 3.4 Conclusions 55

Chapter 4 Integrating Piezoelectric Materials into Bio-Sensing Applications by Printing Ceramic Solutions 57

- 4.1 Introduction 58
- 4.2 Experimental Procedure 60

4.2.1 Silicon on Insulator Substrate Fabrication..60
4.2.2 Patterning SOI Wafers...62
4.2.3 Material Characterization...66
4.3 Results and Discussion 67
4.3.1 Device Material Stack...67
4.3.2 Ni Hard Mask Deposition 68
4.3.3 Nucleation of PZT on Dry Etched Pt Surfaces 72
4.3.4 Wet Etching PZT 83
4.3.5 Dry Etching Defects...85
4.3.6 Final Device Fabrication...92
4.3.7 Electrical Characterization of PZT 103
4.4 Conclusions...107

Chapter 5 Probing Ferroelectric Domain Wall Mobility of Patterned Thin Films at the Nanoscale..108

5.1 Introduction...109
5.2 Experimental Procedure...111
5.2.1 Film Patterning..111
5.2.2 Structural Characterization 114
5.2.3 Electrical Characterization...115
5.2.4 Band Excitation Piezo-response Force Microscopy 116
5.3 Results and Discussion 119
5.3.1 Global Structural Characterization 119
5.3.1 Global Domain Wall Mobility..121
5.3.1 Local Structural Characterization 133
5.3.1 Local Domain Wall Mobility...138
5.4 Conclusions...155

Chapter 6 Conclusions and Future Work...157

6.1 Conclusions...157
6.1.1 Stamp Optimization 157
6.1.2 Printing Optimization..158
6.1.3 Printing onto Patterned Substrates 158
6.1.4 Nonlinearity of Patterned PZT...159
6.2 Recommendations for Future Work..160
6.2.1 Printing Dynamics 160
6.2.2 Printing Alternative Complex Oxide Solutions 160
6.2.3 Investigation of Pattering Damage at the Nanoscale 166

Appendix A: Wetting of a Liquid on a Surface 170

Appendix B: Cantilever Dynamics for Mass Detection 172

Appendix C: BE-PFM Maps across a 10 μm Lateral Feature Using a Scanning Direction Perpendicular to the Sidewall 173

Appendix D: Area Equations and Parameters Used in Parallel Mixing Model..........................174

Appendix E: MATLAB Code for Calculating Nonlinearity Maps..176

References..185

LIST OF FIGURES

Figure 1-1. Schematic depicting the molding of a patterned stamp and the various soft lithographic techniques employed in patterning a precursor liquid. (a) MicroTransfer Molding, (b) Micromolding in Capillaries, (c) Embossing are all single deposition routes which utilize the recessed channels of the stamp in various ways to create the desired pattern. (d) MicroContact Printing directly transfers material from the stamp surface to the substrate 4

Figure 2-1. Schematic depicting the molding of a patterned stamp and the µCP of PZT liquid solutions onto a flat surface 10

Figure 2-2. Pattern transfer of 2-MOE based PZT solutions using PDMS and polyurethane composite stamps. (a) 1st and (b) 2nd stamping cycles using PDMS stamp. (c) 1st and (d) 50th stamping cycle using polyurethane composite stamps 17

Figure 2-3. Optical profilometry images of µCP PZT (a) 500 × 400 µm feature and (b) 5 µm PZT lines. (c) Light intensity map of an intricate µCP PZT design 18

Figure 2-4. (a) Grazing incidence XRD scan of µCP 52/48 PZT on a Pt/Ti/SiO_2/Si(100) wafer (polyurethane stamps). (b) SEM surface micrographs of a blanket film and a (c) µCP film, both of which are 420 nm thick 19

Figure 2-5. Electrical property measurements of µCP sample set compared with a blanket film sample set over a thickness range of 0 to 1 µm. (a) Relative permittivity and loss tangent of the PZT films. (b) Remanent polarization (P_r) and coercive field (E_C) of the PZT films. (c) The transverse piezoelectric coefficient, $e_{31,f}$, for µCP and a blanket film sample set 20

Figure 2-6. (a) Rayleigh plot comparing a blanket and RIE PZT film, thicknesses of 480 and 400 nm, respectively. (b) Reversible and irreversible Rayleigh coefficients for blanket and μCP PZT. (c) Minor hysteresis loop comparing a blanket and RIE PZT film (480 and 400nm thick, respectively). (d) Minor hysteresis loop comparing a blanket and μCP PZT film, thicknesses of 850 and 875 nm, respectively 23

Figure 2-7. (a through c) FORC distribution of blanket and μCP PZT films, thicknesses of 850 and 875 nm, respectively. A reversible FORC distribution (a), and irreversible FORC distributions comparing blanket (b) and μCP (c) PZT films. (d through f) FORC distribution blanket and RIE PZT films, thicknesses of 480 and 400 nm, respectively. A reversible FORC distribution (d), and irreversible FORC distributions comparing unetched blanket (e) and RIE (f) PZT films 25

Figure 3-1. Surface profile of a PZT thin film (a) printed from a 5 μm lateral protrusion feature and (b) molded in microcapillary channels..29

Figure 3-2. Schematic showing sufficient pressure applied for the recesses of the stamp to contact a substrate 29

Figure 3-3. Optical microscopy images of the (a) initial printing step used to clean the protrusions of the stamp of ceramic precursors, and the (b) subsequent printing of PZT precursor solution from the recesses of the stamp. The PZT features are darker in color 33

Figure 3-4. Optical microscopy images of recess printing. (a) Sacrificial printing using a stamp with well recesses which are 10.3 μm deep. (b) Recess printing using a stamp with 3.6 μm, (c) 2.1 μm, and (d) 1.2 μm deep well recesses..34

Figure 3-5. Schematic displaying the (a) protrusion and (b) recess printing process 36

Figure 3-6. Recess printing using PU/PDMS composite stamps. (a) Composite stamp with rough surface and (b) line edge roughness of subsequently printed feature. (c) Composite stamp with smooth surface and (d) line edge roughness of subsequently printed feature 38

Figure 3-7. (a) Optical microscopy image of a PZT feature printed via the recess printing technique, and (b) the corresponding surface profile of feature shown to the left in comparison to a PZT feature of similar size printed from a stamp protrusion 39

Figure 3-8. Stacking of PZT prints through recess printing. (a) Representative stack displaying misalignment between subsequent printing cycles. Electrical measurements of a (b) 5 layer recess printed 300 nm PZT stack. (c) Relative permittivity and loss tangent as a function of frequency. (d) Hysteresis loop as a function of increasing electric field 40

Figure 3-9. Schematic of printing ceramic solutions onto patterned substrates with flat stamps 42

Figure 3-10. Optical microscopy images of PZT solution printed onto patterned substrates. (a) Fluid redistribution and (b) printing defects are evident after the stamp was peeled from the substrate from right to left across the features 43

Figure 3-11. Cross-sectional SEM images of PZT solution printed onto a patterned substrate. Solution was spun onto stamp at (a) 1000 rpm, (b) 1500 rpm, and (c) 3000 rpm 44

Figure 3-12. Cross-sectional SEM images of 300 nm crystallized PZT film printed on a patterned substrate feature. The stamp was separated from the substrate (a) parallel and (b) perpendicular to the viewing direction 45

Figure 3-13. Cross-sectional SEM images of crystallized PZT film printed with various peeling rates of the stamp from the patterned substrate. Printing was done by hand at peeling rates on the order of (a and c) millimeters per second (b and d) meters per second. The substrate features varied in size: (a) 20, (b) 10, and (c and d) 1 µm features. All features had stamp peeling directions parallel to the viewing direction 47

Figure 3-14. SEM micrographs of crystallized PZT film printed with ideal solution thickness per print, stamp peeling direction, and stamp peeling rate for a (a) 10 µm and a (b) 1 µm. The (c) cross-sectional and (d) top down microstructure of a crystallized PZT film deposited by printing is displayed 50

Figure 3-15. SEM micrographs of (a) released Si cantilevers and (b) released Pt/TiO_2/HfO_2/Si cantilevers 51

Figure 3-16. (a) XRD scan of PZT deposited over a Pt/TiO_2/HfO_2/Si substrate. (b) Dielectric and (c) ferroelectric properties of the film 52

Figure 3-17. Optical image of a (a) released 6 µm wide cantilever which was aligned to a patterned stamp. (b) Patterned stamp being peeled from patterned wafer with released cantilever. (c and d) Colorized SEM micrographs of the PZT printed onto a released 2 µm wide cantilever..54

Figure 3-18. Mechanical properties of the released cantilever stack. Resonant frequency as a function increasing number of material layers beginning with bare Si and ending with a PZT/Pt/TiO_2/HfO_2/Si stack 55

Figure 4-1. Schematic process flow to create a bio-mass sensor. The top image in each cell shows a 3D representation of the wafer. The bottom image in each cell represents a vertical cross-section of the device 61

Figure 4-2. Schematic displaying the (a) electroplating of Ni onto a Pt coated Si wafer for use as a dry etch mask and a (b) pulse train from a current power supply 63

Figure 4-3. SEM image of the microstructure of (a) Pt sputtered at room temperature onto a HfO_2 coated SOI wafer, and (b) the subsequent crystallization of blanket PZT 68

Figure 4-4. SEM images of (a) Ni hard masks sputtered onto Pt by a lift-off technique. (b) Cracking of the Ni became evident as the thickness of the Ni was increased. (c) Low sidewall angles of mask resulted in notching around the perimeter of the etched features, as well as a decrease in the size of the features (ex. from 2 to 1.1 µm wide)...69

Figure 4-5. Graphs displaying the internal stress of electroplated metals as a function of (a) pH, (b) current density, and (c) plating temperature 70

Figure 4-6. (a) SEM microstructure of an electroplated Ni deposit from a solution with a pH of 2.7, and the corresponding (b) optical image of 100 mm wafer where the electroplated Ni resulted in delamination of the Pt from the underlying stack. (c) SEM microstructure of an electroplated Ni deposit from a solution with a pH of 4.3, and the corresponding (d) optical image of the 100 mm wafer with no delamination 71

Figure 4-7. Patterns dry etched into a Pt coated Si wafer. Residues from (a and b) electroplated Ni and (b and c) sputtered Ni hard mask remain on the surface of the dry etched Pt after Ni removal 73

Figure 4-8. SEM images of (a) residues on a dry etched Pt feature, (b) PZT crystallized on top of dry etched Pt features with localized areas of etching residues, and (c) high magnification focused on an area where PZT was crystallized over etching residues 74

Figure 4-9. SEM images of PZT crystallized on top of dry etched Pt features. PZT layers crystallized at 700 ˚C for (a) 30 and (b) 600 s. PZT crystallized at (c) 650, (d) 700, (e) 750, (f) and 800 ˚C for 300 s each..76

Figure 4-10. Optical images of Ni residues on Pt features. Removal of residues was attempted by subjecting residues to (a) Nickel etchant TFB, (b) Nickel etchant Type 1, (c) Nickel Etchant TFG, and (d) Nanostrip baths 78

Figure 4-11. SEM images of (a) dry etching Ni residues on Pt features, and (b) removal of residues using ACT 935 78

Figure 4-12. SEM images of PZT, crystallized after every spin-coated layer, on top of dry etched Pt features cleaned with ACT 935 (electroplated Ni mask). (a) Two PZT layers crystallized, with a thickness of 150 nm, with rosette grain formation in a secondary phase matrix. (b) Nine PZT layers crystallized, with a thickness of 1 μm. The grains have impinged and removed a majority of secondary phase. (c) High magnification reveals microcracks formed between PZT grains......................................79

Figure 4-13. SEM images of PZT, crystallized after every spin-coated layer, on top of dry etch Pt features cleaned with ACT 935 (evaporated Ni mask). (a) Five PZT layers crystallized, with a thickness of 400 nm, with rosette grain formation alongside a secondary phase (dark spots). (b and c) High magnification images of PZT microstructure 80

Figure 4-14. Optical images of (a) 100 nm of Pt sputtered additionally over dry etching Ni residues on a Pt feature, (b) PZT crystallized over Pt feature shown to the left. (c) High magnification focused on an area where PZT was fired specifically over etching residues (region A) and (d) an area where no etching residue was present (region B)..81

Figure 4-15. SEM image of (a) PZT crystallized over a dry etched Pt feature cleaned with ACT 935 to remove Ni residues followed by 100 nm sputtered Pt. (b) High magnification showing the PZT microstructure from the center of the Pt feature shown to the left..82

Figure 4-16. Optical image of (a) 30/70 PZT crystallized over a dry etched Pt feature cleaned with ACT 935 to remove Ni residues. (b) High magnification SEM image showing the PZT microstructure from the center of the Pt feature shown to the left........83

Figure 4-17. Cross-sectional SEM images of the undercut from wet etching of 52/48 PZT. Photoresist mask was baked at (a) 115 ˚C for 60 s and (b) hard backed at 145 ˚C for 30 min. (c) Top down SEM image of wet etched PZT protected with 145 ˚C hard bake..84

Figure 4-18. Optical images of wet etching 30/70 PZT utilizing an SPR 1813 photoresist mask. (a) BOE 10:1 and (b) BOE 6:1 wet etchant was used to expose the bottom Pt surface..85

Figure 4-19. (a) Low and (b) high magnification optical images of etching defects in the surface of an electroplated Ni hard mask, and (c) the corresponding defect transferred into the protected Pt surface beneath the hard mask 86

Figure 4-20. Cross-sectional SEM images of etch redeposition after dry etching Pt using (a) Ni and (b) photoresist as an etch mask. (c) Redepositions from a SPR 955 photoresist mask which remained on the sample even after the mask was removed. (d) 400 nm wide sidewall (~ 10˚) in the Pt resulting in enlargement of the etched feature. (e) Cross-sectional SEM image of etch redeposition for comparison purposes with EDS images on right showing the same area of interest. Characteristic $K_{\alpha 1}$ X-rays of (f) carbon, (g) platinum, (h) titanium, and (i) chlorine 88

Figure 4-21. Cross-sectional SEM images of etch redeposition after dry etching Pt (ICP-RIE) (NE-550, ULVAC). (a) Dry etching Pt at 3.5 mTorr base pressure, 15 s etch steps, 50 W chuck bias, and 30 sccm Cl_2 gas. (b) 40 sccm of Ar and (c) 4 sccm of O_2 gas was added to the etch. (d) Chuck power was increased to (d) 90, (e) 175, and (f) 225 W. (g) Base pressure was increased to 10 mTorr. (h) Etch step time was increased to 30 s. (i) Optical image of dry etched Pt feature with no fences after optimized etch and photoresist strip with ultrasonication...90

Figure 4-22. Optical images of (a) Pt features with a Ni hard mask (b) dry etched with Cl_2 gas. (c) Liquid hydrochloric acid formed on the surface of the sample after being left in normal atmospheric conditions for 4 hrs. (d) A water rinse removed liquid acid, revealing etch pits through the mask into the underlying stack 92

Figure 4-23. Variable angle spectroscopic ellipsometry scan with fitted model to determine thickness of SOI stack ($HfO_2/SiO_2/Si/SiO_2/Si$) 93

Figure 4-24. SEM images of sputtered Pt on top of SOI wafer. (a) Continuous Pt with no porosity present. (b) High magnification of the sputtered microstructure 94

Figure 4-25. (a) Optical and (b) SEM image of a 2 μm electroplated Ni feature. (c) SEM image of microstructure of the electroplated Ni. (d) Polarized optical and (e) SEM image of 2 μm dry etched Pt feature after hard mask removal. (f) SEM image of microstructure of the dry etched Pt surface which was protected with electroplated Ni..95

Figure 4-26. Optical images of 275 nm 30/70 PZT printed onto (a) 2 and (b) 30 µm features. (c) SEM image of a printed PZT film crystallized on a 5 µm Pt feature. (d) High magnification SEM image of PZT on 5 µm feature. (e and f) High magnification of microstructure of the PZT crystallized into the perovskite phase with no evidence of secondary phases present 97

Figure 4-27. Optical images of a printed 275 nm thick 30/70 PZT film crystallized on top of a SOI wafer, and wet etched with BOE 6:1 around (a) 2 and (b) 5 µm features...........99

Figure 4-28. SEM images of a 30 nm top Pt electrode evaporated onto a printed 275 nm thick 30/70 PZT film crystallized on top of a (a) 2 and (b) 5 µm feature. (c) High magnification image of the microstructure of the top Pt with no evidence of porosity 100

Figure 4-29. SEM images of dry etched bottom Pt electrode around (a) 5 and (b) 30 µm features...101

Figure 4-30. SEM image of dry etched HfO_2 around (a) 2 and (b) 30 µm PZT printed features...102

Figure 4-31. SEM images of final device stack of Pt/PZT/Pt/Ti/HfO_2/SiO_2/Si with lateral feature sizes of (a) 1, (b) 2, (c) 5, and (d) 30 µm...102

Figure 4-32. (a) Optical image of 30 µm dry etched 52/48 PZT feature. (b) Relative permittivity and loss tangent, (c) PE loop, and (d) CV behavior of a dry etched 30 µm 52/48 PZT feature...104

Figure 4-33. (a) Optical image of 30 µm dry etched 30/70 PZT feature. (b) Relative permittivity, loss tangent and (c) PE loop comparison between a dry etched (red) and printed (black) 30 µm 30/70 PZT feature 275 nm thick. (d) PE loop of RIE film before (red) and after poling (blue). (e) Rayleigh behavior of RIE film used to (f) calculate minor hysteresis loop (green) and compare to measured minor loop (red)......106

Figure 5-1. (Bottom Row) Four different sine waves (blue lines) with four different frequencies. The vertical line highlights the phase shift relative to each of the four sine waves. (Top Row) Combining these four sine waves yields a signal with varying degrees of chirp character. (a) The signal with the most phase variation is the chirp signal. (b) The signal with only slight phase variation is a mixture of chirp and sinc signals. (c) The signal with no phase variation is the sinc signal 118

Figure 5-2. (a) XRD scans of dry etched (black) and printed (red) PZT. (b) SEM micrograph of continuous PZT crystallized on a 4 in Pt-coated Si wafer before the dry etching step. (c) Top down and (d) cross-sectional SEM micrographs of PZT printed onto a pre-patterned substrate 120

Figure 5-3. (a) Optical image showing examples of the various dry etched patterns used in the global electrical measurements. (b) Optical image exhibiting the capacitor configuration used to measure the global electrical properties in the printed PZT samples. (c) PE loop of printed 200 μm diameter electrode (green) in comparison to a RIE 625 μm diameter electrode (orange). (d) PE loops of RIE 5 μm feature before (black) and after (red) poling 123

Figure 5-4. Field dependent relative permittivity scan of poled PZT 52/48 films. The Rayleigh regime of the dry etched (black line) and printed (red line) sample extends up to ~30 kV/cm (2.9 V) and ~35 kV/cm (3.7 V) 124

Figure 5-5. Aging of the field dependent relative permittivity of poled PZT 52/48. (a) RIE 5 μm lateral features exhibit a larger degree of aging of the Rayleigh behavior in comparison to (b) printed PZT. The error bars represent error propagation calculations between multiple electrodes...125

Figure 5-6. Time dependent (a through c) Rayleigh and (d through f) normalized Rayleigh parameters for large pad RIE (blue line), bus arm (green line), 10 μm arm (red line), 5 μm arm (black line), and printed PZT (orange line) electrodes. The error bars represent fitting errors 127

Figure 5-7. Minor hysteresis loops of poled (a) 5 μm RIE and (b) printed PZT 52/48. A comparison between all feature sizes of the (c) ΔP and (d) Normalized ΔP at 0 kV/cm (error bars represent error propagation calculations for capacitance, thickness, and area of multiple electrodes). A comparison between the measured (solid lines) and calculated (dashed lines) (via Rayleigh parameters) minor hysteresis loops for (e) 5 μm RIE and (f) printed PZT 130

Figure 5-8. (a) Top down SEM and (b) cross-section TEM image of the 10 μm feature created by dry etching PZT. (c) Top down SEM and (d) cross-section TEM image of the 10 μm feature created by printing PZT 135

Figure 5-9. High magnification (a) bright field (BF) TEM, (b) HRTEM, and (c) STEM images of cross-sectioned, dry etched PZT (10 μm feature) in close proximity to the sidewall of the feature 136

Figure 5-10. (a) HRTEM and (b) STEM images of cross-sectioned, printed PZT (10 μm lateral feature) in close proximity to the sidewall...137

Figure 5-11. High Angle Annular Dark Field (HAADF) TEM images of (a) dry etched PZT 10 μm arm structures and (b) printed PZT 10 μm lateral features in close proximity to a sidewall. (c) The graphs of the corresponding EDS scans lines in the TEM images. The EDS results exhibit the atomic % of Pb, Zr, and Ti as a function of position in relation to the patterned sidewall of both a RIE (squares) and printed (circles) feature 138

Figure 5-12. Tip amplitude response from a single point on a RIE sample with (a) 100%, (b) 25%, and (c) 3% chirp signal mixed with a sinc function. A_{max} is the maximum amplitude of the cantilever tip extrapolated from SHO equation fittings. 100 consecutive measurements were performed sweeping up and down in frequency (blue lines). The 100 measurements were also averaged for both the up and down frequencies (red lines). (d) ANOVA box plots for excitation waveforms with various degrees of chirp character (chirp up is red box and chirp down is blue box) were created from the 100 measurements, the whiskers represent 1.5 times the interquartile range (IQR)...140

Figure 5-13. ANOVA boxplots for various numbers of repeated waveforms per A_{max} measurement with both chirp up (red box) and chirp down (blue box) signals 141

Figure 5-14. Tip amplitude response from a single point on a RIE sample with (a) 1, (b) 2.5, and (c) 3.5 V excitation amplitude. (d) ANOVA boxplots of chirp up (red box) and chirp down (blue box) signals for various excitation amplitudes 142

Figure 5-15. BE-PFM map showing the (a) resonance, (b) quality factor, (c) piezoresponse phase, (d) quadratic response, (e) linear response, and (f) $\alpha/d_{33,init}$ across a 5 x 5 µm area far away from the RIE patterned sidewall..144

Figure 5-16. A 5 x 10 µm BE-PFM map showing the (a) resonance frequency, (b) quality factor, and (c) piezoresponse phase across an etched 10 µm lateral PZT feature. A 5 x 3 µm BE-PFM map of the material in immediate proximity to a patterned sidewall shows the variation of the (d) quadratic, (e) linear, and (f) $\alpha/d_{33,init}$ as a function of position 145

Figure 5-17. A 2 x 2 µm BE-PFM scan on top of a 5 µm laterally patterned feature which shows the variation of the (a) resonance, (b) quality factor, (c) piezoresponse phase, (d) quadratic response, (e) linear response, and (f) $\alpha/d_{33,init}$ as the sidewall is approached 147

Figure 5-18. (a) Averaged $\alpha/d_{33,init}$ response of both 5 (red line) and 10 (black line) µm arms as a function of distance away from the sidewall (edge of PFM scan). The blue shaded region corresponds to the average $\alpha/d_{33,init}$ from Figure 5-15 (f) (i.e. 4.9 ± 0.8 x 10^{-3} cm/kV) and the red shaded region corresponds to decreased $\alpha/d_{33,init}$. (b) Cross-section TEM image of the dry etched 10 µm PZT feature showing the 750 nm spatial extent of reduced $\alpha/d_{33,init}$ (red region) determined from BE-PFM scans...148

Figure 5-19. (a) Optical and (b) SEM images of top Pt configuration for PFM tips to contact in the local BEPFM measurements 152

Figure 5-20. BE-PFM map showing the (a) resonance, (b) quality factor, (c) piezoresponse phase, (d) quadratic response, (e) linear response, and (f) $\alpha/d_{33,init}$ across a 1 x 1 µm area far away from the printed sidewall...153

Figure 5-21. A 1 x 1.25 μm BE-PFM scan, on top of a 10 μm laterally printed feature, which shows the variation of the (a) resonance, (b) quality factor, (c) piezoresponse phase, (d) quadratic response, (e) linear response, and (f) $\alpha/d_{33,init}$ as the sidewall is approached 155

Figure 6-1. Process flow detailing the creation of a 10 mL 0.4 M 0.5mol% Mn doped KNN solution with 10 % excess Na and K........162

Figure 6-2. Process flow detailing the deposition of a KNN thin film utilizing a 0.4M 0.5mol% Mn doped KNN solution with 10 % excess Na and K........163

Figure 6-3. XRD scan and SEM images of Mn doped KNN films after 500 ˚C (black line) crystallization for 5 min and 600 (red), 650 (blue), 700 (purple) and 750 ˚C (green) anneals for 30 min........164

Figure 6-4. P-E loops of Mn doped KNN thin films annealed at 600 (black), 650 (red), and 700 ˚C (blue) 165

Figure 6-5. Schematic of a single-point FORC BE switching spectroscopy (SS)-PFM measurement. (a) Schematic of a train of DC and BE pulses in BE SS-PFM (b) and the resulting piezoresponse as a function of time and frequency. (c) Piezoresponse as a function of frequency at different bias levels and the (d) corresponding frequency and amplitude loops 168

Figure A-1. Schematic of three phases in a closed system where phase 1 is brought into contact with phase 2 creating a new interface 170

Figure A-2. Schematic of solid, liquid, and vapor system in equilibrium where the liquid is wetting the surface with an arbitrary wetting angle 171

Figure C-1. A 10 x 10 μm BE-PFM scan on top of a 10 μm laterally patterned feature which shows the variation of the (a) resonance, (b) quality factor, (c) phase, (d) quadratic response, (e) linear response, and (f) $\alpha/d_{33,init}$ as the sidewall is approached. The tip-surface nonlinearity was not properly optimized. Therefore absolute values of nonlinearity are not useful but the trends are still valid........173

LIST OF TABLES

Table 2-1. Etching parameters for PZT....................14

Table 3-1. Summary of the etching conditions used to define features in Si....................31

Table 3-2. Recess printing dimensions of PZT features using stamps with various well depths....................35

Table 4-1. Summary of the etching conditions used on Pt/Ti/HfO_2/SiO_2/Si stack....................63

Table 4-2. Summary of the etching conditions used on final SiO_2 etch....................66

Table 4-3. Summary of residual stresses found in electroplated Ni deposited onto Pt coated Si wafers....................72

Table 5-1. Summary of the etching conditions used on Pt/Ti/PZT stack....................112

Table 5-2. Summary of the poled and aged Rayleigh paramters for both RIE and printed PZT (errors from fitting)....................128

Table 5-3. Summary of the aging rates of ε_{init}, α, and $\alpha/\varepsilon_{init}$ ratios. The error of each value represents fitting errors....................128

Table 5-4. Summary and comparison of the effective damaged and undamaged areas, using a damaged thickness of 375 nm from the sidewall into the pattern area, to the global $\alpha/\varepsilon_{init}$ of each RIE pattern....................150

ACKNOWLEDGMENTS

I would like to express my gratefulness and love to all of my family, but in particular to my parents for all the love, wisdom, encouragement, advice, and joy you have imparted into my life. You have been supreme examples on how to model life's priorities and goals. I cannot begin to enumerate the value I place on having been raised in such a wonderful home. I would like to thank you specifically for your constant availability and love over the course of this work.

I am deeply indebted to my advisor Dr. Susan Trolier-McKinstry. My initial memory of her occurred in the crystal chemistry course she taught as part of my undergraduate work. It was the most difficult course I had ever experienced, but it was also the most fruitful academic experiences I had ever received. Her dedication to teaching prompted me to seek further instruction under her supervision in graduate school, and my time working for her has only deepened my respect for her. The dedication she gives to students, family, colleagues, and university is a high standard which I aspire to attain. I would especially like to thank her for the wisdom, guidance, and patience she gave to me over the course of this work.

I would also wish to thank my committee members, professors Clive Randall, Mike Lanagan, and Mike Hickner for their insight and knowledge. Dr. Randall taught my introductory class to materials science in undergraduate work, and he instilled a love for the field in me. I would also like to thank him for taking the time to interact with students both in a professional and relaxed setting while attending scientific conferences. Dr. Lanagan also taught me a course in electronic materials and device in undergraduate work. He piqued my interest in the dielectric and semiconducting materials which resulted in my application to graduate school. I am also grateful to Dr. Lanagan and Dr. Randall for allowing me to attend and present my work on numerous

occasions at the CDS/CDP conferences. There was always an opportunity to gather information and ideas from those with vastly more experience. I would also like to thank Dr. Hickner for his invaluable help with optimizing the elastomeric stamps which I used throughout my work. I am truly grateful for all the times you were willing to answer questions that were geared to polymers. Finally, I would like to thank Dr. Liviu Nicu and his student Denis Dezest for their generous collaboration and hospitality during my visit to Toulouse, France.

My endeavors at Penn State would not have come to fruition without the technical aid of the staff of the MRL, MCL, and MRI cleanroom. I am grateful for the knowledge and time given from Kathy Gehowski, Shane Miller, Nichole Wonderling, Bangzhi Lui, Chad Eichfeld, Andy Fitzgerald, Jeff Long, and Paul Moses. I would like to especially thank Beth Jones, Mike Labella, Bill Drawl, and Guy Lavalee for their extensive aid in the multitude of occurrences of great stress after a tool or fabrication process thwarted my efforts. Without their expertise and flexibility, this thesis would not have been completed. I am grateful to Ke Wang for his help with transmission electron microscopy imaging and interpretation.

I would like to thank all the members of the STM group, past and present, who were all invaluable resources to approach when questions arose: Raegan Johnson, Derek Wilke, Dan Tinberg, Ichiro Fuji, Adarsh Rajaskekar, Charley Yeager, Ryan Keech, Flavio Griggio, Hong Goo Yeo, Margeaux Wallace, Lizz Michael, Song-Won Ko, Jung-In Yang, Dan Marincel, Lauren Garten, Jon Bock, Sun-Young Lee, Wanlin Zhu, Jason Chan, Lyndsey Denis, Trent Borman, Mike Funicelli, Kuan-Po Lee, Dmitriy Davydovich, and Dixiong Wang.

Funding for this project came from the National Security Science and Engineering Faculty Fellowship (NSSEFF) through the Office of the Assistant Secretary of Defense for Research and Engineering.

Chapter 1

Introduction

The following will provide an introduction to the goals and applications of this research. In addition to a summary of the organization of the thesis.

1.1 Patterning of Ferroelectric Thin Films for MEMS Applications

Ferroelectric materials have been researched extensively for a variety of device applications where conversion of electrical to mechanical energy (or vice versa) is desired, such as actuators, resonators, and transducers.[1, 2, 3, 4,] In particular, lead zirconate titanate (PZT) has attracted attention in thin films for microelectromechanical systems (MEMS) applications in order to reduce drive voltages for actuator applications or increase the sensitivity of sensors.[5, 6] Integration of these films into a device requires a means by which to laterally pattern the material into a desire geometry. Subtractive (i.e. top-down) patterning of films is performed after deposition is complete, where undesired material is selectively removed from a continuum. In contrast, patterning of films performed simultaneously as the deposition occurs, results in an additive (i.e. bottom-up) patterning technique.

Removal of material in subtractive patterning techniques can be achieved through physical or chemical means as well as a combination of these two. Wet chemical etching is a subtractive patterning technique which utilizes the removal of material via chemical breaking of bonds in the material. This is an effective etching technique in MEMS due to its high etching rate, etch selectivity, and low cost. Early work on lateral scaling of PZT thin film for MEMS was performed by Mancha *et al.*[7, 8] to create features < 2000 μm^2 in size. Another wet etching chemistry was developed by Zheng *et al*.[9] to create ~50 um wide PZT features. However, undercutting, isotropic etching, low sidewall angles, and varying etch rates with composition are concerns with features of this size.

Ion-beam milling (IBE) is a subtractive technique which utilizes physical bombardment to remove material. A radio frequency field ionizes an Ar gas. A second electric field is used to send the ionized particles toward the substrate with high energy. The target material is physically sputtered away through the kinetic energy transfer from the ion beam to the film. Kawaguchi *et al*.[10] performed early work on lateral scaling of PZT thin films via IBE for use as a waveguide in integrated optical devices. Recently, Smith *et al*.[11] utilized IBE to pattern PZT thin films to provide power for MEMS actuated insect-inspired robotic wings. This technique is highly directional with excellent etch uniformity.[12]

A combination of physical bombardment and chemical reaction components is realized through the use of reactive ion etching (RIE). A strong radio frequency (RF) field (~MHz) ionizes gas molecules, creating a plasma consisting of ions and free radicals (i.e. Cl^- or F^-). A second large electric field (~kHz) results in negative ion drift toward the target. The chlorine/fluorine ions react chemically with the target material and argon ions physically sputter the target atoms through kinetic energy transfer. Saito *et al*.[13] employed RIE patterning of PZT films for use in nonvolatile ferroelectric random access memory. RIE etching offers large etch anisotropy, high resolution, and process control. However, the glow discharge can result in charging effects as well as deposition of unwanted etching residues.[14]

In addition to patterning the film, both dry and wet etching techniques are known to induce damage into ferroelectric thin films which diminish dielectric and piezoelectric properties while also increasing leakage.[15, 16, 17] Mitigation of these etching damages has taken several forms. Kim *et al*.[18] reported that a thermal anneal in O_2 of a dry etched PZT film increased the remanent polarization from the as-etched state, but never fully restored to its initial value. Lee *et al*.[19] reported an increase in the coercive fields in PZT thin films subjected to an RIE plasma; this was accompanied by creation of an amorphous layer. This layer could not be recovered by annealing, but upon exposure to an HF "cleaning" solution, the amorphous material was removed. The coercive fields were restored to original levels, however the polarization response could not be fully recovered. Lee *et al*.[20] also reported that PZT films with pinched hysteresis loops and high leakage current after dry etching could be partially recovered using a buffered oxide etchant "cleaning" solution. Torii *et al*.[16] attempted an oxygen RF-plasma treatment to remove etching damage, but could not achieve complete recovery.

The recovery of functional properties is beneficial for improved performance of the device. However, it is preferable to the long-term reliability of these devices to avoid the introduction of defects into the material altogether. Additive patterning offers an alternative patterning route which does not expose the functional material to etching environments. Soft lithographic techniques developed by George Whitesides[21] provides patterning capabilities on the micro and/or nano-scale while also offering a parallel patterning scheme which is ideal for large area deposition. Soft lithographic techniques employ an elastomeric polymer to pattern liquid precursor into desired patterns either by single-step, confinement techniques (ex. Figure 1-1 (a, b, and c)) or multi-step, contact printing techniques (ex. Figure 1-1 (d)).

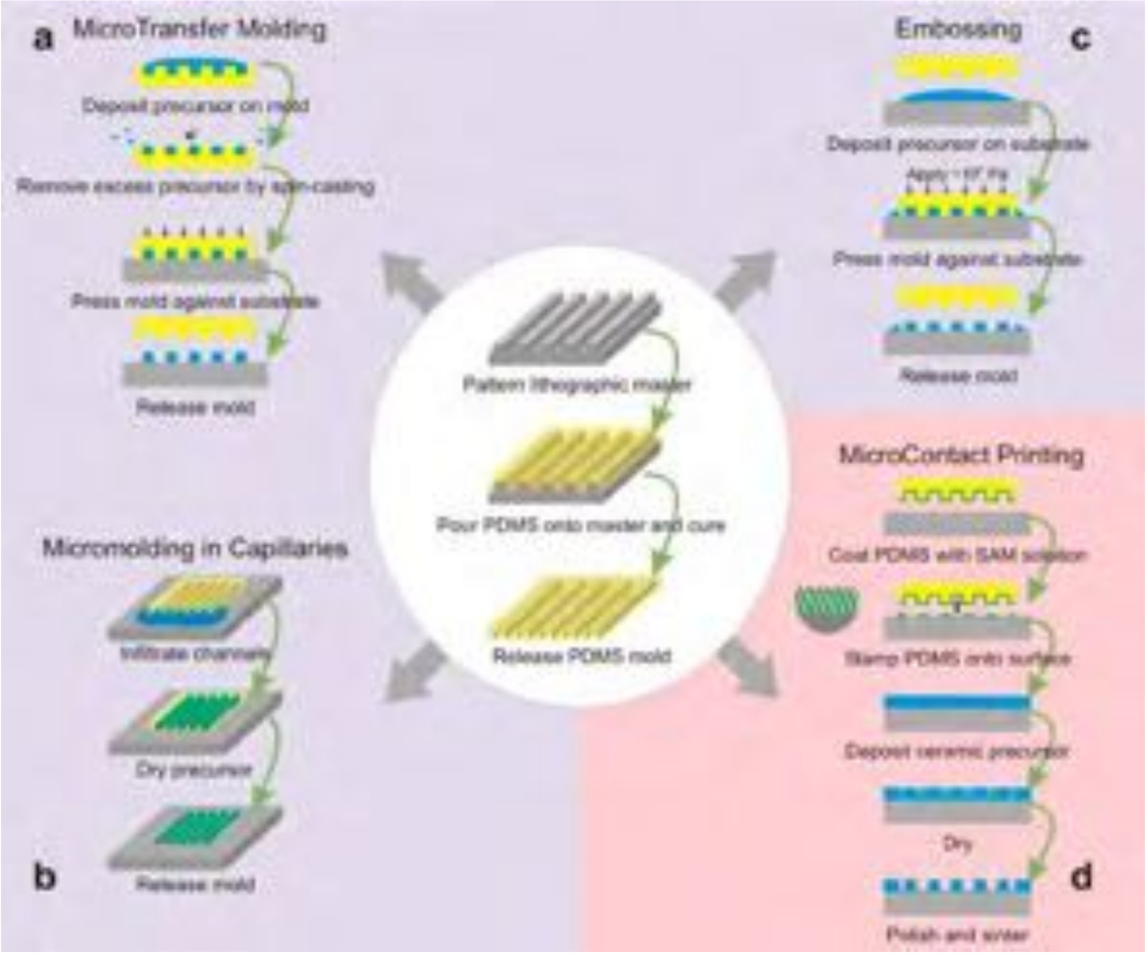

Figure 1-1. Schematic depicting the molding of a patterned stamp and the various soft lithographic techniques employed in patterning a precursor liquid. (a) MicroTransfer Molding, (b) Micromolding in Capillaries, (c) Embossing are all single deposition routes which utilize the recessed channels of the stamp in various ways to create the desired pattern. (d) MicroContact Printing directly transfers material from the stamp surface to the substrate.[22]

Microtransfer molding[23, 24] (Figure 1-1 (a)) employs molded polydimethylsiloxane (PDMS) to pattern polymers. For this purpose, the PDMS was coated with a polymeric solution. Excess solution was removed from the mold, leaving only the desired material in the channels of the PDMS. The PDMS is brought into contact with the substrate, and the target polymer is cured through heat or ultraviolet light. The PDMS is then removed, leaving behind the patterned polymer.

Micromolding in capillaries[25, 26, 27] (Figure 1-1 (b)) utilizes a patterned elastomer as a mold. In this instance, the PDMS is first brought into contact with the substrate. The polymeric solution is dispensed onto the substrate along the edge of the mold where openings to the recessed channels are present. The solution is drawn into the channels through capillary action. The polymer is then cured either through application of heat or ultraviolet light. The mold can be removed and the desired pattern remains on the surface of the substrate.

Soft lithographic embossing[28, 29, 30] (Figure 1-1 (c)) utilizes a patterned elastomer as a mold. In this instance, the solution is initially placed onto the target substrate. The patterned PDMS is brought into contact with the substrate directly on top of the solution. Through application of pressure, the solution de-wets the substrate in areas where the mold and substrate come into contact, and the solution is confined into the recess channels of the PDMS. The solutions are dried and the mold is removed. The patterned material is left behind on the target substrate surface.

Because confinement soft lithographic techniques are single-step deposition patterning processes, there is a limit to the maximum height a deposited feature can yield without large shape deformations resulting from solvent removal from precursor solutions. Alternatively, microcontact printing[31, 32, 33] (Figure 1-1 (d)) transfers thin layers of a material directly from the stamp surface onto a substrate. This process can be repeated multiple times with alignment to build a feature with varying heights without large shape deformations upon drying.

To this end, the work presented in this thesis focused on directly printing PZT solution precursors directly onto target substrates via microcontact printing, with the aim to create and integrate ferroelectric features, with optimal dielectric, ferroelectric, and piezoelectric properties, into MEMS devices.

1.2 Thesis Organization

In an effort to improve wetting properties between polar solutions and the stamping surface, Chapter 2 introduces the employment of a polyurethane elastomer stamp as an alternative to PDMS in the microcontact printing of PZT precursors. The limits of printable feature size and shape are explored. In addition, the longevity of the printing transfer from a single stamp surface is displayed. The dielectric and piezoelectric properties of printed features are then compared and contrasted to RIE patterned films as well as un-patterned continuous films to quantify the amount of damage the microcontact printing process imparts to the functional material.

Chapter 3 aims to improve PZT feature shape (i.e. increase sidewall angles) by modifying how patterned stamps are used to print PZT solutions on various substrate surface geometries. The role of printing dynamics such as stamp removal direction and removal rate was studied to optimize printing with an emphasis on smaller feature sizes. This optimization allowed for printing of ferroelectric PZT on MEMS structures. The end of Chapter 3 and all of Chapter 4 detail the development of the device design, optimization, fabrication, and characterization.

An in-depth study of the effect of subtractive and additive patterning processes on the domain wall mobility in ferroelectric features is discussed in Chapter 5. Both global dielectric and local piezoelectric nonlinearity measurements were made on RIE and microcontact printed films to gain a deeper understanding of the spatial extent over which patterning may damage properties. Local structural and chemical analysis was also employed via transmission electron microscopy to provide insight into the role stoichiometry and crystal quality play in governing the functional properties. Finally, Chapter 6 concludes the thesis and provides suggestions for possible future work derived from this study.

Chapter 2

Low-Cost, Damage-Free Patterning of Lead Zirconate Titanate Films

The ability to pattern piezoelectric thin films without damage is crucial for the development of microelectromechanical systems (MEMS). Direct patterning of complex oxides through microcontact printing was explored as an alternative to subtractive patterning. This process utilized an elastomeric stamp to transfer a chemical solution precursor of a piezoelectric material onto a substrate in a desired pattern. Polyurethane-based stamps improved wetting of polar solutions on the stamp. This allowed for high-fidelity patterning over multiple stamping cycles.

In this chapter, microcontact printing was used to deposit patterned $PbZr_{0.52}Ti_{0.48}O_3$ layers from 0.1 to 1 μm in thickness. The lateral feature sizes attained varied from 5 μm to 500 μm. Upon crystallization at 700 °C, the features formed phase-pure perovskite PZT. The printed features had comparable electrical and electromechanical properties to those of continuous PZT films of similar thicknesses. For example, 1 μm thick PZT features had a relative permittivity of 1050 and a loss tangent of 0.02 at 10 kHz. The remanent polarization was 30 $\mu C/cm^2$, and the coercive field was 45 kV/cm. The piezoelectric coefficient $e_{31,f}$ was -7 C/m^2. These values indicated that the microcontact printing process did not adversely affect the PZT crystallization or properties for the thicknesses explored in this work.

2.1 Introduction

Electrostatic actuators are driven by high voltages in order to accomplish large displacements in microelectromechanical systems (MEMS). Piezoelectric actuation enables lower drive voltages, and hence is attractive for a number of applications. Therefore, ferroelectric films have attracted attention for MEMS applications such as actuators, switches, resonators, accelerometers, piezoelectric energy harvesting, and transducers.[5, 34] In order to integrate ferroelectric materials into MEMS, a means to pattern these complex oxides without degrading the dielectric and piezoelectric properties is required.[35] Consequently, this work was aimed at developing a low cost, damage-free patterning process for piezoelectric MEMS.

Patterning techniques can be classified as subtractive or additive. Subtractive patterning entails selectively removing areas of blanket deposited films. In contrast, additive patterning builds the material from the bottom up into the desired shape. It is important to consider whether or not the patterning method will retain the desired stoichiometry.[36] Lead-based piezoelectric films, such as PZT, typically contain three to five cation species. Both wet and dry subtractive patterning approaches for these complex oxides can lead to preferential removal of cations, thus degrading the stoichiometry near the sidewalls of the patterned film. Dry etching of the ferroelectric material in MEMS applications is generally accomplished by ion milling,[37] or reactive ion etching (RIE),[38] both of which entail some physical bombardment. The energetic ions used in dry etching can create charged point defects such as oxygen and lead vacancies (which may form defect-dipole complexes),[14] amorphize the exposed surface,[35] form OH^- complexes from hydrogen atoms emitted from the photoresist mask,[39] or implant charged ions into the surface of the material.[14] These factors can potentially degrade the piezoelectric response of the material,[40] and could affect the ultimate lifetime of the device in cases where the charged defects are mobile under operating conditions.[41]

Additive patterning of complex oxides builds the desired geometric structure from the bottom up. Methods such as robocasting[42] or three-dimensional printing[43] of ceramic materials use colloidal particles to build complex structures at the macro and meso-scale. Suspensions, solutions, or pastes can be patterned at the micron scale via inkjet printing,[44] embossing,[45] and screen printing.[46] Powder-free patterning can be achieved through soft lithography.[47] This approach employs a soft elastomer as a mold or stamp for patterning at the micro- or nanoscale. The flexible elastomer allows for conformal contact between the stamp and non-planar surfaces.[48] Variations of this approach have been used to pattern a wide variety of materials.[21]

There are a limited number of reports on the use of soft lithography to pattern precursor solutions for electroceramics. Kim *et al*.[49] demonstrated the use of microtransfer molding (μTM, transferring metalorganic precursor solution in the recesses of the stamp features) by patterning $SrBi_2Ta_2O_9$ on $SrTiO_3$. Vartuli *et al*.[50] patterned PZT solutions by micromolding in capillaries (MIMIC). Payne used μCP to pattern Ta_2O_5,[51] $Pb(Zr_{0.52}Ti_{0.48})O_3$,[52] $LiNbO_3$, and $(Pb,La)TiO_3$[53] blanket films by depositing them over self-assembled monolayers. The film deposited over the SAM could be selectively removed by light abrasion, after pyrolysis, due to the poor adhesion between the substrate and the film. Finally, Nagata *et al*.[54] used μCP to directly pattern $BaTiO_3$ solutions for MLCC applications.

One difference between μCP and the other forms of soft lithography is that μTM and MIMIC are confinement-based techniques, while μCP directly builds layers of "ink" on the substrate. Kumar and Whitesides[31, 55] demonstrated that μCP is a parallel patterning technique in which an inexpensive elastomeric stamp is used to directly pattern an "ink" onto a surface, as displayed in Figure 2-1. This technique leverages the wetting* properties of a solution with a stamp surface to create fine scale patterns on a surface. Confinement-based methods enable thick layers to be deposited; however, cracking and cross-sectional shape deformation upon drying of the precursor solutions can be significant obstacles.[56] The μCP process deposits thinner layers to avoid cracking, and it is feasible to stack layers in order to achieve required thicknesses.

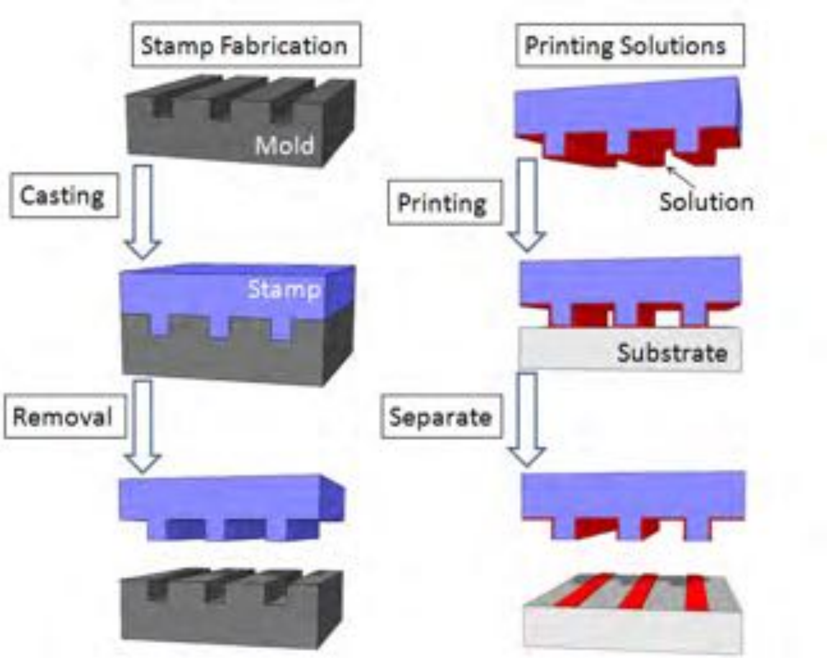

Figure 2-1. Schematic depicting the molding of a patterned stamp and the μCP of PZT liquid solutions onto a flat surface.

Previous reports on microcontact printing of sol-gel precursors to electroceramic films used poly-dimethyl siloxane (PDMS) stamps. The hydrophobic surface of PDMS could be temporarily made hydrophilic by exposing the stamp to low power oxygen plasma. However, exposure to the

---

* Wetting of liquids on surfaces is discussed in detail in Appendix A

solution led to re-development of a hydrophobic surface, and poor solution transfer on subsequent printing cycles.[54] A more robust process requires a surface that remains hydrophilic. In this work, polyurethane-based stamps were examined as an alternative to PDMS for long-lived polarity of the stamping surface and thus robust stamping performance over many printing cycles.

2.2 Experimental Procedure

2.2.1 *Stamp Fabrication*

Sylgard® 184 silicone elastomer base and Sylgard® 184 silicone elastomer curing agent (Dow Corning Corporation) were used to produce the PDMS stamps. Polyurethane stamps were prepared from NOA 73 (Norland Optical Adhesives), due to its comparatively low Young's modulus. However, the stiffness of the cured polyurethane elastomer (~ 11 MPa) significantly exceeds that of the PDMS (~ 2.4 MPa).[57] Poly-ethylene glycol diacrylate (PEGDA) $M_n = 575$ (Sigma-Aldrich), was incorporated into the NOA 73 to reduce the stiffness of the polyurethane stamp. 2-Hydroxy-2-methyl-propiophenone (HOMPP) (Sigma-Aldrich), was used as a photocurable additive to solidify the stamps upon irradiation with UV light.

Photoresist molds for the stamps were prepared on Pt-coated Si wafers using a negative photoresist, NANO^{TM} SU-8-5 (MicroChem) developed in Microposit MF CD-26 for 1 min. PDMS stamps were cast from a 10:1 ratio (by volume) of the PDMS elastomer to the curing agent.[31] The mixture was degassed for ~30 min to remove air bubbles, and poured over the mold. Stamps were cured at room temperature for 24 to 48 hrs to minimize shrinkage of the elastomer. The stamps were then diced to the desired sizes and removed from the molds. The back of the PDMS stamps were self-adhered to glass slides for handling.

Polyurethane stamps were prepared by combining a 95:5 v/v PEGDA/HOMPP photo-initiator mixture with polyurethane in 6:4 wt./wt. ratio to tailor the stiffness of the stamp.[58] The polyurethane/PEGDA/HOMPP mixture was poured over the molds, and cured for 30 min under Black Ray® B100 AP ultraviolet lamp (UVP, LLC). The cured stamps were then backed with a PDMS layer processed as described above. The softer backing layer allowed for improved conformal contact between the stamp and the substrate.[59] The stamps were then diced, removed from the molds, and mounted on glass slides.

2.2.2 *PZT Processing*

The preparation of the 2-methoxyethanol-based $PbZr_{0.52}Ti_{48}O_3$ (PZT) solutions was described in detail by Wolf and Trolier-McKinstry.[60] 10% percent excess lead was used to reduce the likelihood of surface pyrochlore on the PZT films. Lead oxide (0.08M PbO) solutions were also prepared by the same method.

As a reference, microcontact printed films were compared to blanket films of the same thickness. Continuous films were prepared from 0.4 M PZT 52/48 solutions on Pt(111)/Ti/SiO_2/Si(100) wafers (Nova Electronic Materials) by spin-coating layers at 1500 rpm for 30 sec. After each spin-coating step, the sample was subjected to a two-step pyrolysis: 225 °C for 1 min followed by 400 °C for 1 min. The film was then crystallized at 720 °C for 1 min in oxygen[60] in a Modular Process Technology Corporation RTP-600S Rapid Thermal Annealing Furnace (RTA). The process was repeated until the desired thickness of the film (0.1 to 1 µm) was reached.

The 0.08M PbO solutions were spun (3000 rpm for 30 sec) on continuous PZT films which showed surface pyrochlore after the final crystallization step to act as a capping layer for the film.[61]

Following a two-step pyrolysis (150 °C for 1 min and 250 °C for 1 min) the films were heat-treated in a box furnace at 650 °C for 30 min.

Prior to printing with PDMS, the stamp was oxidized with a MetroLine/IPC M4L plasma etcher with an RF power of 100 W for 30 sec.[54] The stamps were stored in de-ionized water after the surface treatment in order to prolong hydrophilicity of the stamp surface.[62] PZT solutions were dispensed onto the treated stamp surface, and spun at 3000 rpm for 30 sec. The coated stamp was mounted to a photomask plate in a Karl Suss MJB-3 mask aligner directly above a Pt-coated Si wafer mounted on a stage. The stamp was optically transparent, which allowed for stamp features to be visually aligned with features on the substrate. The stage was raised until the stamp completely contacted the substrate. The stage was lowered; leaving the patterned PZT. The patterned PZT was crystallized, as described previously. New PZT solution was deposited onto a stamp, the stamp was mounted and aligned with the previously printed PZT features, the PZT solution was printed atop the previously deposited PZT, and the substrate was heat-treated. This process was repeated until the desired thickness of PZT (0.1 to 1 μm) was achieved. Polyurethane stamps have an inherently hydrophilic surface, so no oxidizing treatment was necessary to modify the wetting of the PZT solution on the stamp. Otherwise, identical processing conditions were used as for the PDMS stamps. The patterned films were also capped with a printed 0.08M PbO solution. Identical heat-treatment steps were used for the PbO capping treatment as were done for the continuous films.

To enable electrical measurements, Pt top electrodes (75 to 200 μm diameter) were deposited using a lift off process. The Pt deposition was performed at room temperature by DC magnetron sputtering (CMS-18 Sputter System, Kurt J. Lesker) at a pressure of 5 mTorr with a power density of 4.4 W/cm^2 on the target. Top electrodes were annealed at 500 °C for 1 min in an RTA.

For comparison purposes, PZT films (~1 µm thick) were subtractively patterned by reactive ion etching. The features were defined using a MicroChem KMPR 1010 negative photoresist mask.

Table 2-1. Etching parameters for PZT.

Parameter	PZT Etch
Pressure (mTorr)	5
Ar Flow (sccm)	45
CF_4 Flow (sccm)	28
Cl_2 Flow (sccm)	7
Power Density (W/cm^2)	3.4
Etch Rate (nm/min)	110

Etching of samples were performed in a Tegal 6500 RIE etch tool. The PZT was etched utilizing $Ar/CF_4/Cl_2$ gases to a thickness of 0.4 µm; the RIE etching parameters are given in Table 2-1. The plasma was cycled on for 30 sec and off in order to avoid reticulation of the photoresist. Following RIE, the photoresist was removed by etching in Cyantek Nanostrip at room temperature. Pt top electrodes were deposited on planar PZT regions exposed to the RIE plasma in order to maximize the effect that any etching-induced nonstoichiometry would have on electrical measurements. The top electrodes were deposited using the lift off process described previously.

2.2.3 *Measurements*

X-ray diffraction (XRD) scans were performed at room temperature with a grazing incidence configuration in a Scintag DMC-105 diffractometer with Cu K_α radiation. Grain sizes and surface morphology of the films were observed using a Gemini LEO 1530 field-emission scanning electron microscope (FE-SEM). A Tencor Instruments Alpha-Step 500 surface contact profilometer and a Zygo NewView™ 7200 optical profilometer were used to determine film thicknesses and pattern dimensions.

A Hewlett Packard 4284A precision LCR meter was utilized to measure the relative permittivity and the loss tangent of the PZT films at 10 kHz. Dielectric Rayleigh measurements were conducted at 1 kHz with an AC electric field ranging from 0 to 30 kV/cm (~½ E_c). This enabled the determination of reversible (ε_{init}) and irreversible (α) Rayleigh coefficients of the PZT films. A Radiant Technologies RT-66A standardized ferroelectric test system was used to measure the polarization hysteresis loops and determine the remanent polarization (P_r) and the coercive field (E_C). An AVC Instrumentation 790 Series power amplifier was employed for measurements on thicker films. A custom polarization measurement system was used to acquire first order reversal curves for each film as described elsewhere.[63]

The wafer flexure technique[64] was utilized to measure the transverse piezoelectric coefficient, $e_{31,f}$, of blanket and μCP PZT films. The piezoelectric wafers were mounted to a 3" silicon carrier wafer using Loctite SuperGlue. The carrier wafer was loaded into a pressure fixture, as described elsewhere.[65] A 4 Hz drive signal generated using a SRS Model SR830 DSP lock-in amplifier excited a Harman/Kardon HK770 amplifier which powered an audio speaker plumbed to a cavity under the wafer, thus creating an oscillatory pressure which flexed the carrier wafer. Charge measurements were performed by first poling through the thickness of the film at $5E_C$ for 15 min. The charge generated was measured with a charge-to-voltage converter and the lock-in amplifier using a time constant of 10 sec. The biaxial in-plane strain was measured by mounting two strain gauges (Omega Engineering) in orthogonal directions with Loctite SuperGlue on the surface of the piezoelectric wafer. The magnitude of the strain was determined using the gauge as one leg of a voltage divider; the AC response was measured with the lock-in amplifier using a time constant of 10 sec.

2.3 Results and Discussion

2.3.1 *Printing with Polyurethane-Based Stamps*

Printing of the PZT solution was initially investigated using PDMS stamps. The polar 2-MOE based PZT solution poorly wet the PDMS stamps without a plasma oxidizing treatment to convert the surface of the PDMS from hydrophobic to hydrophilic.[66] The PZT solution was then printed onto the surface of Pt-Si wafers, as shown in Figure 2-2 (a). The initial patterns showed excellent pattern transfer with a line edge roughness of 200 nm. The features were 100 nm in height. Upon printing a second time, significant degradation of the wetting was observed, and the printed pattern was severely disfigured in Figure 2-2 (b). Presumably, the PDMS stamp surface reverted to a hydrophobic surface after exposure to the solvent. In order to recover a hydrophilic surface, the PDMS stamps had to be oxidized after each stamping cycle. This addition of processing steps adds cost and time to the patterning process.

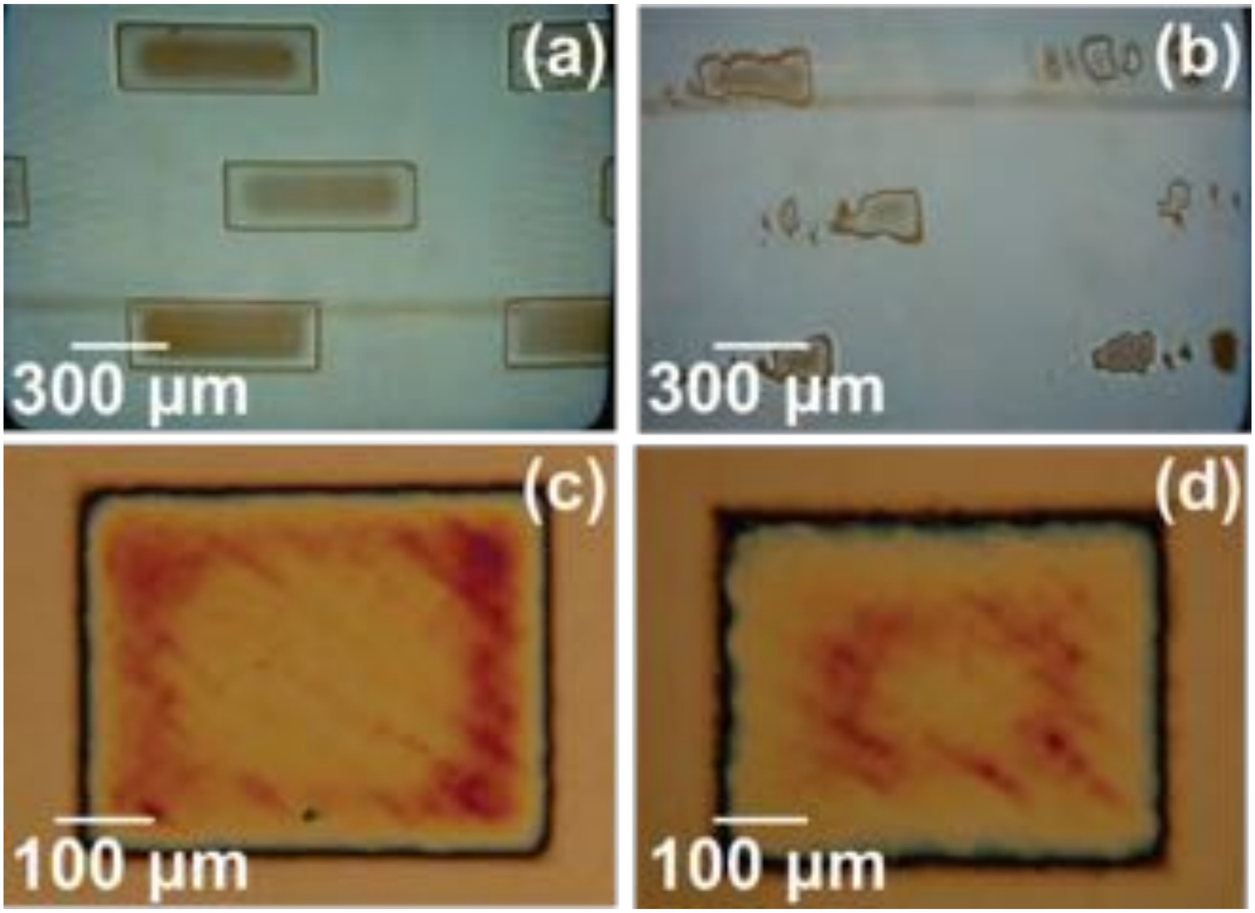

Figure 2-2. Pattern transfer of 2-MOE based PZT solutions using PDMS and polyurethane composite stamps. (a) 1st and (b) 2nd stamping cycles using PDMS stamp. (c) 1st and (d) 50th stamping cycle using polyurethane composite stamps.

In contrast to the case of PDMS, the composite polyurethane/PDMS stamps also displayed excellent pattern transfer as seen in Figure 2-2 (c), and could be used for at least 50 PZT stamping cycles, as shown in Figure 2-2 (d), over a 12 hr period without any discernible loss in pattern transfer definition. The line edge roughness of the features was 200 nm and the feature heights were 80 to 100 nm. The polyurethane composite stamp eliminated the need for surface treatments of the stamp surface before each stamping cycle.

2.3.2 *PZT Prints*

Ferroelectric films deposited from solutions are limited in thickness for a single layer. To create films of larger thickness, multiple layers must be deposited sequentially after aligning to previously patterned PZT features. Stacking of µCP prints prepared with the composite polyurethane stamps was employed to achieve PZT films ranging in thickness from 0.1 to 1µm and approximately 500 × 400 µm in area.

Figure 2-3 shows optical profilometry images of various PZT feature sizes and shapes. Figure 2-3 (a) shows a stack of three successive PZT printed layers. Aligning the stamp with a previously patterned feature was achieved within a tolerance of 1 to 2 µm. However, the wetting of the solution on the stamp was not ideal. The surface profile of the PZT feature had raised edges compared to the center of the feature. This ~20 % variation in height was observed for all printed thicknesses.

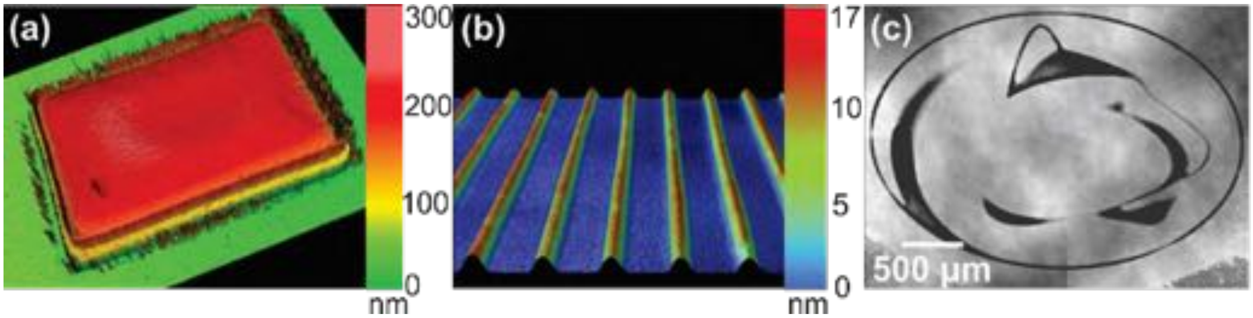

Figure 2-3. Optical profilometry images of µCP PZT (a) 500 × 400 µm feature and (b) 5 µm PZT lines. (c) Light intensity map of an intricate µCP PZT design.

The limit of pattern definition by µCP was explored by printing with a wide variety of features sizes. 500, 200, 100, 50, 20, and 5 µm features were printed with polyurethane stamps. Features were completely transferred over large areas, up to approximately 1cm^2. The 5 µm lines, shown in Figure 2-3 (b), were continuous over millimeter length scales. Complex shapes, shown in Figure 2-3 (c) can also be patterned via μCP.

2.3.3 *Microstructural Characterization*

XRD scans of the PZT films patterned by μCP are shown in Figure 2-4 (a). The data are consistent with randomly oriented polycrystalline perovskite with no deleterious secondary phases, such as pyrochlore or PbO.

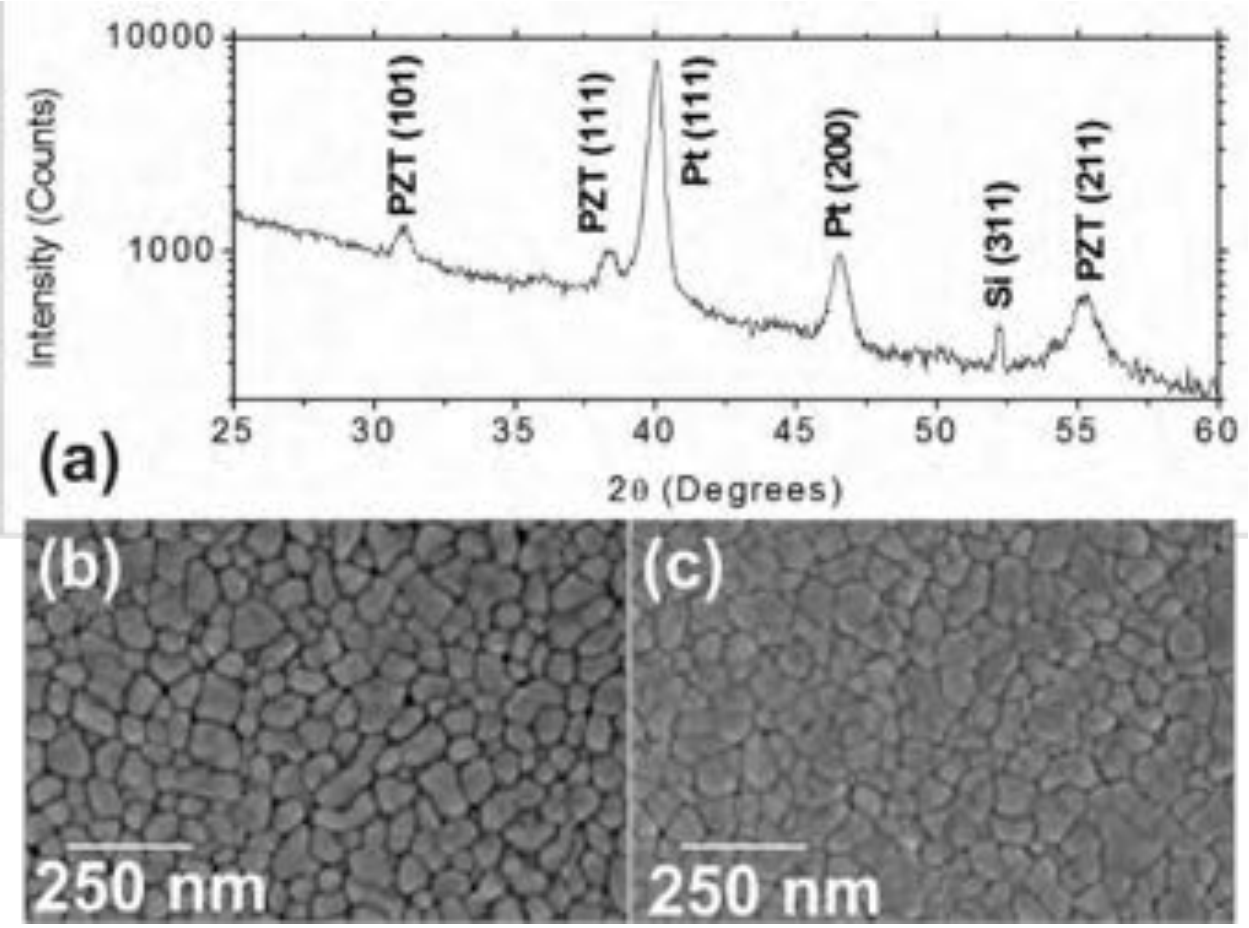

Figure 2-4. (a) Grazing incidence XRD scan of μCP 52/48 PZT on a Pt/Ti/SiO_2/Si(100) wafer (polyurethane stamps). (b) SEM surface micrographs of a blanket film and a (c) μCP film, both of which are 420 nm thick.

The surface morphology and the grain size of the µCP PZT patterns were compared to those of a blanket PZT film of similar thickness. A homogeneous microstructure was observed in both samples; the blanket film (Figure 2-4 (b)) had grains that were 77 ± 26 nm, while the µCP film (Figure 2-4 (c)) had a grain size of 77 ± 30 nm. No secondary phases such as surface pyrochlore at the grain boundaries or PbO particles on the surface were observed. Thus, the µCP process did not adversely affect the crystallization behavior.

2.3.4 *Electrical Characterization*

The electrical properties of µCP and blanket films of various thicknesses were characterized in order to investigate how the deposition methods affected the films. Data are shown in Figure 2-5.

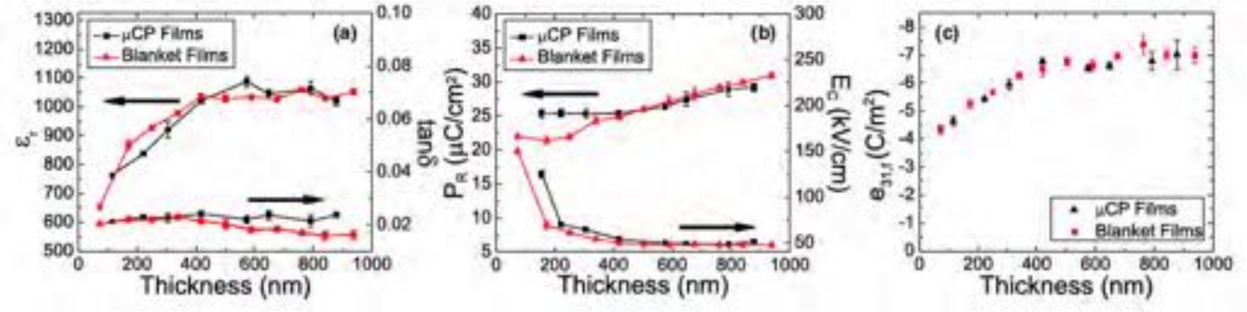

Figure 2-5. Electrical property measurements of µCP sample set compared with a blanket film sample set over a thickness range of 0 to 1 µm. (a) Relative permittivity and loss tangent of the PZT films. (b) Remanent polarization (P_r) and coercive field (E_C) of the PZT films. (c) The transverse piezoelectric coefficient, $e_{31,f}$, for µCP and a blanket film sample set.

Figure 2-5 (a) displays the relative permittivity and the loss tangent as a function of film thickness for the two sample sets. Films thicker than 0.5 µm had a relative permittivity of 1000 to 1100 and loss tangents of 0.02. Films < 0.5 µm in thickness showed decreasing relative permittivity. Figure 2-5 (b) shows the remanent polarization (P_r) and the coercive field (E_C) from the same sample sets. The P_r increased with film thickness, while E_c dropped and then remained constant for films > 0.5 μm in thickness. These data are consistent with previous reports on the thickness dependence of the dielectric properties of PZT films.[67,68] The thickness dependence has been ascribed to low relative permittivity interfacial layers,[69,70] a layer with high levels of charge injection,[71,72] and/or a Schottky depletion region.[73] It is not clear which effect dominates for the films reported here, but it was apparent that there was no significant difference between the blanket layer and the printed features.

Figure 2-5 (c) plots the $e_{31,f}$ values of the films; the μCP films and the blanket films showed excellent agreement with one another. Both processing methods resulted in films that exhibited $e_{31,f}$ values of -7 C/m^2 above 0.5 μm in thickness, that decreased in an approximately linear fashion with thickness to -4.5 C/m^2 at 100 nm. Again, these data were consistent with previous reports on the thickness dependence of blanket films.[40,74] The agreement between the two sample sets indicated that the μCP process did not limit the achievable properties of patterned PZT.

To further assess the μCP process, the properties of PZT films patterned by μCP and RIE were compared to blanket films. To facilitate detection of process-induced damage, the etched surface of the RIE-etched films was electroded. Three methods were used to investigate the resulting properties: Rayleigh measurements, minor hysteresis loops, and first order reversal curve (FORC) measurements. All three approaches should be sensitive to pinning centers that would influence the mobility of domain walls in the films.

Many ferroelectric films show a field dependent relative permittivity which is Rayleigh-like in character,[75,76] and so can be described by Equation 2-1.

$$\varepsilon_r = \varepsilon_{init} + \alpha' E \qquad (2\text{-}1)$$

At low AC electric fields, the reversible Rayleigh coefficient (ε_{init}) is observed due to reversible domain wall motion and the intrinsic lattice response. As the field increases, irreversible domain wall motion contributes to the relative permittivity of the material; this effect is described by the irreversible Rayleigh coefficient (α'). Of particular interest was whether internal fields influenced the behavior of patterned films relative to the blanket layers.[77]

The field dependent relative permittivity can be seen in Figure 2-6 (a). It was clear that the RIE etched films show a decrease in the reversible Rayleigh coefficients (from 1026 to 842) and the irreversible Rayleigh coefficients (from 16.1 to 8.3 cm/kV). This data suggested that the etching process introduces defects that locally stabilize domain states, which in turn pins domain wall motion and ferroelectric switching.[78] The μCP PZT films; however, showed no such effects when compared to the blanket films, as seen in Figure 2-6 (b). The smaller value of α' for the RIE film was also reflected in the minor hysteresis loops, as seen in Figure 2-6 (c). The difference in the polarization values at zero electric field is proportional to the irreversible Rayleigh coefficient, as shown in Equation 2-2.

$$\Delta P(E = 0) = \alpha' E_{max}^2 \qquad (2\text{-}2)$$

The pinching of the loop may be due to defect dipoles (or other source of internal bias) that are not reoriented by an applied electric field[79] and locally stabilize the domain configuration.[80] Comparable behavior is often seen in aged PZT ceramics.[81] The μCP film showed comparable minor hysteresis loops to the blanket film, as seen in Figure 2-6 (d).

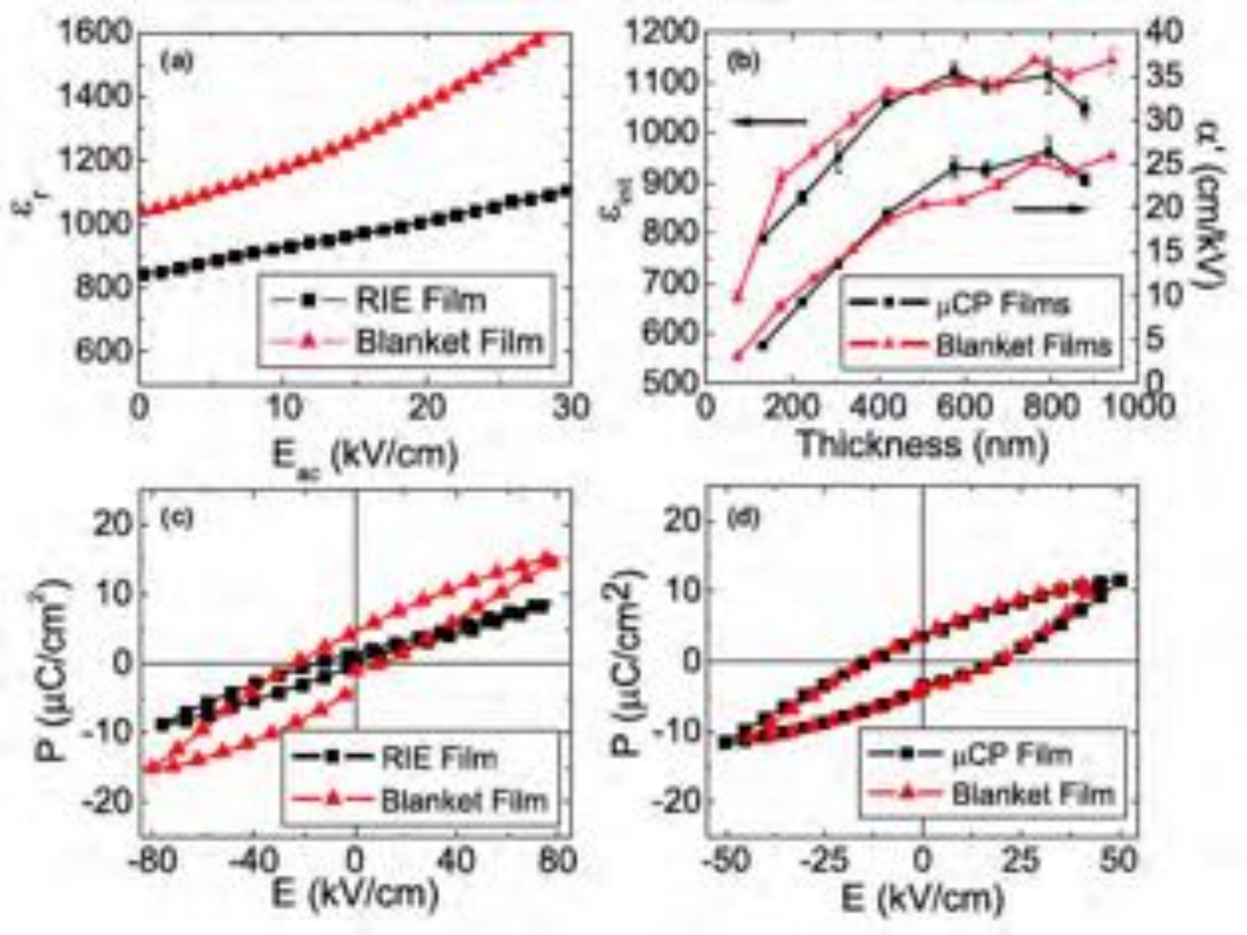

Figure 2-6. (a) Rayleigh plot comparing a blanket and RIE PZT film, thicknesses of 480 and 400 nm, respectively. (b) Reversible and irreversible Rayleigh coefficients for blanket and μCP PZT. (c) Minor hysteresis loop comparing a blanket and RIE PZT film (480 and 400nm thick, respectively). (d) Minor hysteresis loop comparing a blanket and μCP PZT film, thicknesses of 850 and 875 nm, respectively.

Pinching in the hysteresis loops of RIE samples was clearly detected in first order reversal curves (FORC)[82,83] and the associated FORC distributions.[84,63] The FORC measurement was used to extract a distribution of reversible (P_{rev}) and irreversible hysterons that describe the global polarization response of the material in terms of up-switching field α and down-switching field β. A peak in the FORC distribution corresponds to a high density of hysterons contributing to the polarization response. Figure 2-7 displays FORC measurements of blanket, µCP, and RIE patterned films.

The blanket films showed a single peak in the reversible distribution that was slightly shifted along the positive electric field axis (due to built-in polarization having measured the FORC curves beginning from negative saturation). The reversible FORC distributions for both blanket and the µCP PZT films showed identical peak location (25 kV/cm) and magnitude (0.06 µC/kVcm), as seen in Figure 2-7 (a). However, after RIE etching, the reversible distribution split into two distinct peaks of comparable magnitude 0.04 µC/kVcm. The two split peaks were lower than that of the main blanket film peak (0.06 µC/kVcm), as shown in Figure 2-7 (d).

Irreversible distributions with a single peak centered about the α = -β line describe a ferroelectric material with a symmetric PE loop. The irreversible distributions of the blanket and the µCP PZT films in Figure 2-7 (b) and (c) respectively are centered at ~α = 50 kV/cm and β = -50 kV/cm, and have magnitudes of 0.0053 µC/kV^2. This indicated that patterning PZT films by µCP did not introduce a substantial contribution of additional defects into the film.

The existence of two distinguishable peaks in the irreversible distribution is responsible for pinching in the minor hysteresis loop.[85] The degree of pinching in the PE loop is determined by the degree of separation of the two peaks measured perpendicular to the α = -β line. The irreversible distribution of the RIE etched samples (Figure 2-7 (f)) showed split peaks; the peaks were centered at approximately (15, -91 kV/cm) and (149, -19 kV/cm) in (α,β) coordinates with magnitudes 0.00128 µC/kV^2 and 0.00096 µC/kV^2 respectively. In contrast, the blanket PZT of comparable thickness (Figure 2-7 (e)) to the etched film was centered at approximately (50,-50 kV/cm) in (α,β) coordinates with a magnitude of 0.0030 µC/kV^2. The etched film peak centers were shifted significantly, which produced the pinching in the minor hysteresis loops.

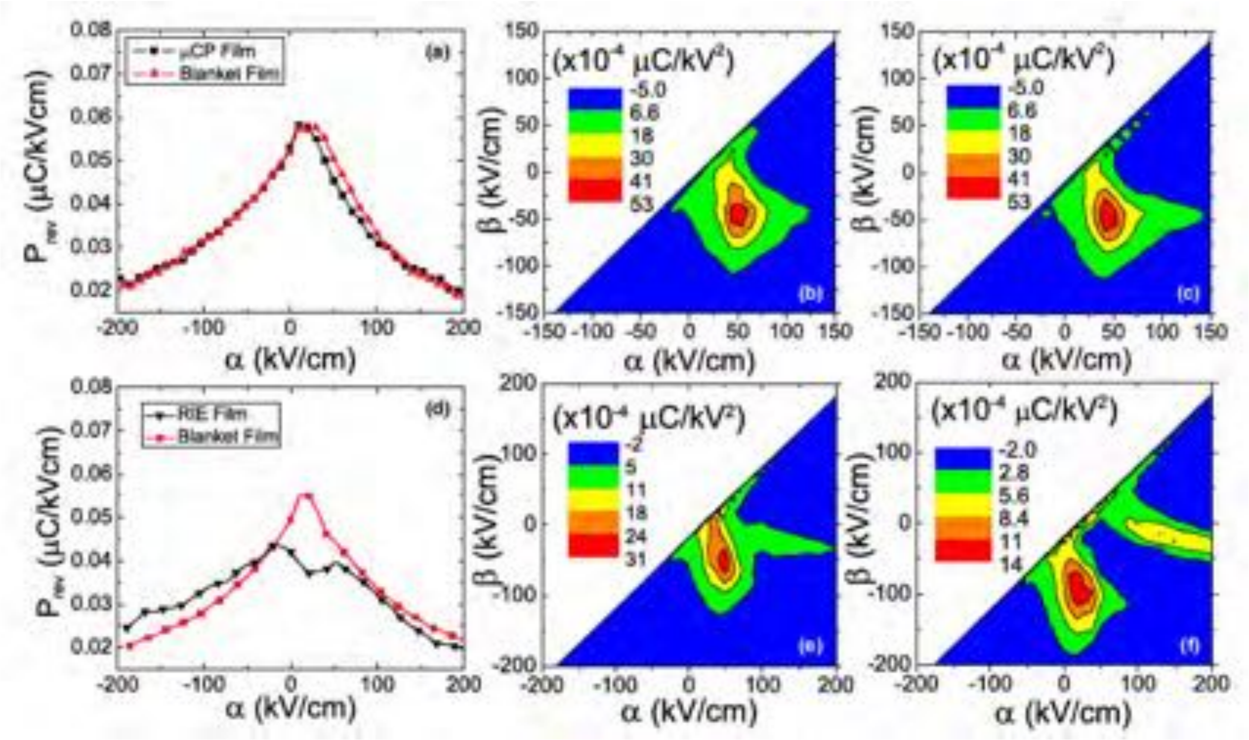

Figure 2-7. (a through c) FORC distribution of blanket and μCP PZT films, thicknesses of 850 and 875 nm, respectively. A reversible FORC distribution (a), and irreversible FORC distributions comparing blanket (b) and μCP (c) PZT films. (d through f) FORC distribution blanket and RIE PZT films, thicknesses of 480 and 400 nm, respectively. A reversible FORC distribution (d), and irreversible FORC distributions comparing unetched blanket (e) and RIE (f) PZT films.

2.4 Conclusions

Microcontact printing was implemented as a means to pattern PZT films. Polyurethane stamps displayed excellent wetting characteristics with respect to the PZT solution over at least 50 stamping cycles. The stamps were optically transparent, which allowed alignment of a previously printed PZT feature with that of the features of the stamp. Thus, PZT solutions could be printed and crystallized sequentially atop previously prepared PZT features. This allowed for PZT films to be patterned with thicknesses ranging from 0.1 to 1 μm. Feature sizes ranging from approximately 1 cm^2 to 5 μm × several mm were patterned. However, several improvements to μCP printing are needed in order to increase the versatility of this patterning technique for device fabrication. Feature height variation need to be improved through further studies of solution wetting and drying characteristics. Also, polyurethane is stiffer than PDMS, which imposes some limitations on the feature geometries that can be patterned. Therefore, further investigation into tailoring the mechanical properties of hydrophilic stamps is needed.

The μCP PZT films crystallized into the perovskite structure, with no secondary phases. The dielectric and piezoelectric response of the μCP films were comparable with blanket PZT films of similar thicknesses. Finally, the Rayleigh behavior, low field hysteresis loops, and FORC distributions reveal that μCP of PZT films did not introduce significant levels of defects into the material. In contrast, under some conditions, PZT films patterned via RIE etching showed properties consistent with a higher concentration of randomly oriented defect dipoles. Therefore, μCP offers a low-cost, damage-free patterning process that could be used to manufacture piezoelectric MEMS devices.

Chapter 3

Increasing Sidewall Angles of Contact Printed Piezoelectric Thin Films

The functional properties of electroceramic thin films can be degraded by subtractive patterning techniques used for MEMS applications. This chapter explores an alternative deposition technique, where lead zirconate titanate (PZT) liquid precursors are printed onto substrates in a desired geometry from stamp wells (rather than stamp protrusions). Printing from wells significantly increased sidewall angles (from ~1 to greater than 35 degrees) relative to printing solutions from stamp protrusions. Arrays of PZT features were printed, characterized, and compared to continuous PZT thin films of similar thickness. 300 nm thick printed PZT features exhibit a relative permittivity of 730 and a loss tangent of 0.022. The features showed remanent polarizations of 26 $\mu C/cm^2$, and coercive fields of 95 kV/cm. The piezoelectric response of the features produced an $e_{31,f}$ of -5.2 C/m^2. This technique was also used to print directly atop pre-patterned substrates. Lateral feature sizes ranged from hundreds of microns down to 1μm. In addition, several device designs were pre-patterned onto SOI wafers ($Si/SiO_2/Si$ with thicknesses of 0.35/1/500 μm). The top patterned silicon was released from the underlying material, and PZT was directly printed and crystallized on the free-standing structures in order to provide actuation and sensing capabilities to the device.

3.1 Introduction

Thin film electroceramics used as sensors, capacitors, actuators, etc. are patterned into specific geometries, commonly by either a wet or dry subtractive patterning approach.[37] These approaches can reduce overall performance[40] and/or lifetime[41] of the final device in cases where patterning-induced damage is produced. Therefore, it is of interest to consider additive patterning techniques for MEMS applications. Ceramic suspensions, pastes, and solutions have been additively patterned at the macro and meso-scale through the use of inkjet printing[44] and screen printing.[46] Powder-free solutions have been patterned through soft lithographic techniques.[86] Soft lithography utilizes elastomeric polymer stamps/molds to deposit or confine solutions onto a substrate. Printing of a ceramic solution from stamp surface directly onto a substrate, termed microcontact printing, has been used to deposit patterned lead zirconate titanate (PZT) thin films with comparable electrical properties to continuous PZT thin films.[87]

When printing liquids onto a surface, it is essential that the liquid wet the stamp surface in order to provide reproducible printed shapes. On printing from raised features (protrusions), the wetting angle of the solution on the stamp largely determines the final sidewall angle of the deposited layers.[88] Protrusion-printing features, ranging in width from 5 to 500 μm, have been used to pattern PZT features with sidewall angles of ~1 degree. Figure 3-1 (a) is an example of a 500 μm printed PZT thin film where the sidewall angle of the feature is >1 degree.[87] Molding-based soft lithography can produce larger sidewall angles. For example, Martin *et al.*,[56] patterned PZT using micromolding in capillaries with ~10 degree sidewall angles, as shown in Figure 3-1 (b).

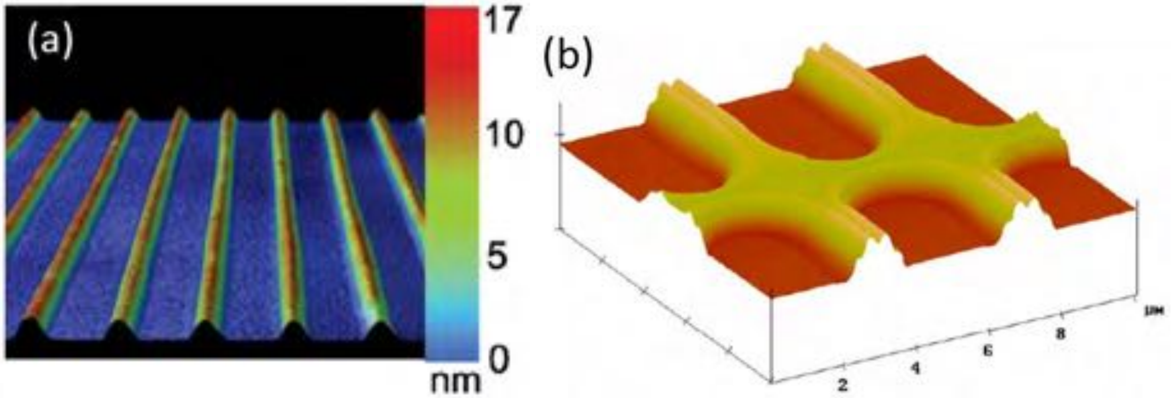

Figure 3-1. Surface profile of a PZT thin film (a) printed from a 5 µm lateral protrusion feature[87] and (b) molded in microcapillary channels.[86]

When printing from stamp recesses rather than stamp protrusions, sufficient pressure must be applied for the recess surface to come into contact with a substrate. Thus, the stamp protrusions act as supports, and only the center of the feature contacts the substrate.[89] A schematic of recess printing is shown in Figure 3-2.

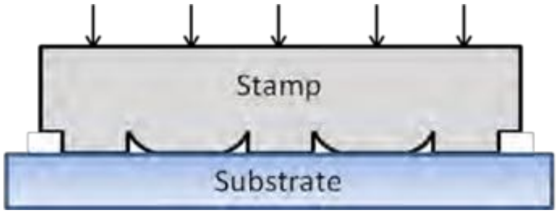

Figure 3-2. Schematic showing sufficient pressure applied for the recesses of the stamp to contact a substrate.

Due to the fact that printing with stamp protrusions yield features with shallow sidewall angles, printing from stamp recesses was investigated as an alternative means to increase sidewall angles of printed features. This printing technique was utilized to deposit PZT thin films on released Si cantilevers for biosensing microelectromechanical (MEMS) devices.

3.2 Experimental Procedure

3.2.1 *Recess Printed PZT Film Fabrication*

Bilayer polymer stamps were made as described elsewhere.[87] A polyurethane (PU)[†] layer was ultraviolet (UV) cured in a desired pattern. The hydrophilic nature of the polyurethane surface allowed the PZT solution to wet the stamp. The compliant, polydimethylsiloxane (PDMS) backing layer allowed the recesses of the stamps to come into contact with the substrates at lower pressures.

Butanol based precursor solutions, 10 wt. % $Pb_{1.1}(Zr_{0.52}Ti_{0.48})O_3$ (Mitsubishi Materials), were spun onto polymer stamps at 3000 rpm for 30 s. An MJB-3 contact aligner was used to align and print the PZT solution onto Pt coated Si wafers (NOVA Electronic Materials). The liquid precursors were dried at 350 °C for 3 min and crystallized at 650 °C for 1 min. The fired film was positioned in the contact aligner, and new PZT layers were printed sequentially on the stack, and heat-treated in the same manner. This process was repeated until the desired thickness was achieved. To enable electrical measurements, Pt top electrodes were deposited on the PZT features using a lift-off process. The Pt was sputter deposited (CMS-18 Sputter System, Kurt J. Lesker) at room temperature.

Physical dimensions of the printed films were analyzed with a LEO 1530 field-emission scanning electron microscope (Gemini). Film thickness was determined using a surface contact profilometer (Alpha-Step 500, Tencor Instruments). An 4284A Precision LCR meter (Hewlett Packard) was utilized, from 0.1 to 100 kHz at a drive amplitude of 0.03 V, to measure relative permittivity and loss tangent. A Multiferroics Test System (Radiant Technologies) was used to

---

[†] Note: PU layer is still a mixture of polyurethane, poly-ethylene glycol diacrylate, and 2-hydroxy-2-methyl-propiophenone

measure the P-E loops of the printed films at 100 Hz. The wafer flexure technique[64] was utilized to measure the transverse piezoelectric coefficient, $e_{31,f}$.

3.2.2 *Patterned Substrate Fabrication*

Silicon wafers were reactive ion etched using an inductively coupled plasma (Speeder 100 Silicon DRIE, Alcatel), as described in Table 3-1, to create desired patterns into the surface of the wafer. The designs were patterned by using SPR 3012 (Shipley Megaposit, Dow) photoresist. The resist was exposed using a contact mask aligner (MJB3, Karl Suss) for 8 s with a UV lamp intensity of 8 mW/cm^2. A Savannah 200 ALD (Cambridge) was used to coat the patterned substrate with 30 nm of hafnia, to act as a chemical diffusion barrier. Finally, a CMS-18 Sputter System (Kurt J. Lesker) was used to sputter 30 nm of titanium and 100 nm of platinum at room temperature, which served as the bottom electrode.

Table 3-1. Summary of the etching conditions used to define features in Si.

Tool (ICP-RIE)	CF_4 Gas (sccm)	SF_6 Gas (sccm)	Antenna Power (W)	Chuck Power (W)	Base Pressure (mbarr)	Temp (˚C)
Speeder 100 Si Etcher	400	300	2,800	60	0.07	-5

3.2.3 *Released Cantilever Fabrication*

The released cantilevers were fabricated from 100 mm diameter silicon on insulator (SOI) wafers with 350 nm device silicon and 1 µm buried SiO_2 on 525 µm thick silicon carriers. 30 nm of hafnia was deposited onto the SOI wafer using a Savannah 200 ALD. The cantilevers were defined by a SPR 3012 photoresist mask. The top silicon was etched for 30 sec using a Speeder

100 Silicon DRIE as described previously. The buried SiO_2 was removed from under the silicon cantilevers using a BOE 6:1 wet etch for 20 min. Titanium was deposited on the surface of the released cantilevers by room temperature sputtering. The Ti was oxidized at 700 ˚C for 1min in an oxygen atmosphere. A 100 nm Pt bottom electrode was sputtered at room temperature onto the surface of the wafer.

Resonance measurements were performed on the released cantilevers under vacuum using an in-house built Fabry-Perot interferometer[90] described elsewhere by Guillon *et al*.[91] of CNRS. Fitting the amplitude response versus frequency to a Lorentzian function allowed the resonant frequency of the cantilever stacks to be determined.

3.3 Results and Discussion

3.3.1 Recess Printing from Patterned Stamps

Recess printing requires that both protruding and recess features come into contact with the stamp. In order to avoid deposition of the solution in undesired areas, a sacrificial print was made where only the protruding features contact the surface, as shown in Figure 3-3 (a). This allows the subsequent printing cycle to deposit only the PZT solution remaining in the stamp wells, as shown in Figure 3-3 (b). It was found that one sacrificial printing cycle completely removed the ceramic solution from the stamp protrusions.

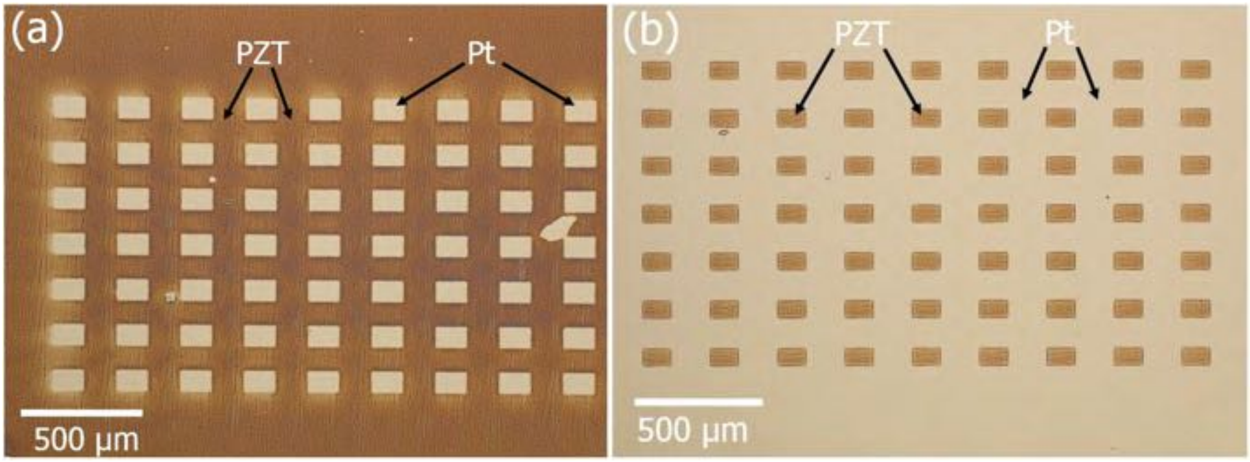

Figure 3-3. Optical microscopy images of the (a) initial printing step used to clean the protrusions of the stamp of ceramic precursors, and the (b) subsequent printing of PZT precursor solution from the recesses of the stamp. The PZT features are darker in color.

When printing from the recesses of wells, the wells must be shallow enough to allow the well surfaces to come into contact with the substrate, while also being sufficiently deep to insure that the recesses do not touch the surface of the substrate during the sacrificial printing step. The stiffness of the polyurethane, coupled with the inherent undulation of the stamp surface, impose restrictions on the ideal recess depth of the stamp. This work used recesses with areas that were 120 x 78 µm, and each recess was separated from the next by over 100 µm. Stamps with recess depths of 10.3 µm were printed onto a Pt coated Si substrate. Sufficient pressure was applied to the stamp that the recesses deformed their lateral shape, as shown in Figure 3-4 (a). However, it was found that for this depth, the recesses could not be forced into contact with the printing surface. Results from printing using stamps with recess depths of 3.6 µm are displayed in Figure 3-4 (b). For this case only ~50% of the recesses come into contact with the printing surface, and of the recesses where printing occurred, only ~20% of the printable area was transferred. Stamps with recess depths of 2.1 µm allowed 100% of the recesses came into contact with the printing surface, as shown in Figure 3-4 (c). The PZT which was transferred onto the printing surface increased to ~60% of the printable area. 100% of stamp well recesses of 1.2 µm depth came into contact with the printing surface, with an increase to ~77% of the printable area being transferred, as shown in Figure 3-4 (d). Finally, sacrificial printing of stamps with recess depths of 0.5 µm was performed. However, it was not possible to avoid printing from stamp recesses during this initial printing step. Stamps, in this work, therefore had ideal recesses depth from 1 to 2 µm. A summary of the stamp and printed dimensions are displayed in Table 3-2.

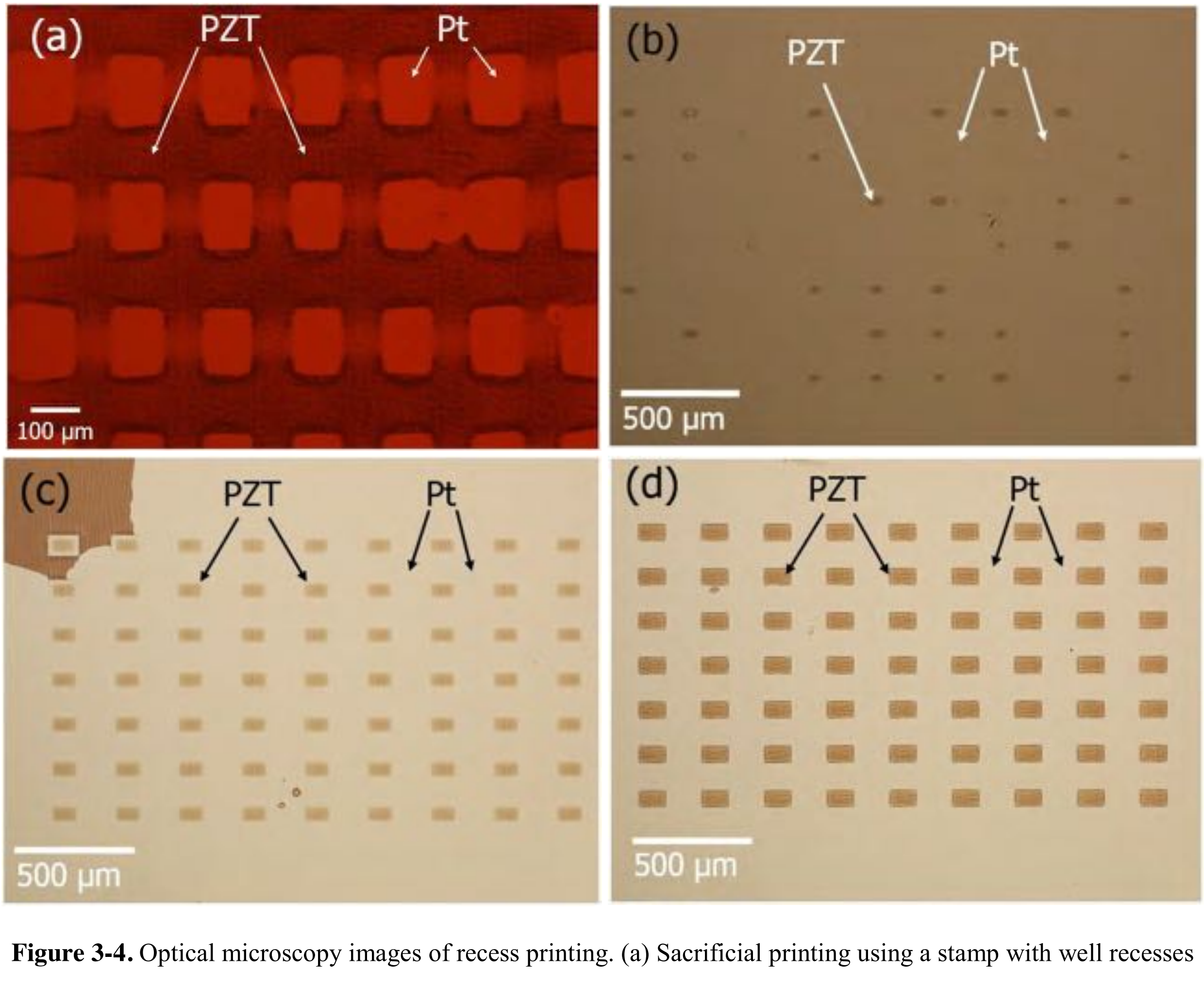

Figure 3-4. Optical microscopy images of recess printing. (a) Sacrificial printing using a stamp with well recesses which are 10.3 µm deep. (b) Recess printing using a stamp with 3.6 µm, (c) 2.1 µm, and (d) 1.2 µm deep well recesses.

Table 3-2. Recess printing dimensions of PZT features using stamps with various well depths.

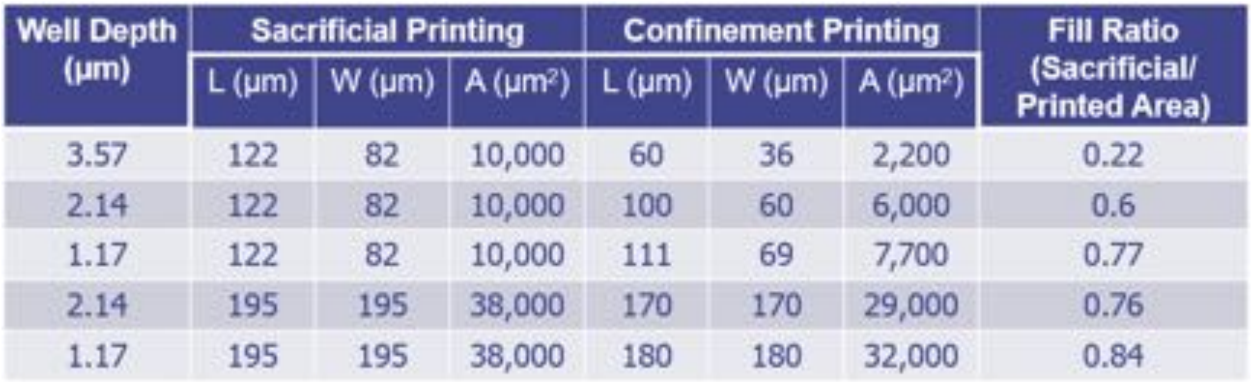

Well Depth (μm)	Sacrificial Printing			Confinement Printing			Fill Ratio (Sacrificial/ Printed Area)
	L (μm)	W (μm)	A (μm^2)	L (μm)	W (μm)	A (μm^2)	
3.57	122	82	10,000	60	36	2,200	0.22
2.14	122	82	10,000	100	60	6,000	0.6
1.17	122	82	10,000	111	69	7,700	0.77
2.14	195	195	38,000	170	170	29,000	0.76
1.17	195	195	38,000	180	180	32,000	0.84

A pivotal difference between printing from stamp protrusions and recesses is edge definition of the printed feature. When printing from stamp protrusions, patterns are defined primarily by the stamp surface features, as displayed in Figure 3-5 (a). This design is often lithographically defined by either a photoresist mold or a design etched into a surface. As was shown in previous work, printed features from stamp protrusions have a typical line edge roughness of a few hundred nanometers.

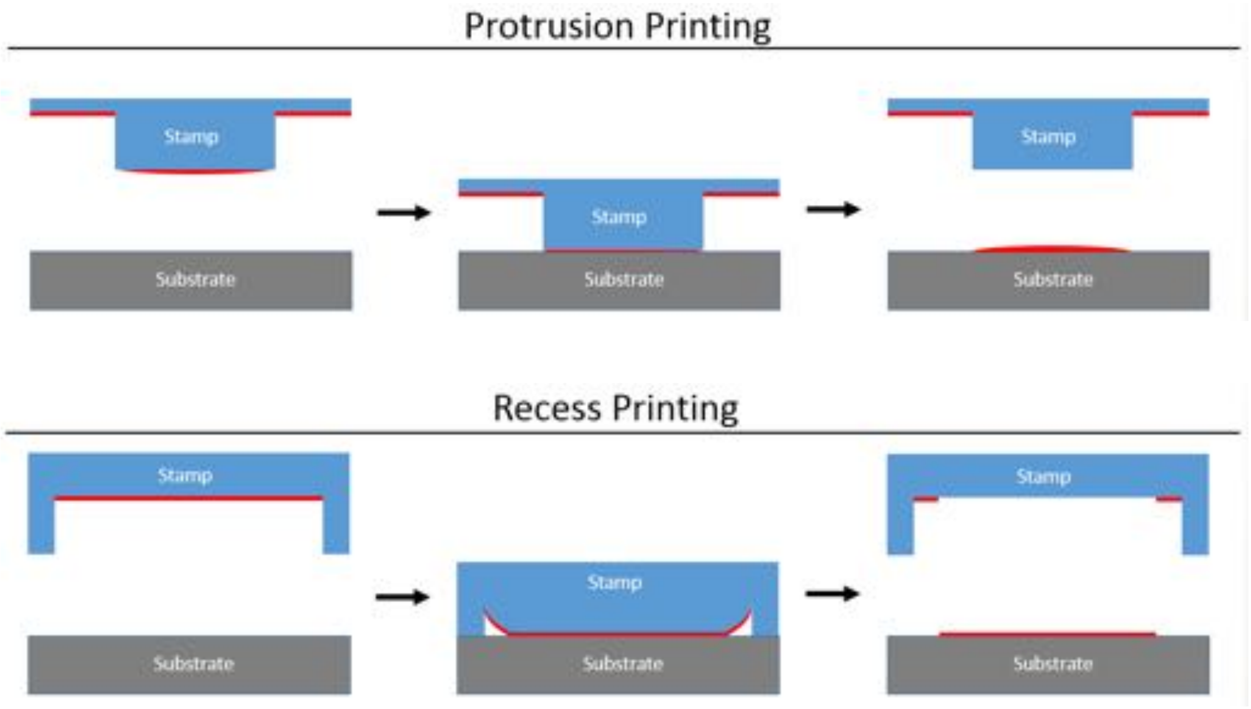

Figure 3-5. Schematic displaying the (a) protrusion and (b) recess printing process.

However, when printing from stamp recesses, the shape of the printed feature is dictated by several stamp parameters which affect how the externally applied stress is experienced locally at the stamp/substrate interface. Because stamp protrusions act as support pillars, feature corners do not fully come into contact with the printing surface even at large applied pressures,[92] as displayed in Figure 3-5 (b); this results in rounding of corners in the printed feature. Long range surface undulation (i.e. ~hundreds of microns), in the vertical direction, also results in various stresses being seen by the printing surface across the stamp, leading to inconsistent printing over these long ranges. Finally, stamp surface roughness plays a crucial role in the printed feature roughness over short ranges (i.e. tens of microns). Surface roughness results in slight variations in the stamp recess depth, producing variations in applied pressure between the stamp and the substrate, seen particularly at the edge of the printed feature. The roughness of the stamps can cause the line edge roughness of features printed from well recesses to be as large as a few microns. Displayed in Figure 3-6 (a) is a stamp were the surface of the stamp exhibited a large degree of surface roughness. Figure 3-6 (b) shows the corresponding PZT feature printed from a stamp recess with a line edge roughness of ~2.5 µm. Displayed in Figure 3-6 (c) is a stamp surface with a small degree of surface roughness. Figure 3-6 (d) shows an angled view along the line edge of the corresponding printed feature with a line edge roughness > 0.5 µm.

When printing from a stamp recess the center of the recess contacts the printing surface. In this configuration the stamp surface does not have a discrete change in surface topography. Hence, the solution should act as a wetting liquid over a flat surface even at the edge of stamp/substrate contact area, as displayed in Figure 3-5 (b). This increases the amount of solution available to be transferred along a printed feature edge, and therefore increases sidewall angles in comparison to features printed from stamp protrusions. Figure 3-7 (a) presents a 15 µm PZT feature printed from the recess of the stamp. The corresponding surface profile of this printed feature is shown in Figure 3-7 (b), which highlights the difference in the surface profile of PZT printed feature by stamp protrusions and stamp recesses. The features printed from the stamp recess has sidewall angles of ~30 degrees, which is an increase by over an order of magnitude compared to features printed by stamp protrusions.

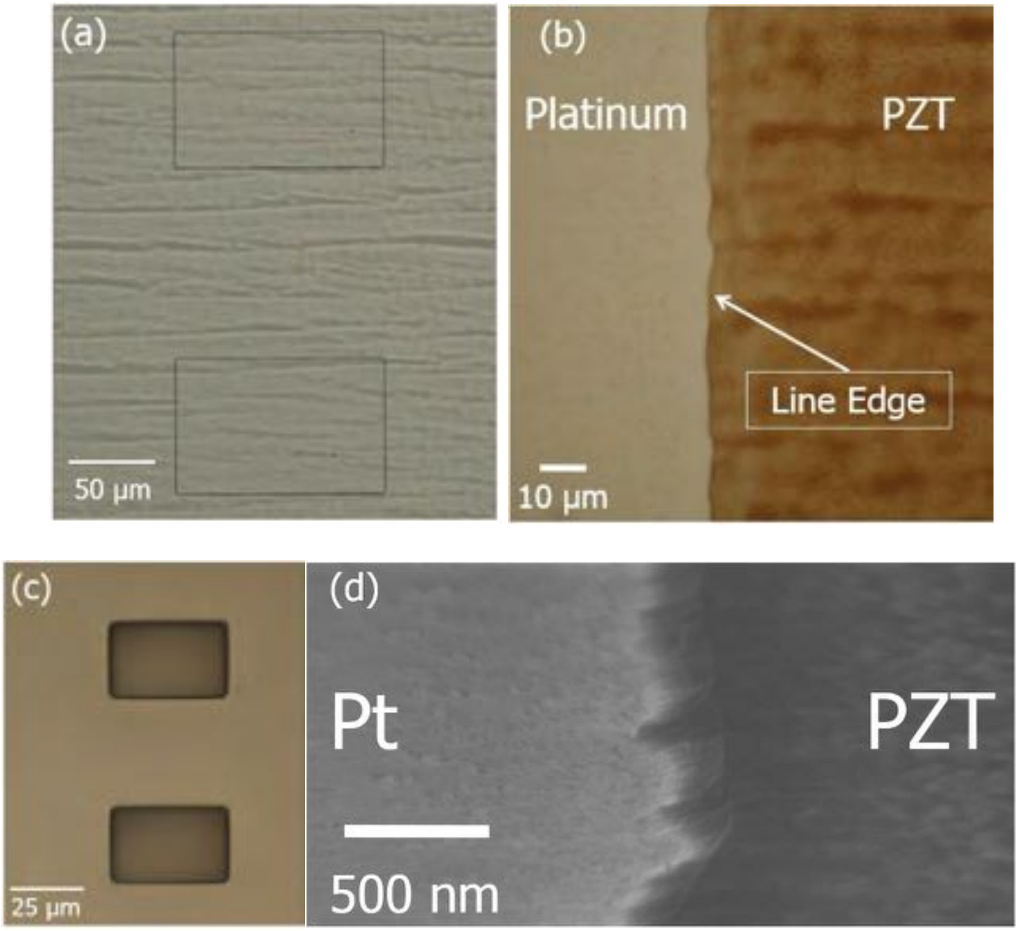

Figure 3-6. Recess printing using PU/PDMS composite stamps. (a) Composite stamp with rough surface and (b) line edge roughness of subsequently printed feature. (c) Composite stamp with smooth surface and (d) line edge roughness of subsequently printed feature.

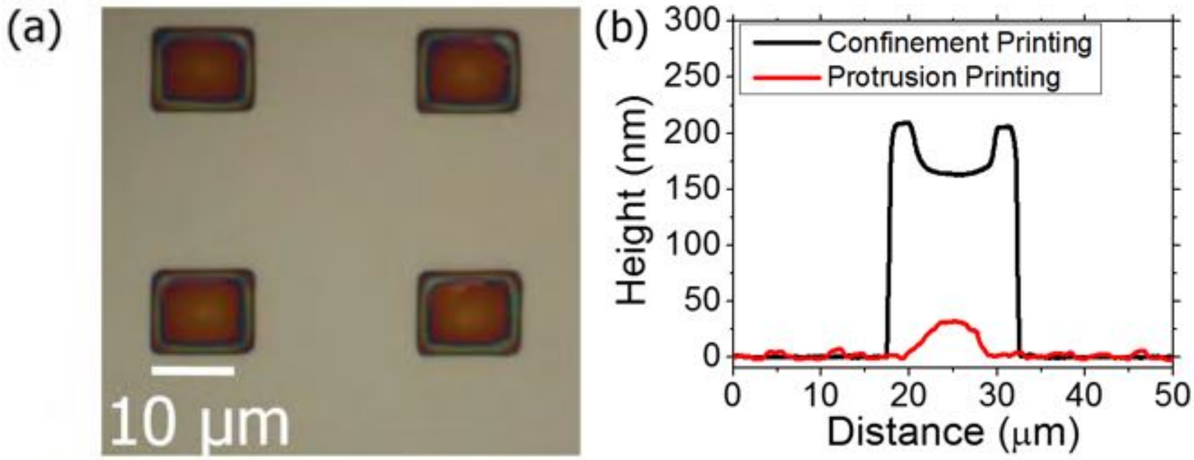

Figure 3-7. (a) Optical microscopy image of a PZT feature printed via the recess printing technique, and (b) the corresponding surface profile of feature shown to the left in comparison to a PZT feature of similar size printed from a stamp protrusion.

To ascertain whether there is an effect on the functional properties of material, the dielectric, ferroelectric, and piezoelectric properties of a PZT stack deposited through recess printing was characterized. The printing alignment was controlled, by eye, using the optical objectives of a contact aligner. Figure 3-8 (a) shows a characteristic degree of misalignment between subsequent, recess printed layers (i.e. ~2.5 μm). This degree of misalignment is on the same order as printing features with stamp protrusions, because both printing methods rely on alignment using optical microscope objectives from a contact aligner. Five recess printed PZT layers, shown in Figure 3-8 (b), yielded a film with a thickness of 300 nm. Figure 3-8 (c) displays the relative permittivity and loss tangent as a function of frequency of the corresponding 300 nm film stack. The stack exhibits a relative permittivity of 730 and loss tangent of 0.022 at 1 kHz. Figure 3-8 (d) shows the polarization-electric field behavior as a function of increasing electric field. The hysteresis loops are well saturated, with no evidence of pinching or imprint. The printed stack had a coercive field of 95 kV/cm and a remanent polarization of 26 μC/cm^2 at 100 Hz.

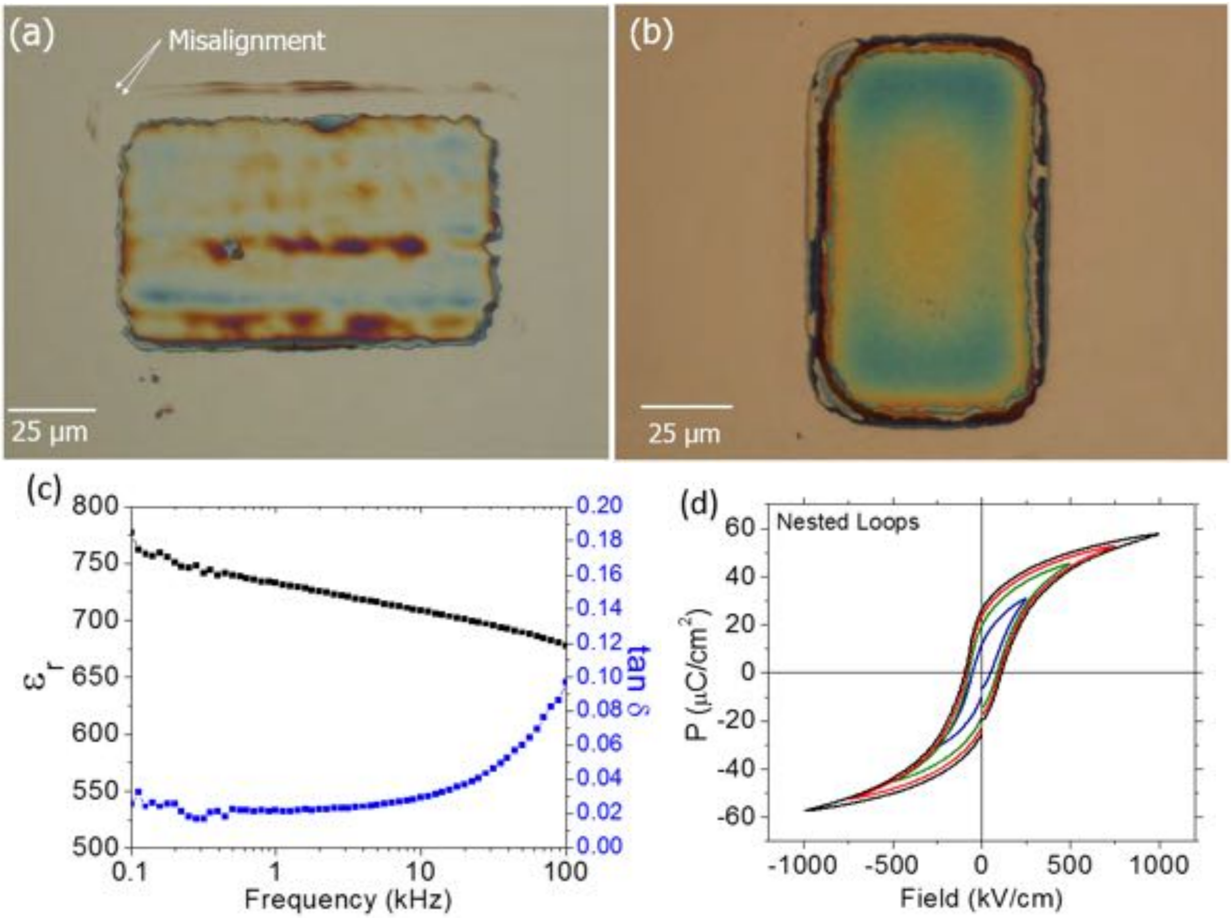

Figure 3-8. Stacking of PZT prints through recess printing. (a) Representative stack displaying misalignment between subsequent printing cycles. Electrical measurements of a (b) 5 layer recess printed 300 nm PZT stack. (c) Relative permittivity and loss tangent as a function of frequency. (d) Hysteresis loop as a function of increasing electric field.

Finally, the transverse piezoelectric coefficient, $e_{31,f}$, of the film was -5.2 ± 0.28 C/m^2. The dielectric, ferroelectric, and piezoelectric properties of the recess printed PZT film was consistent with the functional properties exhibited by blanket PZT films of similar thicknesses.[87] This indicates that the recess printing process does not limit the achievable properties of the patterned features.

3.3.2 Printing on Patterned Substrates

Printing from stamp recesses onto flat surfaces greatly increases sidewall angles of printed features, but at the cost of increasing line edge roughness. In order to mitigate this problem, a flat stamp can be used to print onto a patterned substrate. In this configuration, the printed ceramic design is dictated by a lithographically defined, dry etched geometry into a substrate. This restricts the line edge roughness of the final printed feature to be on the order of features printed by protrusion stamping. The flat stamps are wetted by the printing solution; effectively making an analogous stamp/solution configuration as the central areas of recesses in patterned stamps. Thus, the increased sidewall angles of the printed features, as exhibited in features printed from stamp recesses, should be preserved in this configuration.

In this work, Pt coated silicon wafers were used as the substrate for printing. Prior to printing, an etch mask was photoligraphically defined on their surfaces. The design was dry etched ~1 μm into the substrate, and the etch mask was subsequently removed. The patterns varied from 500 down to 1 μm in lateral size. Unpatterned composite PU/PDMS stamps were inked with PZT solution and brought into contact with the patterned substrate. Once the stamp was removed, the solution had transferred onto the raised features in the patterned substrate, as shown in Figure 3-9. The precursor film was then pyrolyzed and crystallized. This cycle was repeated until the desired thickness was reached. Pre-etching the designs into the surface of the substrate removed the need to align the stamp with the printing surface. Thus, the registry of printing multiple cycles onto a feature became a trivial matter, allowing the printing to be performed by hand.

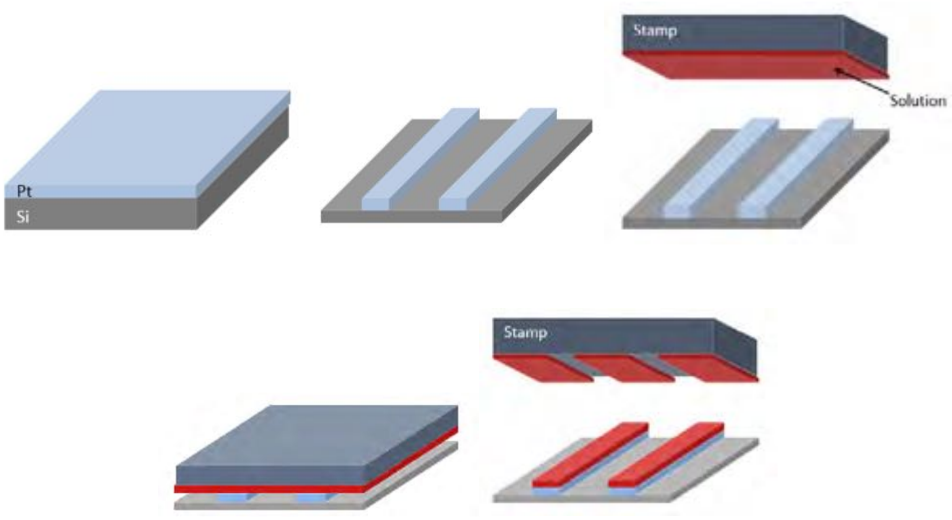

Figure 3-9. Schematic of printing ceramic solutions onto patterned substrates with flat stamps.

Figure 3-10 shows PZT solutions that were printed onto patterned substrate surfaces. Figure 3-10 (a) exhibits the case where a stamp was peeled, from a substrate, from left to right across the feature. The solution clearly experienced redistribution as the stamp was separated from the substrate. The pathlines of the fluid as it interacted with the feature are apparent. On the right side of the image, the fluid was drawn uniformly across the substrate, but it deformed as it reached the leading edge of the feature, causing the pathlines to curve around the feature. Figure 3-10 (b) shows an example of a case where the stamp was peeled, from a substrate, from left to right across the feature; enough fluid redistribution has occurred that almost no solution remains on the leading surface of the printed feature. Therefore, it is critical that printing parameters, such as solution viscosity/solution thickness, peeling speed, and peeling direction, be characterized and optimized in order to ensure pattern fidelity over multiple printing cycles.

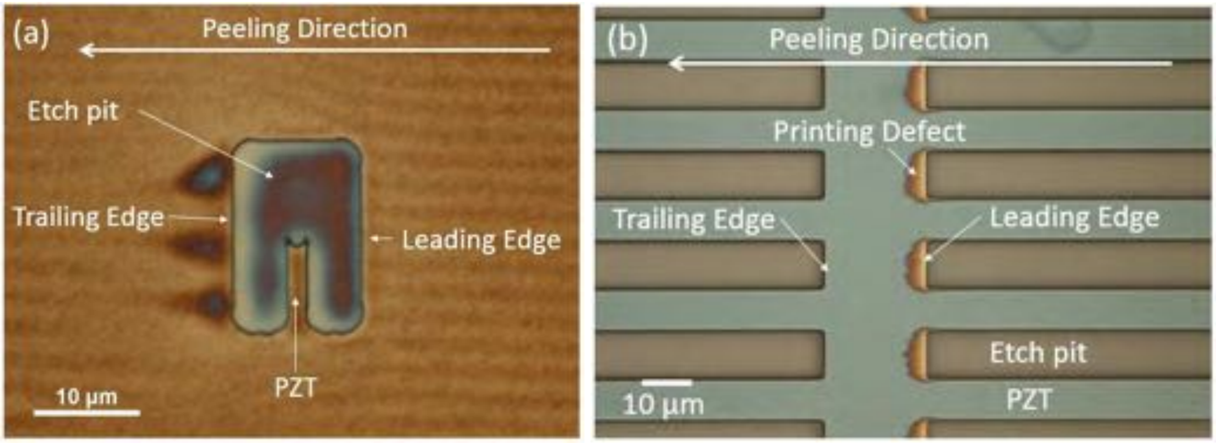

Figure 3-10. Optical microscopy images of PZT solution printed onto patterned substrates. (a) Fluid redistribution and (b) printing defects are evident after the stamp was peeled from the substrate from right to left across the features.

The amount of solution that could be transferred from the stamp surface to the patterned substrate surface was investigated. The thickness of the solution deposited onto the stamp surface was varied by controlling the speed of the spin coating process. In this work, solutions were spun onto the flat stamp surfaces varying from 1000 to 7000 rpm. A coated stamp was spun at a particular spin speed and printed onto a feature. The sample was pyrolyzed and crystallized, and the process was repeated at the same conditions until several hundred nanometers of the PZT film was deposited. The films were cross-sectioned to determine the optimal printing conditions.

Figure 3-11 (a) shows a 325 nm thick crystallized film where the solution was spun onto the stamp at 1000 rpm. The thickness of the printed film was doubled at the sidewall (~600 nm thick). The printed feature was enlarged, and overhung the original etched feature sidewall by ~200 nm. Figure 3-11 (b) exhibits a 500 nm film where the solution was spun at 1500 rpm. The thickness variation of the printed film was only ~25% (~625 nm thick). The film was nearly the same size as the etched substrate design, with printed sidewall between 70 and 80 degrees. Finally,

Figure 3-11 (c) shows a 275 nm film where the solution was spun at 3000 rpm. The thickness variation of the printed film was again only ~25% (~340 nm thick). The film has identical dimensions as the substrate feature with nearly 90 degree printed sidewalls. Films deposited from stamps spun at speeds >3000 rpm did not significantly improve printed sidewall angles or thickness uniformity to justify the decrease in film thickness per layer deposited. In general, ~50 to 60 nm of crystallized PZT thickness per stamping cycle yielded films with steep sidewalls and minimal thickness variation. Thicker coats per print led to significant bulging at feature sidewalls and/or non-uniform solution transfer upon stamp separation from the substrate.

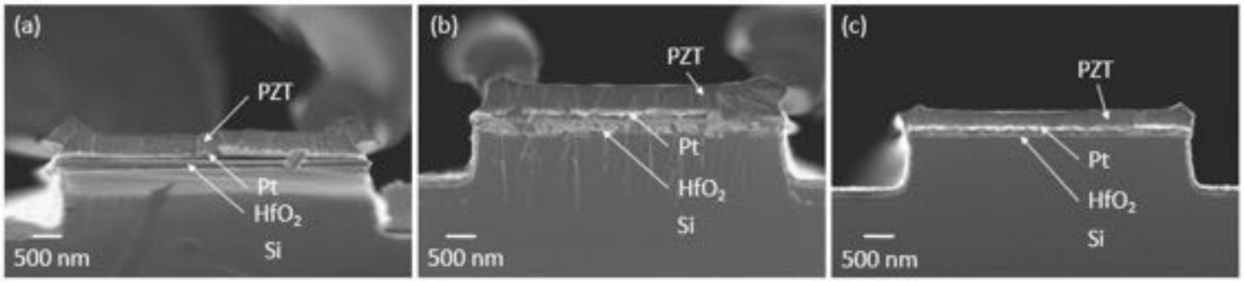

Figure 3-11. Cross-sectional SEM images of PZT solution printed onto a patterned substrate. Solution was spun onto stamp at (a) 1000 rpm, (b) 1500 rpm, and (c) 3000 rpm.

In addition to solution thickness, the effect of the peeling direction of the stamp from the substrate in relation to the feature direction was also investigated. Stamps were spin coated with solution at 3000 rpm and brought into contact with a patterned substrate, the stamp was separated from the substrate, and the print was crystallized. Every subsequent print was peeled in the same orientation as the first printing layer until the final crystallized film was ~300 nm thick. The substrate was cross-sectioned to determine the influence peeling direction had on printed feature sidewall angles.

Figure 3-12 (a) shows a cross-section of a film looking parallel to the peeling direction of the stamp from the substrate feature. In this case, the solution at both right and left sidewalls experience similar dynamic forces upon the separation of the stamp from the substrate. As a result, the printed sidewalls have angles of ~50 to 60 degrees, with an increase in thickness of ~25% (375 nm thick) in comparison to the center of the feature. Figure 3-12 (b) displays a cross-sectioned film looking perpendicular to the peeling direction of the stamp of the substrate, where the stamp was sperated from right to left across the printed feature. The right printed sidewall in Figure 3-12 (b) is the leading edge of the patterned substrate, and the first edge to experience the forces associated with the separation of the stamp from the substrate. The solution at this edge is dragged towards the center of the feature, resulting in a printed sidewall angle of ~30 degrees, with an increase in film thickness of ~13% (340 nm thick) at the sidewall. The left printed sidewall in Figure 3-12 (b) is the trailing edge of the patterned substrate and the final edge to experience the forces associated with the separation of the stamp from the substrate. The solution at this edge is pulled away from the center of the feature, resulting in a printed sidewall of ~60 degrees, accompanied with an increase in film thickness of ~43% (430 nm thick).

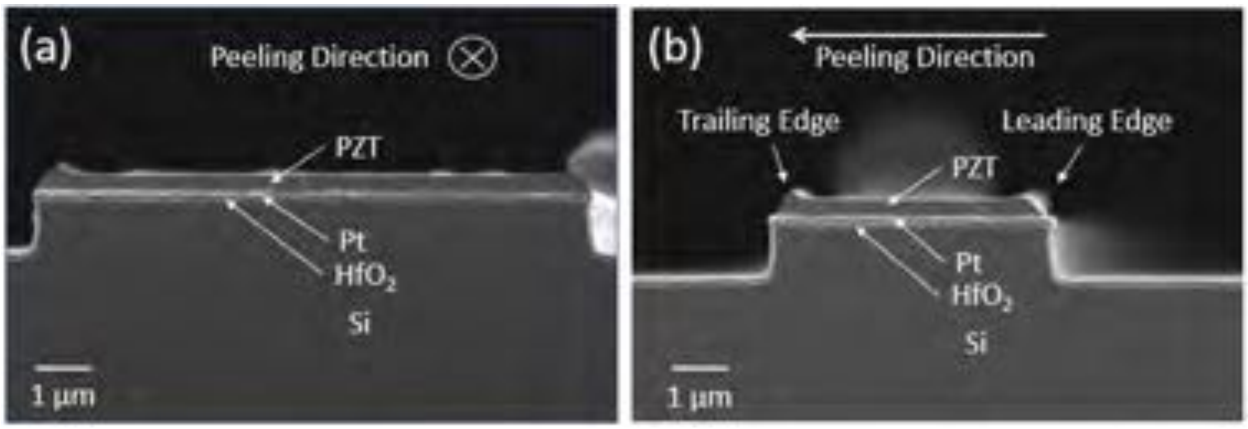

Figure 3-12. Cross-sectional SEM images of 300 nm crystallized PZT film printed on a patterned substrate feature. The stamp was separated from the substrate (a) parallel and (b) perpendicular to the viewing direction.

Finally, the peeling rate of the stamp from the substrate was investigated. Stamps were spin coated with solution at 3000 rpm and brought into contact with a patterned substrate, the stamp was separated by hand from the substrate, and the print was crystallized. Every subsequent printing was peeled at the same rate and orientation as the first printing layer until the final crystallized film was ~300 nm thick. The films were separated at one of two distinctive peeling rates by hand. In the first case, the stamp was peeled slowly enough away from the stamp that the separation front could be tracked clearly by eye. This separation front was on the order of a few millimeters per second. In the second peeling case, the stamp was removed from the stamp as quickly as possible. In this case, the separation front could not be tracked by eye, but is estimated to be on the order of meters per second based on stamp size and time needed. All crystallized films were cross-sectioned perpendicular to the peeling direction to determine the influence that the peeling rate has on the sidewall angles of printed films.

Figure 3-13 (a) shows a cross-sectioned film where the stamp was separated slowly (~mm/sec) from a 20 µm lateral substrate feature. In this case, the printed film has shallow sidewall angles ~20 degrees, however the film has minimal thickness variation across the width of the features. Figure 3-13 (b) displays the cross-section of a film where the stamp was separated quickly from a 10 µm lateral substrate feature (~m/sec). The sidewalls angles of this printed feature sharply increased to between 70 and 90 degrees. The increased peeling rate also resulted in an ~25% increase in thickness of the printed film near the edges of the feature.

Features with small lateral feature sizes were also printed in the same manner. These features require steep sidewall angles in order to build printed films of significant thicknesses. Figure 3-13 (c) is an exmple of a 1 µm lateral feature where the stamp was slowly separated from the subsrate. Again, shallow sidewall angles of ~10 degrees are observed. The low sidewall angles produced significant thickness variation across the width of the substrate, making it impossible to build films thicker than a few hundred nanometers. In contrast, Figure 3-13 (d) shows a 1 µm lateral feature where the stamp was quickly separated from the substrate. As was seen with larger lateral features, the sidewall angles of the printed feature were sharply increased. This sample also has thickness variation across the width of the feature, but could be printed to a similar thickness as the other sample while maintaining a similar width to the original feature.

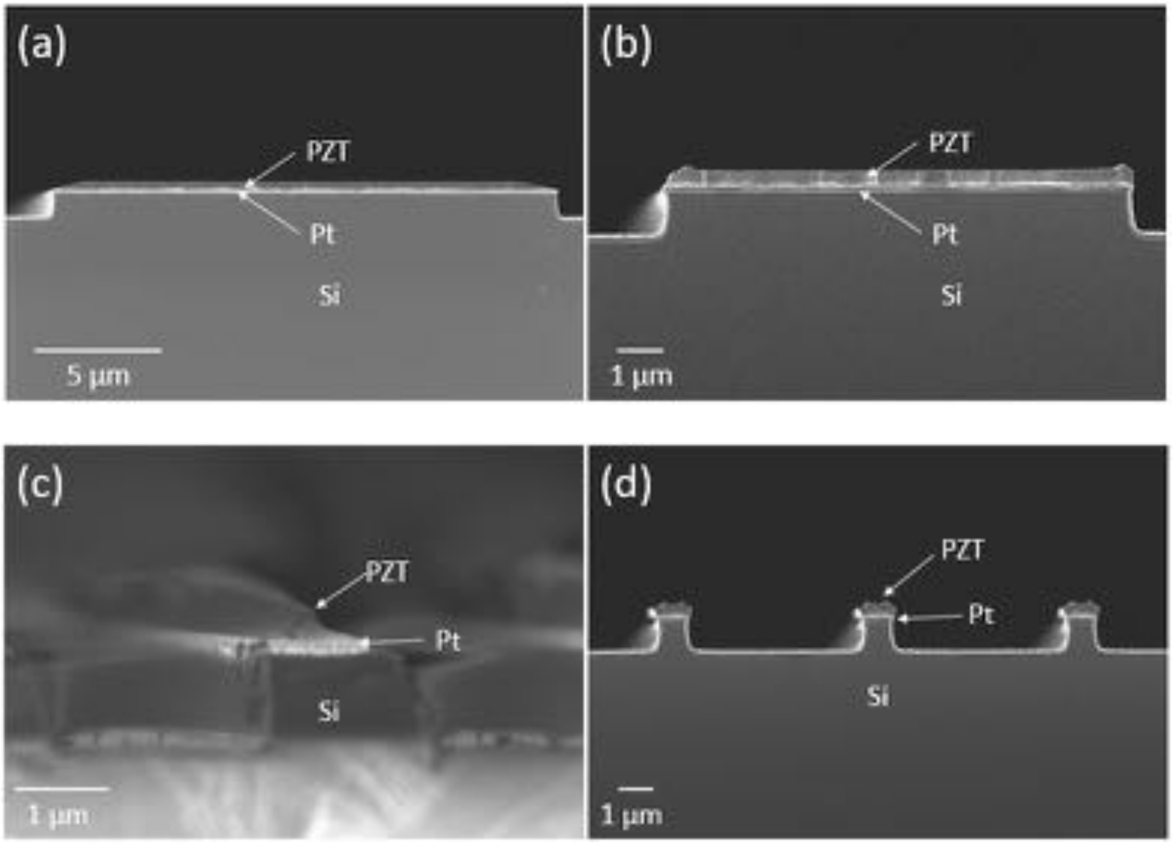

Figure 3-13. Cross-sectional SEM images of crystallized PZT film printed with various peeling rates of the stamp from the patterned substrate. Printing was done by hand at peeling rates on the order of (a and c) millimeters per second (b and d) meters per second. The substrate features varied in size: (a) 20, (b) 10, and (c and d) 1 µm features. All features had stamp peeling directions parallel to the viewing direction.

It is evident that the fluid dynamics of the solution, as the stamp is separated from the substrate, greatly influences the pattern fidelity of the final printed feature. In this printing technique, the solution is spun onto the stamp as a liquid. During the spinning process, the solution is initially thinned by centrifugal forces generated by the rotating surface. However, this eventually gives way to a the second mechanism for film thinning through solvent evaporation. This causes the film to progressively increase in the concentration of non-volatile constituents as time passes, which in turn greatly increases the viscosity.[93] The increase in viscosity results in a a gel state. In this work, the evaporation of volatile solvents was evident up to 5 to 10 seconds after the spinning process. Printing before this evaporation in ambient air was not possible. However, once this gel was formed on the stamp, little to no difference was seen in the printing mechanics whether the printing occurred 30 seconds or 30 minutes after spinning.

The viscous gel state is much more resistant to flow than the original liquid solution. This was most evident in experiments where peeling rates were varied. Slow stamp peeling rates resulted in the gel experiencing low shear rates. This gave the gel adequate time for the high molecular weight organic chains to flow past each other, resulting in printed films where the solution redistributed, resulting in shallow sidewall angles. Fast stamp peeling rates resulted in the gel experiencing high shear rates. This did not allow redistribution of the gel as the stamp was removed from the substrate, producing minimal printing defects and steep sidewall angles.

Another consequence to the printed film being in a gel state is that once the film was transferred to the substrate, the shape of the film was extremely difficult to alter. In this work, films were subjected to ultrasonic vibrations and/or doctor blades directly after printing but prior to drying at elevated temperatures, in an effort to modify prints which had large variations in thickness across a feature. However, none of these attempts were successful.

By tailoring the thickness of each printed layer, alternating peeling directions, and quickly removing stamps from the substrate, it was possible to create printed PZT films with steep sidewalls while minimizing thickness variation across the feature across a wide range of feature sizes. Features printed with optimal printing parameters are shown in Figure 3-14 (a), which displays a printed 10 µm down to a 1 µm wide printed crystallized PZT film with 90 degree sidewall angles, shown in Figure 3-14 (b). These printed films also exhibit excellent perovskite phase formation, showing analogous microstructures to spin-coated PZT films. Figure 3-14 (c) presents the columnar phase growth of the perovskite phase present in a cross-sectioned 10 µm printed PZT feature with no evidence of porosity. Figure 3-14 (d) demonstrates, from the top-down view, that printed PZT films exhibit excellent perovskite phase formation, with no evidence of seconday phases or porosity.

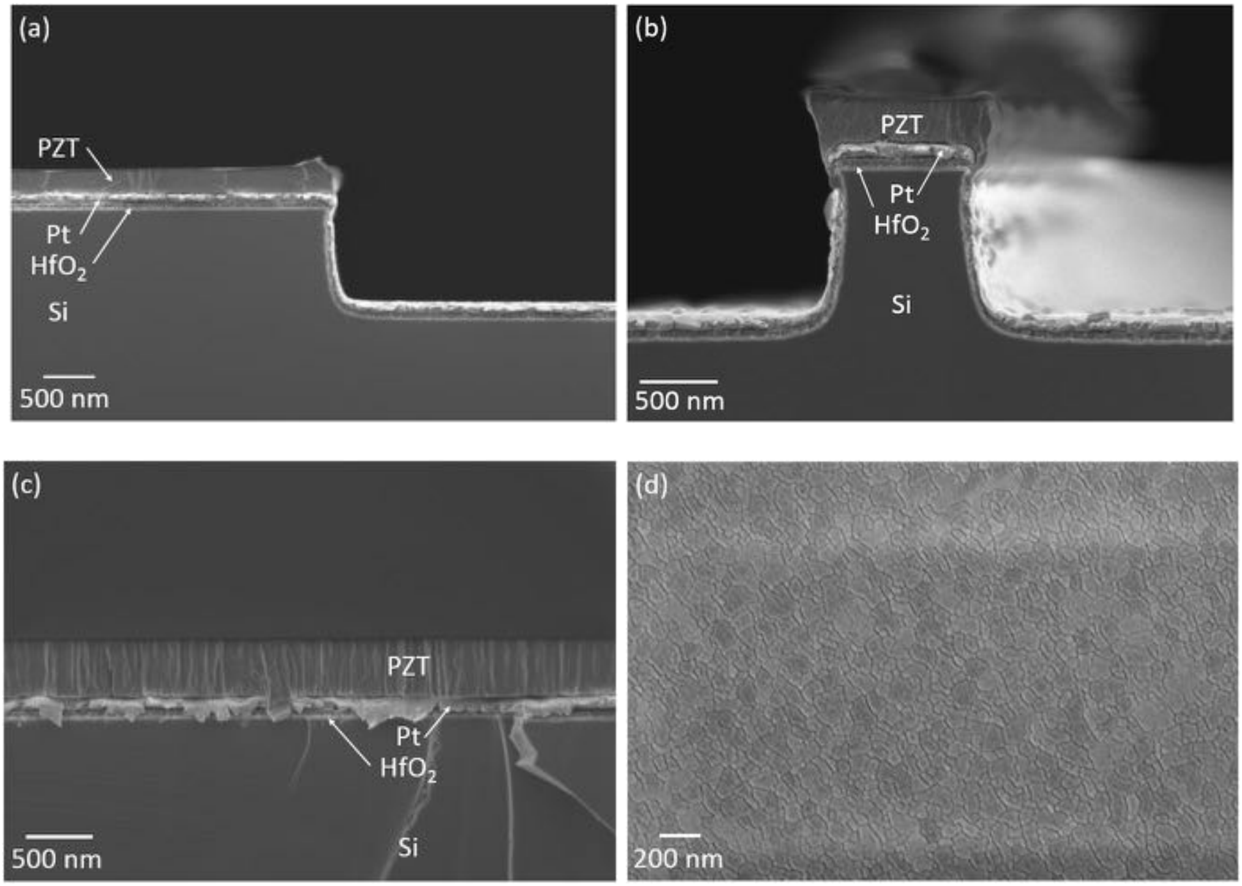

Figure 3-14. SEM micrographs of crystallized PZT film printed with ideal solution thickness per print, stamp peeling direction, and stamp peeling rate for a (a) 10 μm and a (b) 1 μm. The (c) cross-sectional and (d) top down microstructure of a crystallized PZT film deposited by printing is displayed.

3.3.3 Printing on Released Cantilevers

Printing of PZT allows good functional material properties to be retained by avoiding etchants. However, if the device is released after the printed PZT deposition, etchants are usually needed. One way of keeping the functional material from contacting even the releasing etchant is to define and release the structure first, followed by the PZT printing on the released structure.

The printing configuration used in this work utilizes a combination of the work described previously. Patterned wells 1.5 µm deep were defined in the stamp surface. 2 and 6 µm wide cantilevers were defined in the top layer of SOI wafers by a reactive ion etch down to the buried SiO_2 layer. The oxide was subjected to a wet buffered oxide etchant which released the silicon cantilever from the underlying substrate, as shown in Figure 3-15 (a). The cantilevers were 350 nm thick and had a 1 µm gap underneath the structure. A 30 nm layer of HfO_2 was deposited over the silicon cantilevers to act as a chemical barrier between silicon and the lead oxide from the PZT solution. The bottom electrode was grown on the cantilevers by first depositing a 30 nm TiO_2 adhesion layer for the 100 nm Pt bottom electrode. A released cantilever with its bottom electrode is shown in Figure 3-15 (b).

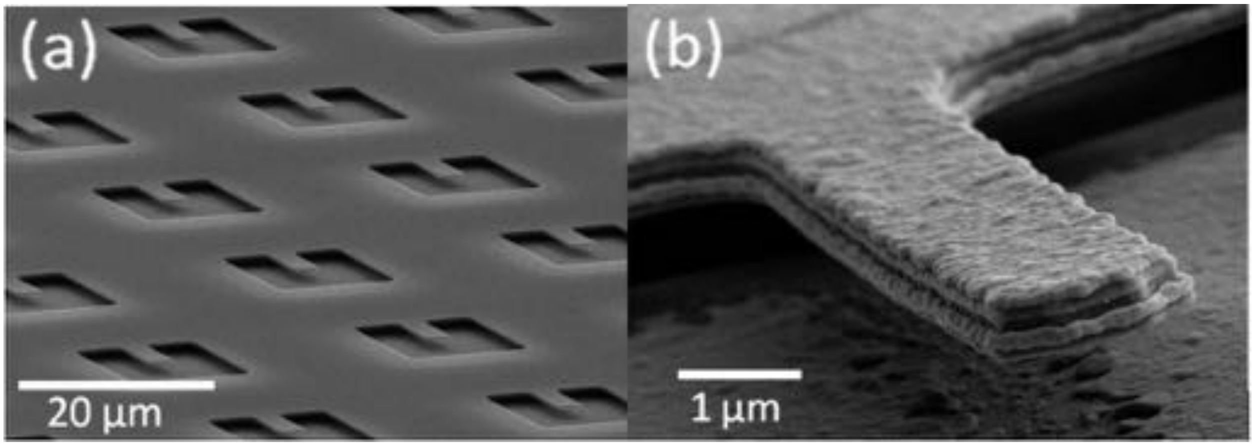

Figure 3-15. SEM micrographs of (a) released Si cantilevers and (b) released $Pt/TiO_2/HfO_2/Si$ cantilevers.

The bottom electrode configuration was tested by depositing a 1 µm blanket PZT on a $Pt/TiO_2/HfO_2/Si$ wafer. The bottom electrode showed no delamination or hillocking during the PZT deposition. The perovskite phase crystallized onto the substrate as displayed in Figure 3-16 (a). The PZT film had a relative permittivity of 1000, a loss of 0.021, shown in Figure 3-16 (b).

The P-E loop was well saturated with a coercive field of 55 kV/cm, and a remanent polarization of 23 μC/cm^2, displayed in Figure 3-16 (c).

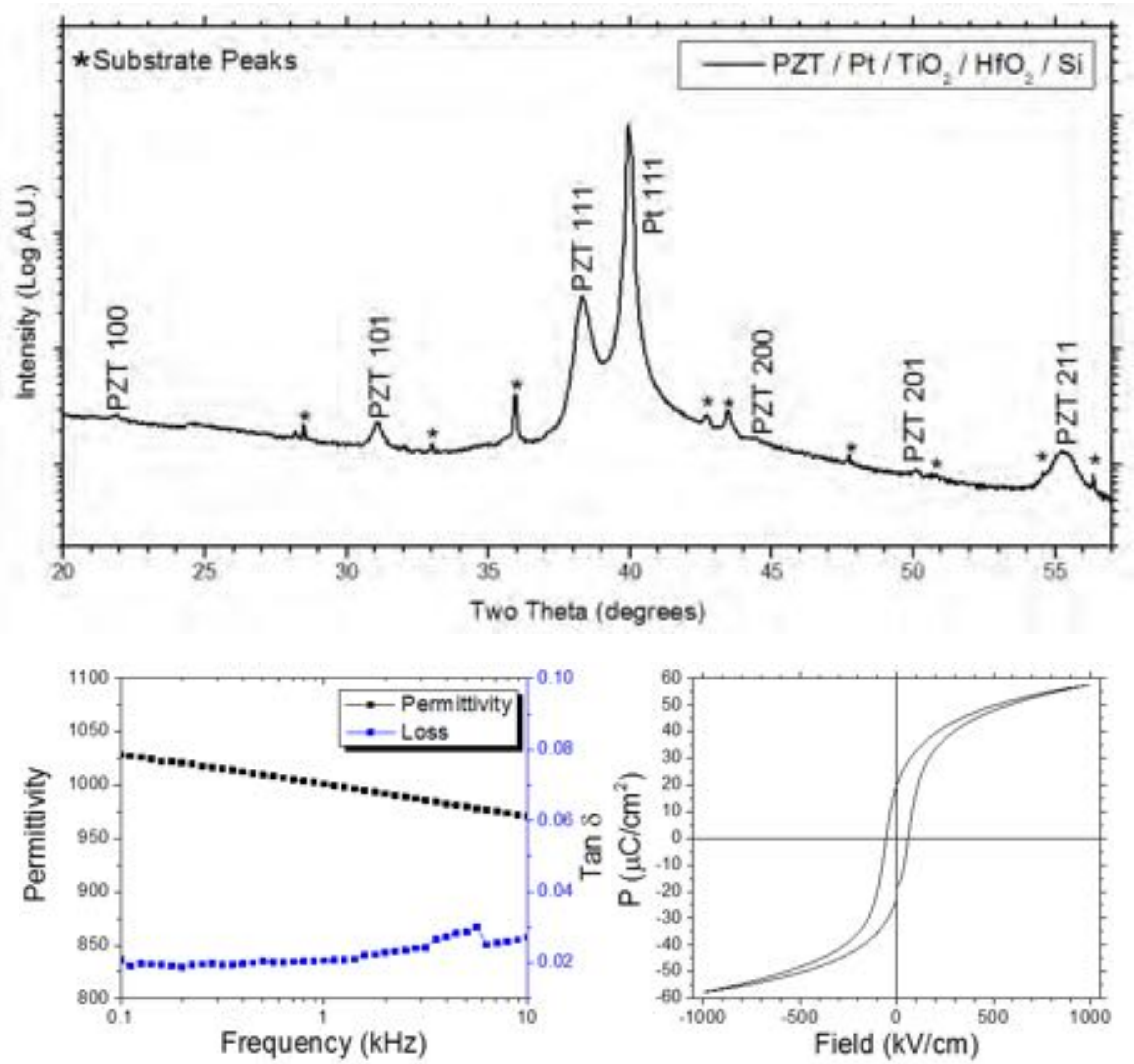

Figure 3-16. (a) XRD scan of PZT deposited over a Pt/TiO$_2$/HfO$_2$/Si substrate. (b) Dielectric and (c) ferroelectric properties of the film.

PZT solution was spun onto the patterned stamp surface, and sacrificial printing was performed to remove solution from the protrusions of the stamp. The stamp recesses were aligned with the released cantilever structures, shown optically in Figure 3-17 (a). To achieve complete contact with the released structure, enough pressure was applied that the stamp recesses contacted and subsequently forced the cantilever to bend and touch the bottom surface of the cavity in the substrate. The pressure was then slowly reduced until the stamp separated from the wafer, as displayed in Figure 3-17 (b). Using patterned stamps in conjunction with patterned substrates resulted in PZT solution printed on the top surface of the released cantilever, as shown in Figure 3-17 (c). This approach also avoids deposition of the PZT in the undesired regions between the released cantilevers, thus avoiding the need for wet etching the PZT from these areas in a subsequent processing step.

Figure 3-17 (d) reveals that the printed PZT completely covered the top surface of the released cantilever, while no solution was deposited on the edges of the cantilever. 100% of released structures survived the printing process. It is extremely important to control the direction of separation during stamp removal. If the free end of the cantilever is pulled up along with the leading edge of the stamp, the cantilever can be deflected to a much greater extent than when the cantilever is pressed to the well floor. This can lead to failure at the base of the structure. However, when the stamp is removed from the base of the cantilever first, as displayed in Figure 3-17 (b), the entire structure releases from the stamp more readily. When performed properly, the recess printing of PZT onto released cantilevers showed no visible cracks in either optical or SEM micrographs.

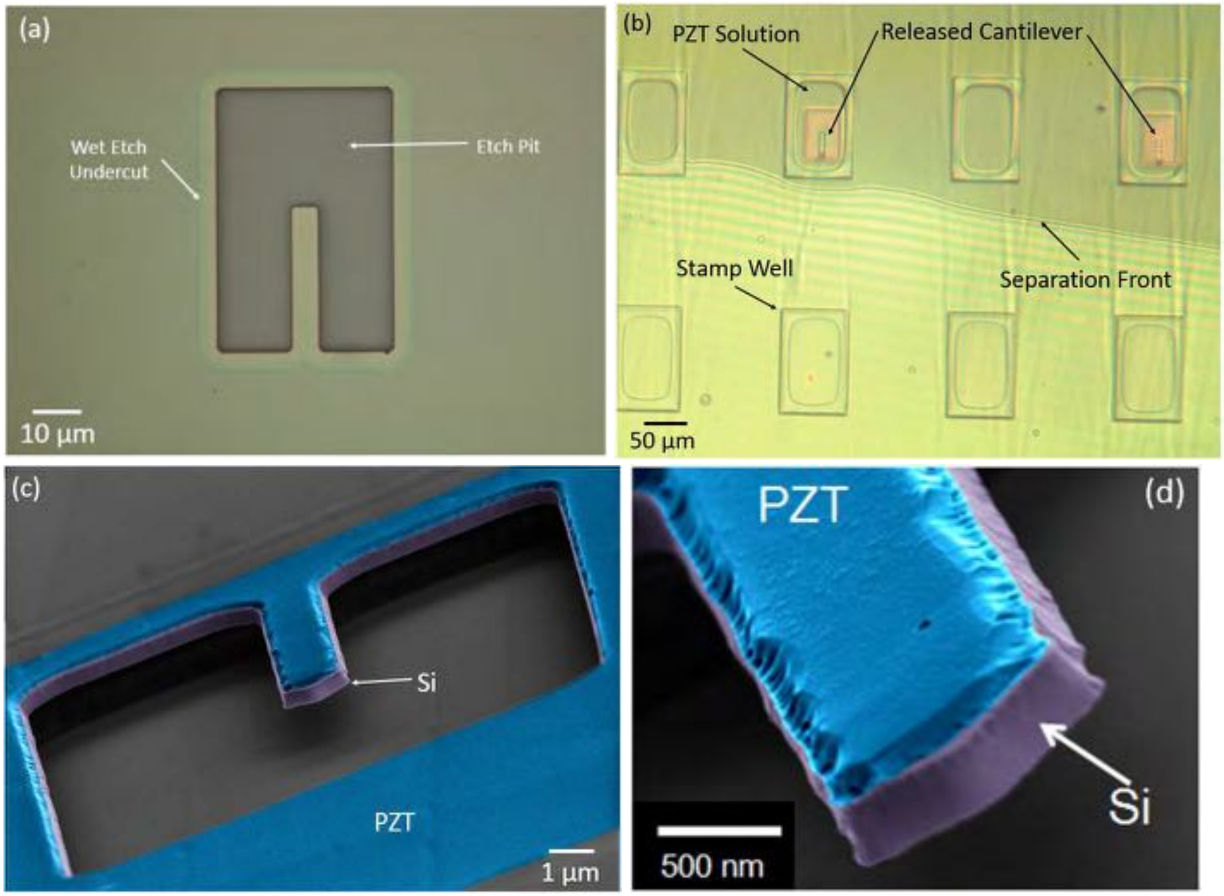

Figure 3-17. Optical image of a (a) released 6 µm wide cantilever which was aligned to a patterned stamp. (b) Patterned stamp being peeled from patterned wafer with released cantilever. (c and d) Colorized SEM micrographs of the PZT printed onto a released 2 µm wide cantilever.

3.3.4 *Mechanical Testing of Released Cantilevers*

Measurements of the resonant frequency and the quality factor corresponding to the fundamental mode of vibration of the released cantilevers were conducted to address the question of whether the released structures preserve their mechanical integrity after the PZT deposition. The cantilevers experience large shape deformations during the recess printing of the PZT solutions. These stresses may introduce cracks in the stack that cannot be visually detected or it may introduce subcritical flaws which could cause failure of the beam during device operation.

Figure 3-18 shows that the measured resonant frequency follows the predicted trends before and after PZT deposition. All devices subjected to operational displacement conditions survived testing. These results, coupled with microscopy characterization of the device, suggest that PZT can be printed directly onto released structures to produce useful devices.

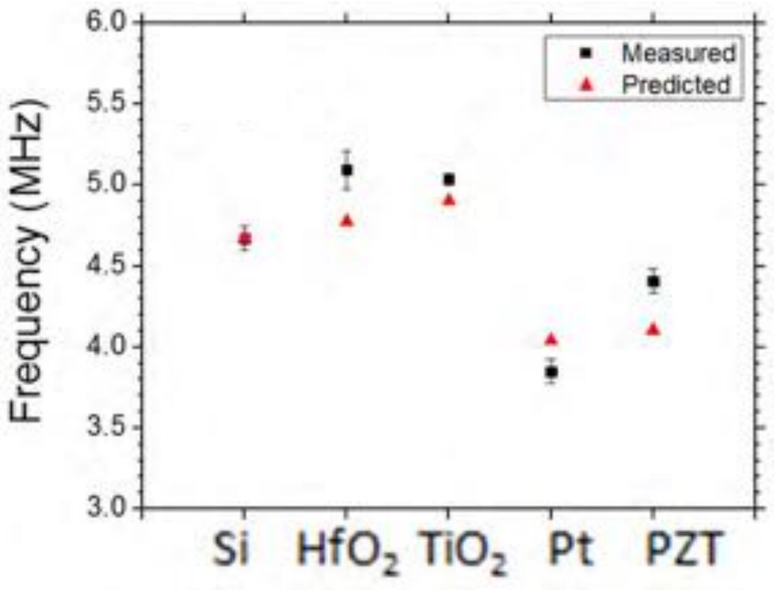

Figure 3-18. Resonance frequency of the released cantilever stack as a function increasing number of material layers beginning with bare Si and ending with a PZT/Pt/TiO_2/HfO_2/Si stack.[‡]

3.4 Conclusions

Printing PZT solutions from the recesses of patterned stamps offers significantly improved sidewall angles in comparison to printing from stamp protrusions; however this comes at the expense of increasing line edge roughness of the printed feature. This was mitigated by defining the feature shape lithographically by etching the desired shape directly into the substrate instead

---

[‡] Predicted resonant frequencies of the cantilever stacks were calculated by using equations found in Appendix B

of defining the shape solely into the stamp surface. This produced a printed feature with line edge roughness comparable to features printed with stamp protrusions, but with the added benefit of increasing sidewall angles by over an order of magnitude. A combination of printing parameters such as thickness of the deposit per layer, peeling direction, and most importantly peeling rate allowed for printed features ranging from hundreds of microns down to 1 μm lateral feature size to exhibit sidewall angles upwards of 70 to 90 degrees. These wall angles are the steepest reported in the literature for ceramic films that have been deposited by an additive patterning technique. Finally, in an effort to produce a free-standing structure where etchants would never see the functional material, printing was performed from stamp recesses directly onto pre-released cantilevers. 100% of the structure survived the stamping process without damaging the mechanical integrity of the resonating device.

Chapter 4

Printed Piezoelectric Bio-Sensing Cantilever Sensors

Defining electroceramic films into required patterns for device applications is realized by one of two routes. A pre-deposited, continuous layer of material can be fashioned into the desired shape by subtracting material from certain regions (etching or machining), or the definition/deposition of the material can be combined into a single step (inkjet printing or soft lithography) in order to create the desired shape. Etching techniques provide closely spaced, high-resolution features, allowing high device densities in a given area. However, these techniques can physically and chemically damage the material, which may lower device performance as well as lifetime. Soft lithography provides the ability to closely space high-resolution features, while minimizing damage to the functional material during the deposition process.

This work employed a composite elastomeric stamp to deposit patterned lead zirconate titanate (PZT) thin films onto pre-patterned cantilever designs for use in a mass-sensor. Lateral feature sizes ranged from 1 to 30 μm. The features were characterized and compared to dry etched PZT thin films of similar thickness and lateral size. Quarter micron thick printed 30/70 PZT features exhibited a relative permittivity of 500 and a loss tangent of 0.9%. The hysteresis loops were well formed, without pinching of the loops. The patterned features showed remanent polarizations of 27 $\mu C/cm^2$, and coercive fields of 110 kV/cm. For this work, the piezoelectric was printed onto pre-patterned silicon cantilevers, to provide actuation and sensing capabilities to a bio-functionalized cantilever for cancer detection in blood samples. Whereby, a site specific "fingerprint" biomolecule in the testing media attaches to the cantilever, and the device acts as a mass sensor.

4.1 Introduction

Domain wall motion of ferroelectric materials contributes to the electromechanical coupling constants and the piezoelectric coefficients.[40, 94, 95] Ferroelectric films with large piezoelectric constants are attractive for use in microelectromechanical systems (MEMS) as the lower the voltages needed in actuation applications and increase the charge sensitivity of sensors.[5, 6] The energy density available in these materials also provides the ability to scale these devices down to the micron scale and beyond.[96] However, fine patterning often entails dry etching the ferroelectric material, which can physically and chemically alter the material.[35, 14, 39] These alterations degrade the functional properties of the active material and can limit the usefulness of the material in the device application.[40, 41] It has been shown that patterning of the ferroelectric material during the deposition process by microcontact printing avoids patterning damage and allows the material to retain the desired high performance even at micron lateral length scales.[87] To date, this patterning technique has not been used to integrate ferroelectric materials into an electromechanical device at these length scales.

A potential application that would benefit from integrating microcontact printed PZT is nanoelectromechanical systems for biomolecule sensing.[97, 98, 99] Such mass sensor devices use biological receptors which are precisely located, e.g. by microcontact printing, atop resonating cantilever structures. The device is immersed in a liquid test environment containing multiple compounds (i.e. blood). The receptors on the sensor surface use site-specific biomolecules to ensure only target molecules in the sample react with the surface of the sensor. When the target molecules attach to the surface of the resonator, the total effective mass and stiffness of the resonating structure increases. In the case where the mass effect dominates, increasing the mass results in a proportional lowering of the resonance frequency[§] of the sensing structure.[100, 101, 102, 103, 104] Measurement of the resonance frequencies can be achieved using multiple techniques, including Fabry-Perot interferometry.[90] In this sensing scheme, the chip is mounted to an external piezoelectric actuator to vibrate the cantilever structures. For this measurement, the chip is typically placed inside a vacuum chamber to reduce viscous damping effects. This technique has been used to measure the frequency shifts of bio-functionalized resonating cantilevers with a lateral width of 1.7 μm before and after the cantilevers were subjected to targeted antibodies.[91]

This chapter aims to integrate piezoelectric materials, specifically lead zirconate titanate (PZT), into a biomolecule mass sensing NEMS device. A 1.5 x 1.5 cm chip can hold more than 10^5 cantilevers which are 7 μm long and 1.7 μm wide. The co-integration of site-specific biomolecules onto cantilevers with piezoelectric materials allows for internal circuitry to provide actuation and sensing capabilities without the need for vacuum chambers and laser interferometry. This allows an ensemble of cantilevers to be tested in quick succession, rather than measuring each cantilever serially with an interferometer.

The approach used for integration of the PZT was microcontact printing of the ferroelectric precursor solutions directly onto pre-patterned silicon cantilevers; crystallization of the patterned solutions was conducted immediately after printing. This process was repeated until the PZT reaches the desired thickness. The devices were then released from the underlying substrate through backside etching, and subsequently functionalized with biomolecules through microcontact printing. Cantilevers ranged in lateral width from 30 to 1 μm. The resonators were designed by Denis Dezest of CNRS (National Center for Scientific Research), University of

---

[§] The equations which describe the variation of the resonant frequency with changes of the effective mass of the cantilevers is described in Appendix B

Toulouse, in in France, and the process flow developed was a result of collaboration between the two groups.

4.2 Experimental Procedure

4.2.1 *Silicon on Insulator Substrate Fabrication*

Figure 4-1 depicts the process flow for creation of the bio-mass sensor. 100 mm diameter silicon on insulator (SOI) wafers were used as a substrate for resonating cantilever devices, as seen in Figure 4-1 (1). The carrier Si wafer was 525 μm thick, the buried SiO_2 was 1 μm thick, and the top Si layer was 335 nm thick. First, the bottom electrode of the device layer was prepared on the device Si layer. For this purpose, the top Si layer was oxidized at 1000 ˚C for 155 min with O_2 flowing at 10 L/min using a vertical diffusion furnace (c.DIFF, Centrotherm). This created a 100 nm thick SiO_2 on top of 290 nm of Si, as displayed in Figure 4-1 (2). A chemical diffusion barrier layer was created by atomic layer deposition (ALD) of HfO_2 (ALD 150 LE, Kurt J. Lesker) on the thermal SiO_2. The deposition occurred at 200 ˚C with a chamber pressure of 0.72 Torr. The reactant pulse time for H_2O and tetrakis(ethylmethylamino)hafnium (TEMAH) was 0.03 and 0.15 s respectively, with a purge time of 10 s between each pulse. These cycles were repeated 619 times to create an amorphous 60 nm thick HfO_2 layer which was crystallized with a 700 ˚C heat treatment in an O_2 ambient for 1 min, as shown in Figure 4-1 (3). A bottom electrode was sputter deposited (CMS-18 Sputter System, Kurt J. Lesker) over the HfO_2 layer. A 30 nm titanium adhesion layer was sputtered at room temperature using a power of 200 W, a bias of 460 V, a current of 0.47 A, a deposition pressure of 2 mTorr, and an Ar flow rate of 8 sccm, for 300 s. Without breaking vacuum, a 125 nm Pt bottom electrode was sputtered at room temperature using a power of 200 W, a bias of 580 V, a current of 0.34 A, a deposition pressure of 2.5 mTorr, and an Ar flow rate of 11 sccm, for 417 s, as seen in Figure 4-1 (4).

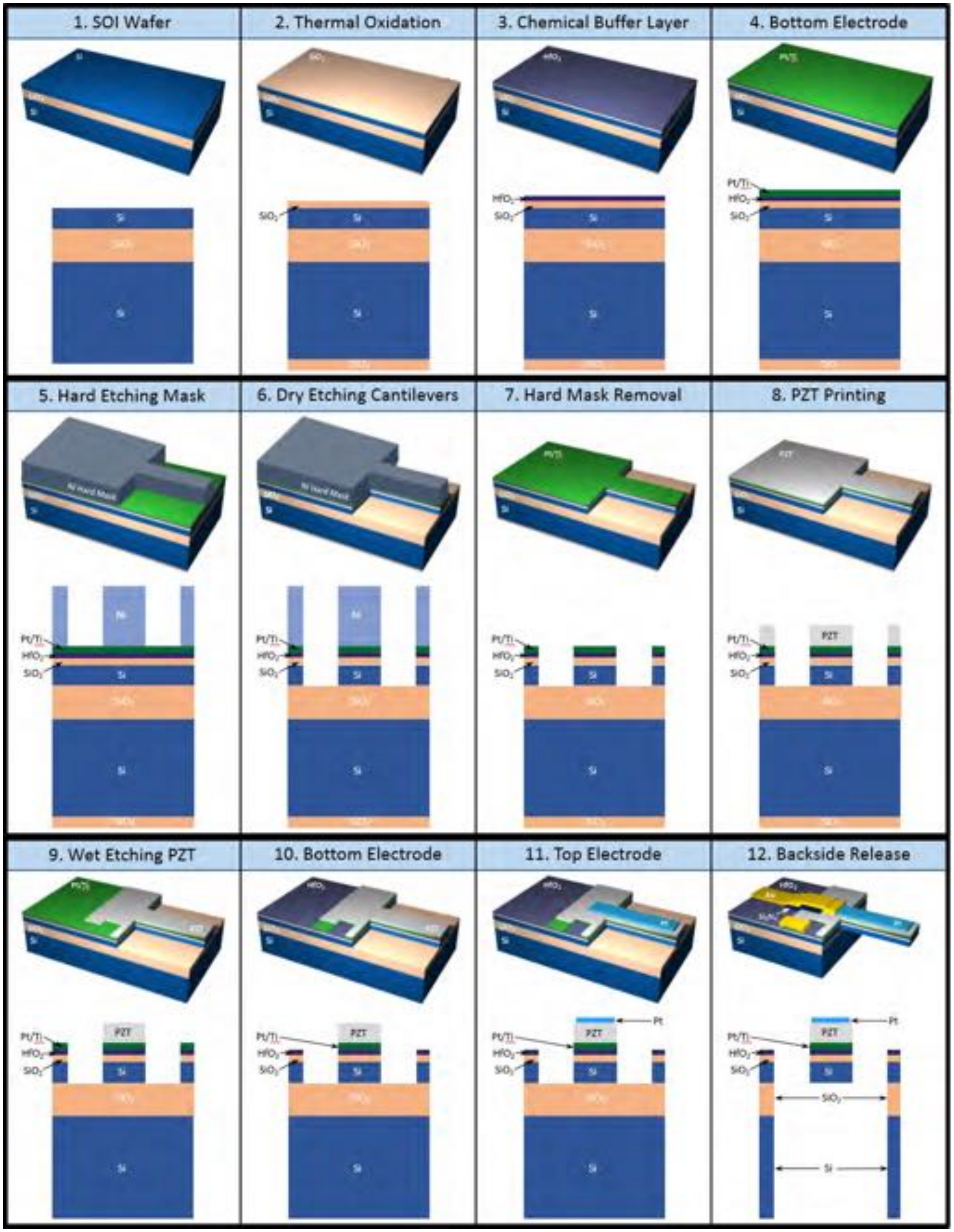

Figure 4-1. Schematic process flow to create a bio-mass sensor. The top image in each cell shows a 3D representation of the wafer. The bottom image in each cell represents a vertical cross-section of the device.

4.2.2 *Patterning SOI Wafers*

Cantilever patterns were etched into the surface of the SOI wafers. In order to achieve this, the inverse design of the cantilever patterns was deposited onto the Pt bottom electrode by patterning of a photolithographic resist. SPR 3012 (Shipley Megaposit, Dow) was spun onto the wafers at 4000 rpm for 45 s and soft baked at 95 ˚C for 60 s. The exposure was carried out using a wafer stepper (Model 8500 DSW, GCA) with 365 nm light and a power density of 125 mW/cm^2 for 0.25 s. The resist was developed in CD-26 (Microposit MF, Dow) for 1 min. The surface was cleaned with an oxygen plasma ash (M4L Plasma System, Metroline) for 180 s, utilizing a power of 300 W, a chamber pressure of 400 mTorr, and a 100 and 50 sccm gas mixture of O_2 and He, respectively.

Ni was then electroplated into the photoresist mold, as shown in Figure 4-1 (5). This was done using a $Ni(SO_3NH_2)_2$ solution (Ni Sulfamate RTU, Technic Inc.). Figure 4-2 (a) illustrates the use of the Pt coated wafer as the cathode and the Ni as an anode in conjunction with a pulse power supply (DuP 10-1-3, Dynatronix). The bath was held at room temperature, with a pH of 4.2, and mixed at 500 rpm. The pH levels in Ni solution baths were monitored using a pH meter (Orion Star A121, Thermo Scientific). Residual stresses and thickness non-uniformity were minimized in the Ni deposit by utilizing an optimized pulsed power train of current;[105,106] an example is shown in Figure 4-2 (b), with a forward current of 0.612 A, a reverse current of 0.061 A, a forward on time of 1 ms, a forward off time of 3 ms, a forward duration of 5 ms, a reverse on time of 0.3 ms, reverse off time of 0.5 ms, and a reverse duration of 0.8 ms. The photoresist was removed after the deposition of the electroplated Ni by immersion into a ultrasonic bath of PRS 3000 (J.T. Baker) at 60 ˚C for 1 hr. This was followed by an oxygen plasma ash for 600 s, at the same conditions previously described. The Ni served as a hard mask for the Pt etch.

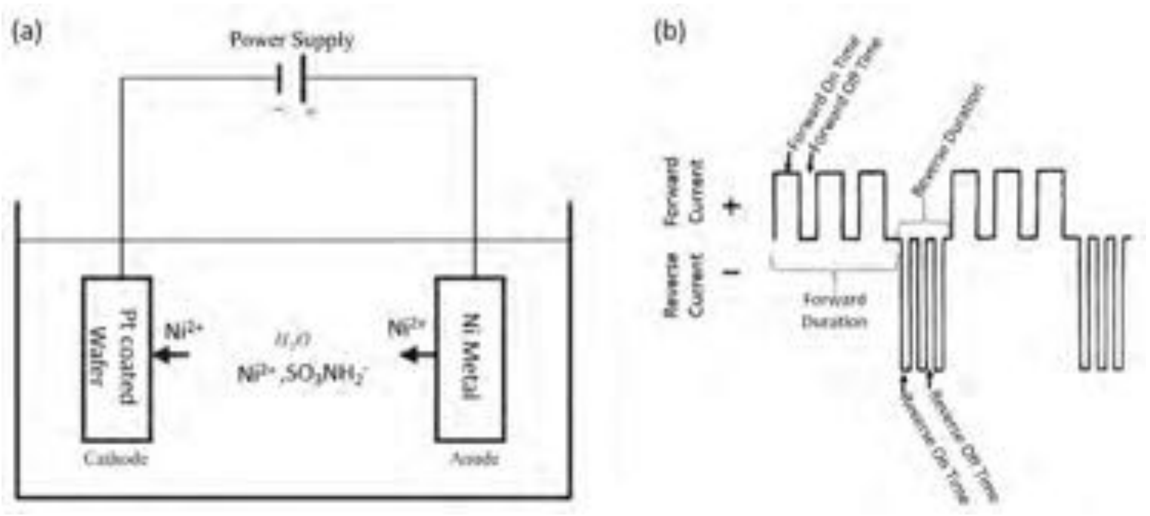

Figure 4-2. Schematic displaying the (a) electroplating of Ni onto a Pt coated Si wafer for use as a dry etch mask and a (b) pulse train from a current power supply.

Figure 4-1 (6) displays the dry etching of the exposed Pt/Ti/HfO_2/SiO_2/Si layers with an inductively coupled plasma (ICP) reactive ion etch (NE-550, ULVAC) using a single etch chemistry as described in Table 4-1. In an effort to avoid over-etching, each etch was cycled for 30 s to allow for inspection. Following the etch, the Ni hard mask was removed, as illustrated in Figure 4-1 (7), by immersion of the wafer into an ultrasonic bath of Ni Etchant TFB (Transene Company, Inc.) at 40 ˚C for 10 min, followed by an immersion into an ultrasonic bath of ACT 935 UP (Air Products and Chemicals, Inc.) at 40 ˚C for 1 hr.

Table 4-1. Summary of the etching conditions used on Pt/Ti/HfO_2/SiO_2/Si stack.

Tool	Cl_2 Gas (sccm)	O_2 Gas (sccm)	Ar Gas (sccm)	Antenna Power (W)	Chuck Power (W)	Chuck Bias (V)	Base Pressure (mTorr)
ULVAC (ICP-RIE)	30	4	10	900	225	210	3.5

Bilayer polymer stamps were made as described elsewhere.[87] A polyurethane (PU) layer was ultraviolet (UV) cured on top of a flat Si wafer with no patterned features. The hydrophilic nature of the polyurethane surface allowed the PZT solution to wet the flat stamp. A compliant polydimethylsiloxane (PDMS) backing layer allowed the stamp to come into contact with the substrates around surface imperfections at low pressures. The stamp surface was cleaned prior to printing by oxygen plasma ashing at a power of 300 W, a pressure of 400 mTorr, oxygen flow rate of 100 sccm, helium flow rate of 50 sccm, and a duration of 5 min. Butanol based precursor solutions, 10 wt. % $Pb_{1.1}(Zr_{0.3}Ti_{0.7})O_3$ (Mitsubishi Materials), were spun onto polymer stamps at 4000 rpm for 30 s. The alignment and printing of the PZT solutions onto patterned Pt coated SOI wafers was performed by hand. The liquid precursors were dried at 350 °C for 5 min and crystallized at 650 °C for 1 min. Subsequently, the fired film was printed with a new PZT layer and heat-treated in the same manner. This process was repeated until the desired thickness was achieved, as observed in Figure 4-1 (8).

Figure 4-1 (9) exhibits the removal of PZT from between cantilever features by wet etching. To protect the PZT on the cantilevers, SPR 1813 (Shipley Megaposit, Dow) photoresist was spun on top of the printed PZT features at 4000 rpm for 45 s to act as the wet etching mask. The resist was soft baked at 100 ˚C for 60 s, and patterned using a wafer stepper with 365 nm light, a power density of 125 mW/cm^2, and an exposure time of 0.12 s. The resist was developed in CD-26 for 60 s, followed by a hard bake at 145 ˚C for 30 min. The wafers were immersed into a buffered oxide etchant (BOE) of 6:1 ratio of ammonium fluoride to hydrofluoric acid for 120 s and were then rinsed in de-ionized (DI) water. To remove insoluble residues, the wafers were immersed into hydrochloric acid for 3 s and finally washed in DI water. The etching cycle was repeated until the PZT was removed and the underlying Pt surface was exposed. The wet etch mask was removed from the wafers by ultrasonication in PRS 3000 at 60 ˚C for 60 min. The wafers were then cleaned using a 300 W oxygen plasma ash for 5 min.

Figure 4-1 (10) depicts the dry etching of the Pt in order to pattern the bottom electrodes. SPR 955 (Shipley Megaposit, Dow) photoresist was spun on top of the SOI wafers at 1200 rpm for 35 s to act as the dry etching mask. The resist was soft baked at 105 ˚C for 120 s. A second SPR 955 layer was deposited onto the wafer with the same deposition parameters. The resist was exposed in a wafer stepper using 365 nm light, a power density of 125 mW/cm^2, and an exposure time of 1.0 s. The resist was developed in CD-26 for 5 min. The Pt layer was dry etched (NE-550, ULVAC) using the etching parameters described in Table 4-1. In an effort to avoid over-etching, each etch was cycled for 15 s to allow for inspection. The mask was removed after dry etching by immersion of the SOI wafers upside down in a heated, ultrasonic bath of PRS 3000 at 60 ˚C for 60 min. This allowed for any etching fences or debris to fall off the wafer upon removal, thus avoiding redeposition of etching byproduct onto the wafer surface upon removal from the bath.

Pt top electrodes were deposited on the PZT features using a lift-off process, as shown in Figure 4-1 (11), to enable electrical actuation/sensing capabilities to the device. An electron beam resist (ZEP520A, ZEONREX Electronic Chemicals) was spun on top of the printed PZT features at 4000 rpm for 45 s. The resist was baked at 180 ˚C for 180 s. The resist was patterned via electron beam lithography (EBPG 5200, Vistec) using a beam current of 40 nA, a dose of 365 μC/cm^2, an aperture size of 400 μm, and a beam step size of 25 nm. The resist was developed in N-amyl acetate for 180 s, immersed into an isopropyl alcohol (IPA) bath for 60 s, and rinsed in DI water. Pt was sputter deposited at room temperature using a power of 200 W, a bias of 580 V, a current of 0.34 A, a deposition pressure of 2.5 mTorr, and an Ar flow rate of 11 sccm for 126 s. The photoresist was removed by immersion of the SOI wafers upside down in a heated, ultrasonic bath of Remover-PG (MicroChem) at 60 ˚C for 60 min.

The HfO_2/SiO_2 surface was dry etched in order to pattern an electrical ground plane for the device to minimize electrical cross-talk.[107] Two SPR 955 photoresist layers were spun on top of the SOI wafers, as described previously, to act as the dry etching mask. The resist was exposed in the wafer stepper for 1.0 s. The resist was developed in CD-26 for 5 min. The HfO_2 layer was dry etched (NE-550, ULVAC) using the etching parameters described in Table 4-1. The SiO_2 layer was dry etched (NE-550, ULVAC) using the etching parameters described in Table 4-2. In an effort to avoid over-etching, each etch was cycled for 15 s to allow for inspection. The mask was removed after dry etching by immersion of the SOI wafers upside down in an ultrasonic bath of PRS 3000 at 60 ˚C for 60 min.

Table 4-2. Summary of the etching conditions used on final SiO_2 etch.

Tool	CF_4 Gas (sccm)	Antenna Power (W)	Chuck Power (W)	Chuck Bias (V)	Base Pressure (mTorr)
ULVAC (ICP-RIE)	40	500	200	400	10

4.2.3 *Material Characterization*

The surface morphology of the deposited films as well as the physical dimensions of the printed and etched cantilevers were characterized with a field-emission scanning electron microscope (FESEM; LEO 1530, Gemini). Residual stress levels in electroplated Ni were measured with a thin film stress analyzer (Flexus 2320, Tencor Instruments). Film thicknesses and etch depths were determined using a surface contact profilometer (Alpha-Step 500, Tencor Instruments) in conjunction with an automated variable angle spectroscopic ellipsometer (M-2000, J. A. Woollam) using incident angles of 55, 65, and 75°. Etch byproducts were analyzed with energy-dispersive X-ray spectroscopy (EDS) using an accelerating voltage of 14 keV in a FESEM (Nova Nano SEM 630, FEI Company). An LCR bridge (4294A Precision LCR, Hewlett Packard) was utilized, from 0.1 to 100 kHz at a drive amplitude of 0.03 V, to measure relative permittivity and loss tangent of the ferroelectric films. A Multiferroics Test System (Radiant Technologies) was used to measure the P-E loops of the ferroelectric films at 100 Hz.

4.3 Results and Discussion

The optimization of each processing step was necessary in order to produce the highest quality final device. Therefore, the following section begins by describing the short loop experiments designed to overcome specific processing hurdles associated with each processing step of the final device. This is followed by the results of the deposition of the final device wafers.

4.3.1 Device Material Stack

The foundation of the mass-sensor stack was comprised of a 300 nm Si layer. 100 nm of SiO_2 was thermally oxidized on top of the Si to provide electrical insulation from subsequent layers. 60 nm of HfO_2 was deposited by ALD to provide a chemical diffusion barrier between the PZT and the underlying stack during crystallization of the ferroelectric. Finally, as observed in Figure 4-3 (a), Ti/Pt (30 nm/100 nm) bottom electrode was sputtered at room temperature on top of the HfO_2. This provided a surface for nucleation of the ferroelectric, as well as a bottom electrode for the device. In order to insure that the device stack could produce high quality PZT, test crystallizations were first conducted using blanket PZT layers prepared by spin coating on top of the SOI wafers, as displayed in Figure 4-3 (b). The microstructure of the PZT shows no secondary phase formation, porosity, or delamination from the underlying stack.

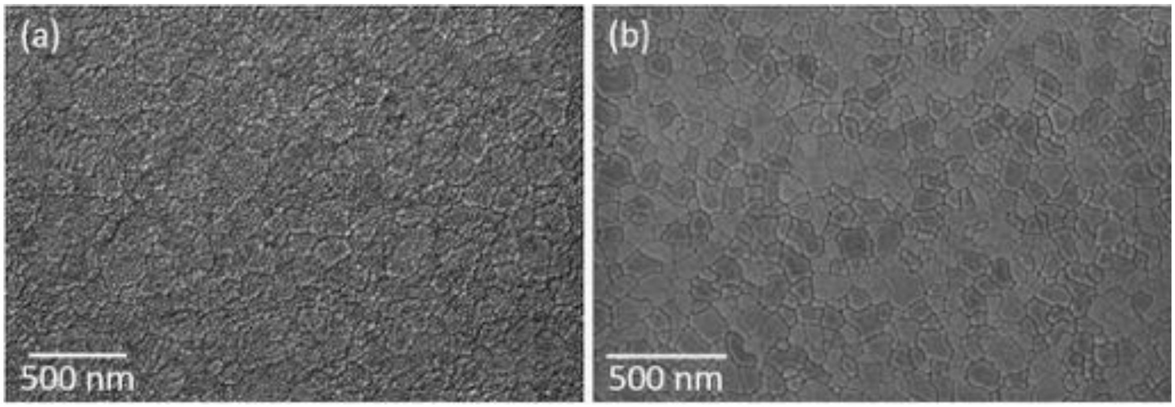

Figure 4-3. SEM image of the microstructure of (a) Pt sputtered at room temperature onto a HfO_2 coated SOI wafer, and (b) the subsequent crystallization of blanket PZT.

4.3.2 Ni Hard Mask Deposition

A variety of cantilever sizes, with a lateral width ranging from 30 to 1 μm, were used to test the limit of printing multiple layers of PZT without losing functionality from processing defects or limitations associated with the printing process itself. Prior to printing, cantilevers were defined by etching the design through the $Pt/Ti/HfO_2/SiO_2/Si$ layers and stopping on the buried SiO_2 layer. A nickel hard mask was utilized as the dry etch mask, allowing etching to depths ≥ 600 nm into the substrate with vertical sidewalls.

Two different approaches were explored for preparation of the Ni hard mask. In the first, a bi-layer photoresist lift-off process was used to define sputtered Ni cantilever designs on top of the SOI wafers. Figure 4-4 (a) displays Ni that was sputtered[**] on the Pt surface with a maximum thickness of ~415 nm. Utilization of a lift-off process resulted in sputtered Ni features with ~60° sidewall angles. Microcracking was evident in the surface of the sputtered Ni, as highlighted by Figure 4-4 (b). The mask was sufficiently thick to prevent transfer of defects from the microcracks into the protected Pt surfaces after dry etching. However, the low sidewall angles of the hard mask resulted in lateral shrinkage of the etched pattern into the substrate, ~0.5 µm by each edge, resulting in the loss of features approaching 1 µm in width. A second consequence of using a hard mask with low sidewall angles was the increased probability, along the etching perimeter, that thinned Ni would be removed prematurely by the physical bombardment component of the dry etch. This resulted in the formation of notches along the perimeter of any pattern, exhibited in Figure 4-4 (c). These notches not only altered the shape of the designed pattern, but hindered the transfer of the PZT printing solution onto the patterned feature.

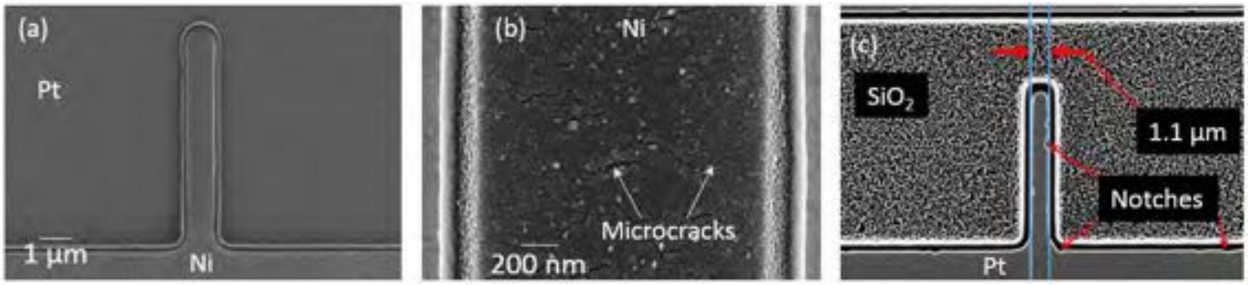

Figure 4-4. SEM images of (a) Ni hard masks sputtered onto Pt by a lift-off technique. (b) Cracking of the Ni became evident as the thickness of the Ni was increased. (c) Low sidewall angles of mask resulted in notching around the perimeter of the etched features, as well as a decrease in the size of the features (ex. from 2 to 1.1 µm wide).

[**] Sputter Conditions: 204 W, 580 V, 0.338 A, 10 mTorr, 1 sccm Ar gas, 18 °C, 1.8 x10^{-8} Torr (base pressure), 4,000 sec

As an alternative, the Pt surface covering the SOI wafers provided a conductive surface, which allowed for electroplating of Ni to create a hard mask with vertical sidewalls. However, when electroplating metals onto a surface, residual stresses were a primary concern. High residual compressive stresses resulted in blister formation on the electroplated surface, while high tensile stresses caused delamination of the stack. Current density, solution pH, and plating temperature were identified as means to control the degree of residual stress[108, 109, 110] in electroplated Ni,[111] as summarized in Figure 4-5.

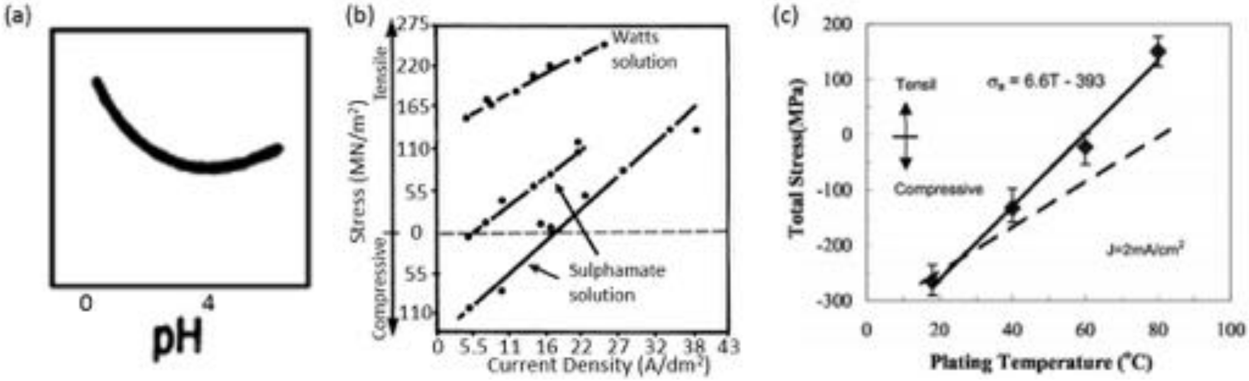

Figure 4-5. Graphs displaying the internal stress of electroplated metals as a function of (a) pH,[112] (b) current density,[113] and (c) plating temperature.[114]

Deposits from Ni sulfamate solutions have been reported to have lower residual stress levels than deposits from Ni sulfate solutions.[115] However, Ni electroplated from sulfamate solutions, in this work, displayed large residual tensile strains. After extensive experimentation, it was determined that aged, stratified, solutions of nickel sulfamate displayed a pH level of 2.7. This resulted in rough, fine grained Ni deposits,[116] as shown in Figure 4-6 (a), non-uniform deposition thicknesses, and catastrophic delamination of the titanium adhesion layer from the underlying HfO_2, as seen in Figure 4-6 (b). Ni sulfamate solutions with pH levels of 4.3 yielded Ni deposits, as exhibited in Figure 4-6 (c), with a smooth surface with larger grains than seen in Figure 4-6 (a).

Excellent thickness uniformity, displayed in Figure 4-6 (d), along with a reduction in the residual stress level resulted in Ni deposits up to 1 μm in thickness without delamination.

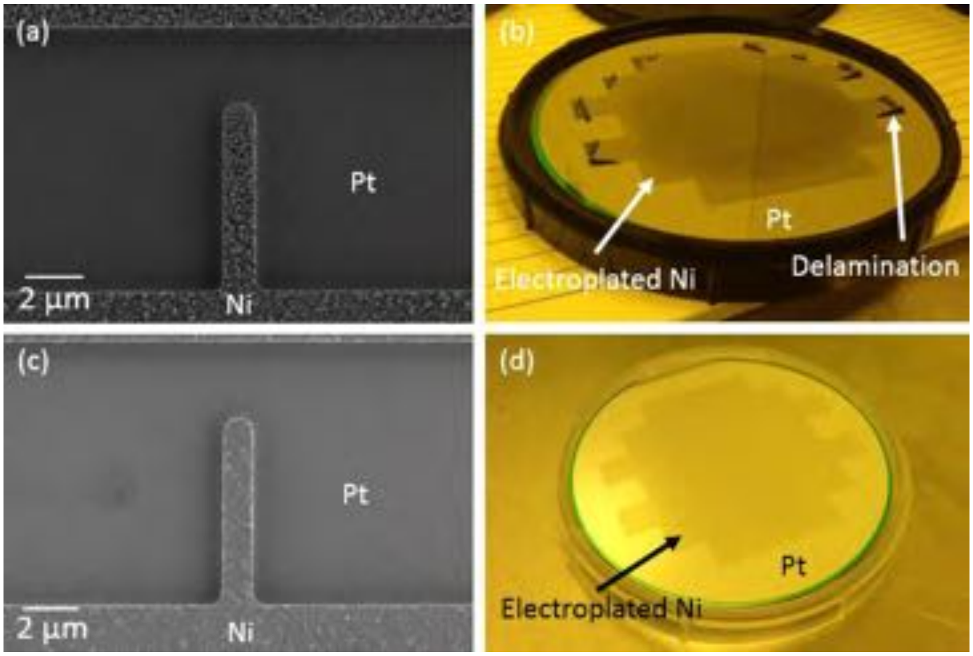

Figure 4-6. (a) SEM microstructure of an electroplated Ni deposit from a solution with a pH of 2.7, and the corresponding (b) optical image of 100 mm wafer where the electroplated Ni resulted in delamination of the Pt from the underlying stack. (c) SEM microstructure of an electroplated Ni deposit from a solution with a pH of 4.3, and the corresponding (d) optical image of the 100 mm wafer with no delamination.

The residual stress of electroplated Ni on top of a Pt/Ti/SiO_2/Si wafer stack was quantified using the Stoney Equation.[117,118] Altering the pH of the Ni sulfamate bath from 2.7 to 4.3 changed the stress from 500 to -60 MPa. Reducing the current density from 5 to 2 mA/cm^2 led to a slightly increased compressive strain from -60 to -90 MPa. Increasing the plating bath temperature from 25 to 55 ˚C increased the tensile strain in the deposited Ni from -60 to 40 MPa. It was also found that increasing the plating bath temperature can lead to evaporation of the water in the solution, and over time this can alter the pH of the solution. Residual stress in the film remained at -60 MPa up to 1 µm in thickness, which was more Ni than needed for the etching process. Therefore, the optimal plating conditions for a 600 nm thick Ni mask were therefore chosen to be deposition from a Ni sulfamate solution with a pH of ~ 4, at a current density of 5 mA/cm^2, and a bath temperature of 25 ˚C. A summary of the Ni plating conditions is shown in Table 4-3.

Table 4-3. Summary of residual stresses found in electroplated Ni deposited onto Pt coated Si wafers.

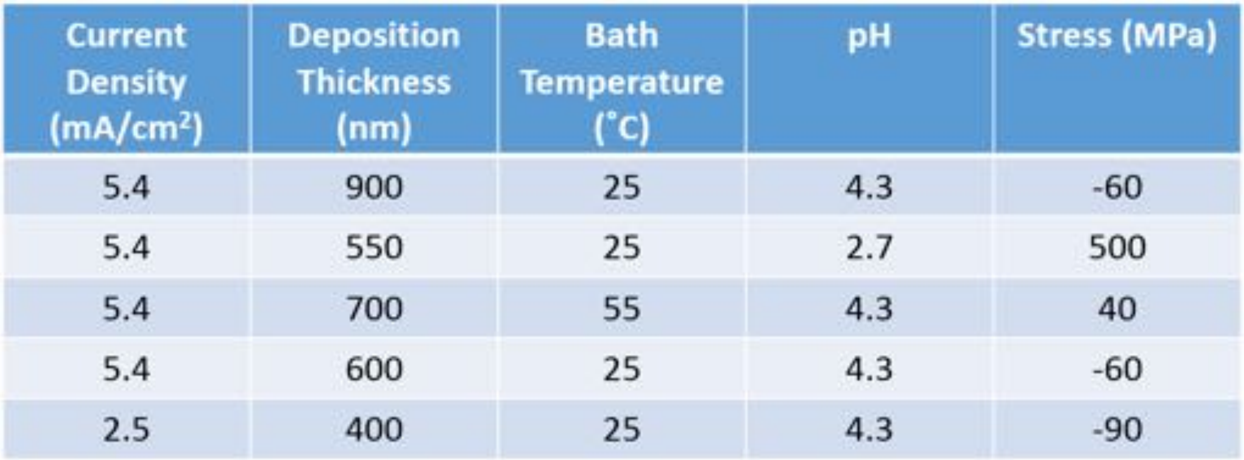

Current Density (mA/cm^2)	Deposition Thickness (nm)	Bath Temperature (˚C)	pH	Stress (MPa)
5.4	900	25	4.3	-60
5.4	550	25	2.7	500
5.4	700	55	4.3	40
5.4	600	25	4.3	-60
2.5	400	25	4.3	-90

4.3.3 Nucleation of PZT on Dry Etched Pt Surfaces

After dry etching the cantilever patterns into the substrate surface, the Ni was removed to leave the Pt surface exposed for PZT crystallization. The goal was to remove the hard mask while not affecting the integrity of the substrate stack or the Pt surface, which acts as a nucleation site for perovskite grain formation in the PZT.

However, upon wet removal of the electroplated Ni hard mask, defects were observed in dry etched Pt surfaces, as shown in Figure 4-7 (a). White light optical microscopy could be used to identify large defects on etched Pt surfaces; however, polarized light in an optical microscope greatly aided in identifying the presence of less noticeable defects. The defects were investigated in the SEM and appeared to be thin sheets of material that could cover large areas of the Pt surface. Figure 4-7 (b) shows an example where the sheet folded on itself, making it easier to identify (Note: If the Pt feature was a discreetly etched "island" it was difficult to identify these defects in the SEM due to charging).

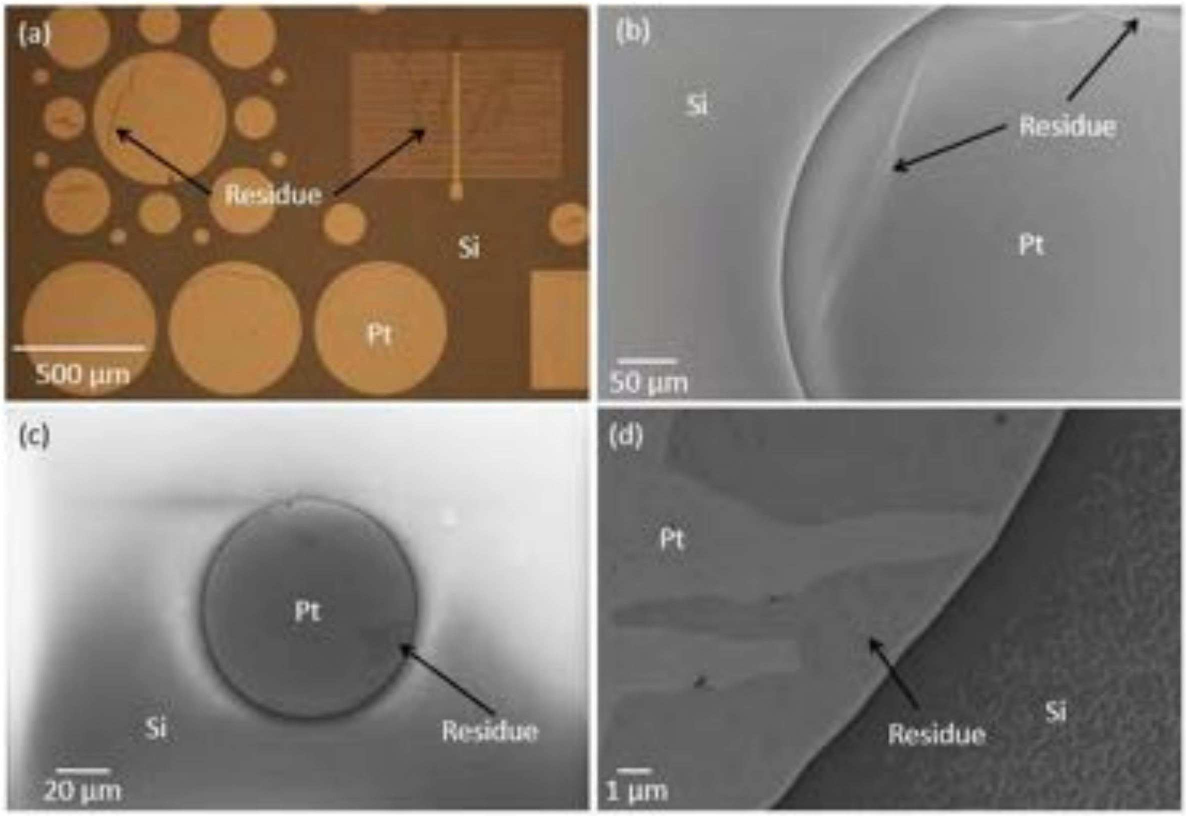

Figure 4-7. Patterns dry etched into a Pt coated Si wafer. Residues from (a and b) electroplated Ni and (b and c) sputtered Ni hard mask remain on the surface of the dry etched Pt after Ni removal.

Similar defects were observed when sputtered[††] Ni was utilized, as seen in Figure 4-7 (c) and (d). This indicates that the defects resulted from either the dry etching process or the Ni wet

---

[††] Note: Evaporated Ni was also used in this work, but will be discussed later.

etchant exposure. EDS was utilized in an attempt to identify the composition of these residues. However, no secondary elements, such as Cl or F from the dry etch gases, could be identified. This may have arisen from the interaction volume of the measurement being too large to detect the thin residue sheets.

PZT was crystallized over a Pt feature with identifiable defect areas, to determine the extent that these residues play on the crystallization behavior of PZT on patterned Pt surfaces. Figure 4-8 (a) shows a dry etched Pt feature where the etching residue has dislodged from the edge of the feature and folded in toward the center of the feature. Figure 4-8 (b) exhibits a 1 μm thick PZT film crystallized after every layer over the same Pt feature. A reduced number and area of perovskite grains in an amorphous matrix was present on area where the residues were present. Figure 4-8 (c) displays a high magnification image of the PZT crystallization within the area where the residues covered the Pt surface.

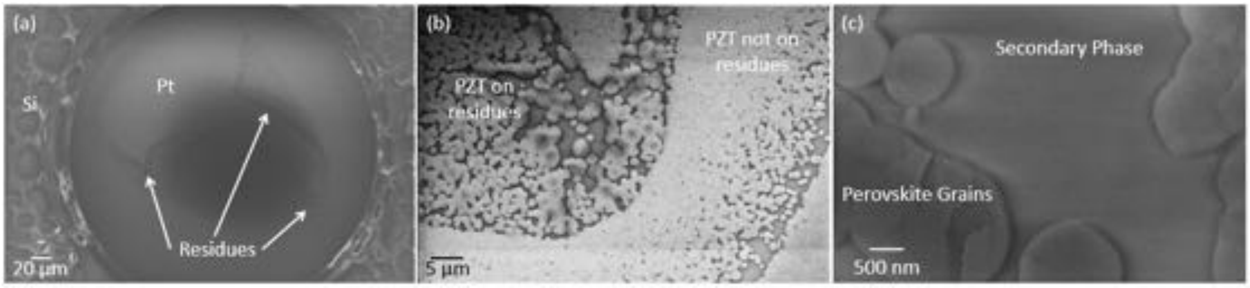

Figure 4-8. SEM images of (a) residues on a dry etched Pt feature, (b) PZT crystallized on top of dry etched Pt features with localized areas of etching residues, and (c) high magnification focused on an area where PZT was crystallized over etching residues.

In order to fully crystallize the perovskite phase, it was necessary to improve the nucleation from the bottom Pt. In an attempt to increase the driving force for nucleation of PZT on these surfaces, the crystallization temperatures and soak times were varied. PZT was spun on top of the patterned substrate at 2000 rpm, pyrolyzed at 200 and 400 ˚C for 5 min each. Optimal crystallization conditions were investigated by varying the firing times from 30 to 600 s at a particular temperature, and varying firing temperatures from 600 to 800 ˚C. Figure 4-9 (a) displays the surface microstructure of a 150 nm thick PZT layer crystallized at 700 ˚C for 30 s. Perovskite grains have been nucleated in an amorphous matrix. Figure 4-9 (b) exhibits the microstructure of the film after firing time was increased to 600 s. There was no significant increase in the number of nucleation centers of perovskite grains, nor was there significant growth in the size of the perovskite grains. Figure 4-9 (c), (d), (e), and (f) shows 150 nm thick PZT crystallized for 300 s at 650, 700, 750, and 800 ˚C, respectively. The number and size of perovskite grains did not vary with varying crystallization temperatures. These results indicated that increasing firing temperatures and times could not increase the driving force for perovskite nucleation sufficiently to fully convert the film.

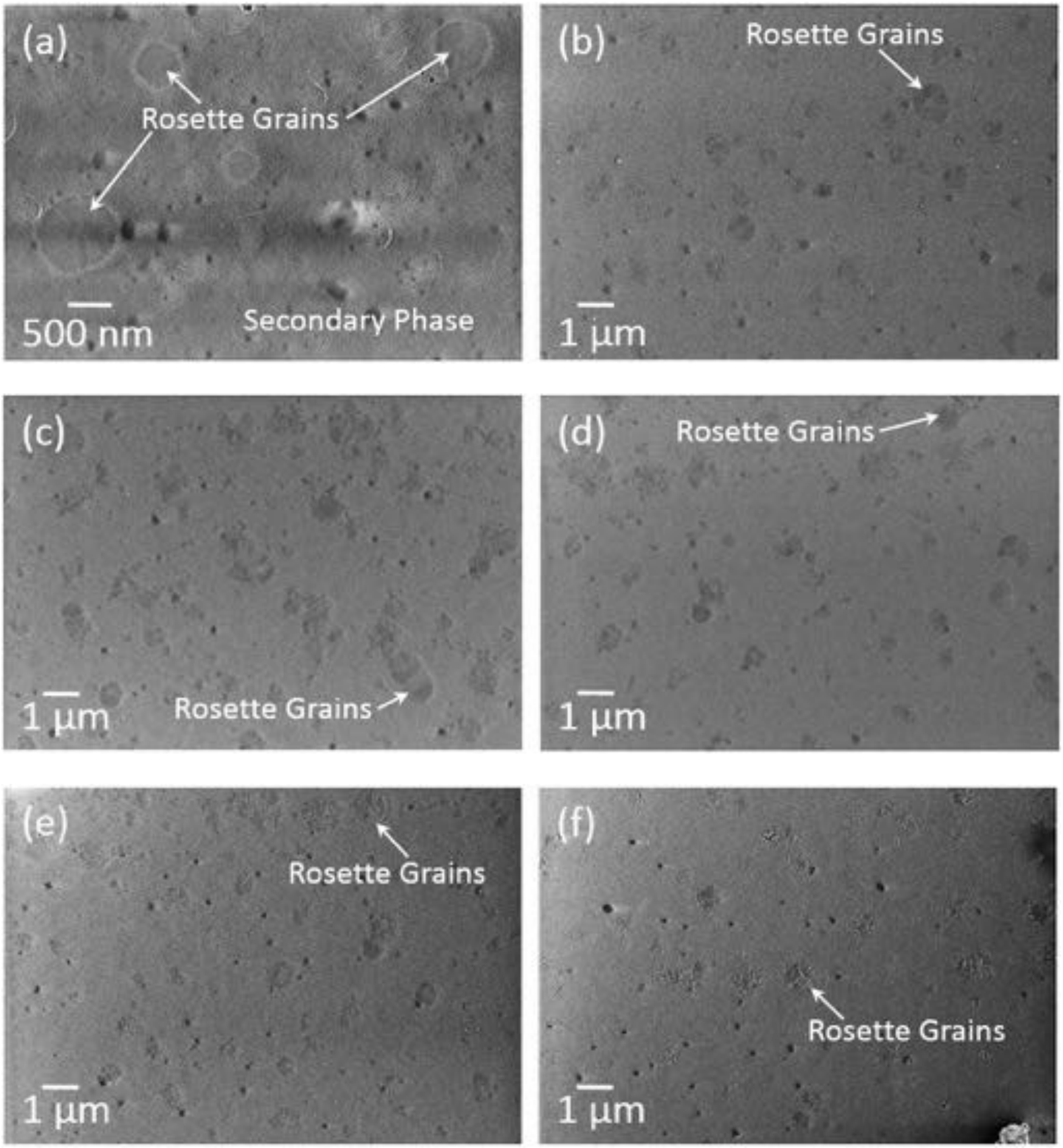

Figure 4-9. SEM images of PZT crystallized on top of dry etched Pt features. PZT layers crystallized at 700 ˚C for (a) 30 and (b) 600 s. PZT crystallized at (c) 650, (d) 700, (e) 750, (f) and 800 ˚C for 300 s each.

It was hypothesized that if the residues could be removed from the surface of the Pt after dry etching, full crystallization would be achievable. Various Ni wet etchants and etch byproduct strippers were used in an attempt to remove these defects. Figure 4-10 shows the results for use of nickel etchant TFB, a nitric acid based etchant, nickel etchant Type 1, a hydrochloric acid based etchant, nickel etchant TFG, a sulfuric acid based etchant, and Nanostrip, a sulfuric acid based etchant. In each case, the nickel hard mask was exposed to the etchant after dry etching was performed on a Pt surface. Samples were placed into each bath at ≥ 40 ˚C, to increase etching rates, in conjunction with ultrasonication for over 1hr. None of the etchants fully removed the residues found on the Pt surface post dry etching.

A dry etched Pt feature, which had sheet residues remaining on its surface after being subjected to Ni etchant TFB, as shown in Figure 4-11 (a), was immersed in ACT 935, a hydroxylamine based solvent stripper. Figure 4-11 (b) highlights the removal of a majority of etching residues by ACT 935, which were left behind by the wet Ni etchant TFB.

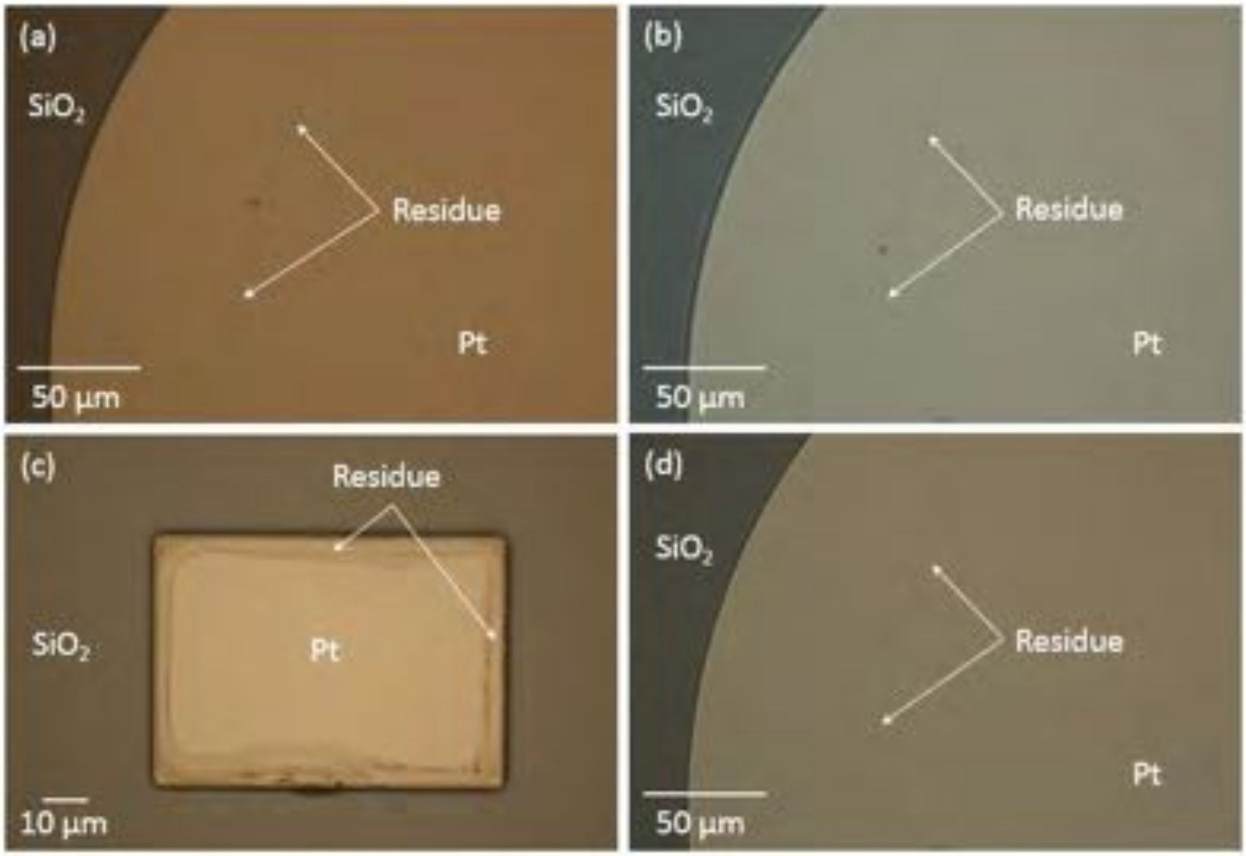

Figure 4-10. Optical images of Ni residues on Pt features. Removal of residues was attempted by subjecting residues to (a) Nickel etchant TFB, (b) Nickel etchant Type 1, (c) Nickel Etchant TFG, and (d) Nanostrip baths.

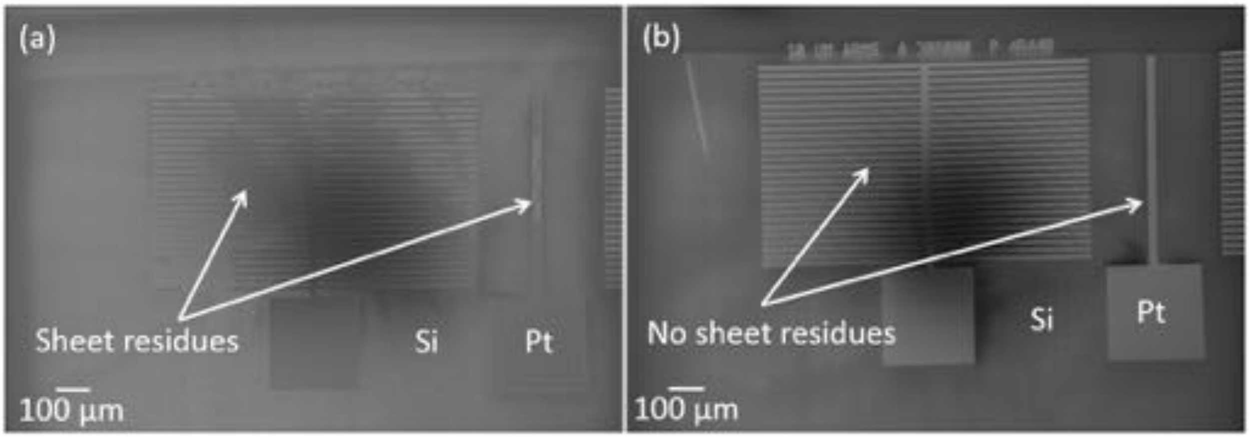

Figure 4-11. SEM images of (a) dry etching Ni residues on Pt features, and (b) removal of residues using ACT 935.

Figure 4-12 (a) shows 150 nm of PZT crystallized over a dry etched Pt surface, which was protected with an electroplated Ni hard mask, exposed to Ni etchant TFB, and cleaned with ACT 935. The surface appears to slightly inhibit perovskite nucleation as large rosette grains are surrounded by a secondary matrix, as seen in the initial layers of the film. Figure 4-12 (b) shows that after the PZT reached a thickness of 1 μm the grains have impinged and the film has largely crystallized into the perovskite phase. Figure 4-12 (c) demonstrates that the residual stress in the film has resulted in microcracking along grain boundaries. This was due to the presence of porosity at the grain boundaries as seen in Figure 5-2 (d) which also nucleated rosette grains.

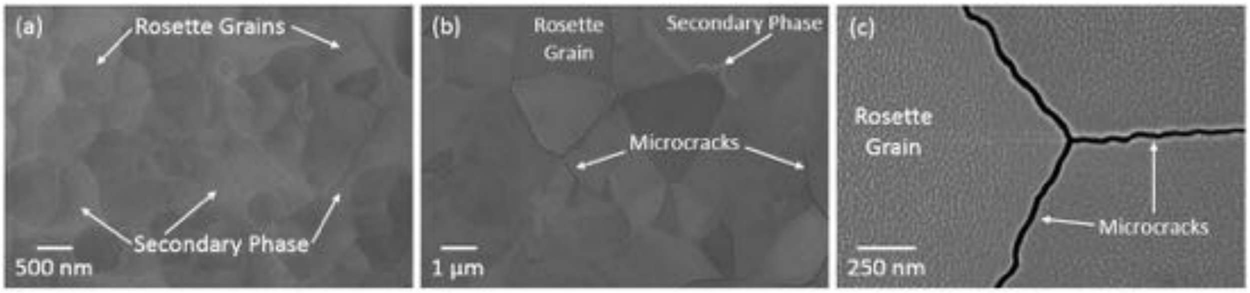

Figure 4-12. SEM images of PZT, crystallized after every spin-coated layer, on top of dry etched Pt features cleaned with ACT 935 (electroplated Ni mask). (a) Two PZT layers crystallized, with a thickness of 150 nm, with rosette grain formation in a secondary phase matrix. (b) Nine PZT layers crystallized, with a thickness of 1 μm. The grains have impinged and removed a majority of secondary phase. (c) High magnification reveals microcracks formed between PZT grains.

In addition to electroplating and sputtering, electroplating of Ni was used as a source for depositing a Ni hard mask. PZT was deposited over a dry etched Pt surface which was protected with an evaporated Ni hard mask to confirm that the surface defects were not limited to the electroplating process. The mask was removed with Ni etchant TFB and cleaned with ACT 935.

Figure 4-13 (a) shows the crystallization behavior of a film 400 nm thick. Figure 4-13 (b) and (c), are high magnification of the PZT microstructure of the PZT. Again, rosette grain formation occurred with secondary phase present between the grains. Thus, it was concluded that the contamination that retarded nucleation in Figure 4-12 was present in Figure 4-13 and thus the defects on the patterned Pt surface were independent of the Ni film source.

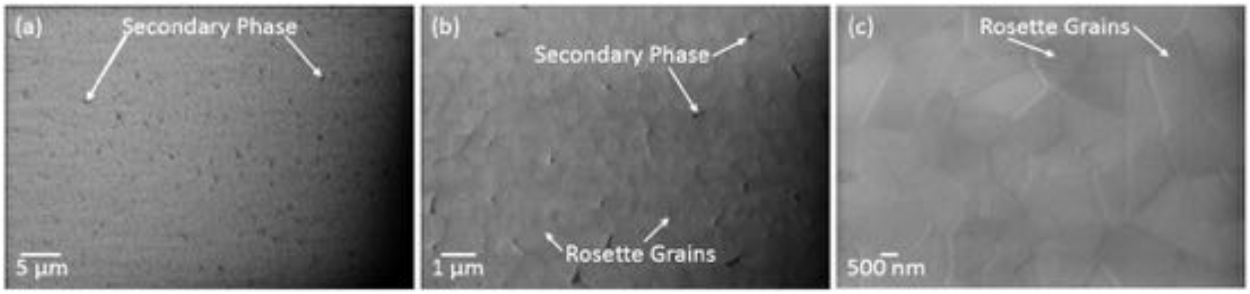

Figure 4-13. SEM images of PZT, crystallized after every spin-coated layer, on top of dry etch Pt features cleaned with ACT 935 (evaporated Ni mask). (a) Five PZT layers crystallized, with a thickness of 400 nm, with rosette grain formation alongside a secondary phase (dark spots). (b and c) High magnification images of PZT microstructure.

To determine definitively if the crystallization of PZT was being surface nucleation inhibited by modification of the Pt surface after dry etching, a dry etched Pt feature with clear etching residues was selected (similar to the feature selected in Figure 4-9 (a)). As opposed to directly crystallizing PZT over this etching residue, the etched substrate was coated with an additional 100 nm sputtered Pt layer in order to coat the etch residue with a surface which had never been exposed to the dry etch process, as exhibited in Figure 4-14 (a). The sample was then coated with a 1 µm thick PZT film and crystallized after every layer at 650 ˚C, as displayed in Figure 4-14 (b). SEM micrographs were then taken from areas where the newly sputtered Pt covered etching residues (region A), and where no residue appeared (region B). Both microstructures show identical perovskite grains with no rosette grain formation or microcracking.

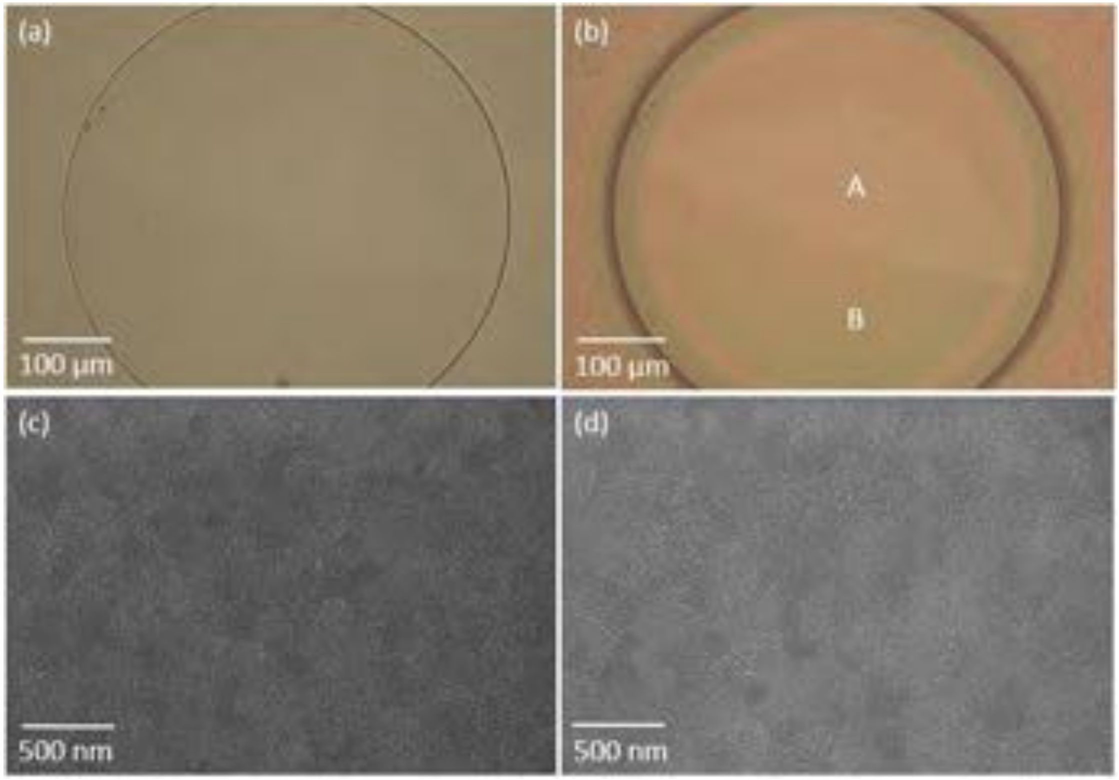

Figure 4-14. Optical images of (a) 100 nm of Pt sputtered additionally over dry etching Ni residues on a Pt feature, (b) PZT crystallized over Pt feature shown to the left. (c) High magnification focused on an area where PZT was fired specifically over etching residues (region A) and (d) an area where no etching residue was present (region B).

A dry etched Pt feature with no detectable residues, where the hard mask had been removed with nickel etchant TFB and subsequently cleaned with ACT 935, was also coated with 50 nm of newly sputtered Pt. The sample was then coated with a 1 µm thick PZT film and crystallized after every layer at 650 ˚C, displayed in Figure 4-15 (a). SEM micrograph from Figure 4-15 (b) shows that the microstructure of the PZT nucleated perovskite grains with no rosette grain formation or microcracking. This sample confirms that the secondary phase seen in Figure 4-14 (b and c) is a lead deficient surface pyrochlore which can be avoided. From these experiments, it is clear that the surface of the dry etched Pt inhibited nucleation of the perovskite grains; a pristine surface could not be fully recovered using etch byproduct strippers or Ni etchants.

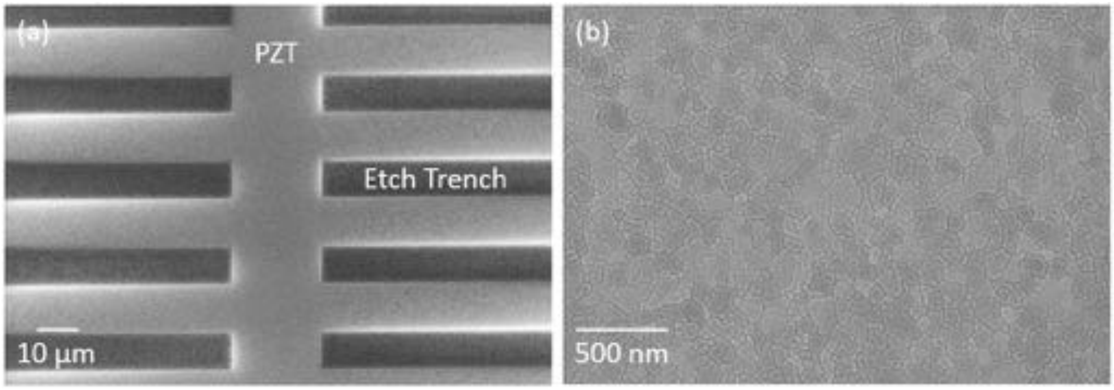

Figure 4-15. SEM image of (a) PZT crystallized over a dry etched Pt feature cleaned with ACT 935 to remove Ni residues followed by 100 nm sputtered Pt. (b) High magnification showing the PZT microstructure from the center of the Pt feature shown to the left.

An alternative to creating a fresh sputtered nucleation surface on a previously dry etched Pt surface, would be to lower the energy for nucleation of the perovskite phase. Ti rich compositions have a lower nucleation energy than Zr rich PZT.[119] To assess whether this approach could be used, PZT 30/70 was explored as a nucleation layer. For this purpose, a dry etched Pt feature with no detectable residues, where the hard mask had been removed with Nickel etchant TFB and subsequently cleaned with ACT 935, was coated with a 1 µm thick 30/70 PZT film and crystallized after every layer at 650 ˚C; the results are displayed in Figure 4-16 (a). SEM micrograph from Figure 4-16 (b) shows 30/70 PZT crystallized directly on cleaned, dry etched Pt exhibits well-nucleated perovskite grains with no rosette grain formation, secondary phase, or microcracking.

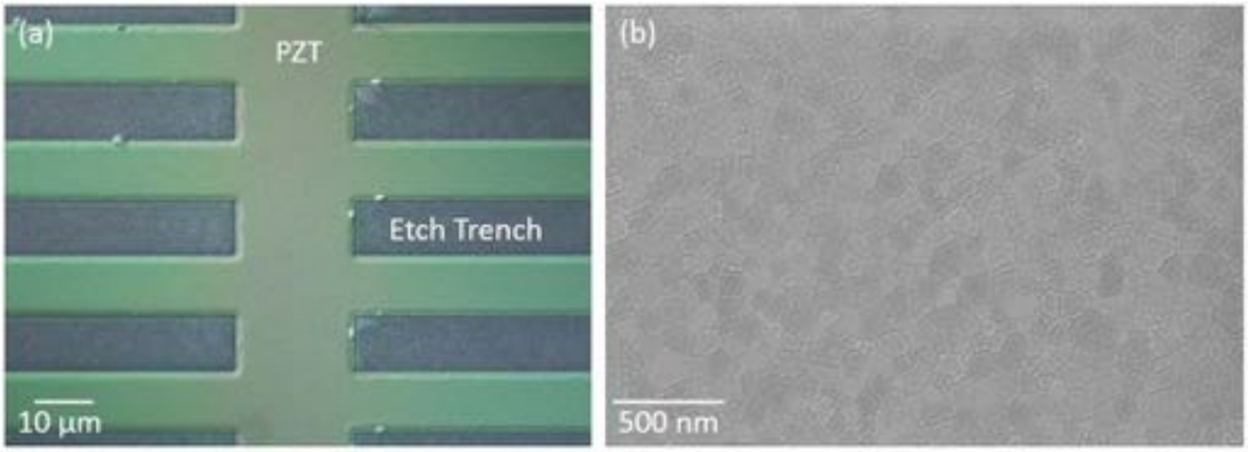

Figure 4-16. Optical image of (a) 30/70 PZT crystallized over a dry etched Pt feature cleaned with ACT 935 to remove Ni residues. (b) High magnification SEM image showing the PZT microstructure from the center of the Pt feature shown to the left.

4.3.4 Wet Etching PZT

Printing of PZT onto patterned substrates avoids degradation of functional properties for the active device area on top of the cantilever. PZT between features was not necessary for the functionality of the final device. One could use patterned stamp in conjunction with patterned substrates to confine the PZT in specific regions and completely avoid any etch step. However, this dictates that the stamp be aligned for every single stamping step, which was practically challenging. As an alternative, a flat stamp was used to print everywhere on the patterned substrate, and a single wet etch step was used to remove PZT far away from the active device area. The PZT was etched with a buffered oxide etchant, and protected in the device area with a photoresist mask. Conditions were optimized in order to limit undercutting of the wet etch.

SPR 1813 photoresist is designed for use with wet etchants. The soft baking step for this photoresist is ~ 100 ˚C for 60 s. Adhesion between the photoresist and the PZT was found to influence the degree of undercut. If adhesion is poor, the wet etchant readily attacked the PZT/photoresist interface, leading to a larger undercut. For example, using SPR 3012 photoresist as a wet etching mask provided inferior adhesion to the PZT surface than SPR 1813; thus, when wet etching a 300 nm thick 52/48 PZT film, the undercut was ~ 3 μm yielding a 10:1 undercut to etch depth ratio. Hard baking of the photoresist after developing can improve the adhesion between the oxide and photoresist. Hard baking can be done at any temperature between the initial bake temperature and the point at which the resist re-flows or cracks. In this work, hard bake temperatures were varied from 115 to 145 ˚C for the SPR 1813 photoresist. Figure 4-17 (a) shows a 260 nm 52/48 PZT thin film wet etched after the resist was hard baked at 115 ˚C for 60 s. The undercut of the wet etch was ~ 2 μm. In contrast, a 260 nm film etched with a photoresist hard baked at 145 ˚C for 30 m resulted in an undercut of ~ 1 μm, as shown in Figure 4-17 (b), thus improving the undercut to etch thickness ratio from 7:1 to 4:1. It is evident from Figure 4-17 (c) that the wet etchant attacks the grain boundaries in the PZT more readily than the grains.

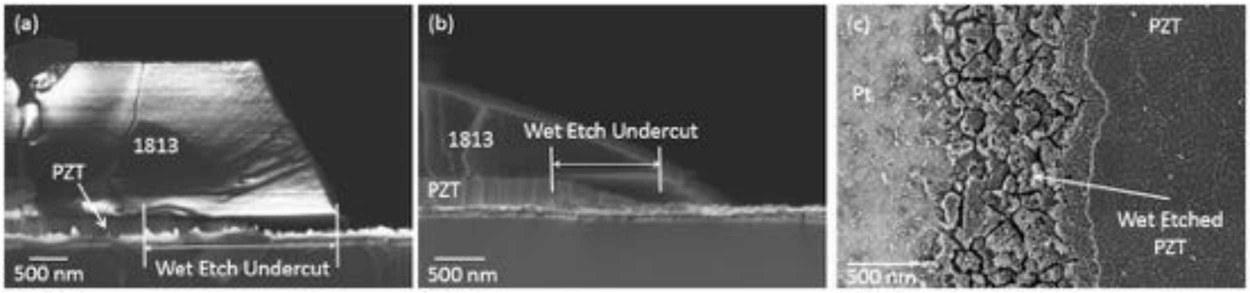

Figure 4-17. Cross-sectional SEM images of the undercut from wet etching of 52/48 PZT. Photoresist mask was baked at (a) 115 ˚C for 60 s and (b) hard backed at 145 ˚C for 30 min. (c) Top down SEM image of wet etched PZT protected with 145 ˚C hard bake.

Limiting the amount of time the PZT is exposed to the wet etchant may also reduce the undercutting of the photoresist. Varying the concentration of the hydrofluoric acid in the buffered oxide etch was found to decrease etching times, but led to a degradation in process control. BOE 10:1 and 6:1 were both used to etch 300 nm of 30/70 PZT. Figure 4-18 (a) illustrates that the undercut of this BOE 10:1 etch was ~ 10 μm. Figure 4-18 (b) shows that the undercut of this BOE 6:1 etch was ~ 6 μm. However, higher concentrations of HF resulted in uncontrolled etching along the perimeter of the masked areas.

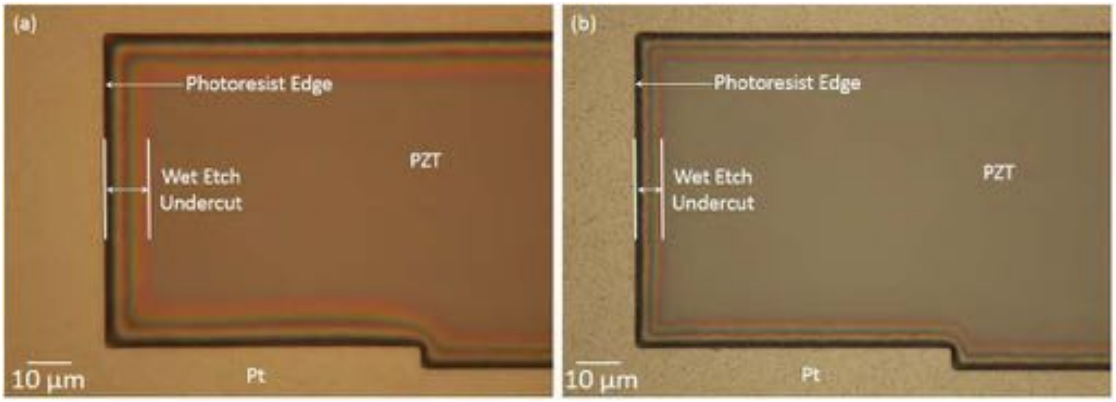

Figure 4-18. Optical images of wet etching 30/70 PZT utilizing an SPR 1813 photoresist mask. (a) BOE 10:1 and (b) BOE 6:1 wet etchant was used to expose the bottom Pt surface.

4.3.5 Dry Etching Defects

The final device was designed to be mounted into electrical packaging for wire bonding. The design required trace lines for both top and bottom electrode contacts so that the bond pads were clear of the active device area. This dictated that the bottom electrode be patterned to allow trace lines to be laid out without the threat of electrical shorting from top to bottom electrode. In this work, dry etching was used to etch through 100 nm Pt, 30 nm Ti, and stop on the HfO_2 layer.

Dry etching of Pt was undertaken using an ICP plasma (NE-550, ULVAC) with a coil power of 700 W and a chuck power of 50 W with 40 sccm of Ar and 30 sccm of Cl_2 gas. Initially, using a Ni hard mask over the Pt surface resulted in etching defects; the Ni surface was pitted due to a high physical bombardment component, as seen in Figure 4-19 (a) and (b). This pitting was severe enough to be transferred through the protective mask and into the underlying Pt surface, as displayed in Figure 4-19 (c). Lowering the amount of Ar gas from 40 to 10 sccm decreased the physical component of the dry etch and eliminated these defects.

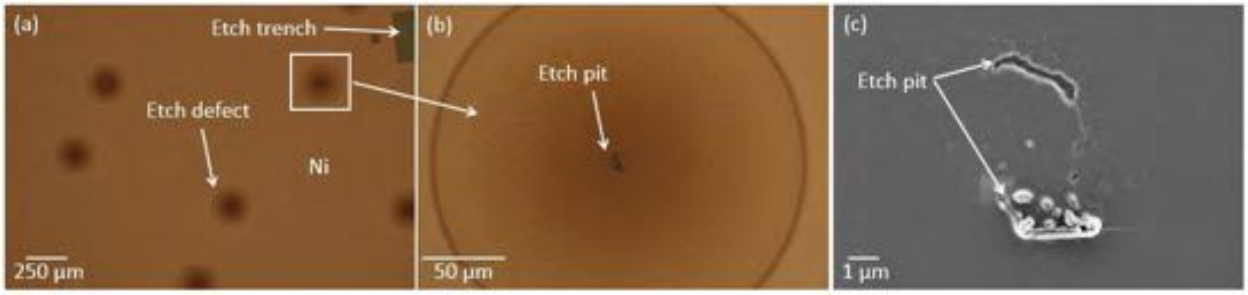

Figure 4-19. (a) Low and (b) high magnification optical images of etching defects in the surface of an electroplated Ni hard mask, and (c) the corresponding defect transferred into the protected Pt surface beneath the hard mask.

In addition to sputtering defects, the dry etch resulted in redeposition of etched material onto the sidewalls of both Ni and photoresist protective etch masks, as shown in Figure 4-20 (a) and (b) respectively. This redeposited material needed to be removed along with the protective mask after patterning was completed. However, this was often difficult, and resulted in “fences” of the redeposited material which fell over once the etch mask was removed, as shown in Figure 4-20 (c). This both complicated processing of subsequent layers and increased the lateral sizes of the designed features. Figure 4-20 (d) displays a feature where etching through a Pt layer ~ 150 nm thick resulted in a sidewall with a thickness of ~ 400 nm. In this work, a 1 μm feature doubled in width due to this defect.

Figure 4-20 (e) shows a cross-section of a Pt surface which was protected with a photoresist etch mask, and redeposition from the dry etch process along the perimeter of the mask. This sample was examined using EDS in order to determine the chemical makeup of the redeposited layer. Figure 4-20 (f), (g), (h), and (i) display the characteristic $K_{\alpha 1}$ X-rays of carbon, platinum, titanium, and chlorine respectively. These maps overlay with the corresponding SEM image observed in Figure 4-20 (e). These maps show that the redeposited material is a mixture of carbon from the photoresist mask, the etched platinum from the etched surface, as well as the chlorine from the dry etch gases.

The Pt in the redeposited material makes is extremely difficult to remove chemically with photoresist strippers (e.g. PRS 3000, Remover-PG, or Nanostrip) or etch residue removers (e.g. ACT 935). Use of mechanical agitation, e.g. ultrasonication, aided in removal of these fences. A comparison of using solely a photoresist stripper bath in Figure 4-20 (c), and a stripping bath with the addition of ultrasonication is shown in Figure 4-20 (d). While ultrasonication greatly reduced the amount of fences remaining on the etched sidewalls, the entire perimeter could not be fully cleared of these defects.

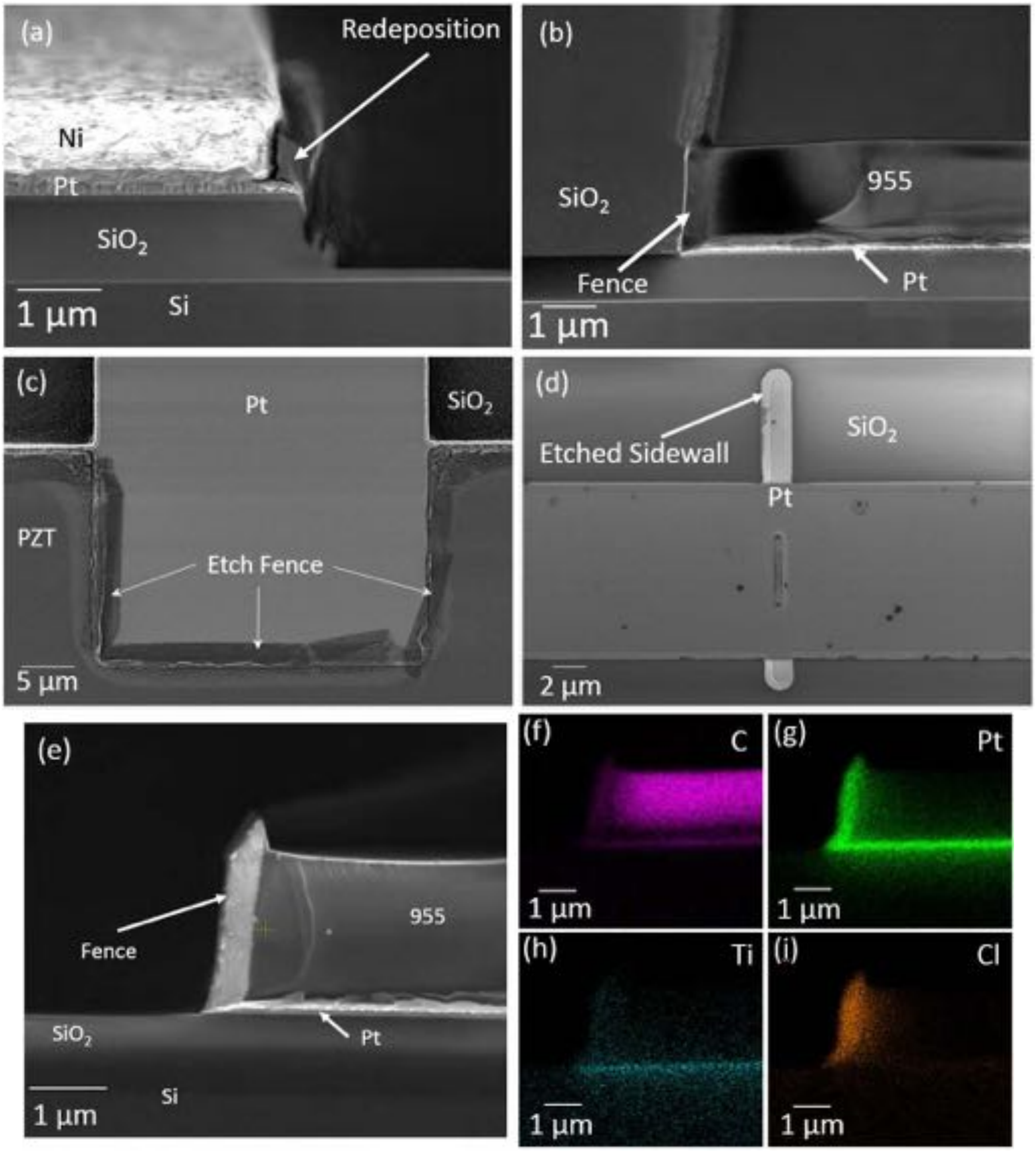

Figure 4-20. Cross-sectional SEM images of etch redeposition after dry etching Pt using (a) Ni and (b) photoresist as an etch mask. (c) Redepositions from a SPR 955 photoresist mask which remained on the sample even after the mask was removed. (d) 400 nm wide sidewall (~ 10˚) in the Pt resulting in enlargement of the etched feature. (e) Cross-sectional SEM image of etch redeposition for comparison purposes with EDS images on right showing the same area of interest. Characteristic $K_{\alpha 1}$ X-rays of (f) carbon, (g) platinum, (h) titanium, and (i) chlorine.

Therefore, it was necessary to reduce the thickness of these redepositions to a thickness where either resist strippers would chemically remove the defect, or ultrasonication would reproducibly break the fences off the surface of the etched surface. Initially, the etch chemistry was altered. The Ar content in the etch gas was varied from 0 to 40 sccm as presented in Figure 4-21 in an attempt to vary the physical bombardment of the dry etch. The redeposition thickness remained ~ 250 nm for each case. Lee *et al*. showed that the addition of oxygen to a dry etch reduced sidewalls when etching Pt.[120] Figure 4-21 (c) verifies that the addition of 4 sccm O_2 did not discernibly reduce the etch redeposition thickness. The chuck power was also varied to alter the physical energy of the bombarding ions impacting the sample surfaces in the dry etch. A 50 W etch displays a redeposition thickness of ~ 250 nm. Increasing the power to 90 W reduced the sidewall thickness ~ 200 nm as seen in Figure 4-21 (d). Power was increased to 175 and 225 W displayed in Figure 4-21 (e) and (f), respectively. The thickness further decreased to 125 and 100 nm, respectively. The base pressure was also varied to determine if the mean free path of the atoms could be limited and reduce the thickness of the redepositions. However, varying base pressure only slightly varied redeposition thicknesses. The thickness of the redeposited layer on the sidewall of samples etched at 175 W at 3.5 mTorr (Figure 4-21 (d)) and 10 mTorr (Figure 4-21 (g)) was ~ 125 and 150 nm, respectively. Finally, increasing the chuck power increased the sample temperature during the dry etch. Samples dry etched for ≥ 30 s cycles at 225 W reticulated, as shown in Figure 4-21 (h). Therefore, the dry etch chamber was kept at -10 ˚C and the etch steps were limited to 15 s. With redeposition thickness held to a 100 nm thickness, using a stripping bath in conjunction with ultrasonication allowed for complete removal of the etch fences, as shown in Figure 4-21 (i).

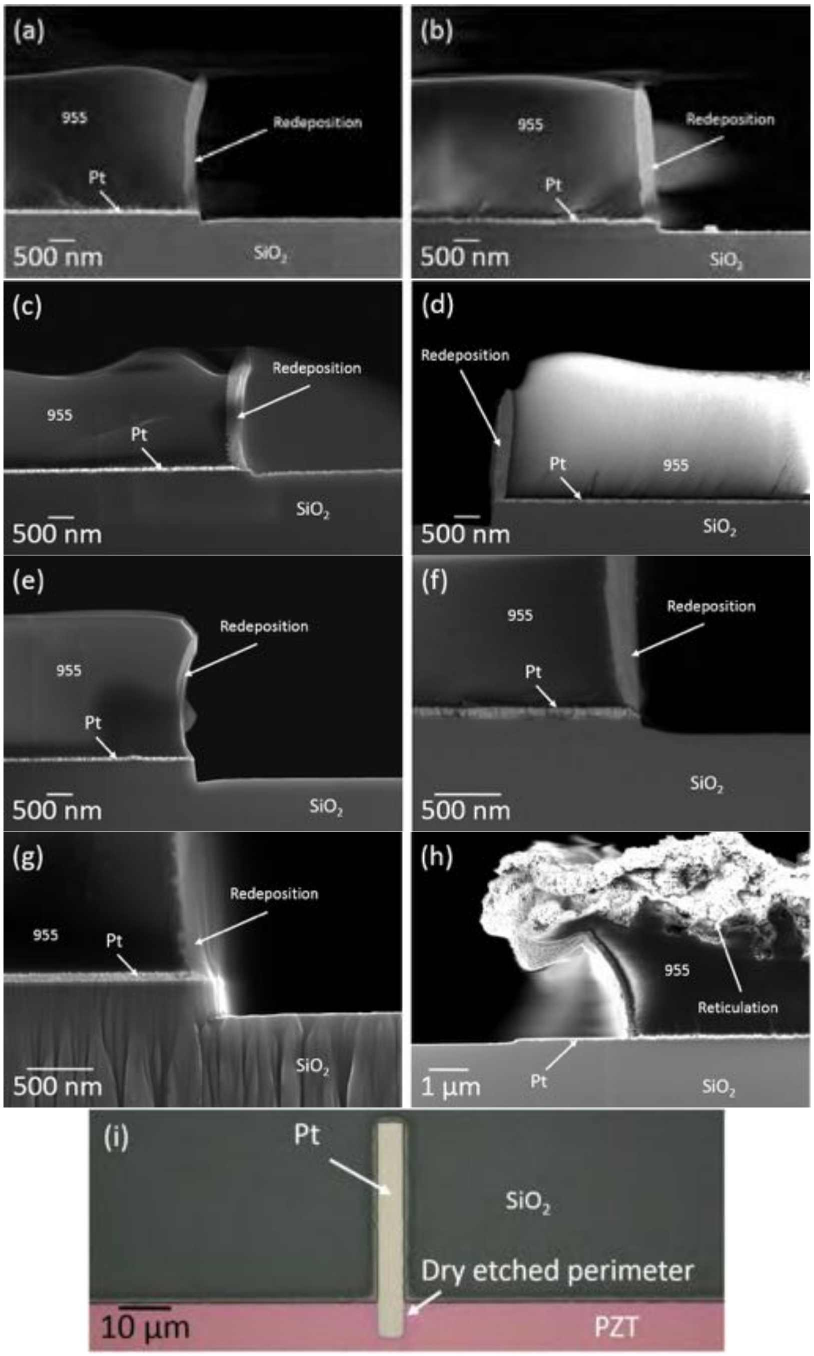

Figure 4-21. Cross-sectional SEM images of etch redeposition after dry etching Pt (ICP-RIE) (NE-550, ULVAC). (a) Dry etching Pt at 3.5 mTorr base pressure, 15 s etch steps, 50 W chuck bias, and 30 sccm Cl_2 gas. (b) 40 sccm of Ar and (c) 4 sccm of O_2 gas was added to the etch. (d) Chuck power was increased to (d) 90, (e) 175, and (f) 225 W. (g) Base pressure was increased to 10 mTorr. (h) Etch step time was increased to 30 s. (i) Optical image of dry etched Pt feature with no fences after optimized etch and photoresist strip with ultrasonication.

Dry etching over 600 nm into the SOI wafers necessitated multiple dry etching cycles. Typical etch cycles were limited to 15 or 30 s. This allowed for inspection with optical microscopy and ellipsometry to avoid over etching into the substrate and through underlying layers. While total etching time was approximately ~12 min, removal and inspection of the wafers caused the actual etch process to take ~4 to 6 hrs. It was found that if etch gases from the dry etch remained on the surface of the wafer between etching cycles, this could cause etch defects. Figure 4-22 (a) shows a Pt coated wafer with a Ni electroplated hard mask. The sample was dry etched for 1 min with a chlorine based etch: Figure 4-22 (b). The sample was then allowed to sit in ambient atmosphere for ~4 hrs. As shown in Figure 4-22 (c), following this wait time, the sample shows significant etching defects that were not present immediately after removing from the etch chamber. The sample was then washed in a deionized water bath, as depicted in Figure 4-22 (d). Residual chlorine from the dry etch adhered to the surface of the sample and reacted with the ambient moisture in the air to form HCl. The liquid attacked the Ni hard mask, leaving etch pits. This not only attacked the mask surface, but also the exposed perimeter of the underlying stack as the dry etch process continues. Therefore, it was critical that the wafer was cleaned in DI water after every etch cycle to remove residual Cl on the etched surfaces.

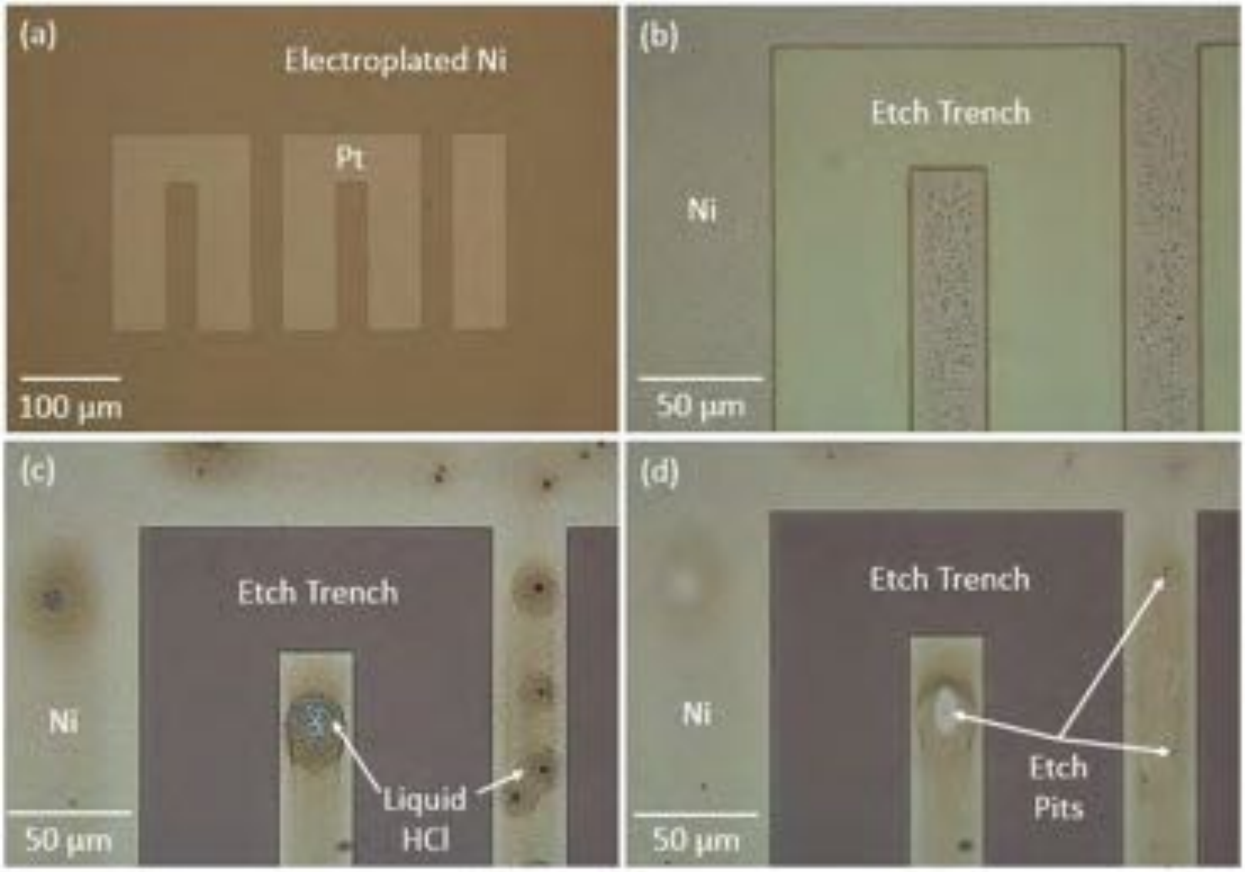

Figure 4-22. Optical images of (a) Pt features with a Ni hard mask (b) dry etched with Cl_2 gas. (c) Liquid hydrochloric acid formed on the surface of the sample after being left in normal atmospheric conditions for 4 hrs. (d) A water rinse removed liquid acid, revealing etch pits through the mask into the underlying stack.

4.3.6 Final Device Fabrication

The SOI wafer was characterized using spectroscopic ellipsometry to determine each layer thickness. An example of the experimental ellipsometry data overlaid with a fitted model (mean squared error of 35) is shown in Figure 4-23. The buried SiO_2 layer was determined to have a thickness of 996 ± 1 nm. The top Si layer, which is the foundation of the device stack, had a thickness of 290 ± 5 nm. SiO_2 was grown thermally onto the Si surface at 1000 ˚C and was a thickness of 100 ± 1 nm. The ALD coated HfO_2 layer was 60.5 ± 1 nm. The surface roughness of the stack was 3 nm.

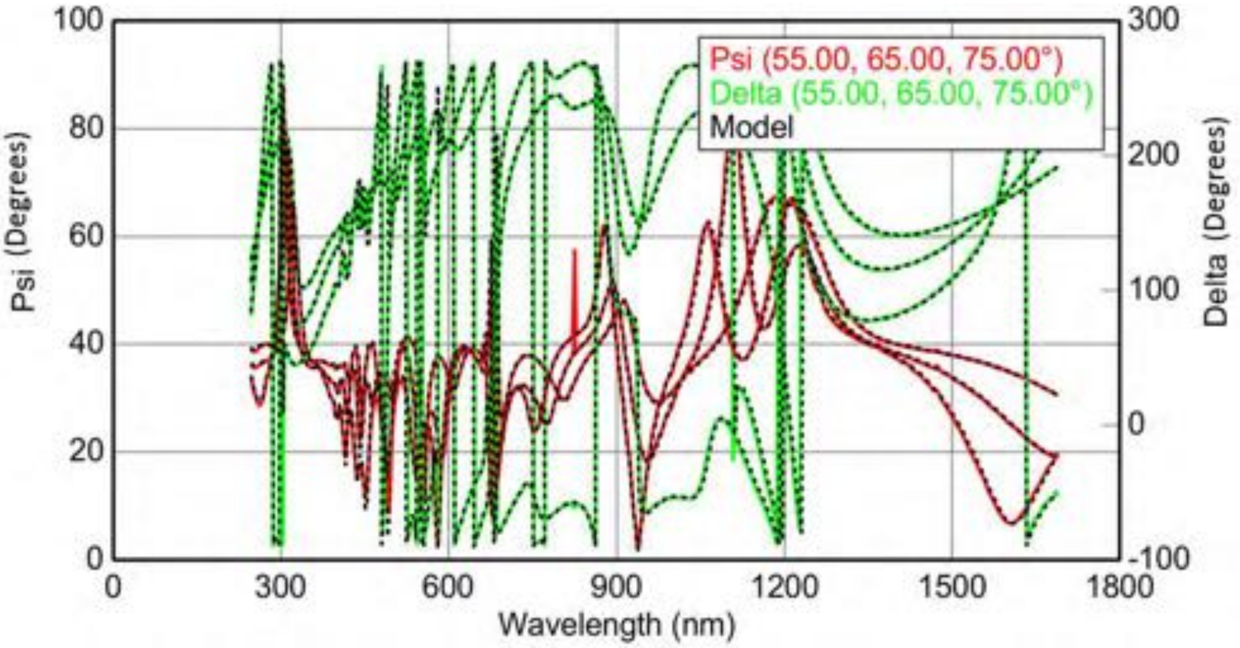

Figure 4-23. Variable angle spectroscopic ellipsometry scan with fitted model to determine thickness of SOI stack ($HfO_2/SiO_2/Si/SiO_2/Si$).

The Ti/Pt bottom electrode was sputtered onto the HfO_2 surface at room temperature. Figure 4-24 (a) indicates that a continuous layer of Pt with no porosity was deposited onto the SOI wafer. A high resolution microstructure of the sputtered electrode is seen in Figure 4-24 (b). The Ti layer was 30 nm thick and the Pt layer was ~ 125 nm. The total bottom electrode thickness was 155 ± 5 nm. The absorption depth of light in Pt was much smaller than the actual thickness; therefore, the thickness of the bottom electrode could not be determined by ellipsometry. Instead, the thickness was determined by contact profilometry.

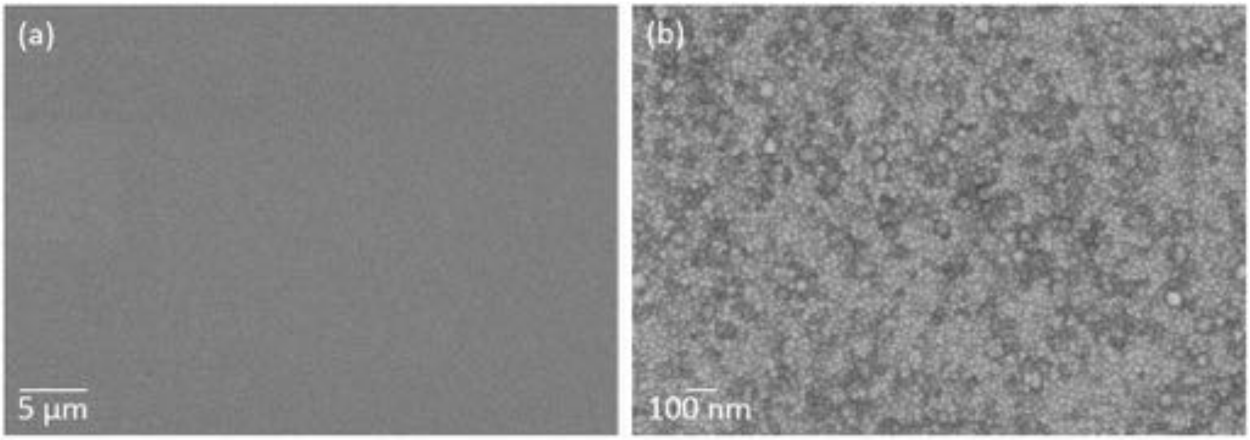

Figure 4-24. SEM images of sputtered Pt on top of SOI wafer. (a) Continuous Pt with no porosity present. (b) High magnification of the sputtered microstructure.

A Ni hard mask was electroplated onto the surface of the bottom electrode to define the cantilever patterns to be etched into the SOI wafer surface. The mask was pulse plated for 15 min onto the Pt surface with a forward current of 0.612 A and a reverse current of 0.061 A, resulting in an effective current of 0.208 A (calculated by power supply) based on the times for each step as discussed in section 4.2.2. The effective current for the device plating area resulted in a plating current density of 5 mA/cm^2. The minimum height of the mask was 580 ± 10 nm, at the center of the wafers. The maximum Ni height was at the edges of the patterned areas approaching the edge of the SOI wafer; this could be due to non-uniform field effects. Corners of the features are also areas where field concentrations can cause an increase in Ni deposition rate.[121] The maximum Ni height never exceeded the maximum height of the photoresist layer that defined the Ni features: 1.2 ± 0.1 µm. An example of the Ni electroplated features is given in Figure 4-25 (a) and (b) which display an optical and SEM image of the 2 µm wide features. The electroplated Ni did not result in delamination of the underlying stack. Figure 4-25 (c) indicates that the Ni was dense, with no evidence of cracking.

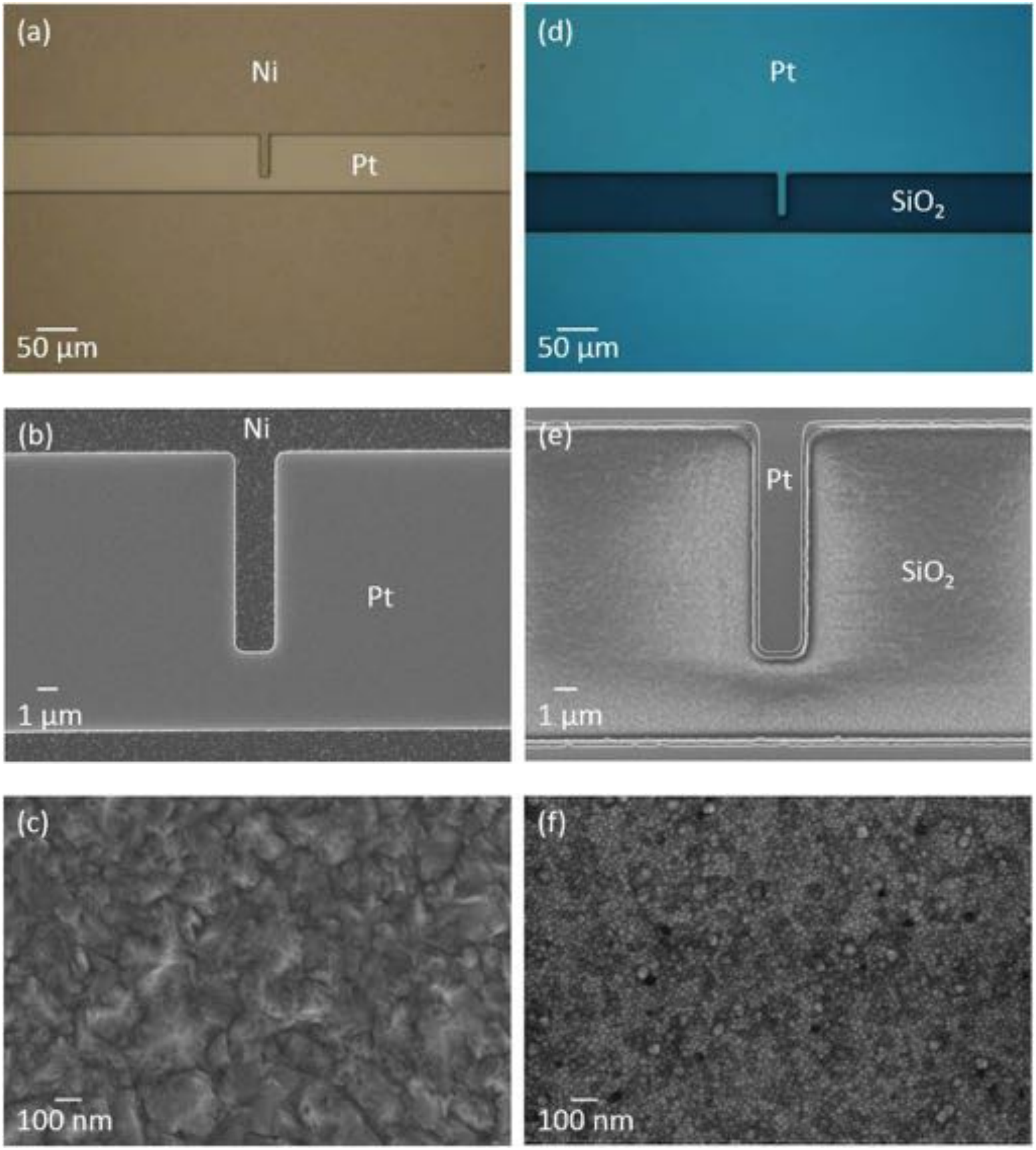

Figure 4-25. (a) Optical and (b) SEM image of a 2 µm electroplated Ni feature. (c) SEM image of microstructure of the electroplated Ni. (d) Polarized optical and (e) SEM image of 2 µm dry etched Pt feature after hard mask removal. (f) SEM image of microstructure of the dry etched Pt surface which was protected with electroplated Ni.

The substrate was dry etched using a chlorine based etch chemistry with a chuck power of 225 W for a total etching time of 6 min using 30 s etch steps (Ni hard masks are not as susceptible to increases in sample temperature as photoresist masks). Ellipsometry, contact profilometry, and optical and/or SEM microscopy were used to determine when the etching of a particular layer was complete. Ellipsometry results showed the wafers were etched ~ 60 ± 30 nm into the buried SiO_2 layer beneath the 290 nm Si layer. The wafer was immersed in Ni etchant TFB in an ultrasonic cleaner at 40 ˚C for 10 min followed by an ACT 935 bath in an ultrasonic cleaner for 1 hr. Figure 4-25 (d) display a polarized optical microscopy image and Figure 4-25 (e) presents an SEM microscopy image of a 2 µm etched feature with no Ni etching residues on the surface of the Pt. Figure 4-25 (f) exhibits the microstructure of platinum that was beneath the Ni hard mask; there is no evidence of damage to the surface. The contact profilometer determined the depth of the etch trench after the Ni removal to be 685 ± 30 nm deep, confirming that the etch penetrated through the $Pt/Ti/HfO_2/Si$ layers and stopped on the buried SiO_2. Contact profilometry determined that 300 ± 10 nm of Ni was removed during the etch, resulting in an etch rate of 50 nm/min for the Ni hard mask.

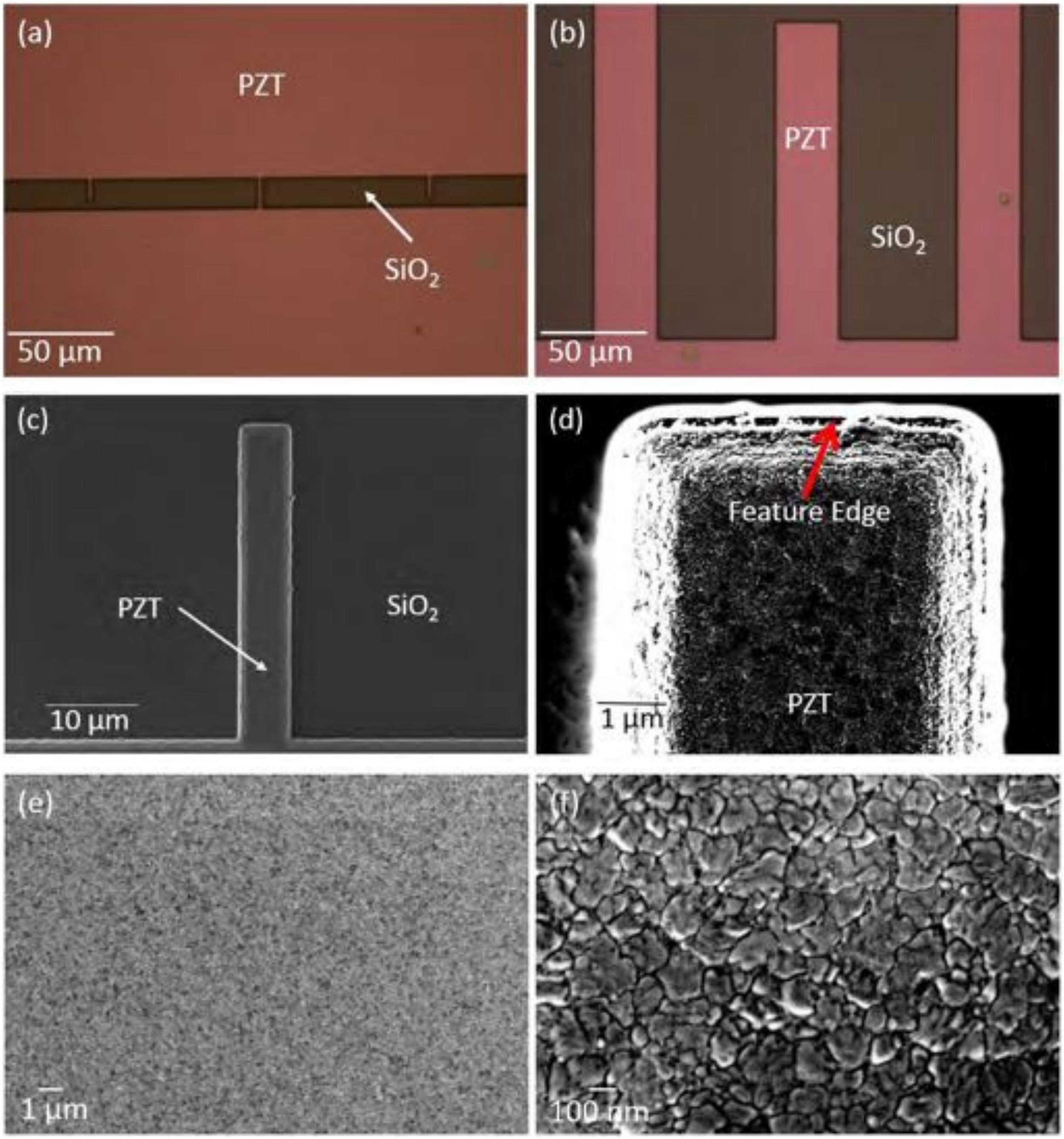

Figure 4-26. Optical images of 275 nm 30/70 PZT printed onto (a) 2 and (b) 30 µm features. (c) SEM image of a printed PZT film crystallized on a 5 µm Pt feature. (d) High magnification SEM image of PZT on 5 µm feature. (e and f) High magnification of microstructure of the PZT crystallized into the perovskite phase with no evidence of secondary phases present.

Flat composite PU/PDMS stamps were created as described previously. The Mitsubishi PZT solution (described in section 4.2.2) was spin coated onto the wafers at 5000 rpm for 30 s. The stamp was aligned over the patterned SOI substrate; the stamp was brought into contact and removed by hand. The sample was pyrolyzed and crystalized after each printing cycle. Seven printing cycles yielded a PZT film ~275 ± 5 nm thick on top of the etched cantilever features. Examples of the PZT films printed on top of 2 and 30 µm structures are shown in Figure 4-26 (a) and (b) respectively. The sidewall angles of the printed PZT was ~35˚, which is displayed in Figure 4-26 (c) and (d). The PZT fully crystallized into the perovskite phase. As observed in Figure 4-26 (e), rosette grain formation was avoided as well as any residual matrix phase. No significant porosity was evident; however, a slight amount of surface pyrochlore was present at the grain boundary triple points, as noted in Figure 4-26 (f). This also indicates that there were not high amounts of excess PbO in the film, which can lead to conduction pathways under applied fields.

PZT films were prepared for wet etching by coating in SPR 1813 photoresist and hard baking at 145 ˚C for 30 min. The samples were immersed in BOE 6:1 for 2 min etch cycles. The sample was then immersed in HCl for ~1 to 3 s, to remove any slow etching metal complexes on the etch surface. The samples were then immersed in DI water and inspected visually, looking for the bottom Pt surface beneath the PZT layer. Wet etching of ~275 nm of 30/70 PZT required a total of 7 to 8 cycles (13 to 16 min of total BOE etch time). Wet etched films with the photoresist mask on the surface covering 2 and 5 µm features are seen in Figure 4-27 (a) and (b) respectively. The wet etching resulted in an undercut of 5.5 µm. The undercut did not reach the active areas of the PZT printed on top of the cantilever structures.

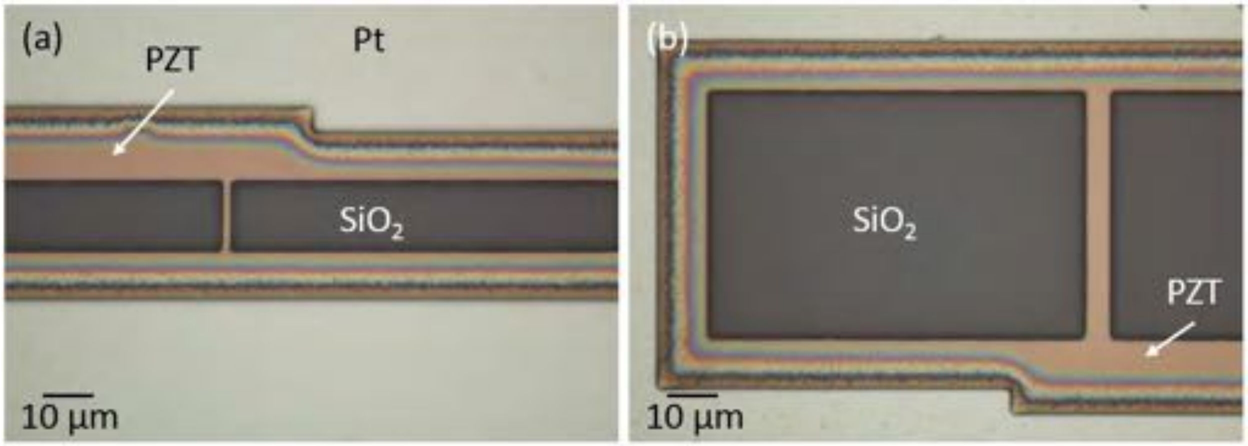

Figure 4-27. Optical images of a printed 275 nm thick 30/70 PZT film crystallized on top of a SOI wafer, and wet etched with BOE 6:1 around (a) 2 and (b) 5 µm features.

Top Pt electrodes were deposited through a lift-off process where the photoresist was spin coated over the 1 µm deep patterned features into the SOI surface. The top electrode patterns were aligned to the patterned cantilever structure and exposed with e-beam lithography. The photoresist was ~250 nm taller than the raised features. The top Pt was sputtered onto the PZT surface at room temperature. Figure 4-28 (a) and (b) are examples of the top Pt aligned and sputtered onto a 2 and 5 µm wide printed PZT cantilever, respectively. The Pt features were not as wide as the printed PZT feature. This permitted minor alignment errors in the lithography and sidewalls of the printed PZT. The top Pt was deposited only over flat PZT areas. Pt sputtered down the sidewalls of the printed PZT would result in an increased likelihood of shorting the device, as well as non-uniform fields to be experienced through the material during operation or upon poling of the PZT. The Pt was sputtered to a thickness of 35 nm. This allowed for a continuous layer of Pt on the PZT, as displayed in Figure 4-28 (c). When Pt was ≥ 50 nm thick, the removal of the single layer photoresist resulted in Pt fences to remain along the perimeter of the patterned electrode area.

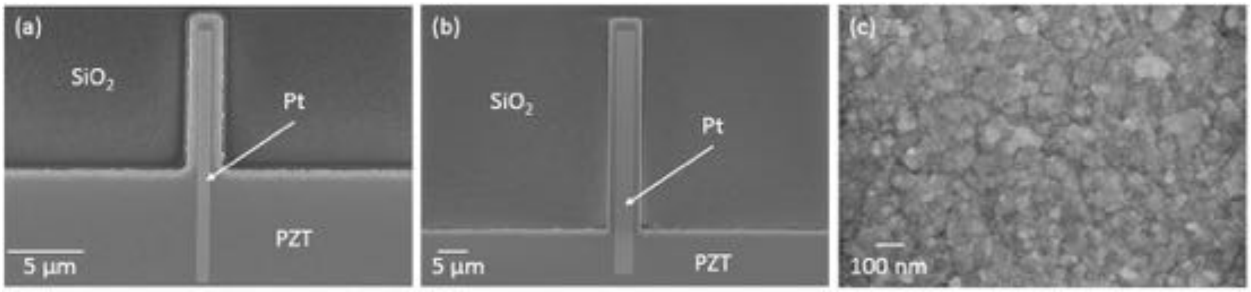

Figure 4-28. SEM images of a 30 nm top Pt electrode evaporated onto a printed 275 nm thick 30/70 PZT film crystallized on top of a (a) 2 and (b) 5 µm feature. (c) High magnification image of the microstructure of the top Pt with no evidence of porosity.

A 6 µm thick photoresist mask was used to protect the device stack for the dry etching of the bottom Pt layer. The substrate was dry etched using a chlorine based etch chemistry with a chuck power of 225 W for a total etching time of 2 min using 15 s etch steps. Ellipsometry, contact profilometry, and optical and/or SEM microscopy was used to determine when the etching of a Pt layer was complete. Ellipsometry results showed the wafers were etched ~ 30 ± 15 nm into the HfO_2 buffer layer beneath the 155 nm Ti/Pt layer. The photoresist mask was removed by immersion in a PRS 3000 ultrasonication bath at 60 ˚C for 1 hr. The contact profilometer determined the depth of the etch trench after the photoresist removal to be 180 ± 10 nm deep, confirming that the etch penetrated through the Pt/Ti layers and stopped in the HfO_2 buffer layer. Figure 4-29 (a) and (b) are examples of the bottom Pt electrode patterned around 5 and 30 µm wide printed PZT cantilever, respectively. Contact profilometry determined that 1.3 ± 0.1 µm of photoresist was removed during the etch, resulting in an etch rate of ~0.65 µm/min for the photoresist mask.

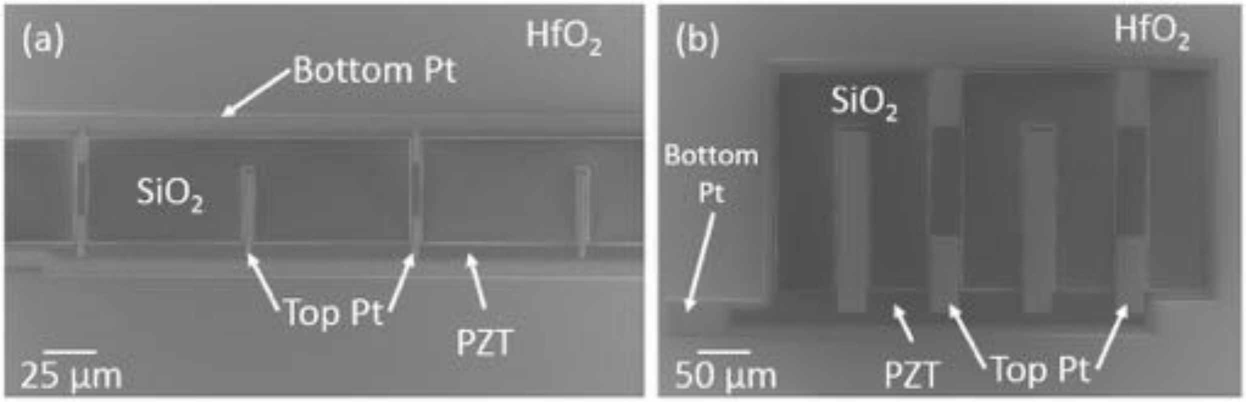

Figure 4-29. SEM images of dry etched bottom Pt electrode around (a) 5 and (b) 30 µm features.

A 6 µm thick photoresist mask was used to protect the device stack for the dry etching of the HfO_2/SiO_2 layers. The HfO_2 layer was dry etched using a chlorine based etch chemistry (described in Table 4-1) with a chuck power of 225 W for a total etching time of 75 to 90 s using 15 s etch steps. The SiO_2 layer was dry etched using a CF_4 based etch chemistry (described in Table 4-2) with a chuck power of 200W for a total etching time of 12 to 15 s. Ellipsometry, contact profilometry, and optical and/or SEM microscopy was used to determine when the etching of the HfO_2 and SiO_2 layers were complete. Ellipsometry results showed the wafers were etched ~ 80 ± 10 nm into the Si layer beneath the 30 nm HfO_2 layer and the 100 nm SiO_2 layer. The photoresist mask was removed by immersion in a PRS 3000 ultrasonication bath at 60 ˚C for 1 hr. The contact profilometer determined the depth of the etch trench after the photoresist removal to be 190 ± 10 nm deep, confirming that the etch penetrated through the HfO_2/SiO_2 layers and stopped in the Si layer. Figure 4-30 (a) and (b) show examples of the HfO_2/SiO_2 patterned around 2 and 30 µm wide printed PZT cantilever, respectively. Examples of the 1, 2, 5, and 30 µm wide cantilevers final device structures with 275 nm of printed PZT are seen in Figure 4-31 (a), (b), (c), and (d), respectively.

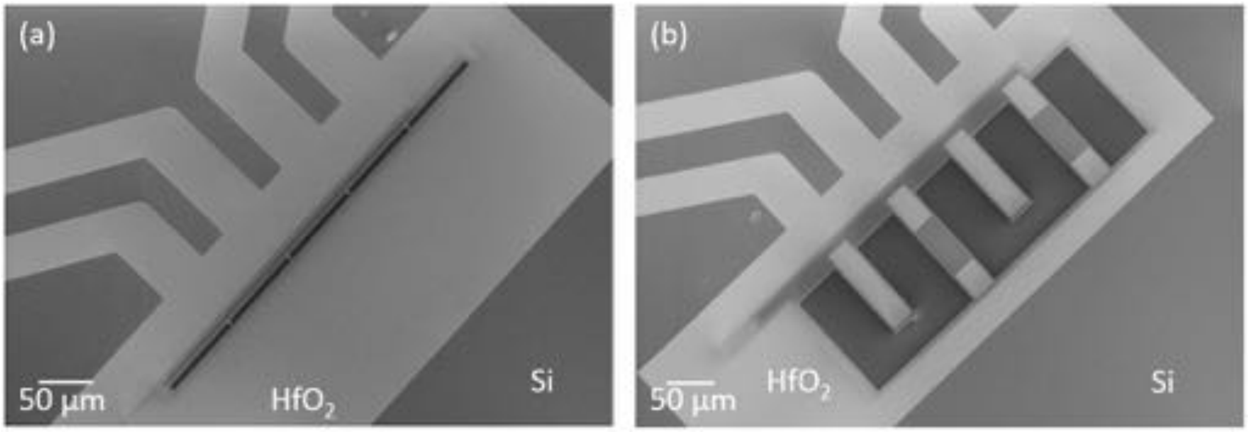

Figure 4-30. SEM image of dry etched HfO$_2$ around (a) 2 and (b) 30 µm PZT printed features.

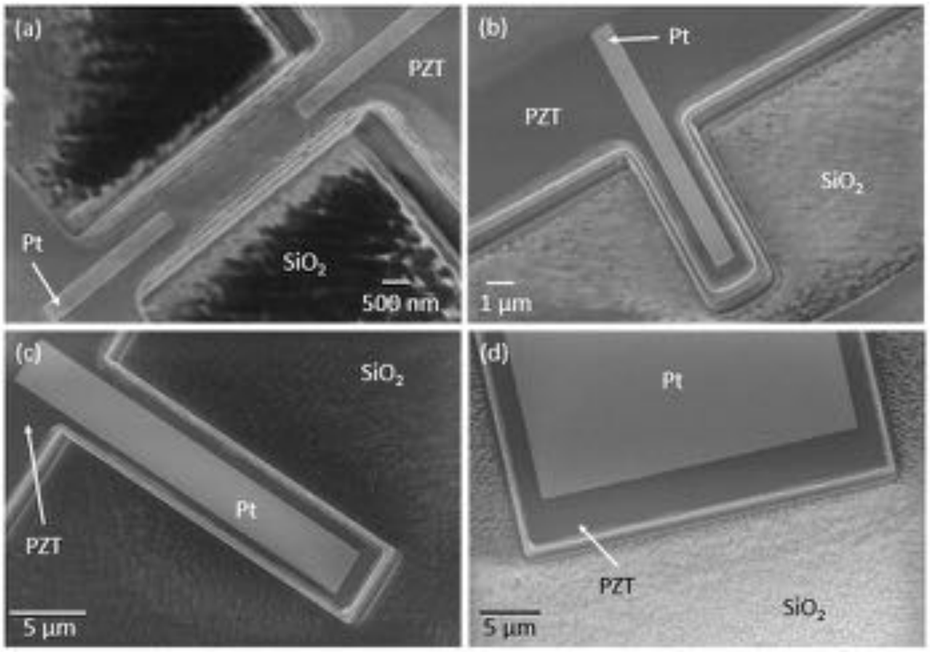

Figure 4-31. SEM images of final device stack of Pt/PZT/Pt/Ti/HfO$_2$/SiO$_2$/Si with lateral feature sizes of (a) 1, (b) 2, (c) 5, and (d) 30 µm.

4.3.7 Electrical Characterization of PZT

Printed PZT devices on SOI wafers were electrically characterized and compared to an analogous PZT device created through dry etching. The dry etched PZT devices were created by spin coating PZT on top of a non-patterned Pt coated Si wafer and were blanket sputter coated with a top Pt electrode. Electroplated Ni was patterned on top of the top Pt layer as previously described. The sample was then dry etched at 3.8 mTorr using a 25 sccm Cl_2 gas based etch chemistry at 90 W chuck power for a total etching time of 12 min using 30 s etch steps The etch penetrated 100 nm of Pt, 300 nm of 52/48 PZT, 150 nm of bottom Pt, and 500 nm of SiO_2. The Ni was removed as previously described with nickel etchant TFB. The sample top electrode was patterned using a photoresist mask and chlorine based etch as previously described. An example 30 μm wide dry etched PZT feature, which is analogous to the printed PZT features on SOI wafers, is observed in Figure 4-32 (a). Figure 4-32 (b) plots the relative permittivity and loss tangent as a function of frequency. The dry etched stack exhibits a reduced relative permittivity of 305 and loss tangent of 0.018 at 1 kHz. A 300nm thick printed PZT feature as displayed in section 2.3.4 exhibits a relative permittivity of 900 and a loss tangent of 0.02 with a remanent polarization of 22 $\mu C/cm^2$. Figure 4-32 (c) plots the polarization-electric field behavior as a function of electric field. The dry etched PZT hysteresis loops are imprinted and are not saturated. The electrodes show charge injection on the positive side of the PE loop. The coercive field is 250 kV/cm and the remanent polarization was 7 $\mu C/cm^2$ at 100 Hz. The CV sweep shows the characteristic ferroelectric curve, as highlighted by Figure 4-32 (d). The samples show evidence of charge injection, resulting in an increased dielectric loss at high positive excitation fields. This sample clearly demonstrates the large reduction of properties that can occur on dry etching a ferroelectric film.

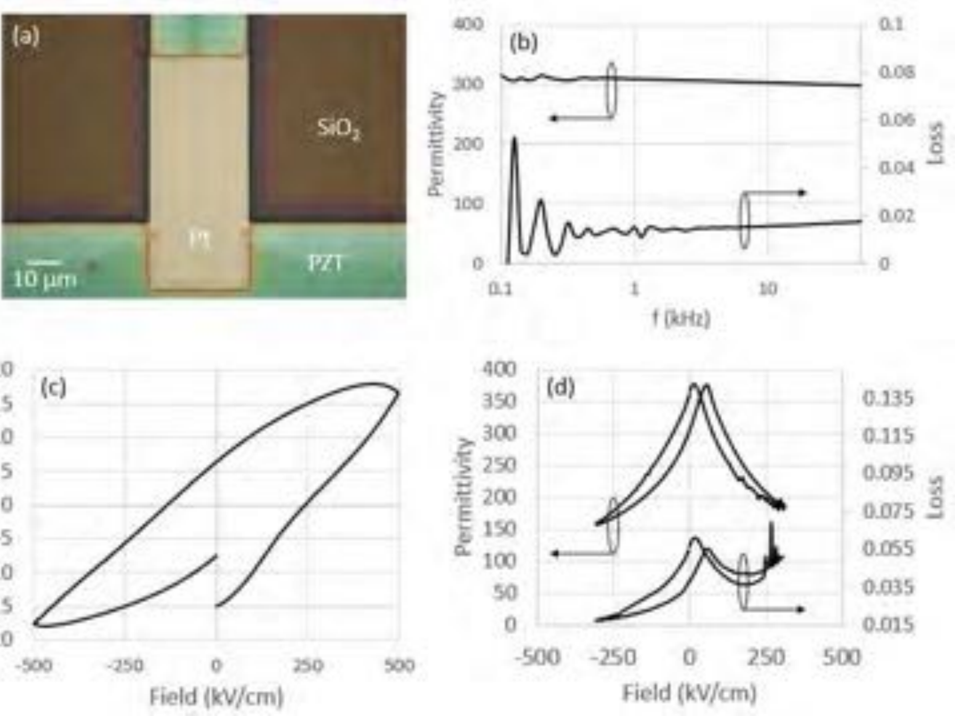

Figure 4-32. (a) Optical image of 30 µm dry etched 52/48 PZT feature. (b) Relative permittivity and loss tangent, (c) PE loop, and (d) CV behavior of a dry etched 30 µm 52/48 PZT feature.

Altering the etch chemistry and etching parameters can yield improved functional properties in dry etched PZT. In this work, a second sample was etched with an improved etch chemistry developed by the Nanofabrication staff. The sample was dry etched at 3.8 mTorr using a 3.5/7 sccm Cl_2/CF_4 gas mixture at 150 W chuck power for a total etching time of 8 min using 30 s etch steps. The etch penetrated 100 nm of Pt, 275 nm of 30/70 PZT, 150 nm of bottom Pt, and 500 nm of SiO_2. The Ni was removed as described before. The sample top electrode was patterned using a photoresist mask and chlorine based etch as described before. An example 30 µm wide dry etched PZT feature, which is analogous to the printed PZT features on SOI wafers, is presented in Figure 4-33 (a). Both printed and dry etched 30/70 PZT layers on top of a 30 µm patterned cantilever structure yielded a film with a thickness of 275 nm. Figure 4-33 (b) plots the relative permittivity and loss tangent as a function of frequency of the corresponding 275 nm film stacks. The printed stack (black line) exhibits a relative permittivity of 500 and loss tangent of 0.009 at 1 kHz. The dry etched stack (red line) exhibits a reduced relative permittivity of 445 and loss tangent of 0.009 at 1 kHz. Figure 4-33 (c) plots the polarization-electric field behavior as a function of electric field. The printed PZT hysteresis loops (black line) are well saturated with a coercive field of 110 kV/cm and a remanent polarization of 24 μC/cm^2 at 100 Hz. The dry etched film (red line) exhibits a coercive field of 112 kV/cm and a remanent polarization of 24 μC/cm^2 at 100 Hz which are very similar to the printed PZT. The loops are well saturated, however the loops show evidence of pinching, which is indicative of the presence of randomly oriented defect dipoles in the film. Figure 4-33 (d) shows that after poling the film the defects in the film aligned to the electric field resulting in an imprinted hysteresis loop (blue line) as well as a reduced remanent polarization of 20 μC/cm^2. These defects also strongly influence the functional properties of the film at sub-switching fields. Figure 4-33 (e) shows the field dependent relative permittivity of the dry etched film. The Rayleigh parameters were extracted by performing a linear fit to the curve. The Rayleigh parameters were used to calculate an ideal minor hysteresis loop (green line); this is compared to the measured hysteresis loop (red line) in Figure 4-33 (f). As was the case for the major hysteresis loop, significant pinching of the minor loop is evident. Clearly, and the agreement between the calculated and measured minor loops is poor. As a results, the dielectric response of the films is not properly Rayleigh-like, although the relative permittivity does increase linearly over a finite field range. It is most likely that the distribution of pinning centers is not random, but arranged in a way that leads to an internal bias field, akin to hard PZT ceramics.[122] Domain walls move in a deep potential well with a single minimum as opposed to a random potential.[123] It is evident that these defects influence device performance at both switching and sub-switching excitation levels.

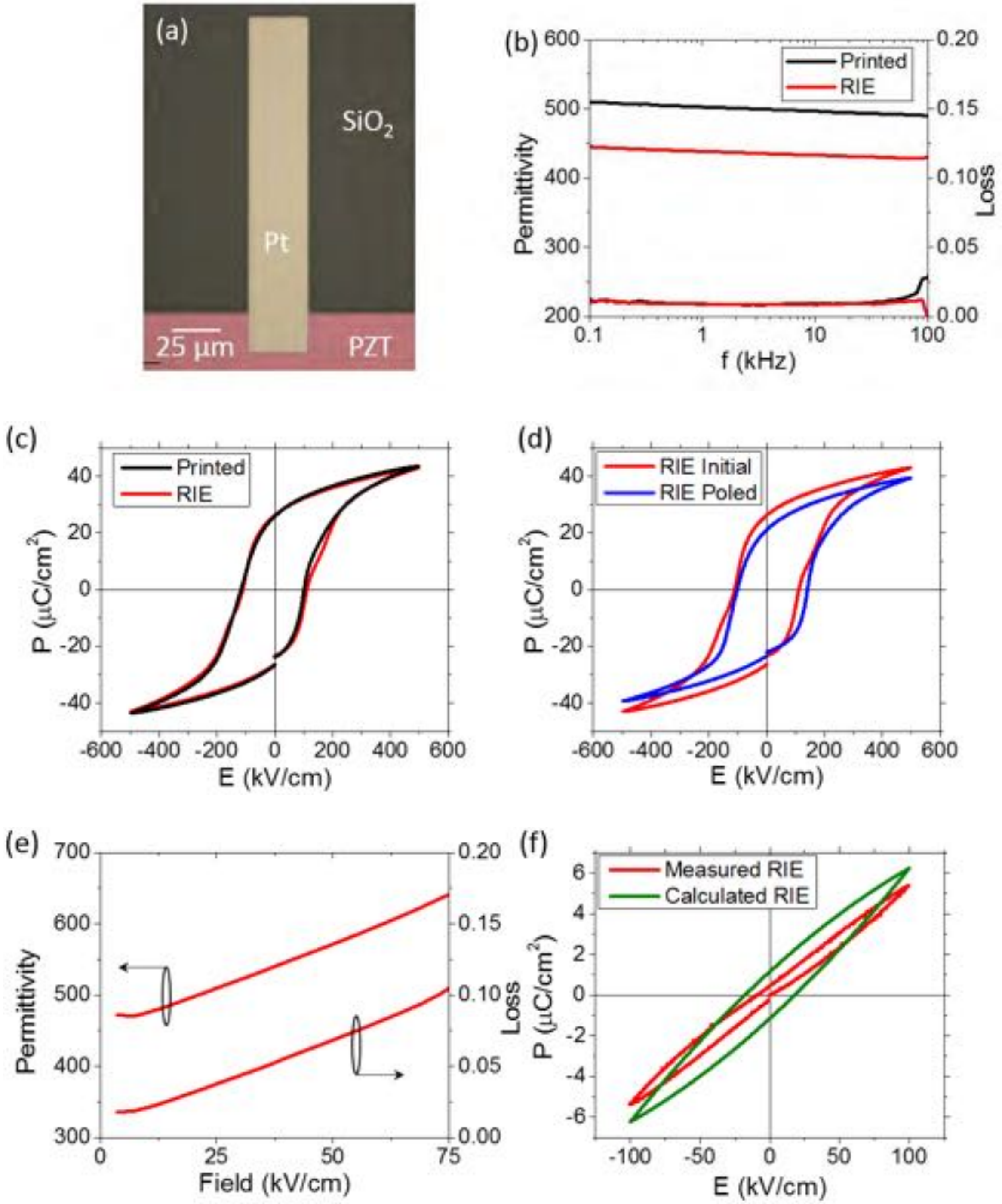

Figure 4-33. (a) Optical image of 30 µm dry etched 30/70 PZT feature. (b) Relative permittivity, loss tangent and (c) PE loop comparison between a dry etched (red) and printed (black) 30 µm 30/70 PZT feature 275 nm thick. (d) PE loop of RIE film before (red) and after poling (blue). (e) Rayleigh behavior of RIE film used to (f) calculate minor hysteresis loop (green) and compare to measured minor loop (red).

4.4 Conclusions

Microcontact printing of PZT solutions onto patterned SOI substrates was implemented as a means to incorporate piezoelectric films into a bio-mass sensor. Pulsed power electroplating of Ni sulfamate solutions was optimized in order to minimize the residual stress of the deposited metal. This allowed 1 to 30 µm wide cantilever structures with vertical sidewalls to be etched into the surface of the wafer. Etching altered the Pt surfaces that were protected by Ni masks. The altered surface inhibited perovskite phase nucleation, which led to rosette grain nucleation, residual secondary phases, and microcracking. The density of surface nucleation of perovskite phase was increased with cleaning of the Pt surface post etching, but Ti rich compositions of PZT were needed to lower the activation energy of nucleation in order to fully convert the films to perovskite PZT. The influence of the altered Pt surfaces on device performance, including lifetime, is unknown.

The integration of ferroelectric PZT into the bio-mass sensor device was successful. The PZT was printed onto all feature sizes. The printed PZT films crystallized into the perovskite structure, with no secondary phases. The dielectric and ferroelectric response of the printed films were superior or comparable with dry etched PZT films of similar thicknesses. However, the P – E hysteresis and the low field relative permittivity reveal that PZT patterned via dry etching showed properties consistent with a higher concentration of randomly oriented defect dipoles, which were not seen in the printed samples. Therefore, microcontact printing offers a damage-free patterning route by which piezoelectric materials can be incorporated into the manufacturing of MEMS devices. The bio-mass sensors were delivered to collaborators at CNRS in France for subsequent characterization.

Chapter 5

Probing Ferroelectric Domain Wall Mobility of Patterned Thin Films at the Nanoscale

The piezoelectric nonlinearity in patterned PZT films was mapped quantitatively using band excitation piezo-response force microscopy (BE-PFM). This permits the influence of pinning centers on domain wall motion to be explored, particularly near patterned feature sidewalls. An understanding of the influence of patterning on the material properties is essential to predicting and controlling the behavior of polycrystalline films for microelectromechanical system (MEMS) applications. Patterned features in $PbZr_{0.52}Ti_{0.48}O_3$ films, ranging from 500 to 5 μm in lateral dimension, were fabricated by both reactive ion etching (RIE) and microcontact printing. The RIE and printed features displayed 70˚ and 80˚ sidewalls, respectively. The RIE features exhibited a relative permittivity of 827 ± 7 with a loss tangent of 1.8 ± 0.06 %, remanent polarizations of 23.8 ± 0.7 $\mu C/cm^2$, and coercive fields of 44.6 ± 1.3 kV/cm. The printed features exhibited a relative permittivity of 983 ± 3 with a loss tangent of 1.5 ± 0.09 %, remanent polarizations of 20.4 ± 0.6 $\mu C/cm^2$, and coercive fields of 43 ± 1 kV/cm. Measurements of the piezoelectric nonlinearity a function of position across a patterned RIE feature showed a $\alpha/d_{33,init}$ of $4.9 \pm 0.8 \times 10^{-3}$ cm/kV. Defects from the etching process introduced large concentrations of pinning centers near the patterned sidewalls, resulting in large reductions in $\alpha/d_{33,init}$ as far as 750 nm from the sidewall. BE-PFM measurements on a printed feature showed a reduced $\alpha/d_{33,init}$ of $3.3 \pm 0.4 \times 10^{-3}$ cm/kV in the center of the feature due to a mixture of rosette grains alongside a secondary phase. Minimal defects from the printing process alongside mechanical declamping of the film near the patterned sidewall resulted in increased $\alpha/d_{33,init}$ values when approaching the sidewall.

5.1 Introduction

Ferroelectric films exhibit large dielectric and piezoelectric responses in comparison to non-ferroelectric piezoelectric materials,[124, 125] due in part to domain wall motion within the material.[126] The contribution of domain wall motion to the dielectric, ferroelectric, and piezoelectric properties is a function of both composition and crystallographic structure.[127, 128, 129, 130] The large electromechanical coupling in ferroelectric materials lowers the operating voltage[5] and increases the charge sensitivity[6] for microelectromechanical systems (MEMS). Incorporating these materials into devices requires patterning of the ferroelectric. Patterning often utilizes dry etching the ferroelectric material, which can physically and chemically alter the material.[35, 14, 39] limiting the achievable properties.[40, 41] It has also been shown that patterning of the ferroelectric material by microcontact printing avoids etching damage.[87] An open question is the manner in which domain walls behave at patterned sidewalls, coupled with the length scale over which the sidewall influences the material response.

The Rayleigh law describes the dielectric and piezoelectric nonlinearity with respect to the magnitude of the ac electric field.[75] The model describes mobile interfaces, such as domain walls, interacting with a distribution of pinning centers. The excitation field should not alter the domain structure of the material during the Rayleigh measurement to allow quantification of the irreversible extrinsic contribution to the dielectric or piezoelectric properties.[131] The stability of a domain structure is a function of both the electrical and mechanical boundary conditions, which may vary locally as a function of sample geometry[132] or defect population.[133, 127]

Point,[134, 135] line,[136, 137, 138] and planar[139] defects all act as pinning centers for domain wall motion, leading to nonlinearity and hysteresis in the dielectric and piezoelectric response at sub-switching excitation fields.[140, 141] Knowledge of the local piezoelectric nonlinearity is extremely valuable for ferroelectric films which often operate in the nonlinear regime due to their small thickness.

Investigation of ferroelectric phenomena at the nanometer length scale has become accessible through the use of piezo-response force microscopy (PFM).[142, 143, 144] PFM can provide information on local domain structures, domain wall interactions with defects, domain dynamics, built-in electric fields, surface potential.[145, 138, 146, 147, 148] PFM measurements have established experimentally that dislocations, defect dipoles, 90˚ domain walls, grain boundaries, and point defects limit ferroelectric domain wall motion through local electric and elastic fields.[133, 149, 150, 138, 151]

The quantitative extent that pinning centers, introduced from film patterning, limit the extrinsic contribution to the piezoelectric response of the material at a sidewall is unknown. Therefore, exploring the influence of these pinning centers on local nonlinear domain wall motion in patterned features is necessary to understand how to maximize the piezoelectric response for future MEMS devices. This work aims to understand the influence of patterning approaches on the local piezoelectric properties, particularly near feature sidewalls through the implementation of a band excitation (BE) PFM method[152, 153, 154, 155] which allows for higher sensitivity PFM measurements with less influence from topographical crosstalk.[156] Structural information through the use of transmission electron microscopy (TEM) in conjunction with the local piezoelectric response probed with BE-PFM will be compared to global dielectric and ferroelectric properties in an attempt to provide a link between local and global functional properties of patterned ferroelectric films.

5.2 Experimental Procedure

5.2.1 *Film Patterning*

The preparation of the 2-methoxyethanol-based (2-MOE) $PbZr_{0.52}Ti_{48}O_3$ (PZT) solutions was described in detail by Wolf and Trolier-McKinstry. [60] Continuous films were prepared from 0.4 M PZT 115/52/48 solutions on Pt(111)/Ti/SiO_2/Si(100) wafers (Nova Electronic Materials) by spin-coating layers at 1500 rpm for 30 sec. After each spin-coating step, the sample was subjected to a two-step pyrolysis: 225 °C for 1 min followed by 400 °C for 1 min. The film was then crystallized at 650 °C for 1 min in oxygen in a Modular Process Technology Corporation RTP-600S Rapid Thermal Annealing Furnace (RTA). The process was repeated 11 times until the desired thickness of 1.02 μm was reached. A top electrode was sputter deposited (CMS-18 Sputter System, Kurt J. Lesker) over the PZT layer. A 30 nm titanium adhesion layer was sputtered, at room temperature using a power of 200 W, a bias of 460 V, a current of 0.47 A, a deposition pressure of 2 mTorr, and an Ar flow rate of 8 sccm, for 300 s, as an adhesion layer between the Pt and the PZT. Without breaking vacuum, a 50 nm Pt top electrode was sputtered at room temperature using a power of 200 W, a bias of 580 V, a current of 0.34 A, a deposition pressure of 2.5 mTorr, and an Ar flow rate of 11 sccm, for 210 s.

The inverse design of the desired features was deposited onto the Pt bottom electrode by patterning of SPR 3012 (Shipley Megaposit, Dow) photoresist, which was spun onto the wafers at 4000 rpm for 45 s and soft baked at 95 ˚C for 60 s. The exposure was carried out using a wafer stepper (Model 8500 DSW, GCA) with 365 nm light and a power density of 125 mW/cm^2 for 0.25 s. The resist was developed in CD-26 (Microposit MF, Dow) for 1 min. The surface was cleaned with an oxygen plasma ash (M4L Plasma System, Metroline) for 180 s, utilizing a power of 300 W, a chamber pressure of 400 mTorr, and a 100 and 50 sccm gas mixture of O_2 and He, respectively. Ni was then electroplated into the photoresist mold. This was done using a $Ni(SO_3NH_2)_2$ solution (Ni Sulfamate RTU, Technic Inc.) and a pulse power supply (DuP 10-1-3, Dynatronix). The bath was held at room temperature and mixed at 500 rpm with a forward current of 0.612 A, a reverse current of 0.061 A, a forward on time of 1 ms, a forward off time of 3 ms, a forward duration of 5 ms, a reverse on time of 0.3 ms, reverse off time of 0.5 ms, and a reverse duration of 0.8 ms. The Ni deposition rate was 40 nm/min with a final thickness of 700 nm. The photoresist was removed after the deposition of the electroplated Ni by immersion into an ultrasonic bath of PRS 3000 (J.T. Baker) at 60 ˚C for 1 hr. This was followed by an oxygen plasma ash (M4L Plasma System, Metroline) for 600 s, at the same conditions previously described.

The dry etching of the exposed Pt/Ti/PZT layers was performed at 20 ˚C with an inductively coupled plasma (ICP) reactive ion etch (RIE) (Speeder 100 Oxide Etcher, Alcatel) using a single etch chemistry as described in Table 5-1. Following the etch, the Ni hard mask was removed by immersion of the wafer into an ultrasonic bath of Ni Etchant TFB (Transene Company, Inc.) at 40 ˚C for 10 min, followed by an immersion into an ultrasonic bath of ACT 935 UP (Air Products and Chemicals, Inc.) at 40 ˚C for 1 hr.

Table 5-1. Summary of the etching conditions used on Pt/Ti/PZT stack.

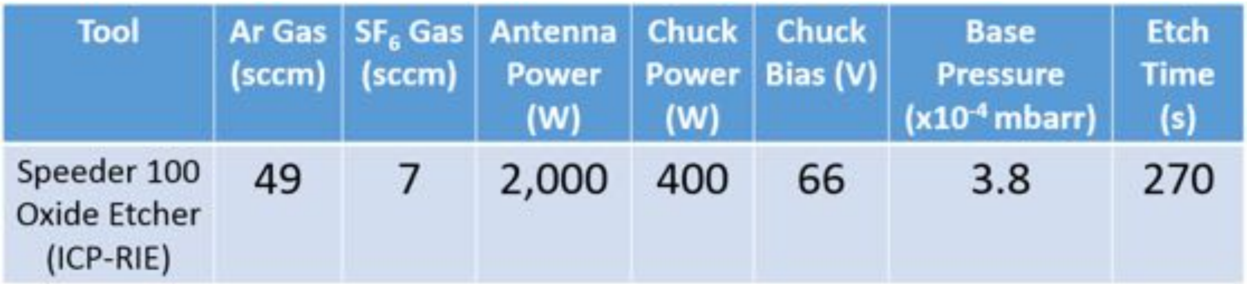

Tool	Ar Gas (sccm)	SF_6 Gas (sccm)	Antenna Power (W)	Chuck Power (W)	Chuck Bias (V)	Base Pressure ($\times10^{-4}$ mbarr)	Etch Time (s)
Speeder 100 Oxide Etcher (ICP-RIE)	49	7	2,000	400	66	3.8	270

The features intended for printed PZT were defined by a 1 μm thick negative photoresist (NFR-105G, JSR Micro) mask spun on top of a 4 in Si wafer at 3000 rpm for 35 sec and baked at 100 ˚C for 60 sec. The resist was exposed using a contact mask aligner (MA/BA6, Suss MicroTec) for 30 s with a UV lamp intensity of 8 mW/cm^2. The resist was developed in CD-26 (Microposit MF, Dow) for 1 min. The surface was cleaned with an oxygen plasma ash (M4L Plasma System, Metroline) for 60 s, as described previously. The silicon was etched 1.1 μm deep using a deep reactive ion etch (DRIE; Speeder 100 Silicon Etcher, Alcatel), as described in Table 3-1, for 150 sec. The photoresist was removed by immersion in a heated, ultrasonic bath of Remover-PG (MicroChem) at 60 ˚C for 60 min. A chemical diffusion barrier layer was created by atomic layer deposition (ALD) of HfO_2 (ALD 150 LE, Kurt J. Lesker) on the patterned Si features. The deposition occurred at 200 ˚C with a chamber pressure of 0.72 Torr. The reactant pulse time for H_2O and tetrakis(ethylmethylamino)hafnium (TEMAH) was 0.03 and 0.15 s respectively, with a purge time of 10 s between each pulse. These cycles were repeated 309 times to grow an amorphous 30 nm thick HfO_2 layer[‡‡] which was crystallized with a 700 ˚C heat treatment in an O_2 ambient for 1 min. A bottom electrode was sputter deposited (CMS-18 Sputter System, Kurt J. Lesker) over the HfO_2 layer. A 30 nm titanium adhesion layer and a 125 nm Pt bottom electrode were sputtered at room temperature as described previously.

Bilayer polymer stamps were made as described elsewhere.[87] A polyurethane (PU) layer was ultraviolet (UV) cured on top of a flat Si wafer with no patterned features. The stamp surface was cleaned prior to printing by oxygen plasma ashing (M4L Plasma System, Metroline) for a duration of 5 min, as previously described. The PZT precursor solutions were spun onto polymer

---

[‡‡] It was subsequently found that thicker HfO_2 barrier layers were preferable. Thus, a 60 nm HfO_2 barrier layer was utilized in Chapter 4 in work performed subsequently to Chapter 5.

stamps at 3000 rpm for 30 s. The alignment and printing of the PZT solutions onto patterned wafers was performed by hand. The liquid precursors were dried at 225 °C for 3 min followed by 400 °C for 3 min and crystallized at 650 °C for 1 min. Subsequently, the fired film was printed with a new PZT layer and heat-treated in the same manner. This process was repeated 17 times until the desired thickness of 1.06 μm was achieved.

Pt top electrodes were deposited on the PZT features using a lift-off process. An electron beam resist (ZEP520A, ZEONREX Electronic Chemicals) was spun on top of the printed PZT features at 4000 rpm for 45 s. The resist was baked at 180 ˚C for 180 s. The resist was patterned via electron beam lithography (EBPG 5200, Vistec) using a beam current of 40 nA, a dose of 365 $\mu C/cm^2$, an aperture size of 400 μm, and a beam step size of 25 nm. The resist was developed in N-amyl acetate for 180 s, immersed into an isopropyl alcohol (IPA) bath for 60 s, and rinsed in DI water. A Ti/Pt top electrode was deposited via evaporation (Semicore Equipment Inc.) at room temperature. 10 nm of Ti was deposited at 0.5 Å/sec at a base pressure of 2.9×10^{-6} Torr. Without breaking vacuum, 30 nm of Pt was deposited at 0.5 Å /sec at a base pressure of 1.72×10^{-6} Torr. A 1 h wait step was performed halfway through the Pt deposition to avoid over-heating of the resist. The photoresist was removed by immersion in a heated, ultrasonic bath of Remover-PG (MicroChem) at 60 ˚C for 60 min.

5.2.2 *Structural Characterization*

X-ray diffraction (XRD) scans were performed at room temperature with a powder incidence configuration with Cu K_α radiation (X'Pert Pro MPD, PANalytical). The surface morphology of the deposited films as well as the physical dimensions of the printed and etched features were characterized with a field-emission scanning electron microscope (FESEM; LEO 1530, Gemini). Film thicknesses and etch depths were determined using a surface contact profilometer (Alpha-Step 500, Tencor Instruments). The crystal structure and quality were investigated locally using a dual aberration corrected configuration scanning/transmission electron microscope (S/TEM; Titan3 62 60-300, FEI Company) operated at 200 kV. Collection of characteristic X-rays allowed elemental mapping via Energy Dispersive Spectroscopy (EDS), which was performed in STEM mode with four Silicon Drift Detectors (SDD) (SuperX, Bruker Corp.). EDS mapping required an acquisition time ~10 min. These TEM experiments were performed in collaboration with Ke Wang.

5.2.3 *Electrical Characterization*

An LCR bridge (4294A Precision LCR, Hewlett Packard) was utilized, from 0.1 to 100 kHz at a drive amplitude of 0.03 V, to measure relative permittivity and loss tangent of the ferroelectric films. The LCR bridge was also used to make dielectric Rayleigh measurements by measuring capacitance as a function of AC voltage at 1 kHz to determine the dielectric nonlinearity of the sample. A Multiferroics Test System (Radiant Technologies) was used to measure the P-E minor loops of the ferroelectric films at 1 kHz in order to compare to the dielectric Rayleigh data. All global electrical measurements applied the excitation signal to the bottom electrode and the return was the top electrode in order to minimize noise. Films were poled at 3Vc for 15 min in the direction which minimizes back-switching of the polarization,[§§] (e.g. parallel to the preferred polarization direction) for all electrical measurements which required poled samples.

[§§] V_c of Etched Films: +6.2 and -5 V; V_c of Printed Films: -6.5 and +5 V. (High was bottom electrode and low was top electrode. Note PFM leads were reversed so poling was reversed)

5.2.4 *Band Excitation Piezo-response Force Microscopy*

For PFM data, samples were mounted into a ceramic package (CCF04002, Spectrum Semiconductor Materials, Inc.) on top of a silicon spacer to bring the top of the sample flush with the top of the package. This allowed PFM tip access to the material without risk of damage by running into the package sides. A wirebonder (iBond 5000-Wedge, Kulicke & Soffa Industries, Inc.) was used on the RIE samples to gold wirebond from the sample top electrodes to the package in order to make electrical connection. The top electrodes for the printed samples were sufficiently small (2 x 2 μm) to be driven with the conductive cantilever. Therefore, no wire bonding was needed.

BE-PFM (Cypher, Asylum Research, Inc.) measurements of the local piezoelectric nonlinear response were performed at the Center for Nanophase Materials Science at Oak Ridge National Laboratory as described previously.[146, 157, 158, 159, 160] The cantilever tips (PPP-EFM-50, NanoSensors) were platinum coated silicon tips. The samples were poled at $3V_c$ for 15 min in the opposite direction to any imprint in the material. The top electrode and the conductive tip were both driven with the same excitation function while the bottom electrode was grounded. The local nonlinearity of the films were measured using global excitation of the material though the use of large area electrodes at least 30 min after poling. The local displacement was detected through the PFM cantilever. The nonlinear BE-PFM measurements were acquired over a 2D spatial grid on top of the global electrode at a specific amplitude and phase content over a defined frequency interval (100 kHz) yielding a multi-dimensional data set of responses as a function of position, frequency, and excitation voltage. Each BE-PFM map took approximately 4hrs to collect. The cantilever tip vertical displacement was fit to a simple harmonic oscillator (SHO) model[146] as a function of the excitation frequency and amplitude, and the local nonlinear response was then calculated from the tip displacement at the resonance frequency.[161]

The amplitude of the response (A_{max}) is a polynomial function of the applied voltage (V_{ac}) as described in Equation 5-1.[146] The measured amplitude response (A_{max}) is proportional to the surface displacement (h) of the sample and the transfer function of the cantilever (β), as shown in Equation 5-2. Differentiation of this equation with respect to V_{ac} results in Equation 5-3, which is analogous to the Rayleigh law in Equation 5-4, where α is the irreversible extrinsic contribution and $d_{33,init}$ is the reversible extrinsic and intrinsic contribution to the longitudinal piezoelectric coefficient ($d_{33,f}$). Therefore, $a_2 \propto d_{33,init}$ and $2a_3 \propto \alpha$, which results in Equation 5-5, where t is the film thickness. This yields a quantitative ratio of the irreversible to reversible contribution to the converse piezoelectric coefficient.

$$A_{max} = a_1 + a_2 V_{ac} + a_3 V_{ac}^2 \qquad (5\text{-}1)$$

$$A_{max} = \beta h \qquad (5\text{-}2)$$

$$\beta d_{33} = \beta a_2 + 2\beta a_3 V_{ac} \qquad (5\text{-}3)$$

$$d_{33} = d_{33,init} + \alpha E_{ac} \qquad (5\text{-}4)$$

$$\frac{\alpha}{d_{33,init}} = \frac{2ta_3}{a_2} \qquad (5\text{-}5)$$

The intent of local nonlinearity measurements with PFM cantilevers is to measure only the material response. However the actual measured response is a combination of both material response and cantilever dynamics. To minimize errors associated with the tip-cantilever interactions, an excitation electric field that combines two different waveforms was employed: 1) The chirp waveform utilizes a phase variation of the excitation frequency over a comparatively longer period of time. An increase in frequency over time is a chirp up signal while a decrease in frequency is a chirp down signal. 2) A pure sinc function utilizes no phase variation to excite the frequency band over a very short time.[162] Figure 5-1 displays varying signals with varying chirp character. The optimization of the excitation function will be discussed in section 5.3.4.

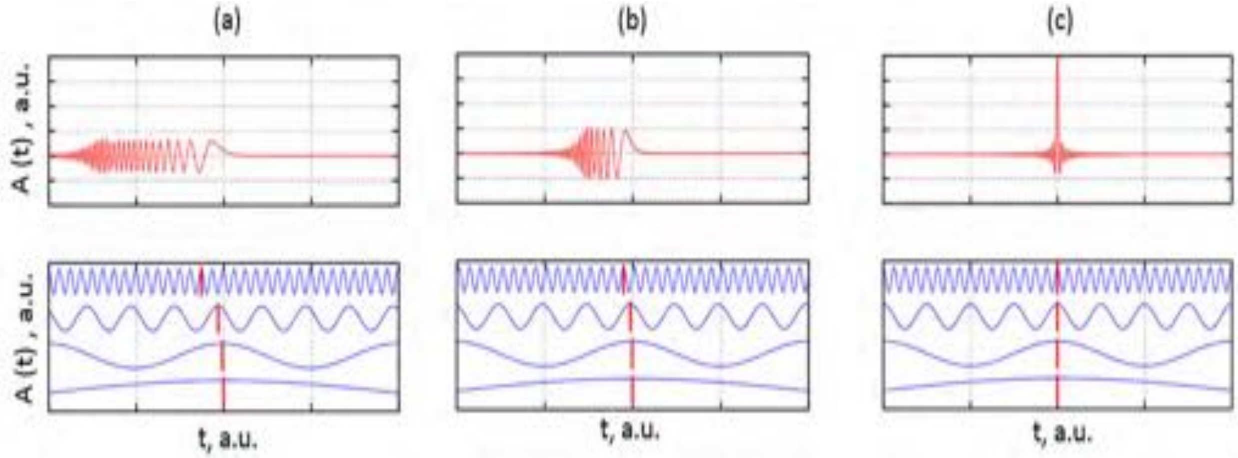

Figure 5-1. (Bottom Row) Four different sine waves (blue lines) with four different frequencies. The vertical line highlights the phase shift relative to each of the four sine waves. (Top Row) Combining these four sine waves yields a signal with varying degrees of chirp character. (a) The signal with the most phase variation is the chirp signal. (b) The signal with only slight phase variation is a mixture of chirp and sinc signals. (c) The signal with no phase variation is the sinc signal.

5.3 Results and Discussion

5.3.1 Global Structural Characterization

In order to examine the influences of patterning on domain wall motion in ferroelectric features produced by different methods, it is imperative to have an understanding of the film structure and microstructure. Therefore the crystallization of both dry etched and printed PZT films was investigated. The XRD scans, shown in Figure 5-2 (a), of both types of films show the perovskite PZT crystal structure. No evidence of pernicious non-ferroelectric phases (i.e. pyrochlore) or conductive phases (i.e. PbO) appears in either set of XRD data.

Dry etching of PZT to pattern features is done with a continuous layer of PZT deposited onto a uniform substrate. The PZT films used for dry etching in this work is displayed in Figure 5-2 (b). The perovskite grains have a grain size ~100nm. No porosity or secondary phases such as pyrochlore or lead oxide were observed, confirming the XRD scan.

Printing PZT solutions directly onto pre-patterned substrates was performed in order to create PZT features with steep sidewalls to mimic the feature shape of PZT patterned through dry etching. Initially, the Si wafer was patterned, followed by deposition of a conformal ALD HfO_2 barrier layer, and platinum to act as the bottom electrode in accordance with the process described in Figure 4-14 of section 4.3.3. As is exhibited in Figure 5-2 (c), the perovskite layer nucleated as rosette grains, which was analogous to the grain formation shown in Figure 4-12 of Chapter 4. In this work, few perovskite grains nucleated in films prepared this way. This was found to be due, in part, to insufficient thickness of the HfO_2 barrier layer. The small thickness of the barrier layer may have allowed sufficient lead to diffuse through the bottom electrode to limit nucleation of the perovskite phase. The limited number of nuclei grew laterally upon each successive printing layer and crystallization step until impingement of the grains was achieved. This resulted in extremely large grains (> 1 μm) with a finite amount of residual secondary phase present between grains, which was not detected in the XRD scan. The cross-section of the film, exhibited in Figure 5-2 (d), displays a small amount of trapped pyrochlore at each crystallization interface as well as a small amount of porosity, which are primarily localized at the grain boundaries between rosette grains. In the future preparation of samples with thicker barrier layers is recommended.

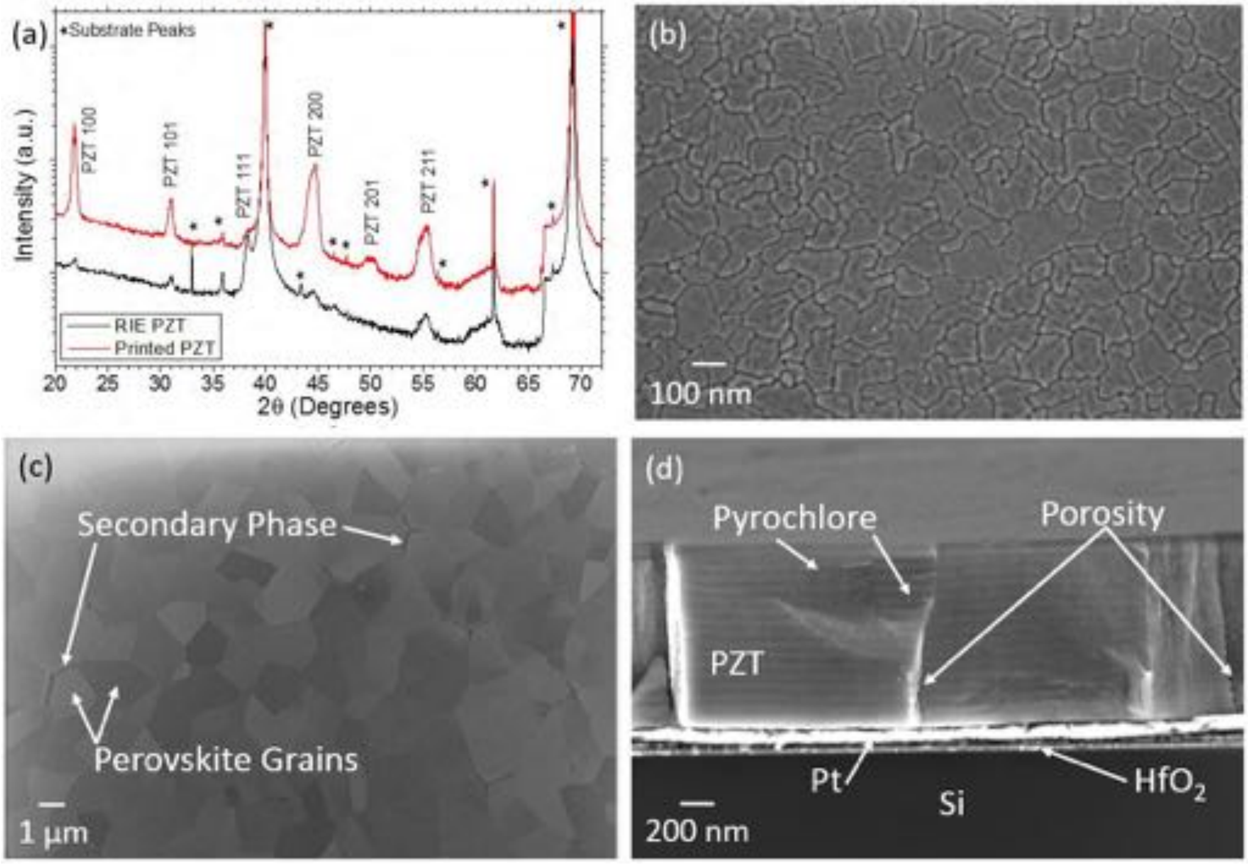

Figure 5-2. (a) XRD scans of dry etched (black) and printed (red) PZT. (b) SEM micrograph of continuous PZT crystallized on a 4 in Pt-coated Si wafer before the dry etching step. (c) Top down and (d) cross-sectional SEM micrographs of PZT printed onto a pre-patterned substrate.

5.3.2 Global Domain Wall Mobility

In order to determine if domain wall motion is affected by the sidewall patterning process, the global dielectric Rayleigh response was compared to the local piezoelectric Rayleigh response of the patterned features. The RIE etched PZT was patterned into features with varying aspect ratios and etch perimeter lengths to examine the role of sidewall damage on the functional properties of the material. Figure 5-3 (a) displays the etch designs used in this work. The largest patterns were circular features with a diameter of 627 ± 1.5 μm. The arm structures have a bond pad with a central bus structure, along with smaller arms which protrude perpendicular to the bus. In this work, all bond pads and central bus arms were held at constant sizes while 5 ± 0.1 and 10 ± 0.1 μm features were used as the protruding arm widths. A third pattern was created where only the bond pad and the central bus arm were present. This structure allowed for the subtraction of the bond pad and central bus arm response from the total arm structure, resulting in measured functional properties from only the 5 or 10 μm features while limiting the effect of parasitic capacitance from the larger structures.[163]

The global dielectric response from the printed PZT was measured using a large circular electrode on a continuous area of printed PZT, as displayed in Figure 5-3 (b). The diameter of the feature was 201.5 ± 0.5 μm. This electrode size was sufficiently large to minimize parasitic capacitances which could alter Rayleigh measurement as well as polarization values. However, this results in the electrode probing both perovskite PZT and secondary phases, as described in Figure 5-2 (c). Thus, the global electrical measurements were altered from the perovskite material response.

The printed 200 μm electrodes exhibited a relative permittivity of 983 ± 3, loss tangent of 1.5 ± 0.09 %, remanent polarizations of 20.4 ± 0.6 $\mu C/cm^2$, and coercive fields of 43 ± 1 kV/cm, as seen in Figure 5-3 (c) (green line). The large 600 μm diameter RIE features dielectric and ferroelectric properties revealed a relative permittivity of 827 ± 7 with a loss tangent of 1.8 ± 0.06 %, along with remanent polarizations of 23.8 ± 0.7 μC/cm^2, and coercive fields of 44.6 ± 1.3 kV/cm, as seen in Figure 5-3 (c) (orange line). The loops are well saturated, however Figure 5-3 (d) reveals pinching of the initial RIE loops (black line) which is indicative of the presence of randomly oriented defect dipoles in the film. This figure also shows that after poling the defects in the film aligned with the electric field, resulting in an imprinted hysteresis loop (red line).

The dielectric and ferroelectric properties of printed features in section 2.3.4 can be recalled to highlight the differences the microstructure has between the two printed sample sets. The 1 μm thick printed samples from Chapter 2 exhibited a relative permittivity of 1050 ± 10, loss tangent of 2.0 ± 0.4 %, remanent polarization of 28 ± 0.3 μC/cm^2, and a coercive field of 50 ± 1 kV/cm. Both the relative permittivity and the remanent polarizations of the printed films with rosette grains are reduced by the residual secondary phases.

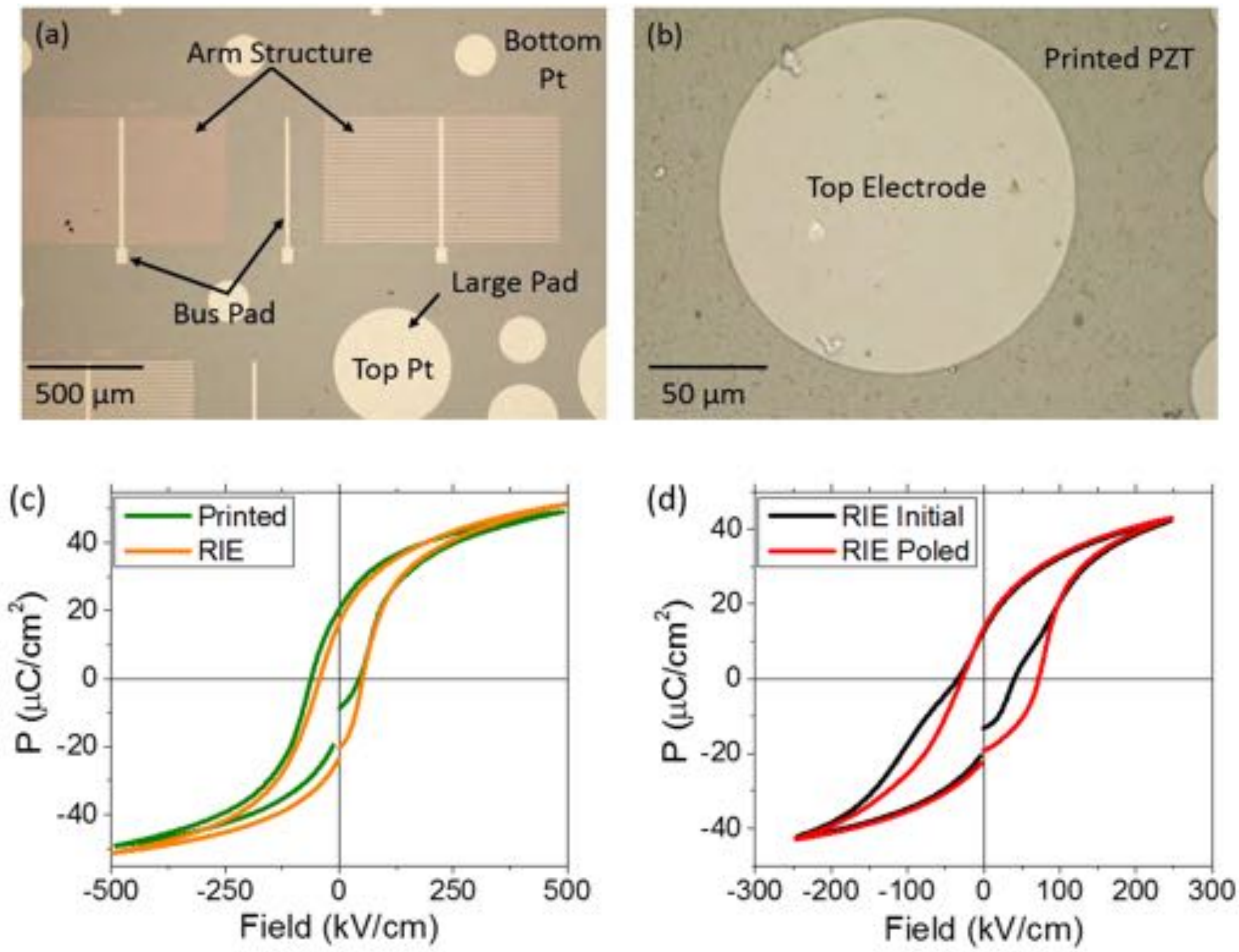

Figure 5-3. (a) Optical image showing examples of the various dry etched patterns used in the global electrical measurements. (b) Optical image exhibiting the capacitor configuration used to measure the global electrical properties in the printed PZT samples. (c) PE loop of printed 200 µm diameter electrode (green) in comparison to a RIE 625 µm diameter electrode (orange). (d) PE loops of RIE 5 µm feature before (black) and after (red) poling.

The global dielectric Rayleigh parameters of the material were measured to determine the domain wall contribution to the dielectric response. The films were poled as described previously, and the field dependent relative permittivity was measured to determine the limits of the Rayleigh regime of each sample. Figure 5-4 shows that the Rayleigh regime for the RIE and printed samples extend up to ~30 and 35 kV/cm respectively. Therefore, subsequent field dependent relative permittivity sweeps used in the determination of Rayleigh parameters for all samples were limited to a maximum of 25 kV/cm.

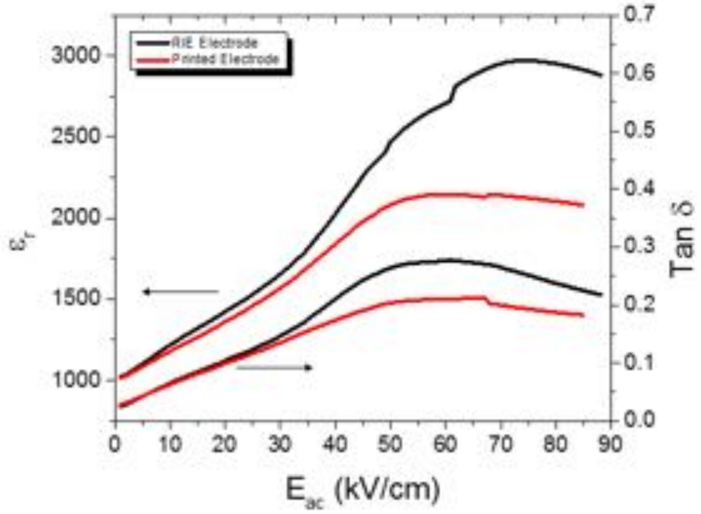

Figure 5-4. Field dependent relative permittivity scan of poled PZT 52/48 films. The Rayleigh regime of the dry etched (black line) and printed (red line) sample extends up to ~30 kV/cm (2.9 V) and ~35 kV/cm (3.7 V).

The field dependent relative permittivity sweeps were performed on multiple electrodes for 5 µm arm, 10 µm arm, central bus arm, and large pad RIE samples as well as the printed PZT samples. The samples were measured after poling. They were then aged for 4 hours, 1 day, and 3 months to probe how patterning influences the short term and aged behaviors. As an example, Figure 5-5 (a) exhibits the field dependent relative permittivity of the 5 µm arm RIE etched samples, while Figure 5-5 (b) displays the field dependent relative permittivity of the 200 µm diameter electrode on continuous printed PZT. The data sets were fit to a linear relationship to determine the reversible (i.e. intercept) and irreversible (i.e. slope) Rayleigh parameters.

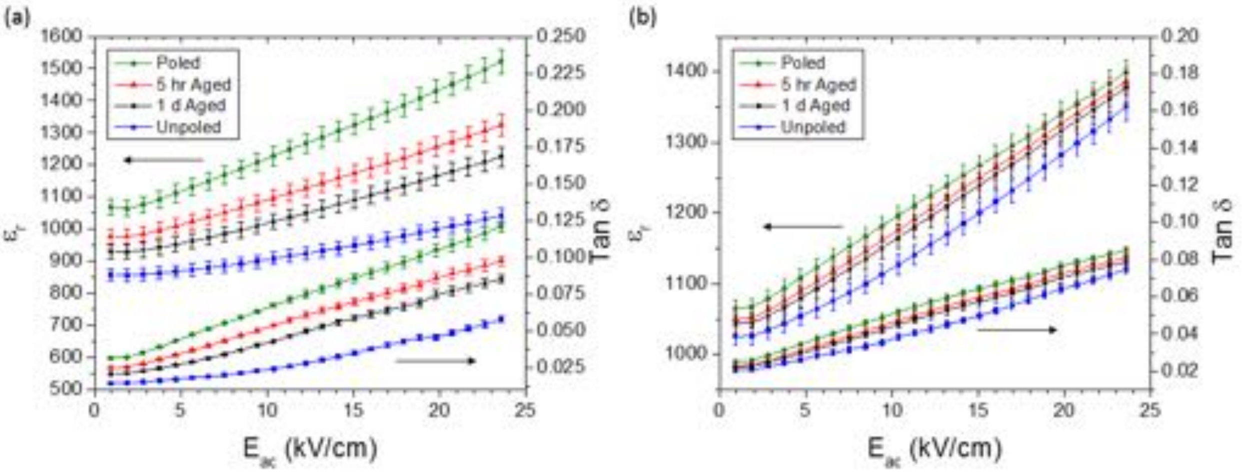

Figure 5-5. Aging of the field dependent relative permittivity of poled PZT 52/48. (a) RIE 5 µm lateral features exhibit a larger degree of aging of the Rayleigh behavior in comparison to (b) printed PZT. The error bars represent error propagation calculations between multiple electrodes.

The fitted Rayleigh parameters ε_{init}, α, and $\alpha/\varepsilon_{init}$ are plotted as a function of time in Figure 5-6 and summarized in Table 5-2. Figure 5-6 (a) shows the maximum ε_{init} is observed immediately after poling for all samples. To facilitate comparison, the data were normalized to the ε_{init} value of that feature size immediately after poling in Figure 5-6 (d). The aging rate is determined by a linear fit to each data set. A summary of the aging rates determined is shown in Table 5-3. It was found that the aging rates for ε_{init} of the printed samples was -1.2 %/decade. Higher aging rates were observed for the etched samples. Moreover, as the etching perimeter of the PZT features increased, the aging rates increased by 75 % from -3 to -5.2 %/decade.

Figure 5-6 (b) shows that the maximum in α was observed immediately after poling for the etched samples. This contrasts with the data for the printed films, where α *increases* slightly after poling. The normalized aging data in Figure 5-6 (e) suggest that either irreversible domain wall motion or the density of mobile domain walls is suppressed as the etched perimeter of the PZT features increases in length; the aging rate increased from -9.4 to -14.6 %/decade.

Figure 5-6 (c) shows a maximum in the ratio of irreversible/reversible Rayleigh parameters for the etched samples after poling. The normalized aging rates of the $\alpha/\varepsilon_{init}$ ratio (Figure 5-6 (f)) increases with etch perimeter lengths from -7 to -11.6 %/decade. In contrast, the printed films show an increase in the irreversible/reversible ratio with time after poling.

All of these data suggest that the RIE process utilized decreases either the domain wall density or domain wall mobility; the larger the perimeter, the more marked the decrease. The fact that the aging rates also increase implies that the etching imparts pinning centers at the sidewalls of the features which limit both reversible and irreversible domain wall motion. This is in agreement with Soyer *et al*.[17] and Liang *et al*.[164] who reported domain wall pinning of dry etched PZT films using a fluorinated gas chemistry along with a high energy Ar bombardment component. Etching damage was also examined with global electrical measurement by both Kim *et al*.[18] and Kang *et al*.[165] which noted decreased remanent polarizations in films dry etched with a chlorinated/fluorinated gas mixture. In addition, Lee *et al*.[19], Chung *et al*.[14], and Pan *et al*.[166] observed increases in the coercive fields as well as imprint in films etched with chlorinated/fluorinated gas mixture.

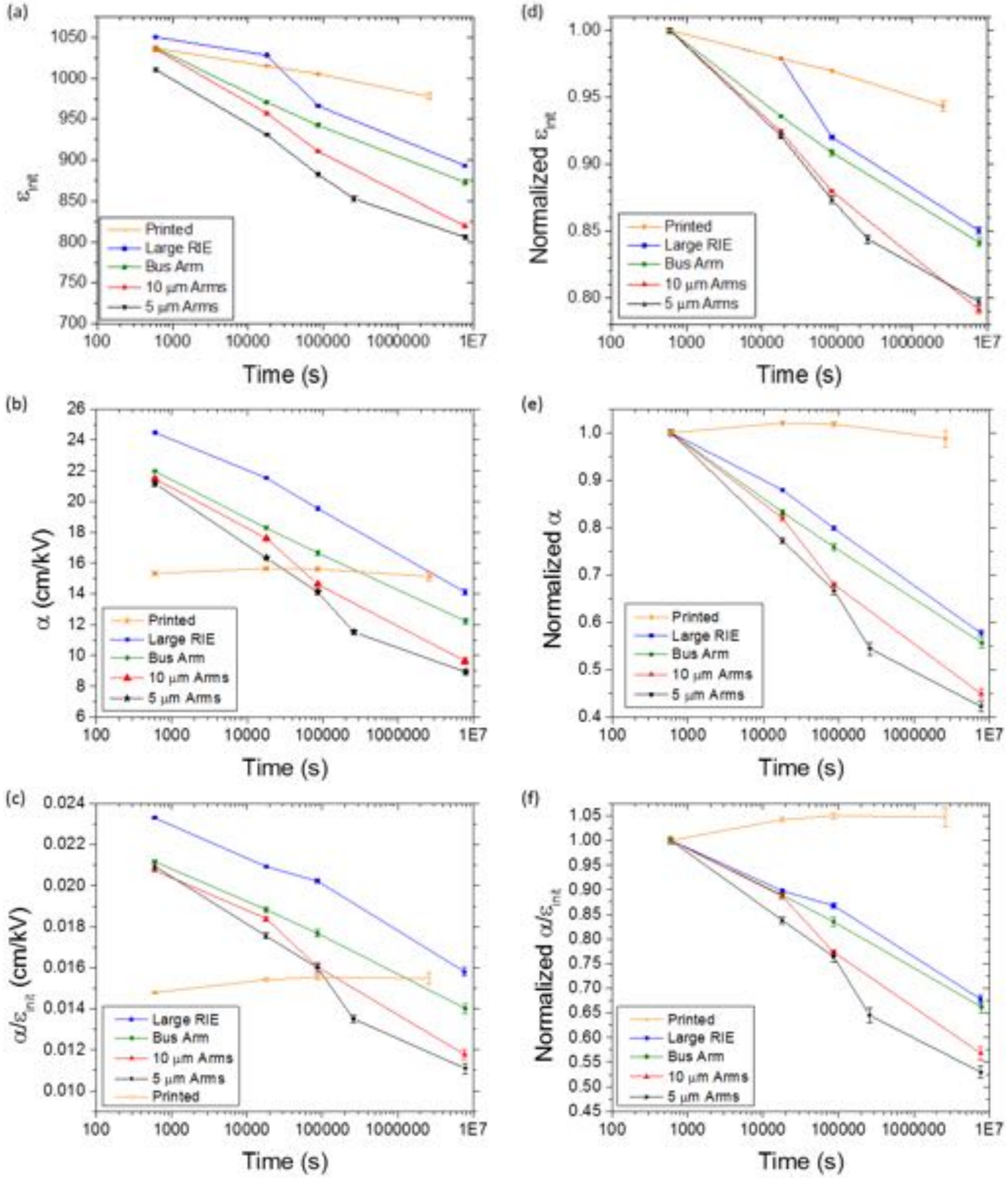

Figure 5-6. Time dependent (a through c) Rayleigh and (d through f) normalized Rayleigh parameters for large pad RIE (blue line), bus arm (green line), 10 µm arm (red line), 5 µm arm (black line), and printed PZT (orange line) electrodes. The error bars represent fitting errors.

Table 5-2. Summary of the poled and aged Rayleigh paramters for both RIE and printed PZT (errors from fitting).

Sample	Time Aged After Poling	ε_{init}	ε_{init} error	α (cm/kV)	α error (cm/kV)	$\alpha/\varepsilon_{init}$ (10^{-3} cm/kV)	$\alpha/\varepsilon_{init}$ error (10^{-3} cm/kV)
Printed	600 s	1037	0.4	15.33	0.03	14.79	0.03
	4 h	1015	0.7	15.65	0.05	15.42	0.05
	1 d	1005	1.0	15.62	0.08	15.53	0.08
	1 m	978	3.5	15.14	0.3	15.49	0.28
Large RIE	600 s	1050	0.6	24.48	0.04	23.31	0.04
	4 h	1028	0.8	21.52	0.02	20.93	0.06
	1 d	966	1.3	19.54	0.02	20.22	0.11
	3m	893	2.3	14.12	0.02	15.8	0.22
BUS Structure	600 s	1037	1.1	21.96	0.08	21.17	0.08
	4 h	971	1.4	18.28	0.10	18.83	0.11
	1 d	943	2.4	16.66	0.18	17.68	0.19
	3 m	873	2.9	12.24	0.21	14.02	0.24
10 µm Arms	600 s	1035	0.6	21.48	0.05	20.74	0.05
	4 h	957	1.5	17.60	0.11	18.39	0.12
	1 d	911	1.3	14.61	0.09	16.04	0.10
	3 m	819	2.6	9.65	0.19	11.78	0.23
5 µm Arms	600 s	1010	1.9	21.16	0.14	20.94	0.14
	4 h	931	1.7	16.34	0.13	17.55	0.14
	1d	882	2.6	14.12	0.19	16.00	0.22
	1 m	853	2.9	11.52	0.14	13.51	0.16
	3 m	806	2.9	8.94	0.21	11.09	0.26

Table 5-3. Summary of the aging rates of ε_{init}, α, and $\alpha/\varepsilon_{init}$ ratios. The error of each value represents fitting errors.

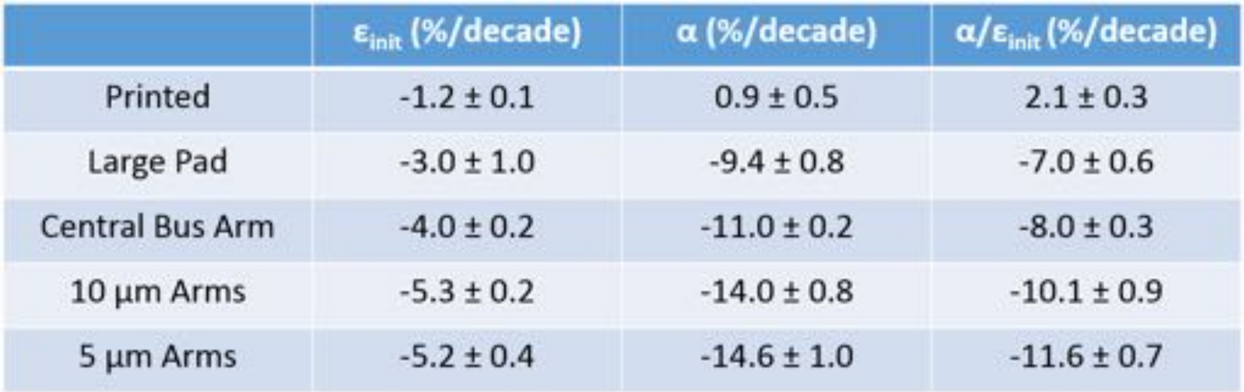

	ε_{init} (%/decade)	α (%/decade)	$\alpha/\varepsilon_{init}$ (%/decade)
Printed	-1.2 ± 0.1	0.9 ± 0.5	2.1 ± 0.3
Large Pad	-3.0 ± 1.0	-9.4 ± 0.8	-7.0 ± 0.6
Central Bus Arm	-4.0 ± 0.2	-11.0 ± 0.2	-8.0 ± 0.3
10 µm Arms	-5.3 ± 0.2	-14.0 ± 0.8	-10.1 ± 0.9
5 µm Arms	-5.2 ± 0.4	-14.6 ± 1.0	-11.6 ± 0.7

The printed films show much lower aging rates than the etched samples with similar dimensions. This is expected since few, if any, significant pinning centers are incorporated into the material upon the printing process.[87] However, the printed films show significantly smaller irreversible Rayleigh coeffients in comparison to the etched films. This likely arises due to the material having a secondary phase that is present throughout the film which is both non-ferroelectric (and hence has no domain walls to move) and acts as an additional pinning center to domain wall motion. This defect in the material is not directly due to the printing process but the nucleation surface underneath the PZT, as shown in section 2.3.4. The 1 μm thick printed samples from Chapter 2 exhibited a ε_{init} of 1050 ± 25 and a α of 25 ± 3 cm/kV, while the printed films with rosette grains exhibit a ε_{init} of 978 ± 3 and a α of 15.5 ± 0.3 cm/kV. Both the reversible and irreversible Rayleigh parameters of the printed films with rosette grains have decreased response in comparison to films printed on pristine Pt surfaces.

The irreversible domain wall motion suggested in the dielectric nonlinearity can be verified via minor hysteresis loops, to asses whether the behavior is really Rayleigh-like. The Rayleigh law state that the hysteresis in the minor loop polarization values at zero electric field is proportional to the irreversible Rayleigh coefficent (i.e. Equation 2-2).[76] To check this, minor hysteresis loops were measured at the same conditions as the Rayleigh measurements for printed and etched films. As an example, Figure 5-7 (a) exhibits the minor hysteresis loops of the 5 μm arm RIE etched samples; Figure 5-7 (b) displays the minor hysteresis loops of the printed PZT.

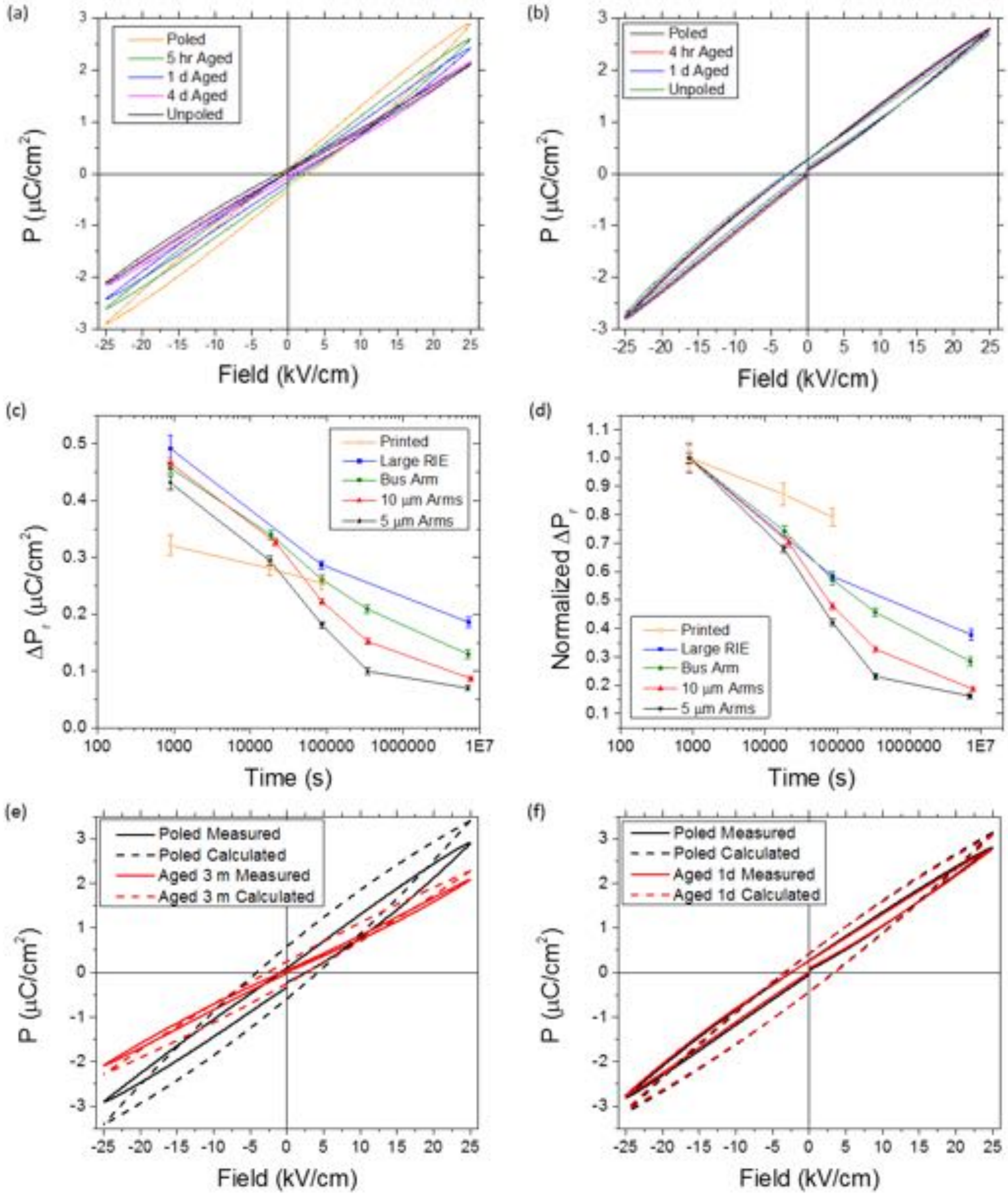

Figure 5-7. Minor hysteresis loops of poled (a) 5 μm RIE and (b) printed PZT 52/48. A comparison between all feature sizes of the (c) ΔP and (d) Normalized ΔP at 0 kV/cm (error bars represent error propagation calculations for capacitance, thickness, and area of multiple electrodes). A comparison between the measured (solid lines) and calculated (dashed lines) (via Rayleigh parameters) minor hysteresis loops for (e) 5 μm RIE and (f) printed PZT.

The difference in the polarization values at zero electric field (i.e. ΔP) was plotted as a function of time, as displayed in Figure 5-7 (c). The aging rates of the irreversible domain wall motion for each sample are compared to one another by normalizing each sample to the poled values, as exhibited in Figure 5-7 (d). The etched films display the same trends in irreversible domain wall motion and aging rates as was seen from the Rayleigh measurements.

The Rayleigh parameters from Figure 5-6 were used to calculate an ideal minor hysteresis loop (dashed lines); these were compared to the measured minor loops (solid lines) from Figure 5-7 (a and b). These calculations were performed according to Equation 5-6.[76]

$$P = \varepsilon_0(\varepsilon_{init} + \alpha E_{max})E \pm \varepsilon_0 \frac{\alpha}{2}(E_{max}^2 - E^2) \qquad (5\text{-}6)$$

It is clear that for the etched films, the minor hysteresis loops are better (but not well) described by the Rayleigh coefficients immediately after poling. On aging, however the minor loops collapse, and the Rayleigh law no longer as good of a descriptor. This is akin to hard PZT ceramics, where the disparity between the minor hysteresis loops and calculations based on the dielectric Rayleigh response suggest that distribution of restoring forces for domain walls cannot properly be described as Gaussian. [122] It is most likely that the distribution of pinning centers is arranged in a way that leads to a local internal bias field.[167] In the printed films, the minor hysteresis loops are not perfectly described by calculations based on the dielectric Rayleigh response, also suggesting that the domain wall motion cannot be described as Gaussian.

Nonetheless, the measured minor hysteresis loops are consistent with the observation that the irreversible domain wall motion in the printed films is lower than the etched films as seen in the Rayleigh measurements; however, the aging rate of the printed films shows a distinguishable variation over time which was not discernable in the Rayleigh data. The minor hysteresis loops show that the hysteresis decreases with time after poling. It can be concluded, based on the minor hysteresis loop data, that the domain wall mobility of the printed films does age, but at a much reduced rate in comparison to any of the etched features.

This work can be compared to Keech *et al*.[163] which also used Rayleigh parameters to quantify the degree of etch damage in various patterned ferroelectric feature sizes. A chlorinated/fluorinated gas mixture was utilized to etch ferroelectric lead magnesium niobate-lead titanate (PMN-PT) films into the same arm configuration used here in the PZT etching work. It was shown that the PMN-PT Rayleigh parameters increase with increasing etched perimeter length. The PZT features in this chapter do not show similar trends over similar feature sizes. The origin of this difference is unknown, but may correlate with the fact that PMN-PT is more susceptible to clamping (and hence declamping) than is PZT, due to the differences in elastic moduli.

Yang *et al*.[168] has used Rayleigh parameters to quantify the degree of etch damage in various ion-milled PZT feature sizes. The etch used in this work was due to physical bombardment of the film with Ar ions. It was shown that the Rayleigh parameters increased with decreasing feature width. Both the PMN-PT and ion-milled PZT samples were subjected to a post etching anneal in an oxygen environment, which has been shown to mitigate some of the damage introduced during dry etching.[165] This was also confirmed when the ion-milled PZT samples were aged, the Rayleigh parameters show a marked decrease with a decrease in feature size. This is analogous to the measurements displayed in Table 5-3 which shows that increased etching perimeter lengths yields increased aging rates for all Rayleigh parameters.

The PZT samples in this chapter were not annealed after etching in order to determine the maximum affect etching altered the functional properties of the ferroelectric material. In addition, the Ti adhesion layer used on the top electrode precluded the ability to anneal at elevated temperatures to avoid conversion of the metal to the insulating rutile structure.

5.3.3 Local Structural Characterization

The structure and microstructure of the material were also examined in proximity to patterned sidewalls through SEM and TEM. This provides direct insight into how the structure is altered through patterning processes, and therefore how the patterning should affect the functional properties.

In this work, PZT was patterned into 10 and 5 μm wide lines by both dry etching and printing. The dry etched samples were patterned after crystallization; therefore, the global microstructure of the patterned features (Figure 5-8 (a)) was identical to the microstructure of the continuous film shown in Figure 5-2 (b). The dry etched features were cross-sectioned and examined using low resolution TEM as displayed in Figure 5-8 (b). At this scale, the patterned features show no secondary phases through the thickness of the film, with minimal amounts of porosity.

The dry etching processes yielded features with ~70˚ sidewall angles alongside scalloping of the film at the top of every crystallization layer. The dry etch used in this work used a high physical bombardment component to the etch,[169] which removes etching residues from the sidewalls of the material during the course of the etch, leading to slightly lower sidewall angles.[170] The presence of scalloping is likely due to the gradient of Zr/Ti ratios in sol-gel deposited PZT films with Ti rich compositions at the bottom of each layer and Zr rich compositions segregating to the top for each crystallization step.[171] The etching gases chemically etch the sidewall surface as the dry etch progresses, which produces the scalloping. In addition, the Zr-O bond is weaker that the Ti-O bond in the perovskite structure,[172, 173] therefore the physical component of the etch may attack the Zr rich PZT more quickly.[170]

The local microstructure of the PZT printed on pre-patterned substrate features was investigated, as seen in Figure 5-8 (c). The microstructure of the patterned PZT was similar to the material crystallized away from the pre-patterned substrate features. A small number of rosette nucleation events began the crystallization of the PZT on top of the features. These grains grew laterally for each subsequent printing and crystallization step, leading to large grain sizes along with a limited amount of secondary phase present between some of the perovskite grains. The printed features were cross-sectioned and examined using TEM as displayed in Figure 5-8 (d). The patterned features show regions where secondary phases and porosity were limited. The printing processes also yielded features with sidewall angles exceeding 80˚.

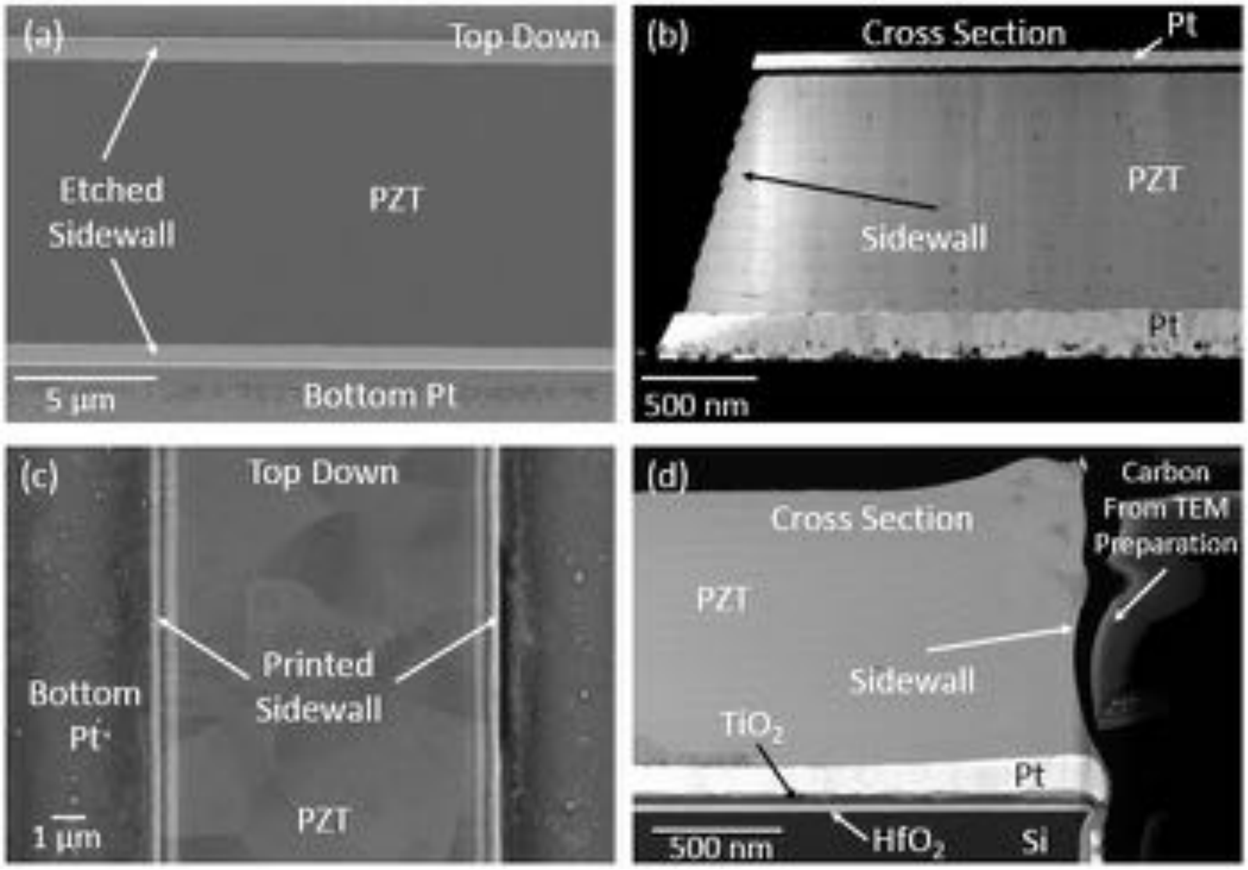

Figure 5-8. (a) Top down SEM and (b) cross-section TEM image of the 10 μm feature created by dry etching PZT. (c) Top down SEM and (d) cross-section TEM image of the 10 μm feature created by printing PZT.

Cross-sectional TEM allows for the local compositional and structural information to be collected near the sidewalls. Dry etched sidewalls were exposed to etching plasmas that have both high energy physical bombardment components and chemical etching components, either of which may alter the crystal structure of the material. Saad *et al*.[174] noted a 20 nm amorphous layer of $BaTiO_3$ upon patterning with a focused ion-beam. Lee *et al*.[19] also reported the creation of a 10 nm amorphous layer in RIE etched PZT films determined from cross-sectional TEM images.

The sidewalls of the dry etched PZT in this work (Figure 5-9 (a)) were investigated through the use of high resolution (HRTEM) and scanning (STEM) TEM, displayed in Figure 5-9 (b) and

(c) respectively. It was found that the lattice fringes of the perovskite phase were continuous to the edge of the features. Thus, the dry etch did not significantly alter the perovskite crystal structure in the immediate proximity to the patterned sidewall.

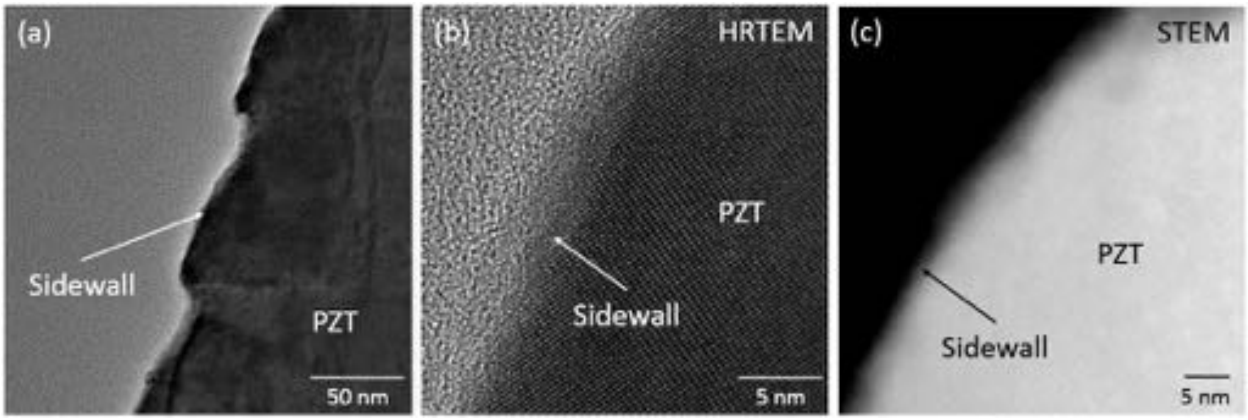

Figure 5-9. High magnification (a) bright field (BF) TEM, (b) HRTEM, and (c) STEM images of cross-sectioned, dry etched PZT (10 µm feature) in close proximity to the sidewall of the feature.

The sidewall of the PZT printed on top of pre-patterned substrates was also investigated through the use of HRTEM and STEM, as displayed in Figure 5-10. In this case, a secondary phase, which is ~ 2 nm thick, is clearly present along the surface of the sidewall. While the printed PZT along this surface did not experience any etching, the surface was exposed to the atmosphere over multiple crystallization excursions as the film was built up in thickness over multiple stamping cycles. Lead is volatile at the crystallization temperatures used in this work.[175, 176] This prolonged exposure time at crystallization temperatures may have caused sufficient Pb to be removed from the material to create the second phase.

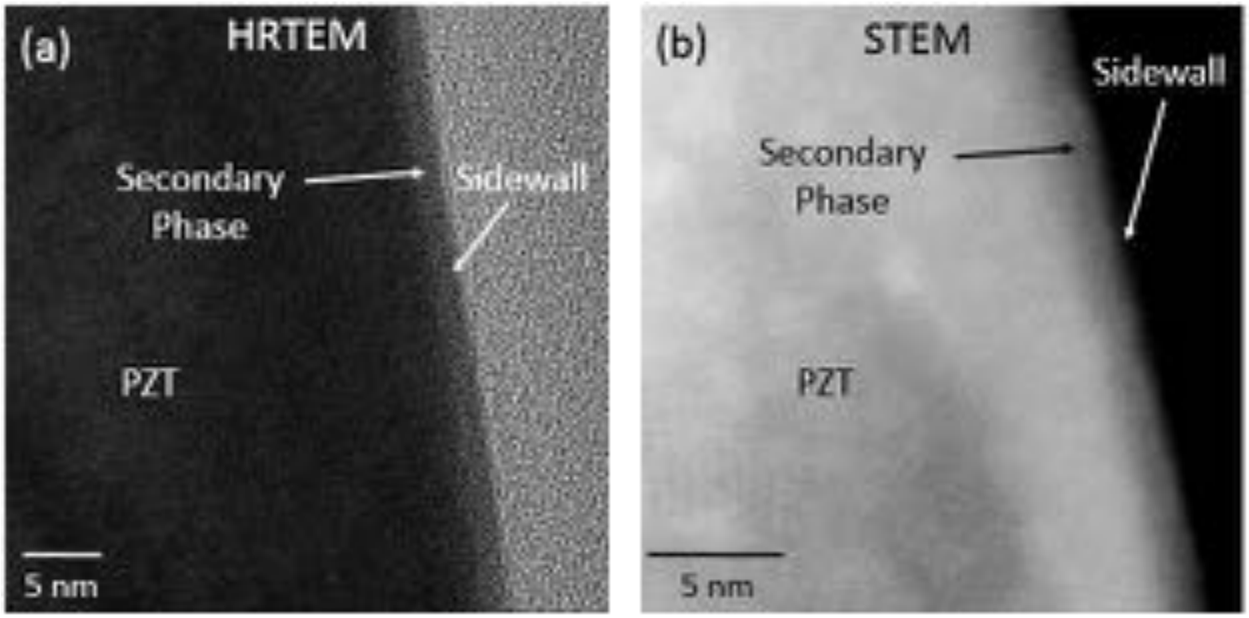

Figure 5-10. (a) HRTEM and (b) STEM images of cross-sectioned, printed PZT (10 µm lateral feature) in close proximity to the sidewall.

The compositional variation of the PZT features was investigated by mapping the concentrations of Pb, Zr, and Ti atoms as a function of distance from the patterned sidewall through EDS. Figure 5-11 exhibits EDS data near the side wall of the dry etched and printed PZT features. The EDS maps were kept as close to the edge of the sidewalls without the mapping area overlapping the open area beyond the sidewalls, as seen in the EDS scan area boxes in Figure 5-11 (a and b). The EDS map area was averaged vertically across the ~150 nm wide scan area to make a line scan (Figure 5-11 (c)) of how the concentrations vary as a function of distance from the patterned sidewalls (recognizing that the sloping nature of the sidewall will reduce the resolution of the measurement). Both samples show similar trends, where the Zr and Ti concentrations are largely unaltered as the sidewall is approached. Similarly, both samples show a decrease in the amount of Pb as the sidewall is approached. The reduction in Pb concentration may be due to the energetic bombardment component of the etch which creates Pb defects within the material. In the case of the printed sample, the lead loss was most likely due to the prolonged exposure times at the crystallization temperature over multiple stamping cycles.

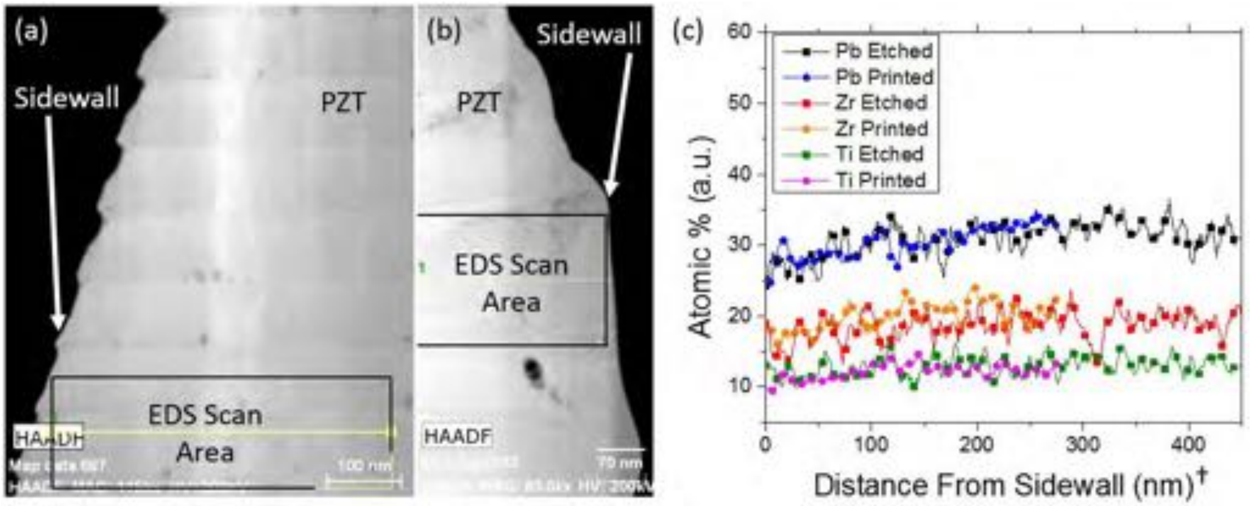

Figure 5-11. High Angle Annular Dark Field (HAADF) TEM images of (a) dry etched PZT 10 μm arm structures and (b) printed PZT 10 μm lateral features in close proximity to a sidewall. (c) The graphs of the corresponding EDS scans lines in the TEM images. The EDS results exhibit the atomic % of Pb, Zr, and Ti as a function of position in relation to the patterned sidewall of both a RIE (squares) and printed (circles) feature.[***]

5.3.4 Local Domain Wall Mobility

The local Rayleigh response of the material was measured using BE-PFM. This technique uses a cantilever to measure the piezoelectric nonlinearity at the nanoscale as the cantilever is scanned over a specific area of the material. In order for the measurement to determine the nonlinearity of the piezoelectric response of the material, nonlinearities that are associated with the tip-surface dynamics must be minimized.[158]

[***] Note: Here, the position marked as "0 nm distance from sidewall" is the closest vertical EDS scan line (black box) to each respective sidewall shown in the TEM images

In this work, before each BE-PFM measurement was performed, the cantilever was placed at a single location on the sample. The sample was subjected to an excitation waveform and the tip amplitude response (A_{max}) was recorded as a function of alternating excitation voltage (V_{AC}), as seen in Figure 5-12 (a). This measurement was performed 100 times at the same position. Individual data sets are shown in blue and the average response is shown in red. These data were used to generate box plots of the distribution of nonlinearity of both increasing frequency sweeps (chirp up) and decreasing frequency sweeps (chirp down), as seen in Figure 5-12 (d).

The dynamics of the cantilever are a function of the energy of the excitation waveform. High amounts of energy produce nonlinearity in the tip-surface interactions. However, low energy will result in a poor signal to noise ratio. As described by Griggio *et al*.,[158] a compromise between these two was achieved by utilization an excitation waveform that was averaged between a chirp and sinc function. The larger the percentage of chirp character in the excitation waveform, the larger the amount of energy is imparted into the material. This is illustrated in Figure 5-12 (d), where a RIE etched sample was subjected to various excitation waveforms with an increasing degree of chirp character in the signal. The red boxes are the chirp up and the blue boxes are the chirp down signals. Figure 5-12 (a) shows that with a 100% chirp signal the response shows a large degree of hysteresis between the chirp up and down signal (as two distinct red lines are evident) thus indicating the presence of tip-surface nonlinearities. Reducing the chirp character of the signal to 25%, as seen in Figure 5-12 (b), results in identical responses from both the averaged up and down chirp signals. Lowering the chirp character further to 3%, as seen in Figure 5-12 (c), degrades the signal to noise ratio. To minimize errors associated with poor signal to noise, the minimum chirp component that still enabled good imaging was used for each sample. Therefore, for the sample shown in Figure 5-12, the optimal % chirp character for the excitation waveform was ~10 % as displayed in Figure 5-12 (d).

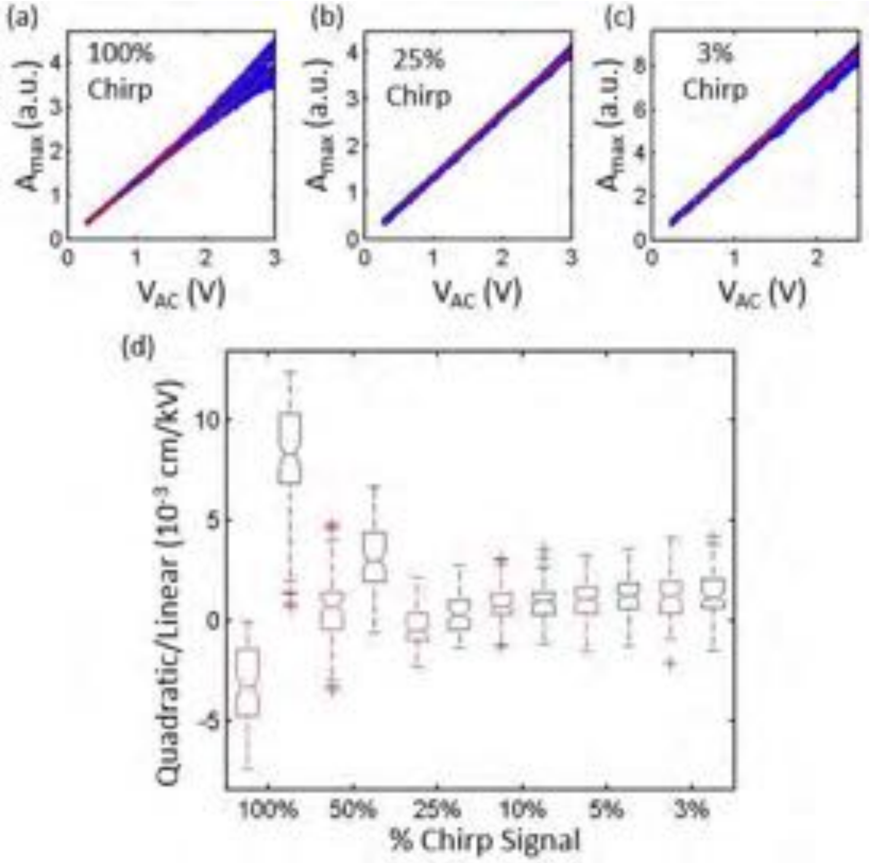

Figure 5-12. Tip amplitude response from a single point on a RIE sample with (a) 100%, (b) 25%, and (c) 3% chirp signal mixed with a sinc function. A_{max} is the maximum amplitude of the cantilever tip extrapolated from SHO equation fittings.[158] 100 consecutive measurements were performed sweeping up and down in frequency (blue lines). The 100 measurements were also averaged for both the up and down frequencies (red lines). (d) ANOVA box plots for excitation waveforms with various degrees of chirp character (chirp up is red box and chirp down is blue box) were created from the 100 measurements, the whiskers represent 1.5 times the interquartile range (IQR).[158]

The excitation waveform can also be repeated multiple times when performing one of the 100 A_{max} measurements in order to increase the signal to noise ratio that is recorded at a single location. The averaging of multiple repeated excitation waveforms had the unexpected benefit of reducing the tip-surface nonlinearity, as illustrated in Figure 5-13. The reasons for this are unknown. However, increasing the number of data cycles at each point also increases the overall time needed to probe a given scan area. This can be a significant issue as BE-PFM scans can take upwards of 4 hrs. In this work, a minimum of 8 repeats was utilized per measurement.

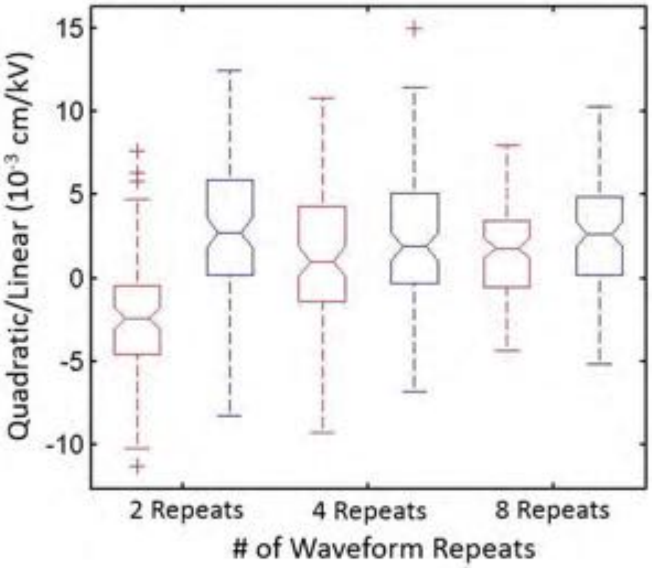

Figure 5-13. ANOVA boxplots for various numbers of repeated waveforms per A_{max} measurement with both chirp up (red box) and chirp down (blue box) signals.

Optimization of the excitation voltage amplitudes was also needed to ensure the maximum signal would be extracted while only probing the Rayleigh regime of the material. To illustrate this point, the A_{max} response of a RIE patterned film is displayed in Figure 5-14. At 1 V_{ac}, as shown in Figure 5-14 (a), the sample show a linear tip response however, the signal to noise is poor, complicating fitting of the material response. Figure 5-14 (b) allows for a stronger signal to be fit, thus leading to a more accurate determination of the material response. Increasing the excitation voltage to 3.5 V_{ac}, as displayed in Figure 5-14 (c), the A_{max} response becomes slightly nonlinear as evident by two distinct red lines. Figure 5-14 (d) shows that the boxplots do not overlap at 3V_{ac}, thus confirming the results seen in Figure 5-4 where the upper bound of the Rayleigh regime for the RIE samples was ~2.9 V_{ac}. The coercive voltage opposite the poling direction for this sample was 6.2V.

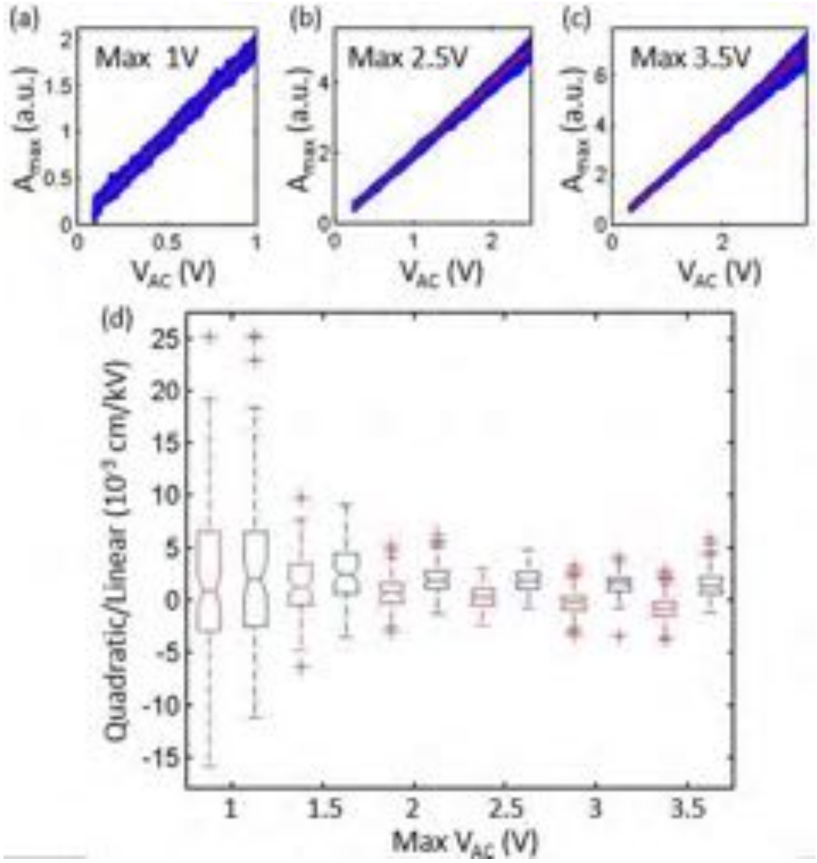

Figure 5-14. Tip amplitude response from a single point on a RIE sample with (a) 1, (b) 2.5, and (c) 3.5 V excitation amplitude. (d) ANOVA boxplots of chirp up (red box) and chirp down (blue box) signals for various excitation amplitudes.

To explore the factors which affect the movement of domain walls near a patterned sidewall, comparison of the domain wall motion both near and far from the patterned edge is essential. BE-PFM measurements of the RIE etched PZT were acquired ~5 μm away from the patterned sidewall in an effort to assess the Rayleigh behavior of the material without varying defect populations in a fully clamped state. The tip-surface nonlinearity was minimized with a 10 % chirp character excitation waveform with 8 repeats per measurement at a maximum amplitude of 2.5 V_{ac}. The scan area was a 5 x 5 μm wide with a grid size of 100 x 100 pixels. It was found that the etched films could not be fully poled into a single domain configuration. It was found that increasing either the poling time > 15 min or the poling voltage > $3V_c$ resulted in dielectric breakdown or little additional domain reorientation. Therefore, the RIE samples were poled at 15V for 15 min (voltage applied to top electrode and bottom electrode was ground) and allowed to age for 30 min. This poling both enabled the piezoelectric measurements, and moved the sample closer to true Rayleigh-like behavior.

Figure 5-15 shows the resonant frequency, the quality factor, piezoresponse phase, quadratic response, linear response, and the domain wall mobility collected at each point on the 5 x 5 μm region using a horizontal scanning direction. As the scan progresses over the area, the cantilever tip can be altered and this may vary the resonance frequency of the tip. Therefore, a 100 kHz wide frequency band was used for this measurement using a center frequency of 410 kHz. The resonant frequency varied by ~40 kHz over the scan area. This allowed any topographical contribution to the nonlinearity measurement to be minimized. The variation in the piezoresponse phase (~90°) reveals the material was not fully poled. The quadratic and linear response both exhibit similar trends which follow the phase of the of the piezoresponse signal. The averaged $\alpha/d_{33,init}$ of the scan area was $4.9 \pm 0.8 \times 10^{-3}$ cm/kV.

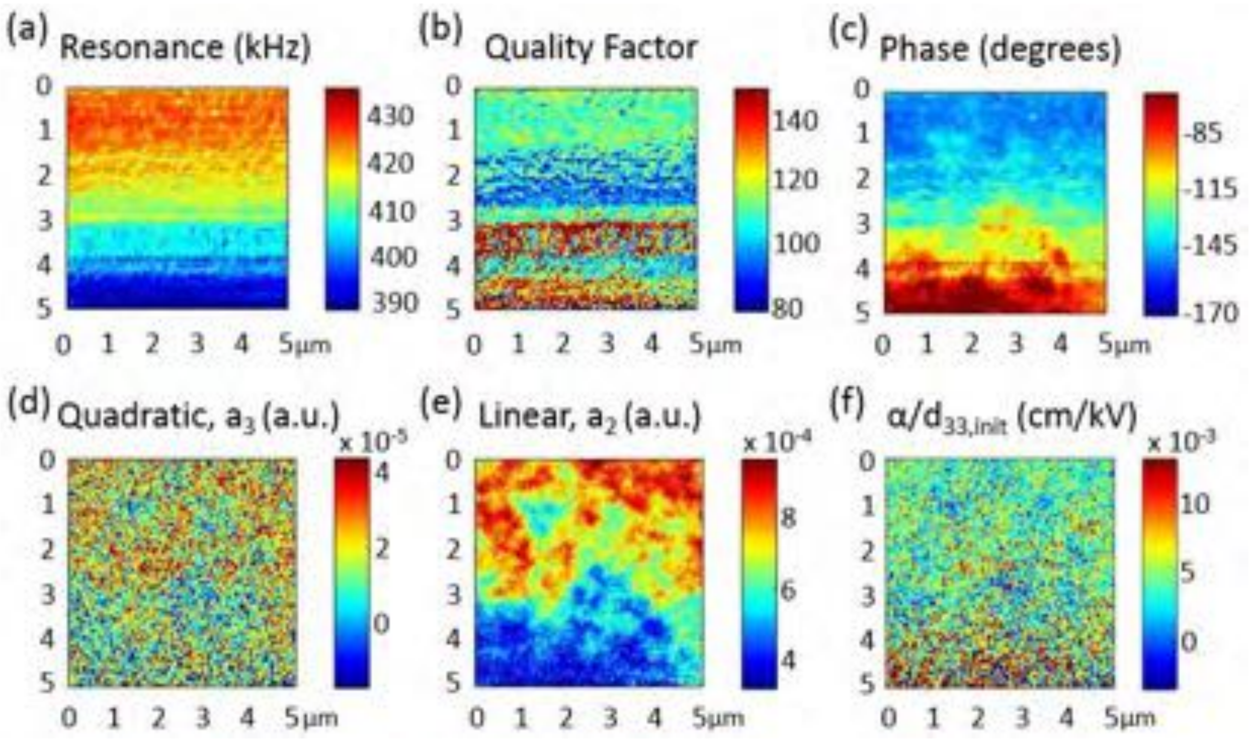

Figure 5-15. BE-PFM map showing the (a) resonance, (b) quality factor, (c) piezoresponse phase, (d) quadratic response, (e) linear response, and (f) $\alpha/d_{33,init}$ across a 5 x 5 µm area far away from the RIE patterned sidewall.

A BE-PFM scan was acquired across the full width of a lateral 10 µm feature, as seen in Figure 5-16. The tip-surface nonlinearity was minimized with a 3 % chirp character excitation waveform with 16 repeats per measurement at a maximum amplitude of 2.5 V_{ac}. The map area was a 5 x 10 µm area with a grid size of 100 x 200 pixels. The sample was poled in the same manner as described previously. It was found that the etched films could not be fully poled into a single domain configuration. Two distinct domain configurations appear across the width of the features which were offset by 180°. This pattern was seen on every arm structure in the same orientation and piezoresponse phase regardless of position, sidewall orientation, or scan direction.

Figure 5-16 (a, b, and c) shows the resonant frequency, quality factor, and piezoresponse phase of the scan area (horizontal scanning direction). A 100 kHz wide frequency band was used for this measurement using a center frequency of 405 kHz. The resonant frequency varied by ~30 kHz over the scan area.

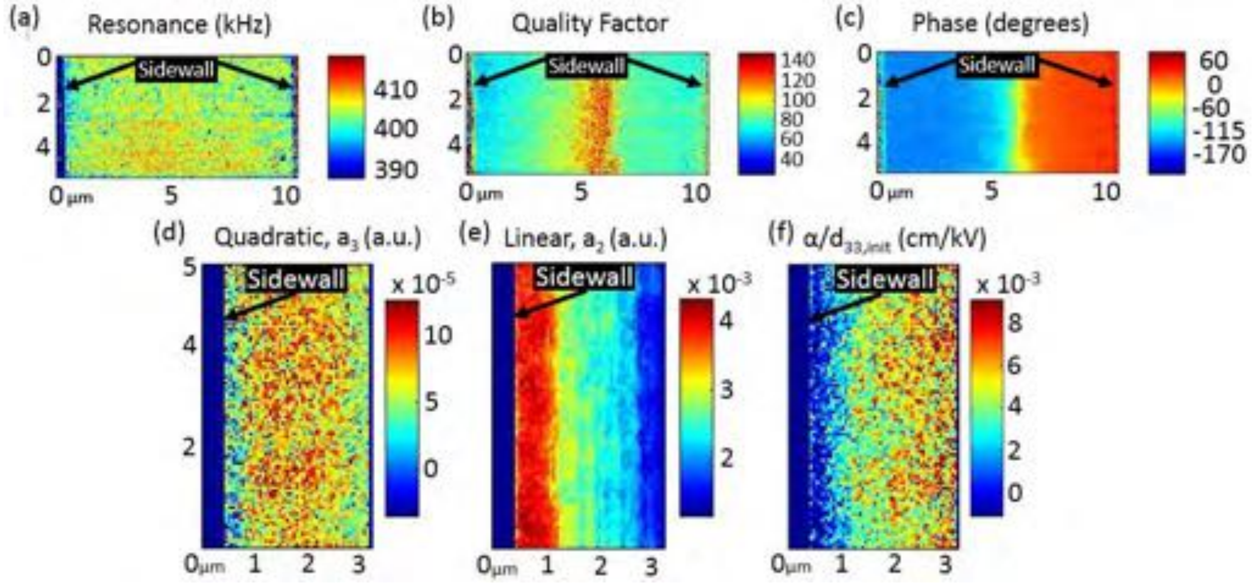

Figure 5-16. A 5 x 10 µm BE-PFM map showing the (a) resonance frequency, (b) quality factor, and (c) piezoresponse phase across an etched 10 µm lateral PZT feature. A 5 x 3 µm BE-PFM map of the material in immediate proximity to a patterned sidewall shows the variation of the (d) quadratic, (e) linear, and (f) $\alpha/d_{33,init}$ as a function of position.

The scan area for the nonlinearity data was truncated to one side of the feature (e.g. to a single poling direction) to determine how patterning affected the domain wall mobility. The reduced area shows a 5 x 3 um area (vertical scan direction) in the immediate vicinity of a patterned sidewall. Figure 5-17 (c, d, and e) show the variation of the quadratic response, the linear response, and the $\alpha/d_{33,init}$ of the material as the sidewall is approached (the area beyond the sidewall edge was removed from these PFM scans). The substrate boundary conditions vary over this scan area. The material next to the sidewall was declamped due to the removal of PZT in the etching process.

The lateral spatial extent of declamping is approximately equal to the film thickness.[132] The result of this declamping is evident in the increase of the linear response of the material next to the patterned sidewall. That is, the patterning allows for an increased intrinsic response from the material, as well as potentially an increase in reversible domain wall motion. However, the etching also introduces an increased defect population (and hence pinning centers) close to the pattern edge. This would be expected to limit the irreversible domain wall motion. Experimentally, a reduction of the quadratic response was observed in proximity to the sidewall.

A BE-PFM measurement of the RIE etched PZT was also acquired in the immediate vicinity of a 5 μm feature sidewall, as seen in Figure 5-17. The tip-surface nonlinearity was minimized with a 3 % chirp character excitation waveform with 8 repeats per measurement at a maximum amplitude of 2.5 V_{ac}. The map area was a 2 x 2 μm area with a grid size of 100 x 100 pixels. The sample was poled in the same manner as described previously. Again, it was found that the etched films could not be fully poled. The 5 μm arm structure always had two distinct net polarization orientations which were offset by 180° across the width of the features.

Figure 5-17 (a, b, and c) shows the resonant frequency, quality factor, and piezoresponse phase of the scan area (vertical scanning direction). A 100 kHz wide frequency band was used for this measurement with a center frequency of 400 kHz. The resonant frequency varied by ~40 kHz over the scan area. Figure 5-17 (d, e, and F) show that the quadratic response and the linear response behave in opposite ways, with the reversible response increasing, and the irreversible response decreasing as the sidewall is approached (the area beyond the sidewall edge was removed from the PFM scans). This suggests that one of three things occurred: 1) There was a reduced density of domain walls at the sidewall, and improved poling allowed higher piezoelectric responses to be achieved, while the hysteresis decreased, 2) the domain wall contribution to the properties dropped at the sidewall, or 3) the domain walls shifted from moving irreversibly in the clamped film to more reversibly near the sidewall, due to a difference in the pinning center distribution. Furthermore, the $\alpha/d_{33,init}$ drops to a negative value near the sidewall, suggesting a deviation from normal Rayleigh behavior. This would be consistent with a non-Gaussian distribution of restoring forces.

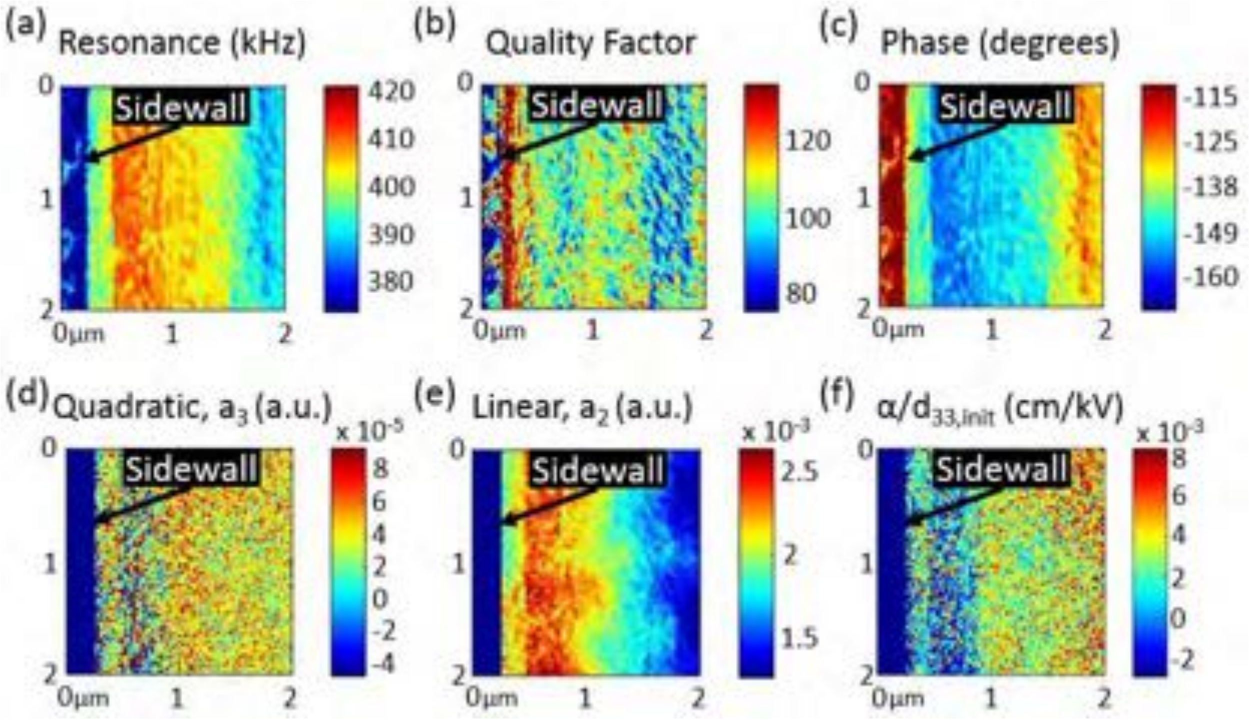

Figure 5-17. A 2 x 2 μm BE-PFM scan on top of a 5 μm laterally patterned feature which shows the variation of the (a) resonance, (b) quality factor, (c) piezoresponse phase, (d) quadratic response, (e) linear response, and (f) $\alpha/d_{33,init}$ as the sidewall is approached.[†††]

[†††] BE-PFM maps with scanning direction perpendicular to the patterned sidewall show uniform resonance frequencies and quality factors in an area with a single orientation for the net polarization, while also exhibiting decreased $a/d_{33,init}$ as the sidewalls are approached (data in Appendix C, Figure C-1).

It is expected that the width of influence to declamping as well as any etch-induced variation in the defect population should be similar in the 5 μm and 10 μm wide arms, as both samples are the same thickness and were etched at the same time. This was investigated by averaging the $\alpha/d_{33,init}$ response parallel to the sidewall (i.e. vertically in the scan area). Figure 5-18 (a) shows the two different datasets superimposed as a function of position perpendicular to the sidewall.

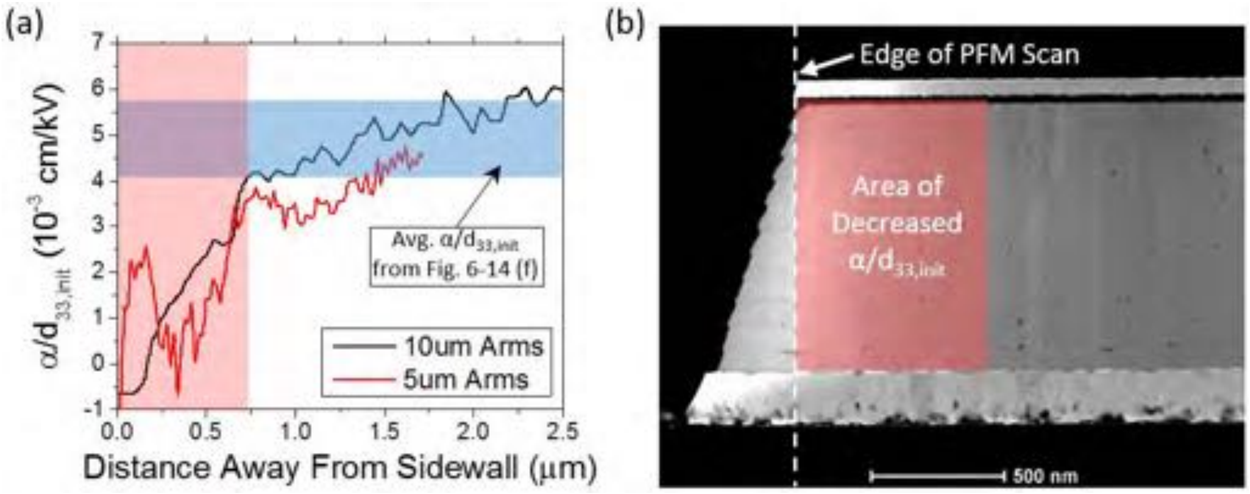

Figure 5-18. (a) Averaged $\alpha/d_{33,init}$ response of both 5 (red line) and 10 (black line) μm arms as a function of distance away from the sidewall (edge of PFM scan). The blue shaded region corresponds to the average $\alpha/d_{33,init}$ from Figure 5-15 (f) (i.e. 4.9 ± 0.8 x 10^{-3} cm/kV) and the red shaded region corresponds to decreased $\alpha/d_{33,init}$. (b) Cross-section TEM image of the dry etched 10 μm PZT feature showing the 750 nm spatial extent of reduced $\alpha/d_{33,init}$ (red region) determined from BE-PFM scans.

BE-PFM maps indicate that the complex shaped arm structures did not uniformly pole throughout the entire structure, as evidenced by all arm structures exhibiting two poling directions from the piezoresponse phase response (Figure 5-16 (c)). This variation lead to an increased nonlinearity at the boundary between these two poling directions as displayed in Appendix C,

Figure C-1 (f). The nonlinearity observed in 5 and 10 μm arms far from the sidewall therefore does not exhibit $\alpha/d_{33,init}$ values for a well-poled state and are larger than the average $\alpha/d_{33,init}$ value from Figure 5-15 (f) (i.e. $4.9 \pm 0.8 \times 10^{-3}$ cm/kV) due to the increased response at the boundary between the two poled regions. Therefore the average $\alpha/d_{33,init}$ from Figure 5-15 (f) was used as a guideline for the average nonlinear response of the material in a single piezoresponse phase area for the arm structures. This is depicted graphically by the blue shaded region in Figure 5-18 (a). Both the 5 and 10 μm features have a decreased $\alpha/d_{33,init}$ that is evident up to ~750 nm away from the sidewall. This is marked by the red shaded region in Figure 5-18 (a).

The spatial extent of the diminished $\alpha/d_{33,init}$ in RIE etched films is also shown in the red region of Figure 5-18 (b) on a cross-sectional TEM image. It is important to notice that the PFM measurement integrates over the column underneath the tip on the top global electrode. Recalling from Figure 5-11, the cation composition is uniform well within 200 nm from the edge of the material. The diminished $\alpha/d_{33,init}$ is observed over much greater lateral distances. This indicates that lead defects are not the dominant factor to diminished domain wall motion in RIE etched features. This also confirms work by Marincel *et al.*[160] which showed lead control in PZT films minimally affected domain wall mobility.

From Figure 5-18 (a), the decrease in $\alpha/d_{33,init}$ was approximated to follow a linear slope. An effective thickness of damaged material equal to half the width of 750 nm was then set. This new effective thickness was used to model each RIE pattern with a damaged area which corresponded to the effective damaged material width (i.e. 375 nm) while the remaining area was treated as undamaged. These two areas were then combined in a parallel mixing model to compare to the experimental $\alpha/\varepsilon_{init}$ values of each RIE feature shape, as seen in Table 5-4.

Table 5-4. Summary and comparison of the effective damaged and undamaged areas, using a damaged thickness of 375 nm from the sidewall into the pattern area, to the global $\alpha/\varepsilon_{init}$ of each RIE pattern.[‡‡‡]

Samples	$\alpha/d_{33,init}$ Effective Damaged Area (%)	$\alpha/d_{33,init}$ Effective Undamaged Area (%)	$\alpha/\varepsilon_{init}$ (10^{-3} cm/kV)	Normalized $\alpha/\varepsilon_{init}$ (%)
Large RIE Electrode	0.2 ± 0.05	99.8 ± 0.05	20.93 ± 0.06	100 ± 0.3
BUS Arm	1.1 ± 0.2	98.9 ± 0.2	18.83 ± 0.11	90.0 ± 0.5
10 µm Arms	7.6 ± 1.5	92.4 ± 1.5	18.39 ± 0.12	87.9 ± 0.6
5 µm Arms	14.8 ± 2.9	85.2 ± 2.9	17.55 ± 0.14	83.9 ± 0.7

BE-PFM maps indicate that the complex shaped arm structures did not uniformly pole throughout the entire structure, as evidenced by all arm structures exhibiting two poling directions from the piezoresponse phase response. This variation led to an increased nonlinearity at the boundary between these two poling directions as displayed in Appendix C, Figure C-1 (f). This was manifested in global dielectric nonlinearity as seen in the variations between global dielectric and local piezoelectric nonlinearity in the large area electrode and the bus arm structure (i.e. 100:90 % $\alpha/\varepsilon_{init}$ versus 100:98.9 % $\alpha/d_{33,init}$) and between bus arms and 10 µm arms (i.e. 90:87.9 % $\alpha/\varepsilon_{init}$ versus 98.9:92.5 % $\alpha/d_{33,init}$). The overall trends between the piezoelectric nonlinearity approximations do confirm the results from the global $\alpha/\varepsilon_{init}$ experimental values. Yet, the variation in poling states between the various patterned shapes makes the direct comparison between the local and global nonlinearity difficult, which emphasizes the need for local measurements on patterning damage to better understand the extent a patterning process influences the material.

[‡‡‡] All parameters, equations, and calculations used to determine this table are found in Appendix D

Local measurements of the piezoelectric nonlinearity were made on both RIE and Printed PZT features in an effort to directly compare the local piezoelectric nonlinearity between subtractive and additive patterning processes. However, the microstructure and domain structures of the two samples are not analogous, making direct comparisons between the two sample sets challenging. Thus, quantitative comparisons were made between different scan areas on the same sample (one near and one far from the sidewall).

Because top electrodes are deposited by a lift-off process onto the printed samples, the top electrodes have to be positioned as close to the patterned sidewall as possible without touching the bottom electrode and creating a short circuit. This was achieved by placing numerous discrete electrodes along the sidewall edge, as seen in Figure 5-19 (a). Each electrode, (i.e. from top to bottom of the image) was staggered ~0.5 μm perpendicular to the sidewall (left to right) with respect to one another. This would allow for some fraction of all the electrodes to be positioned on the sidewall without short circuiting, mitigating alignment errors upon Pt deposition. Figure 5-19 (b) provides an example 2 x 2 μm electrode that was deposited on the sidewall.

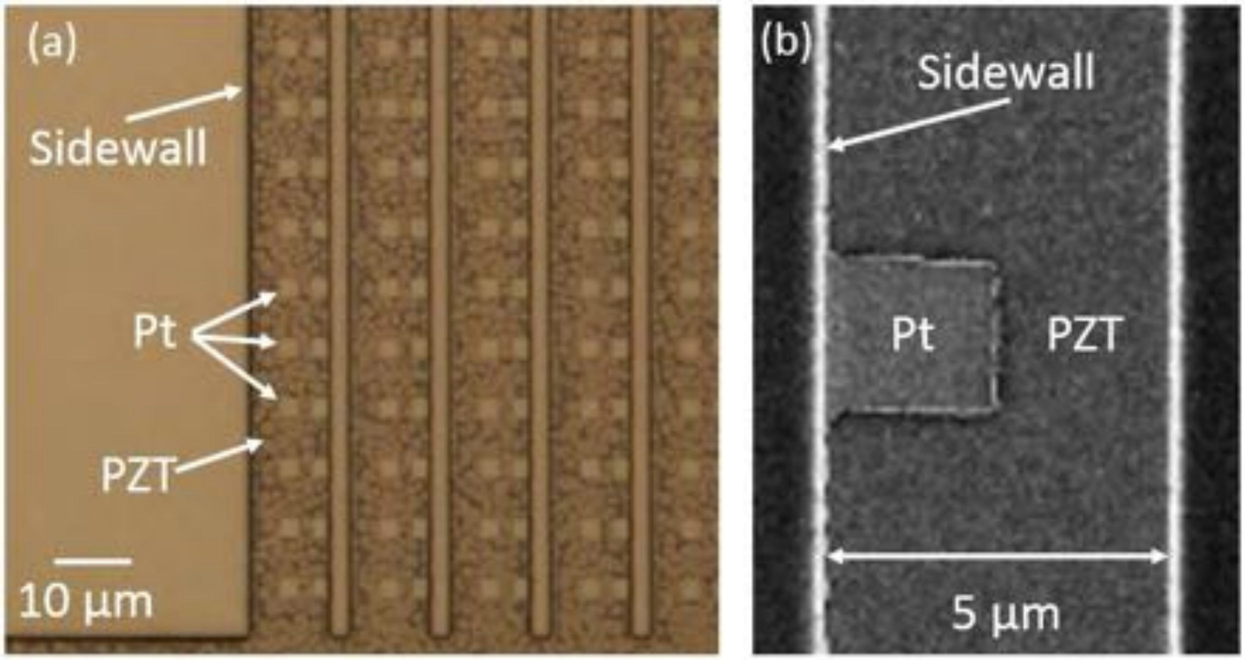

Figure 5-19. (a) Optical and (b) SEM images of top Pt configuration for PFM tips to contact in the local BEPFM measurements.

One BE-PFM measurement of the printed PZT was acquired ~5 µm away from the patterned sidewall in an effort to assess the Rayleigh behavior of the material without varying defect populations in a fully clamped state. The tip-surface nonlinearity was minimized with a 10 % chirp character excitation waveform with 8 repeats per measurement at a maximum amplitude of 2.5 V_{ac}. The printed samples were poled at -16V for 15 min. The voltage was applied to top electrodes and the bottom electrodes were grounded. V_c was -5 V for this poling configuration (refer to section 5.2.3). The samples were allowed to age for 30 min before performing the BE-PFM measurement. The scan area was a 2 x 2 µm area with a grid size of 100 x 100 pixels. The map was truncated to an area in the scan where measurements were collected on top of the electrode.

Figure 5-20 shows the resonant frequency, the quality factor, piezoresponse phase, quadratic response, linear response, and the $\alpha/d_{33,init}$ collected using a horizontal scanning direction. A 100 kHz wide frequency band was used for this measurement using a center frequency of 355 kHz. The resonant frequency varied by ~15 kHz over the scan area. This allowed any topographical contribution to the nonlinearity measurement to be minimized. The variation in the piezoresponse phase shows the material was poled uniformly. The quadratic and linear response both exhibit similar trends which follow the piezoresponse phase of the material. The averaged $\alpha/d_{33,init}$ was $3.3 \pm 0.4 \times 10^{-3}$ cm/kV. This response is lower than the response acquired from the center of the RIE feature, which is consistent with dielectric nonlinearity measurements.

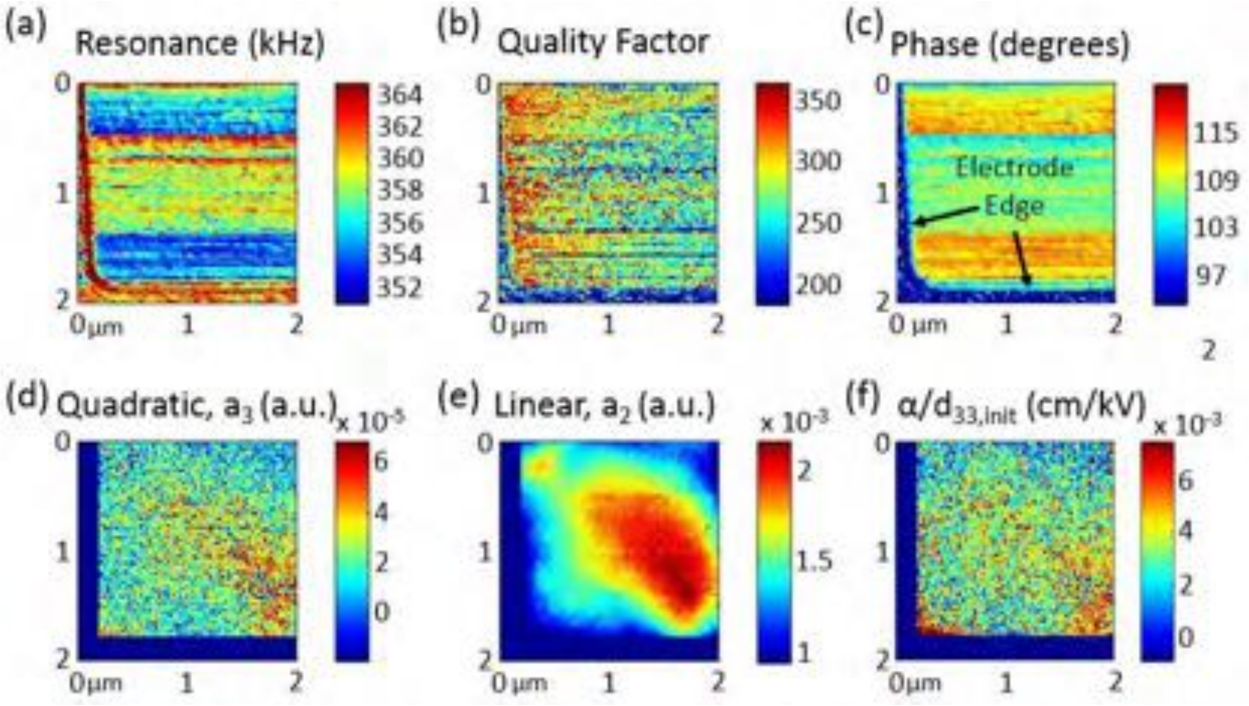

Figure 5-20. BE-PFM map showing the (a) resonance, (b) quality factor, (c) piezoresponse phase, (d) quadratic response, (e) linear response, and (f) $\alpha/d_{33,init}$ across a 1 x 1 μm area far away from the printed sidewall.

The second BE-PFM measurement of the printed PZT was acquired in the immediate vicinity of a 10 μm feature sidewall, as seen in Figure 5-21. The tip-surface nonlinearity was minimized with a 15 % chirp character excitation waveform with 8 repeats per measurement at a maximum amplitude of 2.5 V_{ac}. The sample was poled in the same manner as described previously. The scan area was a 2 x 2 μm area with a grid size of 100 x 100 pixels. The scan was truncated to a 1 x 1.25 μm area map that probed the printed sidewall.

Figure 5-21 (a, b, and c) shows the resonant frequency, quality factor, and piezoresponse phase of the scan area (horizontal scanning direction). Data were removed where the scan fell off the top electrode (i.e. the top of map). A 100 kHz wide frequency band was used for this measurement using a center frequency of 365 kHz. The resonant frequency varied by ~25 kHz over a majority of the scan area. Discrete areas of the PZT in immediate proximity to the feature sidewall were raised, arising from the variation in printing dynamics as the stamp was removed from the printing surface by hand. These raised features resulted in sufficiently large variation in the resonant frequency to fall outside the 100 kHz frequency band. Therefore, any data acquired on these roughened areas of PZT were removed from the PFM scans (ex. arrows point to areas on left side of Figure 5-21 (e) which were removed). The variation in the piezoresponse phase shows the material was poled uniformly. Both the quadratic and linear response show an increase in response as the sidewall is approached; furthermore $\alpha/d_{33,init}$ increased as the sidewall was approached.

As with the RIE features, the printed samples was laterally declamped along the sidewall. The spatial extent of the declamping in the printed sample was approximately equal to that observed in the RIE feature, as both samples are approximately the same thickness. However, $\alpha/d_{33,init}$ increased on approaching the sidewall for the printed features, and decreased for the reactive ion etched features. Therefore, it is believed that the introduction of defects near the patterned sidewalls (which limit domain wall mobility) is the cause for the decreased $\alpha/d_{33,init}$ seen in the RIE features.

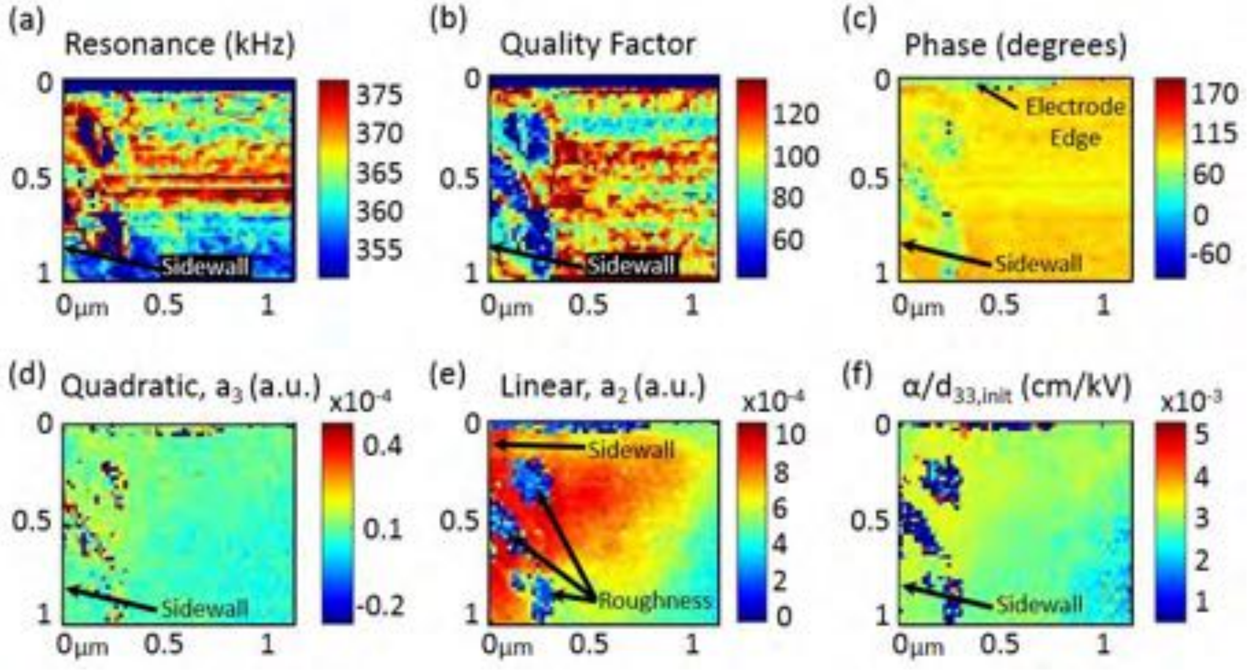

Figure 5-21. A 1 x 1.25 μm BE-PFM scan, on top of a 10 μm laterally printed feature, which shows the variation of the (a) resonance, (b) quality factor, (c) piezoresponse phase, (d) quadratic response, (e) linear response, and (f) $\alpha/d_{33,init}$ as the sidewall is approached

5.4 Conclusions

Variations in $\alpha/d_{33,init}$ close to sidewalls of printed and RIE etched PZT features were investigated by a combination of PFM and larger scale dielectric measurements. The nucleation of the perovskite phase of the printed films was inhibited resulting in rosette grain formation. This variation in microstructure precluded the ability to quantitatively compare the functional properties between these two patterning processes. However, quantitative global dielectric and local piezoelectric Rayleigh measurements were performed on each sample set in order to understand the emergent global response from the nanoscale domain structure and domain wall pinning. The global Rayleigh measurements showed that increasing etch perimeters results in $\alpha/\varepsilon_{init}$, from 23.31 ± 0.04 to 20.94 ± 0.14 cm/kV, as well as increased aging rates for domain wall mobility, from -7.0 ± 0.6 to -11.6 ± 0.7 %/decade.

The local nonlinearity measurements revealed that BEPFM is a powerful tool which can quantitatively measure the spatial scale over which dry etch damage affects the functional film. It was found that dry etching imparts an increased defect population into the` material limiting $\alpha/d_{33,init}$ ~750 nm away from a patterned sidewall regardless of the feature size. In contrast, printed features show an increase in $\alpha/d_{33,init}$ as a result of declamping of the film in immediate proximity to the sidewall.

Local structural characterization was performed using TEM to give insight into crystal quality and stoichiometry of each sample. Dry etched films show only modest variations in the composition or crystal structure over the characteristic length scales at which $\alpha/d_{33,init}$ was found to vary. Further investigations will be required to specify what defects are imparted into the martial which are responsible for the limiting of domain wall motion in RIE patterned films.

Chapter 6

Conclusions and Future Work

6.1 Conclusions

This thesis studies and optimized the additive patterning technique of microcontact printing to offer an alternative to subtractive patterning techniques such as reactive ion etching (RIE) for use in defining ferroelectric thin films. The knowledge gained from the optimization of this printing technique allows for the incorporation of a damage free patterned PZT thin film for use in MEMS applications.

6.1.1 Stamp Optimization

The surface of stamps made from an optically transparent polyurethane (PU) produced by Norland Optical Adhesives displayed excellent wetting properties with polar PZT solutions and remained unchanged over extended periods of time. This allowed for reproducible and repeated printing of PZT solutions onto an unpatterned substrate by a single patterned stamp. The excellent wetting behavior between stamp and solution was evident through the ability to print PZT features only 5 µm wide from raised stamp features. However, the resulting printed PZT features, no matter the lateral width, displayed low sidewall angles of ~ 1 degree.

The PU stamp was relatively stiff which limited the long range printing uniformity due to inherent uniformity of the stamp thickness. Through the addition of a compliant poly-dimethyl-siloxane (PDMS) backing to a PU surface, the composite stamp could deform easily while retaining the desired surface wetting properties.

Printing from stamp recesses was utilized as an alternative printing scheme. This allowed for the solution which came into contact with the substrate to be uniform up to the sidewall of the feature. This increased printed feature sidewalls to ~35 degrees. Printing onto pre-patterned substrates also allowed for the retention of printed PZT features with lithographically defined edges. This allowed printed PZT features to reach 1 µm in width.

6.1.2 Printing Optimization

In this work, solutions were spun onto the stamp surface to provide a uniform thickness to the liquid. Upon spinning the solvents in the solution would evaporate, leaving behind a gel network on the stamp surface. The resulting transferred PZT film could not easily redistribute on the substrate surface. Therefore, the dynamics of the solution upon removal of the stamp from the printing surface was critical to the final shape of the film. Varying of printing direction and peeling rates indicated that increased transfer rates of the solution to the substrate reduced redistribution of the film upon transfer. This allowed for the printing of PZT features onto pre-patterned features with > 80 degree sidewall angles on feature ranging from 500 to 1 µm wide.

6.1.3 Printing onto Patterned Substrates

Crystallization of PZT onto pre-patterned substrate surfaces limited nucleation of the perovskite phase. This was attributed to residues which remained on the patterned nucleation surface after hard mask removal (i.e. Pt) resulting in PZT rosette grain formation, porosity, and cracking of the film. A particular etch residue remover (i.e. ACT 935 UP) was utilized to clean the nucleation surface in conjunction with Ti-rich seed layers (i.e. 30/70 PZT) to promote grain nucleation. Etching of the substrate to define the pattern prior to deposition of bottom electrode is a second route to avoid etching residues on the nucleation surface. However, a sufficiently thick barrier coating (e.g. $\geq$ 60 nm HfO_2) must be used to prevent substantial lead loss through the bottom electrode, as this can also inhibit perovskite phase formation.

Printing PZT solutions directly onto pre-patterned substrates has a range of device applications. Two examples were explored in this thesis. 1) PZT was printed directly onto free-standing cantilevers without limiting the functionality of the resonating structure. 2) PZT was printed directly printed onto fixed cantilever structures sized from 30 to 1 μm in width. The PZT was intended to provide the electromechanical coupling needed to resonate and sense frequency shifts in a bio-functionalized MEMS mass sensor. The PZT displayed ferroelectric switching with no evidence of patterning damage.

6.1.4 Nonlinearity of Patterned PZT

Local nonlinearity of printed and etched PZT was probed utilizing band excitation piezoresponse-force microscopy (BE-PFM). RIE films exhibited a decreased $\alpha/d_{33,init}$ ~750 nm away from a patterned sidewall regardless of the feature size, indicating incorporation of defects into the material by the etching process. BE-PFM of printed features confirmed the avoidance of patterning damage, as an increase of $\alpha/d_{33,init}$ was observed in proximity to the patterned sidewall due to declamping of the film. Transmission electron microscopy (TEM) and energy dispersive spectroscopy (EDS) indicated that neither variations in composition or crystal structure were responsible for the observed trends in the local nonlinearity measurements. Finally, BE-PFM indicated that poling of complex film geometries can lead to non-uniform poling, which would not be discernable through global dielectric Rayleigh measurements.

6.2 Recommendations for Future Work

6.2.1 Printing Dynamics

This work demonstrated the feasibility of printing PZT thin films with sidewall angles > 80° on features only 1 μm wide. It was also shown that the printing dynamics strongly influence the sidewall angles depending on peeling directions with respect to the feature geometry and peeling speed. However, all of the printing was performed by hand. Therefore, only very disparate printing conditions could be controlled reproducibly. Automated printing is essential to fully assess the viability of microcontact printing as a patterning technique. Printing with tools designed to control and systematically vary particular printing parameters (i.e. alignment, printing pressures, and separation rates) would yield insight into optimization of both substrate or stamp geometries (i.e. feature spacing and feature size) and printing dynamics. It is possible that this level of control would allow for contact printing to be performed at the nano-scale. This would also aid in demonstrating the feasibility of the microcontact printing technique as a commercially viable deposition/patterning method.

6.2.2 Printing Alternative Complex Oxide Solutions

To illustrate the versatility of the microcontact printing process, printing of alternative complex oxide solutions should be undertaken. Many commercially important ferroelectrics are lead based materials because they exhibit high piezoelectric properties. Due to the volatility and toxicity of lead, these materials pose environmental and health concerns.[177] One of the most promising lead-free alternatives is potassium sodium niobate (KNN).[178] This material shows high piezoelectric ($d_{33} \sim 40$ pm/V)[179] and ferroelectric properties ($P_r \sim 19$ μC/cm^2)[180] with a high Curie temperature.

It is difficult to obtain good ferroelectric and piezoelectric properties because K and Na are very sensitive to humidity and are volatile during thermal processes.[181, 182, 183] Moreover, it is difficult to obtain saturated P-E hysteresis loops and high piezoelectric properties because of electrical leakage at high electric fields caused by the oxygen vacancies that develop upon crystallization. Several studies have been carried out in order to improve the piezoelectric properties of KNN ceramics and thin films through addition of excess K and Na.[184, 185, 179] In addition, doping has been explored in KNN single crystals,[186, 187] ceramics, [188, 189, 190] and thin films [191, 192 , 193] to aid in defect control and leakage currents. Lee *et al.*[180] has used Mn doping of KNN to create thin films with low leakage and large remanent polarization.

Initial experiments on development of KNN solutions were undertaken as part of this thesis. Thin film 0.5 mol% Mn doped KNN was produced, in collaboration with Sun Young Lee, through a chemical solution deposition process derived from the procedure described by Ahn *et al.*[191] The detailed process flow for solution preparation is illustrated in Figure 6-1. Manganese (II) acetate tetrahydrate ($(CH_3COO)_2Mn \cdot 4H_2O$) was added to the solvents 2-methoxyethanol (2-MOE) ($CH_3OCH_2CH_2OH$) and acetic acid (CH_3COOH) at room temperature in a glove box under Ar atmosphere and mixed for 24 hours; acetylacetone ($CH_3COCH_2COCH_3$) was added (chelating agent) and mixed for 2 hrs; followed by the addition of niobium pentaethoxide ($Nb(OCH_2CH_3)_5$ and mixed for 2 hrs. In a second container, potassium acetate (CH_3COOK) and sodium acetate (CH_3COONa) were added to 2-MOE and acetic acid in a rotary evaporator flask under Ar atmosphere at 80 ˚C and mixed for 2 hours. The two flasks were combined at 40 ˚C under Ar atmosphere and mixed for 2 days. Finally, the stabilizer polyvinylpyrrolidone (PVP) ($(C_6H_9NO)_n$) was added to the solution at room temperature under Ar atmosphere and mixed for 24 hrs. The solution was aged at 4 ˚C for ~100 hr. The final solution was 0.4M.

The solvent ratio of 2-MOE and acetic acid was a 1:1 volume ratio. The manganese and niobium precursors were kept at a 0.995:0.005 molar ratio; the sodium and potassium precursors were kept at a 1:1 molar ratio. To compensate for (K,Na) volatility during crystallization and annealing, a 10 mol% excess was utilized relative to the B site. The acetylacetone to metal ratio was a 2:1 molar ratio, and the acetylacetone to PVP ratio was a 2:1 molar ratio.

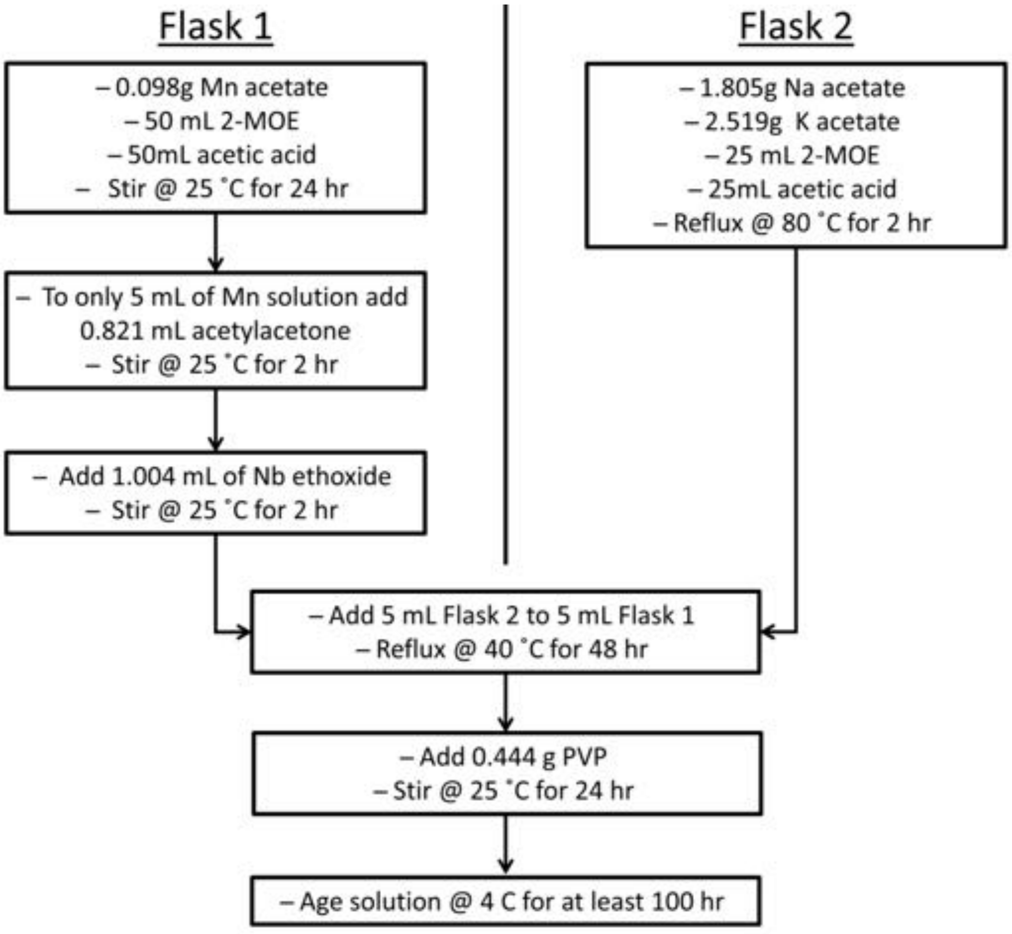

Figure 6-1. Process flow detailing the creation of a 10 mL 0.4 M 0.5mol% Mn doped KNN solution with 10 % excess Na and K.[§§§]

[§§§] Note: Solution preparation used large stock solutions in Mn and Na/K acetate mixing steps in order to simplify weighing of metal precursors. The extra Mn and Na/K acetate solutions could be stored in a refrigerator for use in future solution batch preparations.

The solution was spun onto a Pt-coated Si wafer at 3000 rpm for 30 sec. The film was dried at 200 ˚C for 5 min, then pyrolyzed at 400 ˚C for 5 min on a hot plate. The film was crystallized at 550 ˚C for 5 min under an oxygen atmosphere in a rapid thermal anneal (RTA) furnace. This sequence was repeated 10 times. The KNN solution is extremely hygroscopic and precipitated if repeatedly exposed to the ambient environment. The final film thickness was ~500 nm. The films were annealed in a box furnace at 600, 650, 700, or 750 ˚C for 30 min. The process flow describing the deposition of KNN thin films is illustrated in Figure 6-2.

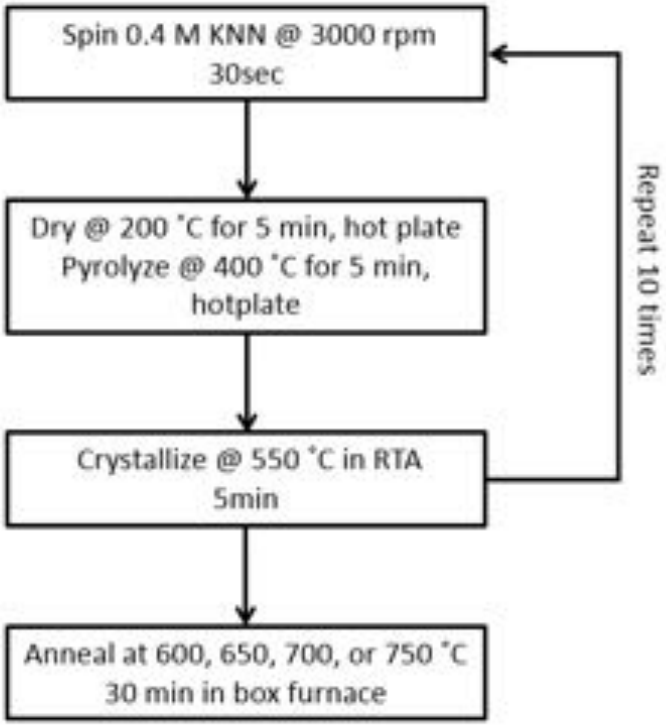

Figure 6-2. Process flow detailing the deposition of a KNN thin film utilizing a 0.4M 0.5mol% Mn doped KNN solution with 10 % excess Na and K.

XRD scans of the KNN films (Figure 6-3 (a)) reveal that the KNN perovskite phase was crystallized after the RTA heat treatment. SEM images (Figure 6-3) show that as the annealing temperature, increases the grains grow and appear equiangular. This is manifested in the XRD scans by a splitting in the 200/002 peaks. No secondary phases are seen in either the XRD scans or the surface microstructure. However, at 750 ˚C annealing temperature, large voids were created in the samples.

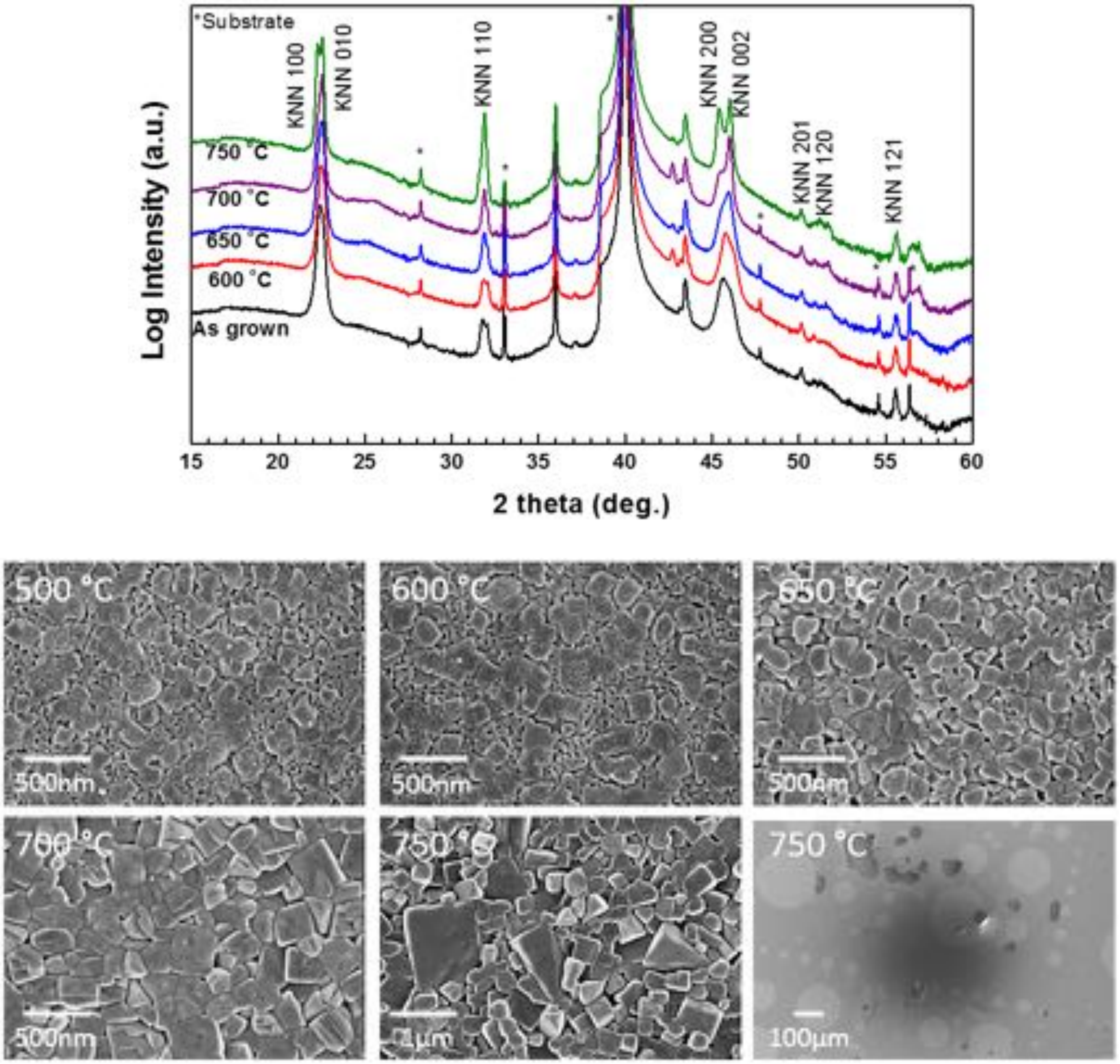

Figure 6-3. XRD scan and SEM images of Mn doped KNN films after 500 ˚C (black line) crystallization for 5 min and 600 (red), 650 (blue), 700 (purple) and 750 ˚C (green) anneals for 30 min.

Each sample was electroded by sputtering 100 nm Pt as described previously through a shadow mask to define the electrode patterns. P-E loops were taken on each sample as shown in Figure 6-4. The films annealed at 600 ˚C have high loss and no evidence of switching. Ferroelectricity is exhibited in films annealed 650 ˚C with a remanent polarization of 10 μC/cm^2. Upon higher annealing temperatures, switching is still present, but clearly conduction pathways have been created in the material, creating high loss.

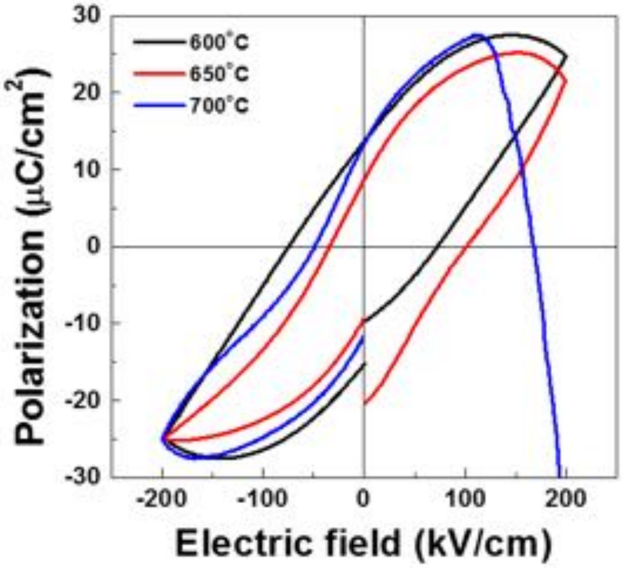

Figure 6-4. P-E loops of Mn doped KNN thin films annealed at 600 (black), 650 (red), and 700 ˚C (blue).

While phase pure ferroelectric KNN was demonstrated, further investigation and optimization of the stoichiometry, dopant levels, pyrolysis, crystallization, and annealing temperatures will result in a further reduction of the loss and increase in the remanent polarizations achievable with these solutions. Because these solutions utilize polar solvents, they should wet the polyurethane stamp surfaces. Future work should be undertaken to demonstrate microcontact printing of optimized KNN solutions.

One problem facing microcontact printing is alignment of a top electrode on the printed film. The top electrodes on printed features intended for device applications used in this thesis were deposited through a lift-off process in combination with either evaporated or sputtered metals. Alignment of these two processing steps was onerous especially as feature size decreased. Yet, even when aligned with enough accuracy for the top electrode to be deposited onto the printed surface, inevitably a finite portion of the printed feature was not covered with metal. One way to mitigate this issue is to continue using the microcontact printing process to deposit the top electrode. It has been shown previously, that printing solutions onto pre-patterned surfaces does not require precise alignment tolerances, and subsequently printed layers are confined to the pre-existing printed area. Therefore, printing of the top electrode directly on top of a printed ferroelectric material would completely cover the top surface. This could be achieved by demonstrating printing of 2-MOE based solutions of conductive oxides precursors such as lanthanum nickelate.[194]

6.2.3 Investigation of Patterning Damage at the Nanoscale

BE-PFM is a powerful characterization technique for determining the magnitude and spatial extent over which patterning techniques influence the functional properties of the material. In this work, efforts were made to create films of identical phase, stoichiometry, microstructure, and boundary conditions by two different patterning techniques. Unfortunately, this was not achieved, and therefore direct quantitative comparison between the patterning techniques was not accomplished.

In the future, to nucleate the perovskite phase on prepatterned substrates, the following steps are recommended: 1) etch the design into the underlying substrate, 2) deposit a thick barrier layer (≥60 nm of HfO_2), 3) sputter the bottom electrode after etching, and possibly 4) utilize a Ti rich (i.e. 30/70 PZT) PZT seed layer as a nucleation aid. This will ensure that rosette grain formation does not occur. Once the initial layer has nucleated the perovskite structure, any PZT composition may be deposited on top of the seed layer for the remainder of the film stack. The etched sample must use the same film stack composition even if nucleation is not a concern. The second matter of importance is to utilize an identical pattern and electrode configuration for both patterning techniques. As was seen in this work, sample geometry can influence poling configurations (i.e. two poling directions seen in every arm structure) which directly affects nonlinearity measurements.

The minor loops of the RIE etched films exhibited non Rayleigh-like character. This was attributed to a non-random distribution of pinning centers within the material. Thus, it is recommended in future work that the nonlinear response be quantified by a Preisach model with an appropriate distribution of switching elements.[85, 195] One potential area of research is in understanding the local switching behavior near feature sidewalls for different families of patterning approaches. Studying the material on the nanometer length scale will provide insight into the microscopic mechanisms of the local switching behavior.

Polarization switching occurs by mechanisms which include nucleation of new domains and reversible/irreversible motion of preexisting ferroelastic and ferroelectric domain walls.[196] The hysteretic response of the material is dependent on the history of the field application, which can be described on the Preisach model determined from First Order Reversal Curve (FORC) measurements. Conventional methods used to investigate hysteresis are confined to sizes above the micrometer length scale. However, the spatial variability of the switching behavior can be investigated using a spatially resolved FORC measurement based on a band excitation (BE) switching spectroscopy PFM (FORC BE SS-PFM) method.[197] In this case, multiple hysteresis loop measurements of varying amplitude are measured at a single location, as illustrated in Figure 6-5. This technique creates a five-dimensional data set of response as a function frequency, bias, sub-loop number, and spatial coordinates. Previous PFM FORC measurements were limited in accuracy – it is anticipated that improvements in microscope design will now enable more quantitative characterization.

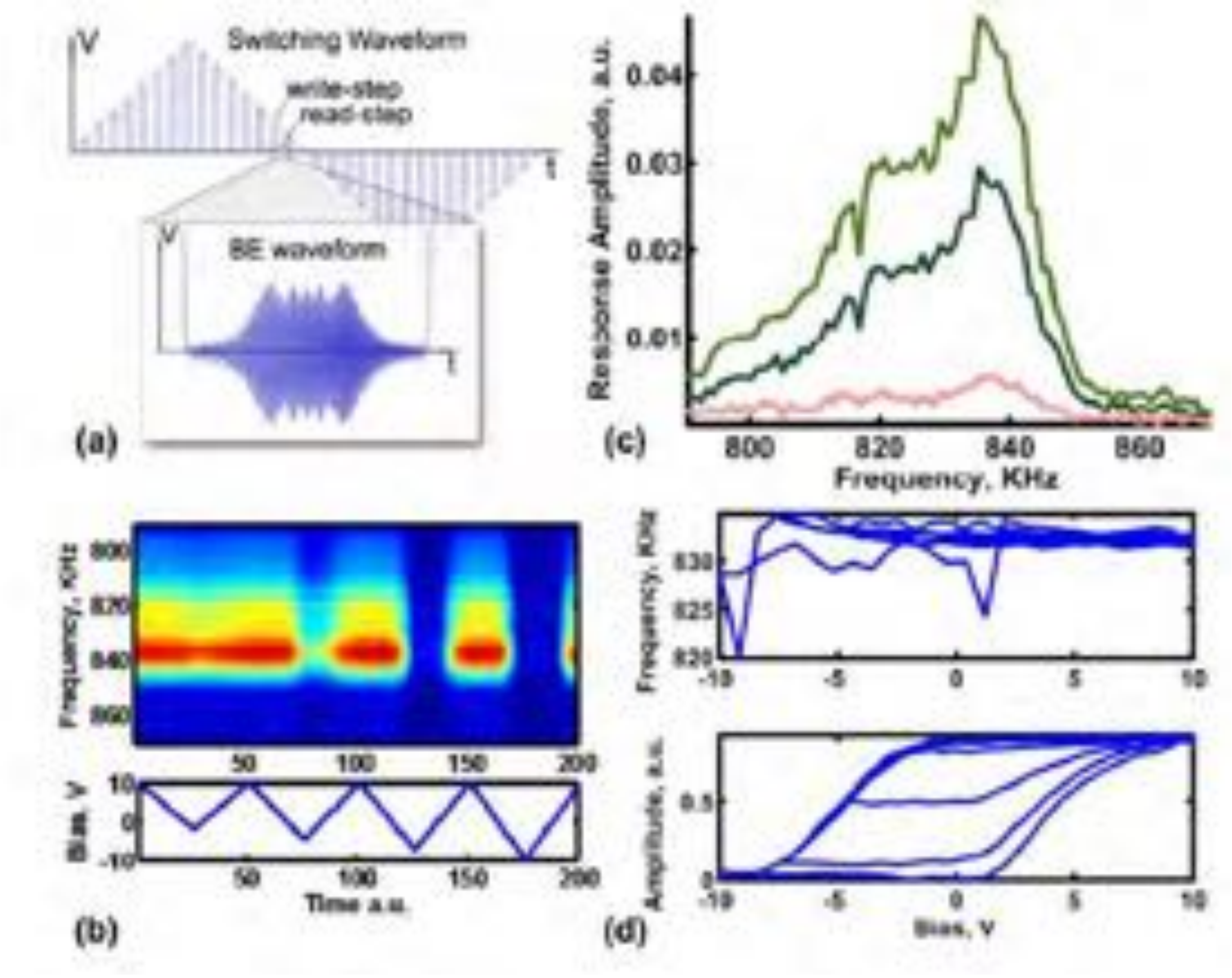

Figure 6-5. Schematic of a single-point FORC BE switching spectroscopy (SS)-PFM measurement. (a) Schematic of a train of DC and BE pulses in BE SS-PFM (b) and the resulting piezoresponse as a function of time and frequency. (c) Piezoresponse as a function of frequency at different bias levels and the (d) corresponding frequency and amplitude loops.[198]

This technique can be implemented on PZT features produced by different patterning techniques. Mapping of the spatial variability of irreversible Preisach densities, imprint, work of switching, and switchable polarization will give insight into how each patterning technique affects the switching properties of the material as related to the distance from a patterned sidewall. This could then be correlated to domain wall mobility to discern if regions of material which show low domain wall mobility also hinder the nucleation and/or growth of domains.

Appendix A: Wetting of a Liquid on a Surface

One phase displaces another when forming an interface resulting in an exchange of interfacial energetics.[199, 200] As shown in Figure A-1, when phase 1 is placed onto a phase 2 there is a net energy cost/gain per unit area in making the interface (i.e. interface l,2). This is opposed by the energy cost/gain per unit area in destroying the original interfaces (i.e. interface 1,3 and interface 2,3) between phase 1, 2, and phase 3. This is described by the following equation where G is the Gibb's free energy, W is the work of the system, and γ_{ab} is the interfacial energy or interfacial tension between phase a and phase b:

$$\Delta G = -W = \gamma_{12} - \gamma_{13} - \gamma_{23}$$

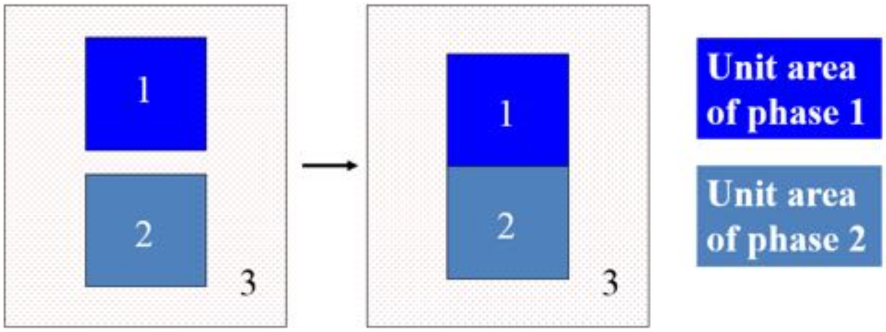

Figure A-1. Schematic of three phases in a closed system where phase 1 is brought into contact with phase 2 creating a new interface.

If phase 1 and phase 2 are both the same liquid phase and phase 3 is a vapor phase, the work of cohesion can be described as:

$$\Delta G_{cohesion} = -W_{cohesion} = \gamma_{ll} - \gamma_{lv} - \gamma_{lv} = -2\gamma_{lv}$$

This shows that cohesion is spontaneous because it takes work to make a surface. However, if phase 1 is a liquid phase, phase 2 is a solid phase, and phase 3 is a vapor phase, the work of adhesion can be described as:

$$\Delta G_{adhesion} = -W_{adhesion} = \gamma_{sl} - \gamma_{sv} - \gamma_{lv}$$

Wetting angles (θ) of liquids on solid surfaces arise out of a competition between the work of cohesion of the liquid and the work of adhesion between the liquid and solid surface. A representative liquid droplet on a solid surface at equilibrium is depicted in Figure A-2.

$$\Delta G = 0 = \gamma_{sv} - \gamma_{sl} - \gamma_{lv} cos\theta$$

$$cos\theta = \frac{\gamma_{sv} - \gamma_{sl}}{\gamma_{lv}}$$

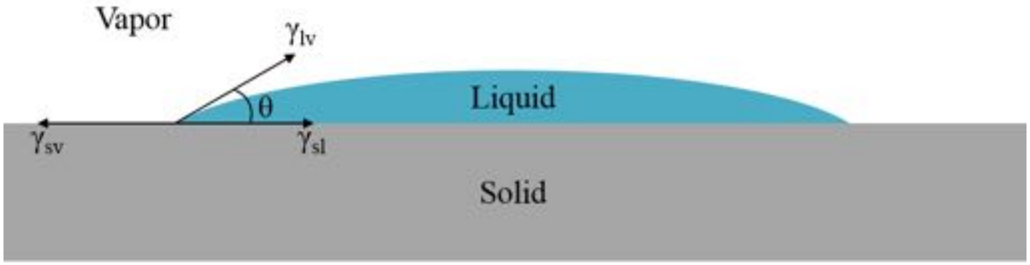

Figure A-2. Schematic of solid, liquid, and vapor system in equilibrium where the liquid is wetting the solid surface with an arbitrary wetting angle.

If a liquid exhibits θ = 180˚, the cohesion forces are much larger than the adhesion forces in the system. Conversely, if a liquid exhibits θ = 0˚ the adhesion forces are much larger than the cohesive forces in the system. Finally, liquids which exhibit 0˚ < θ < 90˚ on a surface are referred to as “high wetting”. While, liquids which exhibit 90˚ ≤ θ < 180˚ on a surface are referred to as “low wetting”.

Appendix B: Cantilever Dynamics for Mass Detection

This chapter describes calculation of the resonant frequency (f_n) of a cantilever with a uniform rectangular cross section with one fixed end and the other free.[201] The calculation of the first resonance frequency utilizes the Young's modulus (E) of the beam material; the cantilever dimensions of length (L), width (w), and thickness (t); the moment of inertia of the beam cross-section (I); and the mass per unit length (m) of the beam:

$$I = \frac{wt^3}{12} \qquad A = wt \qquad m = \rho A$$

$$(rad/s)\colon \omega_1 = 1.875^2\sqrt{\frac{EI}{mL^4}} = 3.52\sqrt{\frac{EI}{\rho AL^4}} = 3.52\sqrt{\frac{Et^2}{12\rho L^4}}$$

$$(Hz)\colon f_1 = \frac{\omega_1}{2\pi} = \frac{3.52}{2\pi}\sqrt{\frac{Et^2}{12\rho L^4}}$$

The addition of antibodies onto the surface of a cantilever, with an effective mass (M_{eff}), increases the total effective mass of the structure (Δm) resulting in proportional shift in the resonant frequency (Δf) from the original resonance frequency (f_0), provided the stiffness does not change as well. Direct measurement of a frequency shift of the cantilever is used to determine the number of antibodies deposited onto the device surface[91] by:

$$\Delta f = \frac{-f_0}{2M_{eff}}\Delta m \qquad \Delta m = \frac{\alpha M_w L w}{N_A \pi r^2}$$

where α is the resonant mode shape coefficient, M_w is the molecular weight of the antibodies, L and w are the cantilever length and width, N_A is Avogadro's number, and r is the radius of he antibody.

Appendix C: BE-PFM Maps across a 10 μm Lateral Feature Using a Scanning Direction Perpendicular to the Sidewall

Figure C-1 displays a BE-PFM map across the width of a 10 μm feature. This scan demonstrates that when the scanning direction is perpendicular to the sidewall direction, the general trends in nonlinearity are still observed as with maps scanned vertically along the same direction as the sidewall. The chirp character was not properly optimized, which resulted in differences in the measured values between the down and up chirp, but the trends still remain valid.

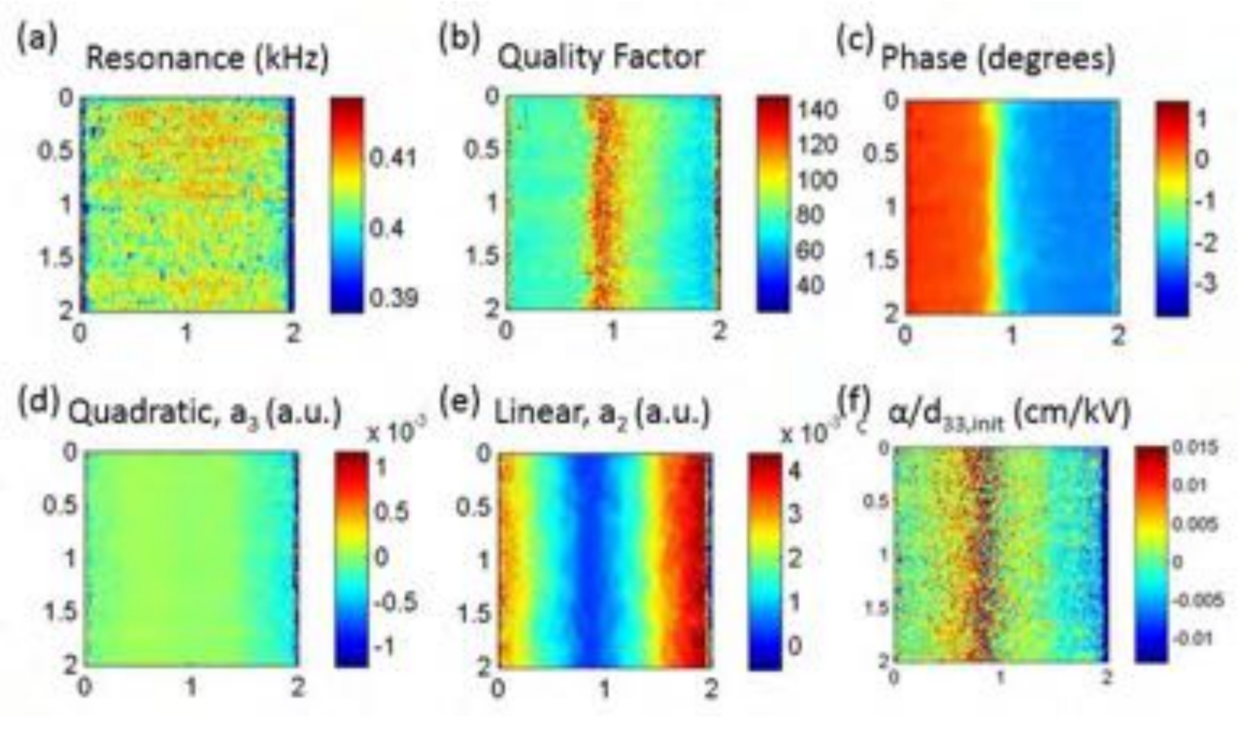

Figure C-1. A 10 x 10 μm BE-PFM scan on top of a 10 μm laterally patterned feature which shows the variation of the (a) resonance, (b) quality factor, (c) phase, (d) quadratic response, (e) linear response, and (f) $\alpha/d_{33,init}$ as the sidewall is approached. The tip-surface nonlinearity was not properly optimized. Therefore absolute values of nonlinearity are not useful but the trends are still valid.

Appendix D: Area Equations and Parameters Used in Parallel Mixing Model

Large RIE Electrode Area Equations:

$$\boldsymbol{t = damaged\ layer\ thickness}$$

$$\boldsymbol{A_{Circle} = \pi * r^2}$$

$$\boldsymbol{A_{Circle,Damaged} = \pi * (r^2 - (r-t)^2)}$$

$$\boldsymbol{A_{Circle,UnDamaged} = \pi * (r-t)^2}$$

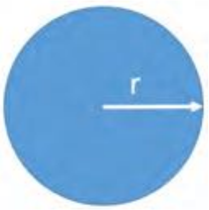

t (µm)	r (µm)
0.375 ± 0.1	313.5 ± 1

BUS Arm Area Equations:

$$\boldsymbol{t = damaged\ layer\ thickness}$$

$$\boldsymbol{A_{BUS} = (H_1 * W_1) + (H_2 * W_2)}$$

$$\boldsymbol{A_{BUS,Damaged} = 2(H_1 * t) + \big((W_1 - 2t)t\big) + 2(W_3 * t) + 2(H_2 * t) + \big((W_2 - 2t)t\big)}$$

$$\boldsymbol{A_{BUS,UnDamaged} = A_{BUS} - A_{BUS,Damaged}}$$

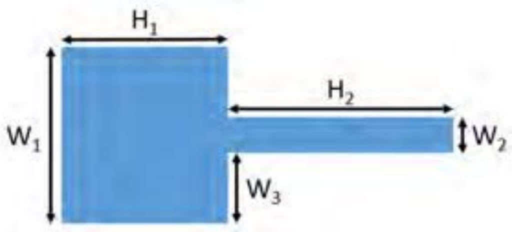

t (µm)	W₁ (µm)	H₁ (µm)	W₂ (µm)	H₂ (µm)	W₃ (µm)
0.375 ± 0.1	250 ± 1	249 ± 1	20 ± 0.1	550 ± 1	115 ± 0.5

10 µm Arm Area Equations: (54 individual arms come out from central BUS arm)

$$\boldsymbol{t = damaged\ layer\ thickness}$$

$$\boldsymbol{A_{10\mu m} = 54(H * W)}$$

$$\boldsymbol{A_{10\mu m,Damaged} = 54\left(2(H * t) + \left((W - 2t)t\right)\right)}$$

$$\boldsymbol{A_{10\mu m,UnDamaged} = A_{10\mu m} - A_{10\mu m,Damaged}}$$

t (µm)	W (µm)	H (µm)
0.375 ± 0.1	10 ± 0.1	435 ± 1

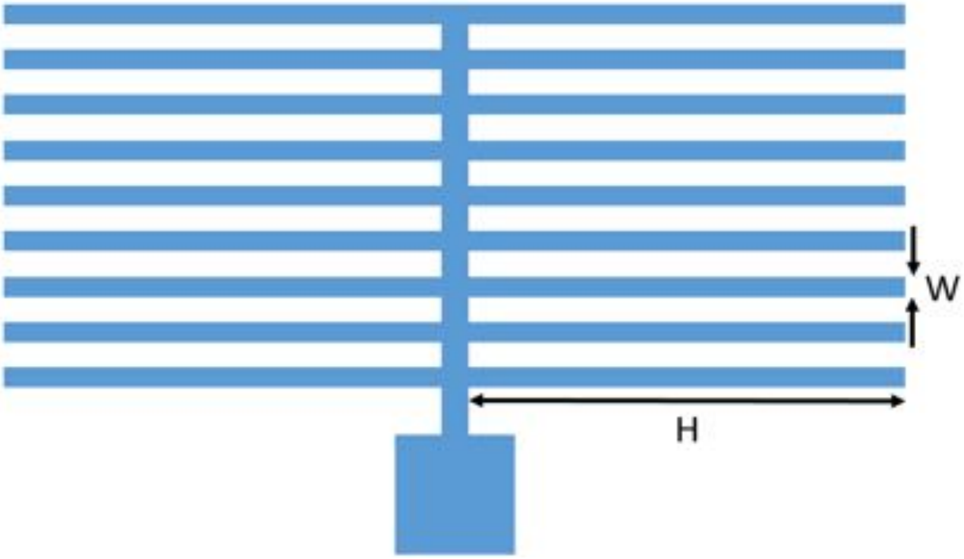

5 µm Arm Area Equations: (108 individual arms come out from central BUS arm)

$$\boldsymbol{t = damaged\ layer\ thickness}$$

$$\boldsymbol{A_{10\mu m} = 108(H * W)}$$

$$\boldsymbol{A_{10\mu m,Damaged} = 108\left(2(H * t) + \left((W - 2t)t\right)\right)}$$

$$\boldsymbol{A_{10\mu m,UnDamaged} = A_{10\mu m} - A_{10\mu m,Damaged}}$$

t (µm)	W (µm)	H (µm)
0.375 ± 0.1	5.1 ± 0.1	435 ± 1

Appendix E: MATLAB Code for Calculating Nonlinearity Maps

```
% % Modified to quadratic / linear normalized by thickness (cm/kV).
% % multiply m1, m2, max_out, bin_size by 2 to get back to a/d33

close all
clear all
clc

file_path = 'C:\Users\Daniel\Desktop\CNMS\2014.01\Data\PZT52_19';
file_name = 'nl_0001';
fit_suffix = 'nlinfit ri SHO parms';

% load([ file_path '\' file_name ])
load([ file_path '\' file_name '\' file_name ' ' fit_suffix ])

% % To use data from fast SHO fit, change SHO_fit above to fast_SHO_fit and
% % uncomment following line.

coef_mat4 = squeeze(cat(5, A, w.*(10^-3), q, p.*(pi/180)));
coef_mat4(isinf(coef_mat4)) = NaN;

% coef_mat4 = coef_mat4(6:end,:,:,:);

dc_amp_vec_full = V;

% % size_x and size_y are the dimensions of the measured region. These are
% % used to set the dimensions of the spatial plots.

size_x = 5;
size_y = 5;

% coef_mat4 = coef_mat4(1:60,:,:,:);
% size_y = 3;

% % min_ind is the index of the starting voltage for fit, n_std is the
% % number of standard deviations the colorbar shows in plots, max_out is
% % the maximum a/d33 before start removing data, bin_size is the size of
% % bins for a/d33 histogram

min_ind = 3;
n_std = 2;
```

```
max_out = 0.05;
bin_size = 0.0005;

% % First part here is to remove noise at low voltage steps.

Oldsize = size(coef_mat4,3)/2;
Newsize = Oldsize - min_ind +1;
coef_mat4_01(:,:,1:Newsize,:) = coef_mat4(:,:,min_ind:Oldsize,:);
coef_mat4_01(:,:,Newsize+1:2*Newsize,:) =
coef_mat4(:,:,Oldsize+min_ind:2*Oldsize,:);

dc_amp_vec_full_01(1:Newsize) = dc_amp_vec_full(min_ind:Oldsize);
dc_amp_vec_full_01(Newsize+1:2*Newsize) =
dc_amp_vec_full(Oldsize+min_ind:2*Oldsize);

coef_mat4 = coef_mat4_01;
dc_amp_vec_full = dc_amp_vec_full_01;

% % Plot spatial map of mean resonance frequency with respect to voltage

[num_rows,num_cols,num_steps,num_coefs] = size(coef_mat4);

res_mat3 = coef_mat4 (:,:,:,2);

mean_res_1 = nanmean(res_mat3(:,:,1:num_steps/2),3);
mean_res_2 = nanmean(res_mat3(:,:,num_steps/2+1:end),3);
std_res_1 = nanstd(res_mat3(:,:,1:num_steps/2),0,3);
std_res_2 = nanstd(res_mat3(:,:,num_steps/2+1:end),0,3);

mean_res = reshape([mean_res_1 mean_res_2],2*num_rows*num_cols,1);
m_mean_res = nanmean(mean_res);
std_mean_res = nanstd(mean_res,1);

std_res = reshape([std_res_1 std_res_2],2*num_rows*num_cols,1);
m_std_res = nanmean(std_res);
std_std_res = nanstd(std_res,1);

fh1 = figure(1);
set(fh1, 'color','white');
clf

subplot(3,2,1)
imagesc([0 size_x],[0 size_y],mean_res_1)
colorbar
% set(colorbar,'fontsize',20);
title('Resonance Map Chirp Up in kHz');
```

```
caxis([m_mean_res-n_std*std_mean_res m_mean_res+n_std*std_mean_res])
axis image

subplot(3,2,2)
imagesc([0 size_x],[0 size_y],mean_res_2)
colorbar
% set(colorbar,'fontsize',20);
title('Resonance Map Chirp Down in kHz');
caxis([m_mean_res-n_std*std_mean_res m_mean_res+n_std*std_mean_res])
axis image

% % Plot spatial map of mean quality factor with respect to voltage

q_mat3 = coef_mat4 (:,:,:,3);

mean_q_1 = nanmean(q_mat3(:,:,1:num_steps/2),3);
mean_q_2 = nanmean(q_mat3(:,:,num_steps/2+1:end),3);
std_q_1 = nanstd(q_mat3(:,:,1:num_steps/2),0,3);
std_q_2 = nanstd(q_mat3(:,:,num_steps/2+1:end),0,3);

mean_q = reshape([mean_q_1 mean_q_2],2*num_rows*num_cols,1);
m_mean_q = nanmean(mean_q);
std_mean_q = nanstd(mean_q,1);

subplot(3,2,3)
imagesc([0 size_x],[0 size_y],mean_q_1)
colorbar
% set(colorbar,'fontsize',20);
title('Quality Factor Chirp Up');
caxis([m_mean_q-n_std*std_mean_q m_mean_q+n_std*std_mean_q])
axis image

subplot(3,2,4)
imagesc([0 size_x],[0 size_y],mean_q_2)
colorbar
% set(colorbar,'fontsize',20);
title('Quality Factor Chirp Down');
caxis([m_mean_q-n_std*std_mean_q m_mean_q+n_std*std_mean_q])
axis image

% % Plot spatial map of mean phase with respect to voltage

phase_mat3 = coef_mat4 (:,:,:,4);

mean_phase_1 = nanmean(phase_mat3(:,:,1:num_steps/2),3);
mean_phase_2 = nanmean(phase_mat3(:,:,num_steps/2+1:end),3);
```

```
std_phase_1 = nanstd(phase_mat3(:,:,1:num_steps/2),0,3);
std_phase_2 = nanstd(phase_mat3(:,:,num_steps/2+1:end),0,3);

% % Flatten the phase map to reduce influence from changes in tip; this is
% % generally not plotted or used in further calculations

x = 0 : size_x / (num_cols - 1) : size_x;
flat_phase_1 = zeros(size(mean_phase_1));
flat_phase_2 = zeros(size(mean_phase_2));
for k = 1 : num_rows

        y_1 = mean_phase_1(k,:);
        y_2 = mean_phase_2(k,:);

        p_1 = polyfit(x,y_1,1);
        p_2 = polyfit(x,y_2,1);
        p_fit_1 = x*p_1(1) + p_1(2);
        p_fit_2 = x*p_2(1) + p_2(2);
        flat_phase_1(k,:) = y_1-p_fit_1;
        flat_phase_2(k,:) = y_2-p_fit_2;
end

mean_phase = reshape([mean_phase_1 mean_phase_2],2*num_rows*num_cols,1);
m_mean_phase = nanmean(mean_phase);
std_mean_phase = nanstd(mean_phase,1);

flat_phase = reshape([flat_phase_1 flat_phase_2],2*num_rows*num_cols,1);
m_flat_phase = nanmean(flat_phase);
std_flat_phase = nanstd(flat_phase,1);

subplot(3,2,5)
imagesc([0 size_x],[0 size_y],mean_phase_1)
colorbar
% set(colorbar,'fontsize',20);
title('Phase Chirp Up');
caxis([m_mean_phase-n_std*std_mean_phase m_mean_phase+n_std*std_mean_phase])
axis image

subplot(3,2,6)
imagesc([0 size_x],[0 size_y],mean_phase_2)
colorbar
% set(colorbar,'fontsize',20);
title('Phase Chirp Down');
caxis([m_mean_phase-n_std*std_mean_phase m_mean_phase+n_std*std_mean_phase])
axis image
```

```
% % Now fit amplitude to quadratic equation and extract coefficients

amp_mat3 = coef_mat4(:,:,:,1);

include_vec = 1 : num_steps/2;
p_1 = zeros(num_rows,num_cols,3);
p_2 = zeros(num_rows,num_cols,3);

amp_fit_mat3 = zeros(num_rows,num_cols);

for k1 = 1 : num_rows
    disp(k1)
    for k2 = 1 : num_cols

        amp_vec_1 = squeeze(amp_mat3(k1,k2,1:num_steps/2));
        amp_vec_2 = squeeze(amp_mat3(k1,k2,num_steps/2+1:end));

        Vac_1 = dc_amp_vec_full(1:num_steps/2);
        Vac_2 = dc_amp_vec_full(num_steps/2+1:end);

        if sum(~isnan(amp_vec_1(include_vec))) < 3
            p_1(k1,k2,:) = NaN;
            amp_fit_mat3(k1,k2,1:num_steps/2) = NaN;
        else
            p_1(k1,k2,:) =
polyfit(Vac_1(~isnan(amp_vec_1(include_vec))),amp_vec_1(~isnan(amp_vec_1(include_ve
c)))',2);
            amp_fit_1 = p_1(k1,k2,1)*Vac_1.^2 + p_1(k1,k2,2)*Vac_1 +
        p_1(k1,k2,3);
            amp_fit_mat3(k1,k2,1:num_steps/2) = amp_fit_1;
        end

        if sum(~isnan(amp_vec_2(include_vec))) < 3
            p_2(k1,k2,:) = NaN;
            amp_fit_mat3(k1,k2,(num_steps/2) + 1:num_steps) = NaN;
        else
            p_2(k1,k2,:) =
polyfit(Vac_2(~isnan(amp_vec_2(include_vec))),amp_vec_2(~isnan(amp_vec_2(include_ve
c)))',2);
            amp_fit_2 = p_2(k1,k2,1)*Vac_2.^2 + p_2(k1,k2,2)*Vac_2 +
        p_2(k1,k2,3);
            amp_fit_mat3(k1,k2,(num_steps/2) + 1:num_steps) = amp_fit_2;
        end
    end
end
```

```
% % Plot the quadratic, linear, and offset

fh2 = figure(2);
clf
set(fh2, 'color','white');
title_cell = { 'Quadratic' ; 'Linear' ; 'Offset' };
p_3 = zeros(2*num_rows*num_cols,3);

for k1 = 1 : 3

        p_3(:,k1) = reshape([p_1(:,:,k1) p_2(:,:,k1)],2*num_rows*num_cols,1);

        p_mean3 = nanmean(p_3(:,k1));
        p_std3 = nanstd(p_3(:,k1),1);

        subplot(3,2,k1*2-1)
        imagesc([0 size_x],[0 size_y],p_1(:,:,k1))
        colorbar
        axis image
        title([ title_cell{k1} ' Chirp Up' ])
        caxis([p_mean3-n_std.*p_std3 p_mean3+n_std.*p_std3]);

        subplot(3,2,k1*2)
        imagesc([0 size_x],[0 size_y],p_2(:,:,k1))
        colorbar
        axis image
        title([ title_cell{k1} ' Chirp Down' ])
        caxis([p_mean3-n_std.*p_std3 p_mean3+n_std.*p_std3]);
end

% % Determine and plot alpha / d33

thickness = input(['What is the thickness (' texlabel('mu') 'm)?']);

m1 = p_1(2:end,:,1)./p_1(2:end,:,2)/10*thickness*2;
m_mean1_full = nanmean(nanmean(m1));
threshold1 = find(abs(m1)>max_out);
m1(threshold1) = NaN;
m_mean1 = nanmean(nanmean(m1));

m2 = p_2(2:end,:,1)./p_2(2:end,:,2)/10*thickness*2;
% m2(isnan(m2)) = nanmean(nanmean(m2));
m_mean2_full = nanmean(nanmean(m2));
threshold2 = find(abs(m2)>max_out);
m2(threshold2) = NaN;
m_mean2 = nanmean(nanmean(m2));
```

```
m3 = reshape([m1 m2],numel([m1 m2]),1);
m_mean3 = nanmean(m3);
m_std3 = nanstd(m3,1);

fh3 = figure(3);
clf
set(fh3, 'color','white');

subplot(2,2,1)
imagesc([0 size_x],[0 size_y],m1)
title([ 'Chirp Up, mean = ' num2str(m_mean1,3) 'cm/kV'])
% % To display average with outliers, add full to above line (m_mean1_full)
caxis([ m_mean3-n_std*m_std3 m_mean3+n_std*m_std3 ])
colormap(jet)
colorbar
axis image

subplot(2,2,2)
imagesc([0 size_x],[0 size_y],m2)
title([ 'Chirp Down, mean = ' num2str(m_mean2,3) 'cm/kV'])
% % To display average with outliers, add full to above line (m_mean2_full)
caxis([ m_mean3-n_std*m_std3 m_mean3+n_std*m_std3 ])
colormap(jet)
colorbar
axis image

subplot(2,2,3)

m = m1 - m2;
m_mean = nanmean(nanmean(m));
m_std = nanstd(reshape(m,numel(m),1));

imagesc([0 size_x],[0 size_y],m)
title('Difference (cm/kV)')
caxis([ m_mean-n_std*m_std m_mean+n_std*m_std ])
colormap(jet)
colorbar
axis image

subplot(2,2,4)

m_tog = zeros(size(m1,1),size(m1,2),2);
m_tog(:,:,1) = m1;
m_tog(:,:,2) = m2;
m = nanmean(m_tog,3);
```

```
m_mean = nanmean(nanmean(m));
m_std = nanstd(reshape(m,numel(m),1));

imagesc([0 size_x],[0 size_y],m)
title(['Mean, mean = ' num2str(m_mean,3) 'cm/kV'])
caxis([ m_mean-n_std*m_std m_mean+n_std*m_std ])
colormap(jet)
colorbar
axis image

% % Plot histogram of a/d33
fh4 = figure(4);
clf
set(fh4, 'color','white');

m1D = reshape(m,numel(m),1);
bins = ceil((max(m1D) - min(m1D)) / bin_size);
inc = (max(m1D) - min(m1D))/bins;
edges = zeros(bins,1);

for k1 = 1 : bins

        edges(k1) = min(m1D) + (k1-1)*inc;

end

meana = nanmean(m1D);
stda = nanstd(m1D);
[~,~,ci] = ztest(m1D,meana,stda);
confa = meana-ci(1);
edgesc = edges';

[N,X] = hist(m1D,edgesc);
N = N' / sum(N) * 100;
X = X';
max_N = 10*ceil(max(N)/10);

n_elements = histc(m1D,edgesc);
c_elements = cumsum(n_elements)./(num_rows * num_cols)*100;

[ax h1 h2] = plotyy(X,N,edgesc,c_elements,'plot');
set(h1,'color','b')
set(h2,'color','r')
title(['Histogram, maximum = ' num2str(max(N),3) ', mean = ' num2str(meana,3)
' +/- ' num2str(confa,3) 'cm/kV'])
```

```
set(get(ax(1),'Ylabel'),'String','Relative Frequency','Color','k')
ylimits = get(ax(1),'YLim');
yinc = (ylimits(2)-ylimits(1))/5;
set(ax(1),'YColor','k','YTick',(ylimits(1):yinc:ylimits(2)))

set(get(ax(2),'Ylabel'),'String','Cumulative Frequency','Color','k')
ylimits = get(ax(2),'YLim');
yinc = (ylimits(2)-ylimits(1))/5;
set(ax(2),'YColor','k','YTick',(ylimits(1):yinc:ylimits(2)))

xlabel('quadratic / linear (cm/kV)');
axis(ax(1),[-max_out max_out 0 max_N])
axis(ax(2),[-max_out max_out 0 100])

% % Save figures and fit data

sav = input('Save fit data and figures? (y/n) ','s');

while ~((strcmpi(sav,'y')) || (strcmpi(sav,'n')))
        disp('Error: Invalid input.')
        sav = input('Save fit data and figures? (y/n) ','s');
end

if strcmpi(sav,'y')
        save([file_path '\' file_name
'\NLdata.mat'],'Vac_1','Vac_2','amp_mat3','p_1','p_2');
End
```

REFERENCES

[1] P. Muralt, A. Kholkin, M. Kohli, T. Maeder, "Piezoelectric Actuation of PZT Thin-Film Diaphragms at Static and Resonant Condition," *Sensors and Actuators A*, **53**, 398-404 (1996).

[2] T. Morita, M. Kurosawa, T. Higuchi, "An Ultrasonic Micromotor Using a Bending Cylindrical Transducer Based on PZT Thin Film," *Sensors and Actuators A*, **50**, 75-80 (1995).

[3] M. Kohli, C. Wuethrich, K. Brooks, B. Willing, M. Foster, P. Muralt, N. Setter, and P. Ryser, "Pyroelectric Thin-Film Sensor Array," *Sensors and Actuators A*, **60**, 147-53 (1997).

[4] H. Kueppers, T. Leuerer, U. Schnakenberg, W. Mokwa, M. Hoffmann, T. Schneller, U. Boettger, and R. Waser, "PZT Tin Films for Piezoelectric Microactuator Applications," *Sensors and Actuators A*, **97-98**, 680-84 (2002)

[5] S. Trolier-McKinstry and P. Muralt, "Thin Film Piezoelectrics for MEMS," *J. Electroceram.*, **12**, 7-17 (2004).

[6] P. Muralt, "Recent Progress in Materials Issues for Piezoelectric MEMS," *J. Am. Ceram. Soc.*, **91**, 1385-96 (2008).

[7] S. D. Mancha and D. Asselanis, "Method for Patterning PLZT Thin Films," *U.S. Patents*, 4759823 A, (1988).

[8] S. Mancha, "Chemical Etching of Thin Film PLZT," *Ferroelectrics*, **135**, 131-37 (1992).

[9] K. Zheng, J. Lu, and J. Chu, "A Novel Wet Etching Process of Pb(Zr,Ti)O_3 Thin Films for Application in Microelectromechanical System," *Jpn. J. Appl. Phys.*, **43**, 3934-37 (2004).

[10] T. Kawaguchi, H. Adachi, K. Setsune, O. Yamazaki, and K. Wasa, "PLZT Thin-Film Waveguides," *Applied Optics*, **23**, 2187-91 (1984).

[11] G. L. Smith, J. S. Pulskamp, L. M. Sanchez, D. M. Potrepka, R. M. Proie, T. G. Ivanov, R. Q. Rudy, W. D. Nothwang, S. S. Bedair, C. D. Meyer, and R. G. Polcawich, "PZT-Based Piezoelectric MEMS Technology," *J. Am. Ceram. Soc.*, **95**, 1777-92 (2012).

[12] J. Baborowski, "Microfabrication of Piezoelectric MEMS," *Integrated Ferroelectrics*, **66**, 3-17 (2004).

[13] K. Saito, J. H. Choi, T. Fukuda, and M. Ohue, "Reactive Ion Etching of Sputtered $PbZr_{1-x}Ti_xO_3$ Thin Films," *Jpn. J. Appl. Phys.*, **31**, L1260-62 (1992).

[14] C. W. Chung and C. J. Kim, "Etching Effects on Ferroelectric Capacitors with Multilayered Electrodes," *Jpn. J. Appl. Phys.*, **36**, 2747-53 (1997).

[15] T. Kobayashi, M. Ichiki, R. Kondou, K. Nakamura, and R. Maeda, "Degradation in Ferroelectric and Piezoelectric Properties of $Pb(Zr,Ti)O_3$ Thin Films Derived from a MEMS Microfabrication Process," *J. Micromech. Microeng.*, **17**, 1238-41 (2007).

[16] K. Torii, H. Kawakami, H. Miki, K. Kushida, T. Itoga, Y. Goto, T. Kumihashi, N. Yokoyama, M. Moniwa, K. Shoji, T. Kaga, and Y. Fujisaki, "Process and Properties of $Pt/Pb(Zr,Ti)O_3/Pt$ Integrated Ferroelectric Capacitors," *Integrated Ferroelectrics*, **16**, 21-28 (1997).

[17] C. Soyer, E. Cattan, and D. Rèmiens, "Electrical Damage Induced by Reactive Ion-Beam Etching of Lead-Zirconate-Titanate Thin Films," *J. Appl. Phys.*, **97**, 114110-7 (2005).

[18] K. T. Kim, M. G. Kang, and C. I. Kim, "Study on the Etching Damage Characteristics of PZT Films after Etching in Cl-Based Plasma," *Microelectronic Engineering*, **71**, 294-300 (2004).

[19] J. K. Lee, T. Y. Kim, I. Chung, and S. B. Desu, "Characterization and Elimination of Dry Etching Damaged Layer in $Pt/Pb(Zr_{0.53}Ti_{0.47})O_3/Pt$ Ferroelectric Capacitor," *Appl. Phys. Lett.*, **75**, 334-336 (1999).

[20] J. K. Lee, Y. Park, and I. Chung, “Improvement in the Electrical Properties in $Pt/Pb(Zr_{0.52}Ti_{0.48})O_3/Pt$ Ferroelectric Capacitors Using a Wet Cleaning Method,” *J. Appl. Phys.*, **86**, 6376-81 (1999).

[21] Y. Xia and G. M. Whitesides, “Soft Lithography,” *Annu. Rev. Mater. Sci.*, **28**, 153-84 (1998).

[22] C. R. Martin and I. A. Aksay, “Microchannel Molding: A Soft Lithography-Inspired Approach to Micrometer-Scale Patterning,” *J. Mater. Res.*, **20**, 1995-2003 (2005).

[23] X. M. Zhao, Y. Xia, and G. M. Whiteside, “Fabrication of Three-Dimensional Micro=-Structures: Microtransfer Molding,” *Adv. Mater.*, **8**, 837-40 (1996).

[24] P. M. Moran and F. F. Lange, “Microscale Lithography via Channel Stamping: Relationship Between Capillarity, Channel Filling, and Debonding,” *Appl. Phys. Lett.*, **74**, 1332-34 (1999).

[25] E. Kim, Y. Xia, and G. M. Whitesides, “Polymer Microstructures Formed by Moulding in Capillaries,” *Nature*, **376**, 581-84 (1995).

[26] Y. Xia, E. Kim, and G. M. Whitesides, “Micromolding of Polymers in Capillaries: Applications in Microfabrication,” *Chem. Mater.*, **8**, 1558-67 (1996).

[27] E. Kim, Y. Xia, and G. M. Whitesides, “Micromolding in Capillaries: Applications in Materials Science,” *J. Am. Chem. Soc.*, **118**, 5722-31 (1996).

[28] P. Yang, T. Deng, D. Zhao, P. Feng, D. Pine, B. F. Chmelka, G. M. Whitesides, and G. D. Stucky, “Hierarchically Ordered Oxides,” *Nature*, **282**, 2244-46 (1998).

[29] A. Matsuda, Y. Matsuno, M. Tatsumisago, and T. Minami, “Fine Patterning and Characterization of Gel Films Derived from Methyltriethoxysilane and Tetraethoxysilane,” *J. Am. Ceram. Soc.*, **81**, 2879-52 (1998).

[30] C. Marzolin, S. P. Smith, M. Prentiss, and G. M. Whitesides, “Fabrication of Glass Microstructures by Micro-Molding of Sol-Gel Precursors,” *Adv. Mater.*, **10**, 571-74 (1998).

[31] A. Kumar and G. M. Whitesides, "Features of Gold Having Micrometer to Centimeter Dimensions Can Be Formed Through a Combination of Stamping with an Elastomeric Stamp and an Alkanethiol 'Ink' Followed by Chemical Etching," *Appl. Phys. Lett*., **63**, 2002-4 (1993).

[32] A. Kumar, H. A. Biebuyck, and G. M. Whitesides, "Patterning Self-Assembled Monolayers: Applications in Materials Science," *Langmuir*, **10**, 1498-1511 (1994).

[33] N. L. Jeon, P. G. Clem, D. A. Payne, and R. G. Nuzzo, "A Monolayer-Based Lift-Off Process for Patterning Chemical Vapor Deposition Copper Thin Films," *Langmuir*, **12**, 5350-55 (1996).

[34] M. A. Dubois and P. Muralt, "Properties of Aluminum Nitride Thin Films for Piezoelectric Transducers and Microwave Filter Applications," *Appl. Phys. Lett*., **74**, 3032-34 (1999).

[35] M. G. Kang, K. T. Kim and C. I. Kim, "Plasma-Induced Damage in PZT Thin Films Etched by Inductively Coupled Plasma," *Thin Solid Films*, **435**, 222-26, (2003).

[36] H. D. Chen, K. R. Udayakumar, C. J. Gaskey, and L. E. Cross, "Electrical Properties' Maxima in Thin Films of the Lead Zirconate-Lead Titanate Solid Solution System," *Appl. Phys. Lett*., **67**, 3411-13 (1995).

[37] K. R. Oldham, J. S. Pulskamp, R. G. Polcawich, M. Dubey, "Thin-Film PZT Lateral Actuator with Extended Stroke," *Journal of Microelectromechanical Systems*, **17**, 890-99 (2008).

[38] E. Hong, S. Trolier-McKinstry, R. L. Smith, S. V. Krishnaswamy and C. B. Freidhoff, " Design of MEMS PZT Circular Diaphragm Actuators to Generate Large Deflections," *Journal of Microelectromechanical Systems*, **15**, 832-39 (2006).

[39] S. Aggarwal, S. R. Perusse, C. W. Tipton, R. Ramesh, H. D. Drew, T. Venkatsan, D. B. Romero, V. B. Podobedov, and A. Weber, "Effect of Hydrogen on Pb(Zr,Ti)O_3-Based Ferroelectric Capacitors," *Appl. Phys. Lett*., **73**, 1973-75 (1998).

[40] F. Xu, S. Trolier-McKinstry, W. Ren, B. M. Xu, Z. L. Xie, and K. J. Hemker, "Domain Wall Motion and its Contribution to the Dielectric and Piezoelectric Properties of Lead Zirconate Titanate Films," *J. Appl. Phys.*, **89**, 1336-48 (2001).

[41] W. L. Warren, D. Dimos, B. A. Tuttle, R. D. Nasby and G. E. Pike, "Electronic Domain Pinning in $Pb(Zr,Ti)O_3$ Thin Films and its Role in Fatigue," *Appl. Phys. Lett.*, **65**, 1018-20 (1994).

[42] S. C. Danforth and A. Safari, "Solid Freeform Fabrication: Novel Manufacturing Opportunities for Electronic Ceramics," *Proceedings of the Tenth IEEE ISAF Symposium*, 183-8 (1996).

[43] S. A. Uhland, R. K. Holman, M. J. Cima, E. Sachs, and Y. Enokido, "New Process and Materials Development in 3-Dimensional Printing, 3DP™," *Mat. Res. Soc. Symp. Proc.*, **542**, 153-158 (1999).

[44] J. Windle and B. Derby, "Ink Jet Printing of PZT Aqueous Ceramic Suspensions," *J. Mat. Sci. Lett.*, **18**, 87-90 (1999).

[45] B. Su, T. W. Button, A. Schneider, L. Singleton, P. Prewett, "Embossing of 3D Ceramic Microstructures," *Micro. Tech.*, **8**, 359-62 (2002).

[46] R. Maas, M. Koch, N. R. Harris, N. M. White, A. G. R. Evans, "Thick-Film Printing of PZT onto Silicon," *Mat. Lett.*, **31**, 109-112 (1997).

[47] B. Michel, A. Bernard, A. Bietsch, E. Delamarche, M. Geissler, D. Juncker, H. Kind, J. P. Renault, H. Rothuizen, H. Schmid, P. Schmidt-Winkel, R. Stutz and H. Wolf, "Printing Meets Lithography: Soft Approaches to High-Resolution Patterning," *IBM J. Res. and Dev.*, **45**, 697-719 (2001).

[48] J. A. Rogers, R. J. Jackman, G. M. Whitesides, "Microcontact Printing and Electroplating on Curved Substrates: Production of Free-Standing Three-Dimensional Metallic Microstructures," *Adv. Mat.*, **9**, 475-77 (1997).

[49] J. H. Kim, F. F. Lange, and C. I. Choen, "Epitaxial Growth of Patterned $SrBi_2Ta_2O_9$ Lines by Channel Stamping," *J. Mater. Res.*, **14**, 1194-96 (1999).

[50] J. S. Vartuli, M. Ozenba, C. M. Chun, M. Trau, and I. A. Aksay, "Micropatterned Lead Zirconium Titanate Thin Films," *J. Mater. Res.*, **18**, 1259-65 (2003).

[51] P. G. Clem, N. L. Jeon, R. G. Nuzzo, and D. A. Payne, " Monolayer-Mediated Deposition of Tantalum(V) Oxide Thin Film Structures from Solution Precursors," *J. Am. Ceram. Soc.*, **80**, 2821-27 (1997).

[52] N. L. Jeon, P. Clem, D. Y. Jung, W. Lin, G. S. Girolami, D. A. Payne, and R. G. Nuzzo, "Additive Fabrication of Integrated Ferroelectric Thin-Film Capacitors Using Self-Assembled Organic Thin-Film Templates," *Adv. Mater.*, **9**, 891-95 (1997).

[53] N. L. Jeon, P. G. Clem, R. G. Nuzzo, D. A. Payne, "Patterning of Dielectric Oxide Thin Layers by Microcontact Printing of Self-Assembled Monolayers," *J. Mater. Res.*, **10**, 2996-99 (1995).

[54] H. Nagata, S. W. Ko, E. Hong, C. A. Randall, and S. Trolier-McKinstry, "Microcontact Printed $BaTiO_3$ and $LaNiO_3$ Thin Films for Capacitors," *J. Am. Ceram. Soc.*, **89**, 2816-21 (2006).

[55] A. Kumar, N. L. Abbott, E. Kim, H. Biebuyck and G. M. Whitesides, "Patterned Self-Assembled Monolayers and Meso-Scale Phenomena," *Acc. Chem. Res.*, **28**, 219-26 (1995).

[56] C. R. Martin and A. Aksay, "Topographical Evolution of Lead Zirconate Titanate (PZT) Thin Films Patterned by Micromolding in Capillaries," *J. Phys. Chem. B.*, **107**, 4261-68 (2003).

[57] N. Y. Lee, J. R. Lim, M. J. Lee, S. Park, and Y. S. Kim, “Multilayer Transfer Printing on Microreservoir-Patterned Substrate Employing Hydrophilic Composite Mold for Selective Immobilization of Biomolecules,” *Langmuir*, **22**, 7689-94 (2006).

[58] N. Y. Lee, J. R. Lim, M. J. Lee, J. B. Kim, S. J. Jo, H. K. Baik, and Y. S. Kim, “Hydrophilic Composite Elastomeric Mold for High-Resolution Soft Lithography,” *Langmuir*, **22**, 9018-22 (2006).

[59] T. W. Odom, J. C. Love, D. B. Wolfe, K. E. Paul, and G. M. Whitesides, “Improved Pattern Transfer in Soft Lithography Using Composite Stamps,” *Langmuir*, **18**, 5314-20 (2002).

[60] R. A. Wolf and S. Trolier-McKinstry, “Temperature Dependence of the Piezoelectric Response in Lead Zirconate Titanate Films,” *J. Appl. Phys.*, **95**, 1397-406 (2004).

[61] G. Brennecka, C. M. Parish, B. A. Tuttle, L. N. Brewer, and M. A. Rodriguez, “Reversibility of the Perovskite-to-Fluorite Phase Transformation in Lead-Based Thin and Ultrathin Films,” *Adv. Mater.*, **20**, 1407-11 (2008).

[62] C. Donzel, M. Geisler, A. Bernard, H. Wolf, B. Michel, J. Hilborn, and E. Delamarche, “Hydrophilic Poly(dimethylsiloxane) Stamps for Microcontact Printing,” *Adv. Mater.*, **13**, 1164-67 (2001).

[63] I. Fujii, E. Hong and S. Trolier-McKinstry, “Thickness Dependence of Dielectric Nonlinearity of Lead Zirconate Titanate Films,” *IEEE Transactions on Ultrasonic, Ferroelectrics, and Frequency Control*, **57**, 1717-23 (2010).

[64] J. F. Shepard, P. J. Moses, S. Trolier-McKinstry, “The Wafer Flexure Technique for the Determination of the Transverse Piezoelectric Coefficient (d_{31}) of PZT Thin Films,” *Sens. and Act. A: Phys.*, **71**, 133-138 (1998).

[65] R. H. T. Wilke, P. J. Moses, P. Jousse, C. Yeager, S. Trolier-McKinstry, "Wafer Mapping of the Transverse Piezoelectric Coefficient, $e_{31,f}$, Using the Wafer Flexure Technique With Sputter Deposited Pt Strain Gauges," *Sens. and Act. A: Phys.*, **173**, 152-57(2011).

[66] G. S. Ferguson, M. K. Chadhury, H. A. Biebuych, and G. M. Whitesides, "Monolayers on Disordered Substrates: Self-Assembly of Alkyltrichlorosilanes on Surface-Modified Polyethylene and Poly(dimethylsiloxane)," *Macromolecules*, **26**, 5870-75 (1993).

[67] T. M. Shaw, S. Trolier-McKinstry and P. C. McIntyre, "The Properties of Ferroelectric Films at Small Dimensions," *Annu. Rev. Mater. Sci.*, **30**, 263-98 (2000).

[68] K. R. Udayakumar, P. J. Schuele, J. Chen, S. B. Krupanidhi, and L. E. Cross, "Thickness-Dependent Electrical Characteristics of Lead Zirconate Titanate Thin Films," *J. Appl. Phys.*, **77**, 3981-86 (1995).

[69] R. Hurchania and S. J. Milne, "Characterization of Sol-Gel $Pb(Zr_{0.53}Ti_{0.47})O_3$ Films in the Thickness Range 0.25-10 μm," *J. Mater. Res.*, **14**, 1852-59 (1999).

[70] C. D. E. Lakeman and D. A. Payne, "Apparent Thickness Effect on Properties of Ferroelectric PZT Thin Layers," *Ferroelectrics*, **152**, 145-50 (1994).

[71] R. Bouregba, G. Le Rhun, G. Poullain, and G. Leclerc, "Investigation of Thickness Dependence of the Ferroelectric Properties of $Pb(Zr_{0.6}Ti_{0.4})O_3$ Thin-Film Capacitors," *J. Appl. Phys.*, **99**, 034102 (2006).

[72] A. K. Tagantsev and I. A. Stolichnov, "Injection-Controlled Size Effect on Switching of Ferroelectric Thin Films," *Appl. Phys. Lett.*, **74**, 1326-28, (1999).

[73] J. J. Lee, C. L. Thio and S. B. Desu, "Electrode Contacts on Ferroelectric $Pb(Zr_xTi_{1-x})O_3$ and $SrBi_2Ta_2O_9$ Thin Films and Their Influence on Fatigue Properties," *J. Appl. Phys.*, **78**, 5073-78 (1995).

[74] S. Trolier-McKinstry, “Piezoelectric Films for MEMS Applications,” *J. Ceram. Soc. Jpn.*, **109**, S76-9 (2001).

[75] D. Damjanovic and M. Demartin, “The Rayleigh Law in Piezoelectric Ceramics,” *J. Phys. D: Appl. Phys.*, **29**, 2057-60 (1996).

[76] D. V. Taylor and D. Damjanovic, “Evidence of Domain Wall Contribution to the Dielectric Permittivity in PZT Thin Films at Sub-Switching Fields,” *J. Appl. Phys.*, **82**, 1973-75 (1997).

[77] D. Damjanovic, “Nonlinear Piezoelectric Response in Ferroelectric Ceramics,” pp. 125-35 in *Piezoelectric Materials: Advances in Science, Technology, and Applications. NATO science series. Series 3, High Technology, edited by C. Galassi, M. Dinescu, K. Uchino, and M. Sayer.* (Kluwer Academic Publishers, Dordrecht, 2000).

[78] V. S. Postnikov, V. S. Pavlov, and K. Turkov, “Internal Friction in Ferroelectrics due to Interaction of Domain Boundaries and Point Defects,” *J. Phys. Chem. Solids*, **31**, 1785-91 (1970).

[79] M. E. Lines and A. M. Glass, Principles and Applications of Ferroelectrics and Related Materials. (Clarendon Press, Oxford [Eng.], 1977), pp. xxi.

[80] R. Herbiet, U. Robels, H. Dederichs, and G. Arlt, “Domain Wall and Volume Contributions to Material Properties of PZT Ceramics,” *Ferroelectrics*, **98**, 107-21 (1989).

[81] K. Carl and K. H. Hardtl, “Electrical After-Effects in $Pb(Ti,Zr)O_3$ Ceramics,” *Ferroelectrics*, **17**, 473-86 (1978).

[82] C. R. Pike and A. P. Roberts, “Characterizing Interactions in Fine Magnetic Particle Systems Using First Order Reversal Curves,” *J. Appl. Phys.*, **85**, 6660-67 (1999).

[83] A. Stancu, D. Ricinschi, L. Mitoseriu, P. Postolache, and M. Okuyama, "First-Order Reversal Curves Diagrams for the Characterization of Ferroelectric Switching," *Appl. Phys. Lett.*, **83**, 3767-69 (2003).

[84] F. Preisach, "Über Die Magnetische Nachwirkung," *Zeitschrift fur Physik*, **94**, 277-302 (1935).

[85] G. Robert, D. Damjanovic, and N. Setter, "Preisach Modeling of Ferroelectric Pinched Loops," *Appl. Phys. Lett.*, **77**, 4413-15 (2000).

[86] C. R. Martin and I. A. Aksay, "Submicrometer-Scale Patterning of Ceramic Thin Films," *J. Electroceram.*, **12**, 53-68 (2004).

[87] A. J. Welsh, R. H. T. Wilke, M. A. Hickner, and S. Trolier-McKinstry, "Low-Cost, Damage-Free Patterning of Lead Zirconate Titanate Films," *J. Am. Ceram. Soc.*, **96**, 2799-805 (2013).

[88] A. A. Darhuber, S. M. Troian, and S. M. Miller, "Morphology of Liquid Microstructures on Chemically Patterned Surfaces," *J. Appl. Phys.*, **87**, 7768-75 (2000).

[89] K. J. Hsia, Y. Huang, E. Menard, J. Park, W. Zhou, J. Rodgers, and J. M. Fulton, "Collapse of Stamps for Soft Lithography Due To Interfacial Adhesion," *Appl. Phys. Lett.*, **86**, 154106 (2005).

[90] D.W. Carr and H. G. Craighead, "Fabrication of Nanoelectromechanical Systems in Single Crystal Silicon Using Silicon on Insulator Substrates and Electron Beam Lithography," *J. Vac. Sci. Technol. B*, **15** 2760-4 (1997).

[91] S. Guillon, S. Salomon, F. Seichepine, D. Dezest, F. Mathieu, A. Bouchier, L. Mazenq, C. Thibault, C. Vieu, T. Leichle, L. Nicu, "Biological Functionalization of Massively Parallel Arrays of Nanocantilevers Using Microcontact Printing," *Sens. and Act. B*, **161**, 1135-8 (2012).

[92] Y. Y. Huang, W. Zhou, K. J. Hsia, E. Menard, J. Park, J. A. Rodgers, and A, G. Alleyne, "Stamp Collapse in Soft Lithography," *Langmuir*, **21**, 8058-68 (2005).

[93] L. E. Scriven, “Physics and Application of Dip Coating and Spin Coating,” *Mat. Res. Soc. Symp. Proc.*, **121**, 717-29 (1988).

[94] Q. M. Zhang, H. Wang, N. Kim, and L. E. Cross, “Direct Evaluation of Domain-Wall and Intrinsic Contributions to the Dielectric and Piezoelectric Response and Their Temperature Dependence on Lead Zirconate-Titanate Ceramics,” *J. Appl. Phys.*, **75**, 454-9 (1994).

[95] J. L. Jones, M. Hoffman, J. E. Daniels, and A. J. Studer, “Direct Measurement of the Domain Switching Contribution to the Dynamic Piezoelectric Response in Ferroelectric Ceramics,” *Appl. Phys. Lett.*, **89**, 092901-3 (2006).

[96] J. F. Scott, “Applications of Modern Ferroelectrics,” *Science*, **315**, 954-9 (2007).

[97] L. Nicu and T. Leichle, “Biosensors and Tools for Surface Functionalization form the Macro- to the Nanoscale: The Way Forward,” *J. Appl. Phys.*, **104**, 111101-16 (2008).

[98] B. Ilic, Y. Yang, K. Aubin, R. Reichenbach, S. Krylov, and H. G. Craighead, “Enumeration of DNA Molecules Bound to a Nanomechanical Oscillator,” *Nanoletters*, **5**, 925-9 (2005).

[99] A. K. Naik, M. S. Hanay, W. K. Hiebert, X. L. Feng, and M. L. Roukes, “Towards Single-Molecule Nanomechanical Mass Spectrometry,” *Nat. Nanotech.*, **4**, 445-50 (2009).

[100] H. G. Craighead, “Nanoelectromechanical Systems,” *Science*, **290**, 1532-35 (2000).

[101] B. Illic, Y. Yang, K. Aubin, R. Reichenbach, S. Krylov, and H. G. Craighead, “Enumeration of DNA Molecules Bound to a Nanomechanical Oscillator,” *Nanoletters*, **5**, 925-29 (2005).

[102] L. Feng, F. Gao, M. Liu, S. Wang, L. Li, M. Shen, and Z. Wang, “Investigation of the Mechanical Bending and Frequency Shift Induced by Adsorption and Temperature Using Micro- and Nanocantilever Sensors,” *J. Appl. Phys.*, **112**, 013501-9 (2012).

[103] Z. Shen, W. Y. Shih, and W. H. Shih, "Self-exciting, Self-sensing $PbZr_{0.53}Ti_{0.47}O_3/SiO_2$ Piezoelectric Microcantilevers with Femtogram/Hertz Sensitivity," *Appl. Phys. Lett.*, **89**, 023506-3 (2006).

[104] Z. Shen, W. Y. Shih, and W. H. Shih, "Mass Detection Sensitivity of Piezoelectric Cantilevers with a Nonpiezoelectric Extension," *Rev. Sci. Instrum.*, **77**, 065101-10 (2006).

[105] H. H. Lou and Y Huang, "Electroplating" pp. 1-10 in *Encyclopedia of Chemical Processing* (Taylor & Francis 2006).

[106] T. Pearson and J. K. Dennis, "Facts and Fiction about Pulse Plating," *Trans. Inst. Metal Finish*, **69**, 75-9 (1991).

[107] F. Mathieu, F. Larramendy, D. Dezest, C. Huang, G. Lavallee, S. Miller, C. M. Eichfeld, W. Mansfield, S. Trolier-McKinstry, and L. Nicu, "Reducing Parasitic Effects of Actuation and Sensing Schemes for Piezoelectric Microelectromechanical Resonators," *Microelectronic Engineering*, **111**, 68-76 (2013).

[108] D. S. Park, V. Singh, B. H. You, N. Kim, P. C. Chen, S. A. Soper, D. E. Nikitopoulos, J. Goettert, and M. C. Murphy, "Control of Internal Stress for High Quality Nickel Large Area Mold Inserts," *Proc. of ASME 2009 Int. Mech. Eng. Congr. & Expo.*, IMECE2009-11639 (2009).

[109] R. Weil, "The Structure of Electrodeposits and the Properties That Depend on Them," *Annu. Rev. Mater. Sci.*, **19**, 165-82 (1989).

[110] J. Amblard, I. Epelboin, M. Froment, and G. Maurin, "Inhibition and Nickel Electrocrystallization," *J. Appl. Electrochem.*, **9**, 233-42 (1979).

[111] M. Y. Propereka, "Internal Stresses in Electrolytically Deposited Metals," *J. Electrochem. Soc.*, **115**, 287C (1968).

[112] www.discheminc.com, “Chemistry, Relationships and Trouble Shooting of Optical Media Electroforming Baths,” DisChem, Inc., EFMP 2102, pp 1-18

[113] S. A. Watson, “Nickel Sulfamate Solutions,” pp. 1-5 in *NiDI Technical Series 10052*, (Nickel Development Institute, Toronto, 1989).

[114] J. K. Luo, M. Pritschow, A. J. Flewitt, S. M. Spearing, N. A. Fleck, and W. I. Milne, “Effects of Process Conditions on Properties of Electroplated Ni Thin Films for Microsystem Applications,” *J. Electrochem. Soc.*, **153**, D155-61 (2006).

[115] Y. Tsuru, M. Nomura, and F. R. Foulkes, “Effects of Boric Acid on Hydrogen Evolution and Internal Stress in Films Deposited from a Nickel Sulfamate Bath,” *J. Appl. Electrochem.*, **32**, 629-34 (2002).

[116] T. D. Ziebell and C. A. Schuh, “Residual Stress in Electrodeposited Nanocrystalline Nickel-Tungsten Coatings,” *J. Mater. Res.*, **27**, 1271-84 (2012).

[117] G. G. Stoney, “The Tension of Metallic Films Deposited by Electrolysis,” *Proc. R. Soc. London, Ser. A*, **82**, 172-5 (1909).

[118] M. Gad-el-Hak, “MEMS Design and Fabrication,” pp. 3-199 – 3-120 in *The MEMS Handbook, 2nd Ed.*, (CRC Press, New York, 2001).

[119] C. K. Kwok and S. B. Desu, “Low Temperature Perovskite Formation of Lead Zirconate Titanate Thin Films by a Seeding Process” *J. Mater. Res.*, **8**, 339-44 (1993).

[120] T. J. Lee, H. Y. Song, and D. J. Chung, “ICP Etching Pt Thin Films for Fabrication of SAW Devices,” J. Kor. Phys. Soc., 42, S814-8 (2003).

[121] G. A. Di Bari, “Electrodeposition of Nickel,” pp. 79-114 in *Modern Electroplating, Fifth Ed.,* (John Wiley & Sons, Inc., 2010).

[122] M. Morozov, D. Damjanovic, and N. Setter, "The Nonlinearity and Subswitching Hysteresis in Hard and Soft PZT," *J. Euro. Ceram. Soc.*, **25**, 2483-86 (2005).

[123] U. Robels and G. Arlt, "Domain Wall Clamping in Ferroelectrics by Orientation of Defects," *J. Appl. Phys.*, **73**, 3454-60 (1993).

[124] R. Bechmann, "Elastic and Piezoelectric Constants of Alpha-Quartz," *Phys. Rev.*, **110**, 1060-61 (1958)

[125] B. Jaffe, W. R. Cook, and H. Jaffe, Piezoelectric Ceramics. New York, NY: Academic Press, 1971.

[126] S. Li, W. Cao, and L. E. Cross, "The Extrinsic Nature of Nonlinear Behavior Observed in Lead Zirconate Titanate Ferroelectric Ceramic," *J. Appl. Phys.*, **69**, 7219-24 (1991).

[127] D. Damjanovic and M. Demartin, "Contribution of the Irreversible Displacement of Domain Walls to the Piezoelectric Effect in Barium Titanate and Lead Zirconate Titanate Ceramics," *J. Phys. Condens. Matter*, **9**, 4943-53 (1997).

[128] F. Griggio, S. Jesse, W. Qu, A. Kumar, O. Ovchinnikov, D. S. Tinberg, S. V. Kalinin, and S. Trolier-McKinstry, "Composition Dependence of Local Piezoelectric Nonlinearity in $(0.3)Pb(Ni_{0.33}Nb_{0.67})O_3-(0.7)Pb(Zr_xTi_{1-x})O_3$ Films," *J. Appl. Phys.*, **110**, 044109-10 (2011).

[129] D. Damjanovic, "Contributions to the Piezoelectric Effect in Ferroelectric Single Crystals and Ceramics," *J. Am. Ceram. Soc.*, **88**, 2663-76 (2005).

[130] N. Setter, D. Damjanovic, L. Eng, G. Fox, S. Gevorgian, S. K. Hong, A. I. Kingon, H. Kohlstedt, N. Y. Park, G. B. Stephenson, I. Stolichnov, A. K. Taganstev, D. V. Taylor, T. Yamada, and S. K. Streiffer, "Ferroelectric Thin Films: Review of Materials, Properties, and Applications," *J. Appl. Phys.*, **100**, 051606-46 (2006).

[131] D. A. Hall, "Nonlinearity in Piezoelectric Ceramics," *J. Mater. Sci.*, **36**, 4575-601 (2001).

[132] V. Nagarajan, A. Roytburd, A. Stanishevsky, S. Prasertchoung, T. Zhao, J. Melngailis, O. Auciello, and R. Ramesh, "Dynamics of Ferroelastic Domains in Ferroelectric Thin Films," *Nat. Mater.*, **2**, 43-47 (2003).

[133] P. Paruch, A. B. Kolton, X. Hong, C. H. Ahn, and T. Giamarchi, "Thermal Quench Effects of Ferroelectric Domain Walls," *Phys. Rev. B*, **85**, 214115-7 (2012).

[134] A. Chandrasekaran, D. Damjanovic, N. Setter, and N. Marzari, "Defect Ordering and Defect-Domain Wall Interactions in $PbTiO_3$: A First-Principles Study," *Phys. Rev. B*, **88**, 214116-7 (2013).

[135] P. Jakes, E. Erdem, E. A. Eichel, L. Jin, and Damjanovic, "Position of Defects with Respect to Domain Walls in Fe^{3+}-Doped $Pb[Zr_{0.52}Ti_{0.48}]O_3$ Piezoelectric Ceramics," *Appl. Phys. Lett.*, **98**, 072907-3 (2011).

[136] S. Choudhury, Y. L. Li, C. Krill III, and L. Q. Chen, "Effect of Grain Orientation and Grain Size on Ferroelectric Domain Switching and Evolution: Phase Field Simulations," *Acta Mater.*, **55**, 1415-26 (2007).

[137] A. Y. Emelyanov and N. A. Pertsev, "Abrupt Changes and Hysteretic Behavior of 90° Domains in Epitaxial Ferroelectric Thin Films with Misfit Dislocations," *Phys. Rev. B*, **68**, 214103-10 (2003).

[138] D. M. Marincel, H. R. Zhang, J. Britson, A. Belianinov, S. Jesse, S. V. Kalinin, L. Q. Chen, W. M. Rainforth, I. M. Reaney, C. A. Randall, and S. Trolier-McKinstry, "Domain Pinning Near a Single-Grain Boundary in Tetragonal and Rhombohedral Lead Zirconate Titanate Films," *Phys. Rev. B.*, **91**, 134113-12 (2015).

[139] X. Tan and J. K. Shang, "Partial Dislocations at Domain at Domain Intersections in a Tetragonal Ferroelectric Crystal," *J. Phys. Condens. Matter*, **16,** 1455-66 (2004).

[140] D. V. Taylor and D. Damjanovic, "Domain Wall Pinning Contribution to the Nonlinear Dielectric Permittivity in Pb(Zr,Ti)O_3 Films," *Appl. Phys. Lett.*, **73**, 2045-47 (1998).

[141] A. Pramanick, D. Damjanovic, J. C. Nino, and J. L. Jones, "Subcoercive Cyclic Electrical Loading of Lead Zirconate Titanate Ceramics I: Nonlinearities and Losses in the Converse Piezoelectric Effect," *J. Am. Ceram. Soc.*, **92**, 2291-99 (2009).

[142] C. H. Ahn, T. Tybell, L. Antognazza, K. Char, R. H. Hammond, M. R. Beasley, O. Fischer, J. M. Triscone, "Local, Nonvolatile Electronic Writing of Epitaxial $Pb(Zr_{0.52}Ti_{0.48})O_3/SrRuO_3$ Heterostructures," Science, 276, 1100-03 (1997).

[143] A. Gruverman, H. Tokumoto, A.S. Prakash, S. Aggarwal, B. Yang, M. Wuttig, R. Ramesh, O. Auciello, and T. Venkatesan, "Nanoscale Imaging of Domain Dynamics and Retention in Ferroelectric Thin Films," *Appl. Phys Lett.*, **71**, 3492-94 (1997).

[144] S. Hong, J. Woo, H. Shin, J. U. Jeon, Y. E. Pak, E. L. Colla, N. Setter, E. Kim, and K. No, "Principle of Ferroelectric Domain Imaging Using Atomic Force Microscopy," *J. Appl. Phys.*, **89**, 1377-86 (2001).

[145] A. Gruverman, A. Kholkin, A. Kingon, and H. Tokumoto, "Asymmetric Nanoscale Switching in Ferroelectric Thin Films by Scanning Force Microscopy," *Appl. Phys. Lett.*, **78**, 2751-53 (2001).

[146] P. Bintachitt, S. Jesse, D. Damjanovic, Y. Han, I. M. Reaney, S. Trolier-McKinstry, and S. V. Kalinin, "Collective Dynamics Underpins Rayleigh Behavior in Disordered Polycrystalline Ferroelectrics," *Proc. Natl. Acad. Sci. U. S. A.*, **107**, 7219-24 (2010).

[147] C. Durkan, M. E. Welland, D. P. Chu, and P. Migliorato, “Probing Domains at the Nanometer Scale in Piezoelectric Thin Films,” *Phys. Rev. B*, **60**, 16198-204 (1999).

[148] S. V. Kalinin and D. A. Bonnell, “Local Potential and Polarization Screening on Ferroelectric Surfaces,” *Phys. Rev. B*, **63**, 125411-13 (2001).

[149] T. Tybell, P. Paruch, T. Giamarchi, and J. M. Triscone, “Domain Wall Creep in Epitaxial Ferroelectric $Pb(Zr_{0.2}Ti_{0.8})O_3$ Thin Films,” *Phys. Rev. Lett.*, **89**, 097601-4 (2002).

[150] P. Paruch, T. Giamarchi, T. Tybell, and J. M. Triscone, “Nanoscale Studies of Domain Wall Motion in Epitaxial Ferroelectric Thin Films,” *J. Appl. Phys.*, **100**, 051608-10 (2006).

[151] B. J. Rodriguez, Y. H. Chu, R. Ramesh, and S. V. Kalinin, “Ferroelectric Domain Wall Pinning at a Bicrystal Grain Boundary in Bismuth Ferrite,” *Appl. Phys. Lett.*, **93**, 142901-3 (2008).

[152] S. Jesse, S. V. Kalinin, R. Proksch, A. P. Baddorf, and B. J. Rodriguez, “The Band Excitation Method in Scanning Probe Microscopy for Rapid Mapping of Energy Dissipation on the Nanoscale,” *Nanotech.*, **18**, 435503-8 (2007).

[153] S. Jesse and S. V. Kalinin, “Band Excitation in Scanning Probe Microscopy: Sines of Change,” *J. Phys. D: Appl. Phys.*, **44**, 464006-16 (2011).

[154] S. Jesse, R. K. Vasudevan, L. Collins, E. Strelcov, M. B. Okatan, A. Belianinov, A. P. Baddorf, R. Proksch, and S. V. Kalinin, “Band Excitation in Scanning Probe Microscopy: Recognition and Functional Imaging,” *Annu. Rev. Phys. Chem.*, **65**, 519-36 (2014).

[155] R. Vasudevan, D. M. Marincel, S. Jesse, Y. Kim, A. Kumar, S. Kalinin, and S. Trolier-McKinstry, “Polarization Dynamics in Ferroelectric Capacitors: Local Perspective on Emergent Collective Behavior and Memory Effects,” *Adv. Funct. Mater.*, **23**, 2490-508 (2013).

[156] M. Kopycinska-Müller, R. H. Geiss, and D. C. Hurley, "Contact Mechanics and Tip Shape in AFM-Based Nanomechanical Measurements," *Ultramicroscopy*, **106**, 466-74 (2006).

[157] F. Griggio, S. Jesse, A. Kumar, O. Ovchinnikov, H. Kim, T. N. Jackson, D. Damjanovic, S. V. Kalinin, and S. Trolier-McKinstry, "Substrate Clamping Effects on Irreversible Domain Wall Dynamics in Lead Zirconate Titanate Thin Films," *Phys. Rev. Lett.*, **108**, 49-67 (2012).

[158] F. Griggio, S. Jesse, A. Kumar, D. M. Marincel, D. S. Tinberg, S. V. Kalinin, and S. Trolier-McKinstry, " Mapping Piezoelectric Nonlinearity in the Rayleigh Regime Using Band Excitation Piezoresponse Force Microscopy," *Appl. Phys. Lett.*, **98**, 212901-3 (2011).

[159] D. M. Marincel, H. Zhang, S. Jesse, A. Belianinov, M. B. Okatan, S. V. Kalinin, W. M. Rainforth, I. M. Reaney, C. A. Randall, and S. Trolier-McKinstry, "Domain Wall Motion across Various Grain Boundaries in Ferroelectric Thin Films," *J. Amer. Ceram. Soc.*, **98**, 1848-57 (2015).

[160] D. M. Marincel, S. Jesse, A. Belianinov, M. B. Okatan, S. V. Kalinin, T. N. Jackson, C. A. Randall, and S. Trolier-McKinstry, "A-Site Stoichiometry and Piezoelectric Response in Thin Film $PbZr_{1-x}Ti_xO_3$," *J. Appl. Phys.*, **117**, 204104-8 (2015).

[161] S. Jesse, P. Maksymovyvh, and S. V. Kalinin, "Rapid Multidimensional Data Acquisition in Scanning Probe Microscopy Applied to Local Polarization Dynamics and Voltage Dependent Contact Mechanics," *Appl. Phys. Lett.*, **93**, 112903-3 (2008).

[162] A. U. Kareem and S. D. Solares, "Characterization of Surface Stiffness and Probe-Sample Dissipation Using the Band Excitation Method of Atomic Force Microscopy: A Numerical Analysis," *Nanotech.*, **23**, 015706-14 (2012).

[163] R. Keech, S. Shetty, M. A. Kuroda, X. H. Liu, G. J. Martyna, D. M. Newns, and S. Trolier-McKinstry, “Lateral Scaling of $Pb(Mg_{1/3}Nb_{2/3})O_3$-$PbTiO_3$ Thin Films for Piezoelectric Logic Applications,” *J. Appl. Phys.*, **115**, 234106-8 (2014).

[164] R. H. Liang, D. Rèmiens, C. Soyer, N. Sama, X. L. Dong, and G. S. Wang, “ Etching Characteristics and Absence of Electrical Properties Damage of PZT Thin Films Etched Before Crystallization,” *Microelectronic Engineering*, **85**, 670-74 (2008).

[165] M. G. Kang, K. T. Kim, C. I. Kim, “Recovery of Plasma-Induced Damage in PZT Thin Films with O_2 Gas Annealing,” *Thin Solid Films*, **398**, 448-453 (2001).

[166] W. Pan, C. L. Thio, and S. B. Desu, “Reactive Ion Etching Damage to the Electrical Properties of Ferroelectric Thin Films,” *J. Mater. Res.*, **13**, 362-67 (1998).

[167] K. Carl and K. H. Haerdtl, “Electrical After-Effects in $Pb(Ti,Zr)O_3$ Ceramics,” *Ferroelectrics*, **17**, 473-86 (1978).

[168] J. I. Yang, R. G. Polcawich, L. M. Sanchez, and S. Trolier-McKinstry, “Effect of Feature Size on Dielectric Nonlinearity of Patterned $PbZr_{0.52}Ti_{0.48}O_3$ Films,” *J. Appl. Phys.*, **117**, 014103-7 (2015).

[169] T. Ting-Ao, C. Zheng, L. Ning, and Z. Si-Xun, “Reactive Ion Etching of Sol-Gel Derived PZT Thin Film and Pt/Ti Bottom Electrode for FRAM,” *Ferroelectrics*, **232**, 47-52 (1999).

[170] G. E. Menk, S. B. Desu, W. Pan and D. P. Vijay, “Dry Etching in the Integration of Ferroelectric Thin Film Capacitors,” *Mat. Res. Soc. Symp. Proc.*, **433**, 189-200 (1996).

[171] N. Ledermann, P. Muralt, J. Baborowski, S. Gentil K. Mukati, M. Cantoni, A. Seifert, and N. Setter, “{100}-Textured, Piezoelectric $Pb(Zr_x, Ti_{1-x})O_3$ Thin Films for MEMS: Integration, Deposition and Properties,” *Sensors and Actuators A*, **105**, 162-170 (2003).

[172] I. D. Brown and R. D. Shannon, “Empirical Bond-Strength-Bond-Length Curve for Oxides,” *Acta Cryst.,* **A29**, 266-282 (1973).

[173] A. J. Moulson and J. M. Herbert, *Electroceramics*, England: John Wiley & Sons Ltd, pg. 13, 2003.

[174] M. M. Saad, R. M. Bowman, and J. M. Gregg, “Characteristics of Single Crystal “Thin Film” Capacitor Structures Made Using a Focused Ion Beam Microscope,” *Appl. Phys. Lett.*, **84**, 1159-61 (2004).

[175] M. J. Lefevre, J. S. Speck, R.W. Schwartz, D. Dimos, and S.J. Lockwood, “Microstructural Development in Sol-gel Derived Lead Zirconate Titanate Thin Films: The Role of Precursor Stoichiometry and Processing Environment,” *J. Mater. Res.*, **11**, 2076-84 (1996).

[176] R. W. Schwartz, “Chemical Solution Deposition of Perovskite Thin Films,” *Chem. Mater.*, **9**, 2325-40 (1997).

[177] K. Yoshii, Y. Hiruma, H. Nagata, and T. Takenaka, “Electrical Properties and Depolarization Temperature of $(Bi_{1/2}Na_{1/2})TiO_3$-$(Bi_{1/2}K_{1/2})TiO_3$ Lead-Free Piezoelectric Ceramics,” *Jpn. J. Appl. Phys.*, **45**, 4493-96 (2006).

[178] T. R. Shrout and S. J. Zhang, “Lead-Free Piezoelectric Ceramics: Alternatives for PZT?,” *J. Electroceram.*, **19**, 111-24 (2007).

[179] C. W. Ahn, S. Y. Lee, H. J. Lee, A. Ullah, J. S. Bae, E. D. Jeong, J. S. Choi, B. H. Park, and I. W. Kim, “The Effect of K and Na Excess on the Ferroelectric and Piezoelectric Properties of $K_{0.5}Na_{0.5}NbO_3$ Thin Films,” *J. Phys. D: Appl. Phys.*, **42**, 215304-5 (2009).

[180] S. Y. Lee, C. W. Ahn, A. Ullah, H. J. Seog, J. S. Kim, S. H. Bae, and I. W. Kim, “Effect of Mn Substitution on Ferroelectric and Leakage Current Characteristics of Lead Free $(K_{0.5}Na_{0.5})(Mn_xNb_{1-x})O_3$ Tin Films,” *Curr. Appl. Phys.*, **11**, 5266-69 (2011).

[181] R. E. Jaeger and L. Egerton, “Hot Pressing of Potassium-Sodium Niobates,” *J. Am. Ceram. Soc.*, **45**, 209-213 (1962).

[182] G. H. Haertling, “Properties of Hot-Pressed Ferroelectric Alkali Niobate Ceramics,” *J. Am. Ceram. Soc.*, **50**, 329-330 (1967).

[183] R. Wang, R. Xie, T. Sekiya, Y. Shimojo, Y. Akimune, N. Hirosaki, and M. Itoh, “Piezoelectric Properties of Spark-Plasma-Sintered $(Na_{0.5}K_{0.5})NbO_3$-$PbTiO_3$ Ceramics,” *Jpn. J. Appl. Phys.*, **41**, 7119-22 (2002).

[184] K. Tanaka, H. Hayashi, K. I. Kakimoto, H. Ohsato, and T. Iijima, “Effect of (Na,K)-Excess Precursor Solutions on Alkoxy-Derived $(Na,K)NbO_3$ Powders and Thin Films,” *Jpn. J. Appl. Phys.*, **46**, 6964-70 (2007).

[185] Y. Nakashima, W. Sakamoto, H. Maiwa, T. Shimura, and T. Yogo, “Lead-Free Piezoelectric $(K,Na)NbO_3$ Thin Films Derived from Metal Alkoxide Precursors,” *Jpn. J. Appl. Phys.*, **14**, L311-13 (2007).

[186] Y. Kizaki, Y. Noguchi, and M. Miyayama, “Defect Control for Low Leakage Current in $K_{0.5}Na_{0.5}NbO_3$ Single Crystals,” *Appl. Phys. Lett.*, **89**, 142910-3 (2006).

[187] L. Zheng, X. Huo, R. Wang, J. Wang, W. Jiang, and W. Cao, “Large Size Lead-Free $(Na,K)(Nb,Ta)O_3$ Piezoelectric Single Crystal: Growth and Full Tensor Properties,” *Cryst. Eng. Comm.*, **15**, 7718-22 (2013).

[188] M. Kosec and D. Kolar, “On Activated Sintering and Electrical Properties of $NaKNbO_3$,” *Mat. Res. Bull.*, **10**, 335-340 (1975).

[189] E. Li, H. Kakemoto, S. Wada, and T. Tsurumi, "Effect of Small Amount CuO Doping on Microstructure and Properties of the Alkaline Niobate-Based Lead-Free Ceramics," *Ferroelectrics*, **358**, 153-160 (2007).

[190] D. Lin, K. W. Kwok, and H. L. W. Chan, "Microstructure, Phase Transition, and Electrical Properties of $(K_{0.5}Na_{0.5})_{1-x}Li_x(Nb_{1-y}Ta_y)O_3$ Lead-Free Piezoelectric Ceramics," *J. Appl. Phys.*, **102**, 034102-7 (2007).

[191] C. W. Ahn, E. D. Jeong, S. Y. Lee, H. J. Lee, S. H. Kang, and I. W. Kim, "Enhanced Ferroelectric Properties of $LiNbO_3$ Substituted $Na_{0.5}K_{0.5}NbO_3$ Lead-Free Thin Films Grown by Chemical Solution Deposition," *Appl. Phys. Lett.*, **93**, 212905-3 (2008).

[192] S. Y. Lee, C. W. Ahn, J. S. Kim, A. Ullah, H. J. Lee, H. I. Hwang, J. S. Choi, B. H. Park, I. W. Kim, "Enhanced Piezoelectric Properties of Ta Substituted-$(K_{0.5}Na_{0.5})NbO_3$ Films: A Candidate for Lead-Free Piezoelectric Thin Films," *Journal of Alloys and Compounds*, **509**, L194-L198 (2011).

[193] L. Wang, W. Ren, P. Shi, X. Chen, X. Wu, and X. Yao, "Enhanced Ferroelectric Properties in Mn-Doped $K_{0.5}Na_{0.5}NbO_3$ Thin Films Derived From Chemical Solution Deposition," *Appl. Phys. Lett.*, **97**, 072902-3 (2010).

[194] S. Miyake, K. Yamamoto, S. Fujihara, and T. Kimura, "(100)-Orientation of Pseudocubic Perovskite-Type $LaNiO_3$ Thin Films on Glass Substrates via the Sol-Gel Process," *J. Am. Ceram. Soc.*, **85**,992-4 (2002).

[195] G. Robert, D. Damjanovic, and N. Setter, "Preisach Distribution Function Approach to Piezoelectric Nonlinearity and Hysteresis," *J. Appl. Phys.*, **90**, 2459-64 (2001).

[196] A. K. Tagantsev, L. E. Cross, and J. Fousek, *Domains in Ferroelectric Crystals and Thin Films* (Springer, New York, 2010).

[197] S. Guo, O. S. Ovchinnikov, M. E. Curtis, M. B. Johnson, S. Jesse, and S. V. Kalinin, "Spatially Resolved Probing of Preisach Density in Polycrystalline Ferroelectric Thin Films," *J. Appl. Phys.*, **108**, 084103-10 (2010).

[198] O. Ovchinnikov, S. Jesse, S. Guo, K. Seal, P. Bintachitt, I. Fujii, S. Trolier-McKinstry, and S. V. Kalinin, "Local Measurements of Preisach Densities in Polycrystalline Ferroelectric Capacitors Using Piezoresponse Force Spectroscopy," *Appl. Phy. Lett.*, **96**, 112906 (2010).

[199] W. A. Zisman, "Influence of Constitution on Adhesion," *Ind. Eng. Chem.*, **55**, 18-38 (1963).

[200] D. E. Packham, "Work of Adhesion: Contact Angles and Contact Mechanics," *Int. J. Adhesion and Adhesives*, **16**, 121-28 (1996).

[201] C. Liu, *Foundations of MEMS* (Pearson, New Jersey, 2006).

Vita

Aaron Welsh

Aaron Welsh was born in Pottstown, Pennsylvania on October 25th 1985. He is the youngest of five children. He received his Bachelor in Materials Science and Engineering from the Pennsylvania State University in 2008. After graduating, he worked for the U.S. Department of Energy at the Los Alamos National Laboratory working in the Weapons Component Manufacturing division. In the fall of 2009 he came back to the Pennsylvania State University and began his doctorate degree in Materials Science and Engineering under the guidance of Dr. Susan Trolier-McKinstry.